DOCTORAL THESIS

Imaging ellipsometry as a novel detection method for protein-protein interactions

Author:

John James TOMES

Supervisors:

Dr. Russ MORPHEW

Dr. Dave LANGSTAFF

A thesis submitted in fulfillment of the requirements

for the degree of Doctor of Philosophy

in the joint departments of

Parasitology & Epidemiology

Materials Physics

29th September 2019

Declaration of Authorship

I, John James TOMES, confirm that this thesis titled, "Imaging ellipsometry as a novel detection method for protein-protein interactions"

STATEMENT 1

- This thesis is the result of my own investigations, except where otherwise stated.

- Where ***correction services** have been used, the extent and nature of the correction is clearly marked in a footnote(s). [*this refers to the extent to which the text has been corrected by others]

- Other sources are acknowledged by footnotes giving explicit references.

- A bibliography is appended.

- This work has not previously been accepted in substance for any degree and is not being concurrently submitted in candidature for any degree.

Signed:

_____

Date:

_____

STATEMENT 2

- I hereby give consent for my thesis, if accepted, to be available for photo-copying and for inter-library loan, and for the title and summary to be made available to outside organizations.

Signed:

_____

Date:

_____

"Find something that's good and stick it in here!"

John Tomes

Abstract

Imaging ellipsometry as a novel detection method for protein-protein interactions

by John James TOMES

This thesis describes the use of a novel imaging ellipsometry system to detect protein-protein interactions (PPI) with an emphasis on antigen-antibody interaction (AAI) for potential use as a diagnostic technique. Consequently, a practical method for the detection of AAI using a bio-sensor based approach, imaged by the Aberystwyth Imaging Ellipsometer (AIE) is described. A case study bio-sensor was fabricated by the immobilization of an anti-*Fasciola hepatica* sigma class glutathione transferase (FhGST-S1) antibody and probed with analyte solutions derived from the zoonotic parasite *F. hepatica*. Specifically, incubation of biosensors with recombinant FhGST-S1 produced a detectable change in film thickness of 5.6($\pm$0.91)nm in strong agreement with the protein size as described previously. Furthermore, analysis of the biosensor with *F. hepatica* extracellular vesicles (EV) also generated a detectable change in film thickness of 8.2($\pm$1.02)nm. However, this observed change in thickness was less than that typically expected for EVs, which at a minimum are noted to be 10-50nm. Nevertheless, this approach has indicated the use of AAI in combination with a bio-sensor and AIE, for the potential diagnosis of *F. hepatica* infection. Given the early success documented throughout this work, this research highlights the AIE for detecting AAI in a non-contact, non-destructive and label free way. Specifically the use of the AIE has merit in its simplicity of operation and low cost, which holds the potential for further improvement and development for use in the diagnostics of infectious diseases.

Acknowledgements

This is not something anyone does alone and I would like to acknowledge and thank some of the people who have helped me through my studies. I say some because to truly list all of those who have supported me, with everything from kind words to cold hard cash for kit and equipment, would require a document almost as long as this thesis.

I would first like to thank both my supervisors Dr's Russ Morphew and Dave Langstaff for providing me the opportunity to embark on this incredible journey. Their ceaseless enthusiasm, support and patience has been very much appreciated and vital in getting me through to this point.

I need to thank in alphabetical order! my Physics colleagues and fellow PhD students: Jon A, Jonno A, Simon A, Anita BB, Rachel C, Simon C, Joe D, Les D, Nathan D, Steve F, Carys H, Matt J, David L, Giselle M, Ben R, Barry T, and Kerry W. My biology colleagues and fellow PhD students: Nathan A, Alan C, Clare C, David C, Chelsea D, Alex F, Jo FT, Kat H, Rhys J, Cat P, Claire R, Fiona T, Helen W. They have all made going to work a most enjoyable experience. However, a special mention must go to Dr. Matt Gunn and Dr. Becky Stuart, both of whom I cannot praise highly enough for their friendship, technical support and willingness to pass on skills and knowledge that has been fundamental to making this project possible, I am genuinely indebted to you both.

This study was made possible through the generous funding of Aberystwyth University for which I am very grateful. I have received training funded by the Barrett Center for Helminth Control and once more I would like to express my thanks.

In addition to work colleagues, I must also thank my family and friends who have supported and encouraged me along the way and without whom everything would be much less significant.

Not least, my final and most important thanks must go to Wendy, my long suffering wife, for her constant love, support and understanding.

Contents

List of Figures

List of Tables

List of Abbreviations

AAI	**A**ntigen **A**ntibody **I**nteraction
AFM	**A**tomic **F**orce **M**icroscopy
AIE	**A**berystwyth **I**maging **E**llipsometer
APTES	3-**A**mino**P**ropyl**T**ri**E**thoxy**S**ilane
AU	**A**berystwyth **U**niversity
BCIP	**B**romo **C**hloro **I**ndiol **P**hosphate
BSA	**B**ovine **S**erum **A**lbumin
CBP	**C**almodulin **B**inding **P**eptide
Co-IP	**Co** **I**mmuno **P**recipitation
CTM-T	**C**asein **T**hi**M**erosal **T**hinner
DC	**D**ifferential **C**entrifugation
dH$_2$O	**d**istilled **W**ater
DIM	**D**ynamic **I**maging **M**icroellipsometry
DMEM	**D**ulbecco's **M**odified **E**agle's **M**edium
DPSS	**D**iode **P**umped **S**olid **S**tate
ESI	**E**lectro **S**pray **I**onisation
EV	**E**xtracellular **V**esicle
FCE	**F**inished **C**onsultant **E**pisode
FEC	**F**aecal **E**gg **C**ount
FERG	**F**oodborne **E**pidemiology **R**eference **G**roup
GST	**G**lutathione **S**igma class **T**ransferase
HEPES	4-(2-**H**ydroxy**E**thyl)-1-**P**iperazine**E**thane**S**ulfonic acid
IP	**I**mmuno **P**recipitation

ISEV	International Society for Extracellular Vesicles
LB-ADSA	Low Bond Asymetric Drop Shape Analysis
LCPR	Liquid Crystal Polarization Rotator
LCVR	Liquid Crystal Variable Retarder
LED	Light Emiting Diode
MALDI	Matrix Assisted Laser Desorption Ionization
MTF	Modulation Transfer Function
NBT	Nitro Blue Tetrazolium
NCP	Nitro Cellulose Paper
NHS	National Health Service
PAGE	Poly Acrylamide Gel Electrophoresis
PBS	Phosphate Buffer Solution
PNG	Portable Network Graphics
PPI	Protein Protein Interaction
PSPD	Position Sensitive Photo Diode
PVDF	PolyVinylidene DiFluoride
RA	Roughness Average
RCF	Relative Centrifugal Force
SEC	Size Exclusion Chromatography
SDS	Sodium Dodecyl Sulphate
SNR	Signal Noise Ratio
SOP	Standard Operating Proceedure
SPM	Scanning Probe Microscopy
SPR	Surface Plasmon Resonance
TBS	Tris Buffered Saline
TCA	Theoretical Contact Angle
TCBZ	TriClaBendaZole
TEM	Transmission Electron Microscopy

TEV	**T**obacco **E**tch **V**irus
TGR	**T**hioredoxin **G**lutathione **R**edutase
TOF	**T**ime **O**f **F**light
TRPS	**T**unable **R**esistive **P**ulse **S**ensing
TTBS	**T**ween **T**ris **B**uffered **S**aline
VI	**V**irtual **I**nstrument
WHO	**W**orld **H**ealth **O**rganization
WPI	**W**eeks **P**ost Infection

List of Publications

Publications that have been produced as a result of this thesis include:

Davis, C., Phillips, H., Tomes, J.J., Swain, M., Wilkinson, T., Brophy, P., Morphew, R., "The importance of extracellular vesicle purification for downstream analysis: A comparison of differential centrifugation and size exclusion chromatography for helminth pathogens", *PLOS Neglected Tropical Diseases*, vol. 13, number 2, pages e0007191, 2019, issn 1935-2735, DOI; 10.1371/journal.pntd.0007191, Available: http://dx.plos.org/10.1371/journal.pntd.0007191,

Kuipers M.E., Nolte't Hoen E.N.M., van der Ham A.J., Ozir-Fazalalikhan A., Nguyen D.L., de Korne C.M., Koning R.I., Tomes J.J., Hoffmann K.F., Smits H.H., Hokke C.H., "Extracellular vesicles from *Schistosoma mansoni* larvae are glycosylated and internalised via DC-SIGN to activate monocyte-derived dendritic cells" *Journal of Extracellular Vesicles*, vol. 9, issue: 1, 2020. DOI: 10.1080/20013078.2020.1753420 Available: https://www.tandfonline.com/doi/full/10.1080/20013078.2020.1753420

Allen, N. R., Lock, A., Phillips, H., Tomes, J.J., Brophy, P. M., Morphew, R. M. "The extracellular vesicles of the rumen fluke Calicophoron daubneyi induce species richness in the host microbiome". *Scientific Reports*[Submitted].

I would like to dedicated this work to my father who sadly, did not survive to see it complete . . .

Chapter 1

Introduction

1.1 General introduction: overview

Protein-protein interactions (PPI) are fundamentally important to almost all biological processes [1], [2]. Given this importance, the primary objective of this thesis was to investigate the interaction of light, via ellipsometry, with key target antigen and antibody proteins from *Fasciola hepatica* to better understand the potential of imaging ellipsometry as a diagnostic tool.

The development of suitable observation and characterization techniques is fundamental to the informed understanding of PPI given the complex biological processes involved. This study concentrates throughout on the more distinct PPI of antigen antibody interaction (AAI) , a mechanism first proposed by Goldberg [3]. A novel instrument for the observation of AAI is the Aberystwyth Imaging Ellipsometer (AIE) which unlike many existing methods to detect AAI can provide a non-contact, non-destructive and label free means to optically monitor proteins as they interact to build and form ultra-thin films.

Specifically this study hoped to develop the AIE with the view of optimizing the observation of AAIs. Such an approach required the identification of a suitable model AAI system to validate the AIE. Furthermore, investigation was required to develop the concept and means for constructing a protein micro array, one that can be measured by the AIE in a reliable and informative way.

An AAI case study using proteins from the parasitic flatworm *Fasciola hepatica* has clear societal and economic merit, with the World Health Organization (WHO) estimating between 2.4 and 17 million human individuals suffering from fascioliasis with a further 180 million at risk of infection [4]. Furthermore, the economic costs to livestock production exceed $3billion annually [5]. Proteins and protein containing extracellular vesicles (EVs) released by *F. hepatica* as excretory and secretory products offer themselves as both bio-markers of infection and potential targets for chemotherapeutic and vaccine development [6]–[8].

Proteins are typically in the physical size range of 5-20nm [9] with EVs ranging from 30-300nm [10], placing both beyond the optical diffraction limit imposed by the wave nature of light, a feature that limits conventional optical microscopy to a minimum size resolution limit of around 500nm [11]. However, it is possible to measure the thickness of ultra-thin films down to a sub nanometer resolution by means of the optical technique, ellipsometry. Ellipsometry is a powerful and widely used method which measures the change in state of polarized light on reflection from a sample surface, providing detailed information on the optical properties and structure of the sample and any thin film over-layers. The term ellipsometer was first used by Rothen *et al.* to describe an instrument that was built for the specific purpose of observing AAI in the form of thin films formed on a solid substrate [12].

1.2   Introduction to thesis topics and chapters

Chapter 1: Provides an introduction to the thesis subject by describing the details of ellipsometry and how imaging ellipsometry in particular can advance the observation and exploration of AAI in a new and unique way. A description is given for *Fasciola hepatica* and why the proteins and EVs from this parasite were used as a model system for observation of AAI using the AIE. Importantly, the existing

methods for observing PPI are reviewed, highlighting their relative strengths and weaknesses thus leading to the use of the AIE as a novel approach.

Chapter 2: Presents a detail description of the AIE and development of the unique features of the instrument that make it particularly suited to the observation of AAI.

Chapter 3: Describes the details for the range of supplementary techniques that have been used to develop the concept and construction of a bio-sensor protein array that can be used to indicate the presence of AAIs when measured by the AIE.

Chapter 4: Outlines the selection process to identify model AAI studies and describes the developmental steps necessary to deliver them in a functional way for observation and measurement by the AIE.

Chapter 5: Presents the key findings of the refined AIE instrument as applied to the case study proteins and EVs. Highlighting the findings from specific AAI observations.

Chapter 6: Provides a conclusion and discussion, outlining the areas of weakness and indicating the implications and recommendations for future work.

1.3 Existing PPI and AAI methods

It has been proposed that the human genome encodes over 500,000 separate protein structures and each cell can produce more than 10,000 individual protein types at any given time and in addition it has been suggested that over 80% of proteins do not function in isolation but as some form of stable or transient complex [2]. At present there are a wide range of existing techniques available for investigating PPIs, all with relative merits and weaknesses and which can be grouped into 4 main categories (Table 1.1), from which those most popular and relevant as a comparison to this study are described in more detail.

TABLE 1.1: Existing techniques for monitoring PPIs; ordered by method, outlining the principal advantages and disadvantages.

PPI Group	PPI Method	Advantages	Disadvantages
BioChemical	Western blotting	Low cost, high specificity	Low throughput and difficult to automate
	Immunoprecipitation & co-IP	Low cost	Low throughput, potential for cross reactivity
Optical	Ellipsometry	Label free, can be real time	Low throughput
	Immuno-labeling	Low cost	Binary PPIs, potential for cross reactivity
	ELISA	Low cost, antibody availability	Slow, potential for cross reactivity
BioPhysical	Atomic Force Microscopy	Label free	High cost, low throughput
	F R E T	Low cost, can be in vivo	Dual labeling required
	Surface Plasmon Resonance	Label free, real time	Binary PPIs
	Mass Spectrometry	Label free, high throughput	High cost
Genetic	Yeast 2 Hybrid	Low cost	Binary PPIs
	Tandem affinity purification	Low cost	Binary PPIs

1.3.1 Bio-chemical observation of AAI

1.3.1.1 Western blotting

Reviews by Bass *et al.* [13] and Kurien *et al.* [14] give an excellent overview of technical considerations for western blotting and provides the basis for the description that follows. Western blotting is a very popular and refined technique, where by a specific primary antibody binds to the target protein, a labeled secondary antibody is utilized to bind to the primary antibody forming a protein complex and is visualized through fluorescence, dye staining or less popularly now, radioactivity. The process that became known as the western blot was first described by Towbin *et al.* in 1979 [15]. The process first involves separating proteins by their molecular mass using one dimensional sodium dodecyl sulfate (SDS) polyacrylamide gel electrophoresis (PAGE). Briefly, protein samples are denatured using heat and SDS, loaded onto polyacrylamide gels then subject to a potential difference of around 150 volts, with the negatively charged SDS coated proteins being drawn towards the positive anode during electrophoresis. Once separated on the gel, and to further analyze the proteins, they are transferred, again electrophretically, out of the gel and across onto nitro cellulose paper (NCP) or polyvinylidene difluoride (PVDF) membranes, this is the blotting part of the process. Once transferred, the proteins held on the solid support membrane should be incubated with blocking agents such as bovine serum albumin (BSA) or a non-fat dry milk powder to occupy unoccupied binding sites on the membrane, otherwise in subsequent steps antibodies will bind directly to any available sites on the membrane, producing high background noise. Following blocking the membrane can then be incubated with a primary antibody to a target specific protein. The target protein antibody complex is incubated with secondary antibody which has a binding association with the primary antibody and is conjugated with a visualizing agent, which can be seen using a final developing solution.

Analysis of the results can be both qualitative and quantitative. Typically

qualitative analysis confirms the presence of the protein of interest by visual inspection and comparison to the molecular marker used in the 1D SDS-PAGE separation. Quantitative values can be obtained for protein quantity in relative or even absolute terms by using advanced imaging techniques. Further improvements in protein identification can be made by extending protein separation in two dimensions, one by molecular weight and the second by isoelectric charge, leading to protein spots as opposed to bands which can then be cut out and identified by mass spectrometry.

Western blotting has developed to be a powerful and important procedure for the immuno-detection of proteins via AAI, while predominantly an investigative tool to determine the presence of antigens against specific antibodies, there are many disease diagnostic applications [16], including HIV [17], Lymes disease [18] and bovine spongiform encephalitis [19], in addition to drug screening [20] applications.

Pros: Low cost, can be quantitative, high specificity.

Cons: Low throughput, multiple manual processing steps, not real time and is limited to antigen-antibody interactions, with poor reproducibility in 2 dimensions.

1.3.1.2 Immuno-precipitation and co-immuno-precipitation

Immuno-precipitation (IP) is widely used for antigen identification within a complex protein solution, such as a cell or EV lysate [21]. An antibody raised against a specific target protein is incubated with the target protein solution. The bound antibody/antigen complexes are then removed from the solution, precipitated, by binding attraction of the antibody to a capture antigen, such as protein A, which has been conjugated to a supporting bead. The beads are removed from solution and any protein not bound to the beads washed away. The target protein is eluted from the bead and then analyzed often by SDS-PAGE and mass spectrometry.

An extended derivative of IP, co-immuno-precipitation (co-IP) occurs when the primary target antigen as well as secondary molecules already bound to the primary protein by native attraction are precipitated and then eluted for analysis. The principal difference between IP and co-IP is simply the focus of analysis, either the primary target antigen or the secondary AAI partners. Co-IP is a very popular technique that has identified many AAIs by the use of specific antigen antibody binding affinities [22], [23].

While well established and straightforward in execution, true identification of physiological AAI can be difficult with IP or co-IP resulting from the complexity of non-specific binding. Thus, the high number of process steps to reduce non-specific binding often precludes analysis of low affinity or highly transient interactions [24].

1.3.2 Optical methods for observation of AAI

Optical methods include ellipsometry, immuno-labeling and enzyme-linked immunosorbent assay (ELISA). With the exception of ellipsometry, optical methods require the use of an identifying label of some sort, be it electron dense gold for electron microscopy or a flurophore for ELISA.

1.3.2.1 Immuno labeling

A detailed description of immuno-gold labeling is given in Section 1.7. However, the labeling tag can be any one of a number of different materials. Typical tags include, gold, fluorescent molecules, a colour reactive enzyme or an epitope [25]. This is a popular method to identify AAI between a target antigen and antibody, immuno-labeling has been used to identify the location of antigens on the surface of a number of organisms including, bacteria, on cell products such as EVs or within the cross section of cells [26], [27].

Immuno labeling can be direct, when the primary detection antibody has the tag directly conjugated to it, or indirect when a secondary antibody reactive to the primary is carrying the tag. Indirect labeling is the most popular method employed, with the advantage of more binding opportunities for interaction with the secondary antibody and hence a higher likelihood of multiple secondary antibody attachment, producing a higher output signal [25], [28]. Visualization of the immuno-label AAI is dependent on the type of label used. Gold immuno-labels are observed using transmission electron microscopy (TEM), which is capable of imaging nano size colloidal gold tags, conjugated to antibodies, which are beyond the limit of diffraction based optics. For TEM samples containing antigens for evaluation are first fixed using a cross linking material, typically glutaraldehyde, then if necessary sliced into sections thin enough for the electron beam to pass through, followed by exposure to an analyte solution for direct or indirect labeling [29]. TEM immuno-labeling is predominantly an investigative technique, which is used to identify the presence of antigens using labeled antibodies raised against specific antigens, it is not used commercially as a disease diagnostic.

By contrast, fluorescent immuno-labels are typically used in conjunction with both wide-field and confocal microscopy. Samples, once prepared, are exposed to a light source which stimulates the fluorophore to re-emit light at a longer wavelength which can be observed and quantified.

Pros: Low cost, wide range of tagged secondary antibodies available.

Cons: Limited to binary AAIs, low throughput, potential for cross reactivity.

1.3.2.2 Enzyme-linked immunosorbent assay.

Enzyme-linked immunosorbent assay (ELISA) is a plate based method for the optical detection of AAIs through immuno-labeling and antigen capture. A full historical and technical review is supplied by Aydin [30]. Protein, often antigen capture can be direct where molecules from the sample, such as a cell or EV lysate are directly adsorbed to the surface of the plate well or indirect where wells are

pre coated with specific capture antibodies, which bind to and capture the target antigen from the sample solution. Detection is also described as direct or indirect, with direct detection a primary antibody that has been conjugated with a reporter molecule affinity binding with the captured antigen. Following wash steps to remove any unbound proteins a reaction substrate is added to activate the reporter molecule and produce an optical indication of AAI. For indirect detection a specific primary is incubated in the well and binds to the target antigen, a secondary reporter labeled antibody is incubated which will affinity bind to the primary antibody. As with direct detection once any free molecules are washed away a reaction substrate is added to activate the enzyme conjugated to the secondary antibody and produce an optical indication of the AAI. The indirect method offers an opportunity for more than one reporter antibody to attach to the primary antibody and this amplifies the output signal increases the system sensitivity. Indirect ELISA capture is referred to as a sandwich ELISA because the target antigen is trapped between a capture antibody immobilized on the plate well surface and a primary detection antibody. A coproantigen ELISA (cELISA), detects the presence of specific *F. hepatica* antigens found in small samples of host faeces. Typical protocols and further process descriptions can be found at Thermofisher.com [31].

Advantages of ELISA include, speed, low cost and wide availability of commercial secondary antibodies. For indirect ELISA the high binding affinity of the primary antibody is retained because it is not labeled and sensitivity can be increased due to increased binding between primary and secondary antibodies where several epitopes allow opportunities for a signal amplification. Disadvantages however, may include the potential for cross reactivity between target antigen and secondary antibody producing a non-specific output signal. Typical processing times of 2-4 hours. Monitoring AAIs in real time to determine the binding kinetics of PPI is limited to those of the specific antibody.

1.3.3 Bio-physical methods for observation of AAI

Biophysical techniques all rely on a physical response from the individual protein or AAI under analysis and are often used in combination with bio-chemical methods of isolation.

1.3.3.1 Mass spectrometry for AAI analysis

Mass spectrometry (MS) is widely used within the biological sciences to identify molecules based on the mass to charge ratio of their ions. In a very simplified description, a sample is ionized by bombardment with electrons or laser ablation, charging and often fragmenting sample molecules. These ionized fragments are electric field accelerated to a common kinetic energy and then separated through an analyzer using magnetic fields, into similar mass to charge fractions, with lighter ions undergoing greater deflection than heavier ones. The relative abundance of ions arriving at the detector provides a spectral finger print of the original sample. This output can be compared to a protein database using statistical search engines and a degree of confidence assigned to the identification of individual proteins.

MS analysis of AAIs purified from bio-chemical processes such as SDS-PAGE and western blotting can identify the individual bound partners. The most popular MS techniques for this type of proteomic analysis are electrospray ionisation (ESI) and matrix assisted laser desorption / ionization (MALDI) time-of-flight (TOF). ESI disperses proteins which are suspended in a liquid, into a fine aerosol by passing the solution through a fine capillary tube which is subject upto a 5kV potential. The liquid droplets progressively evaporate, inducing charge. When the charge exceeds the Rayleigh instability limit the droplets further reduce, leaving a stream of positive ions to enter the detector. MALDI-TOF by way of comparison uses a laser to ablate the proteins which are embedded into a matrix on a solid support surface. The matrix is principally used to dilute and isolate

the proteins under analysis and the correct choice is important to the success of the process. Popular matrix for protein and peptide analysis are α-Cyano-4-hydroxycinnamic acid and nicotinic acid. The basic principle of TOF is that protein ions of different mass to charge ratio are subject to the same electro-motive force and are separated in time during their flight along a path of fixed length, with lighter particles arriving at the detector sooner than heavier ones with the same charge. A review of current methods employing mass spectrometry analysis for the study of AAIs is given by Kool *et al.* [32] and Rockwood *et al.* [33].

Pros: Well established data bases, high throughput, high sensitivity.

Cons: High cost, analysis is statistical and can be time consuming.

1.3.3.2   Surface plasmon resonance observation of AAI

Surface Plasmon Resonance (SPR) is a detection technique similar to that of ellipsometry. The principal of SPR is as follows; polarized light is incident on a metal film through a high refractive index prism. When the light beam is set at a resonant angle, the surface plasmons resonate which results in absorption of the incident light. The incident light is spread over a narrow range of incident angles and the reflected beam projects over a similar range. Within the reflected beam is a dark band resulting from the plasmon absorption. An intensity profile is plotted against the range of reflection angles (Figure 1.1).

Affinity binding of an antibody from solution to an antigen immobilized on to the surface of the metallic substrate, changes the refractive index and causes the SPR angle to change, producing a position shift in the angle at which the absorption band is detected. This gives a measurable indication of AAI and is often employed as a bio-sensor detector [34]. The effect is caused by a local resonance of group electron charge oscillations which occur in metallic particles that are excited by stimulation from incident light [35], [36].

SPR in the form of the Biacore instrument has become the industry standard method for measuring the affinity of AAI. Biacore is a highly developed system
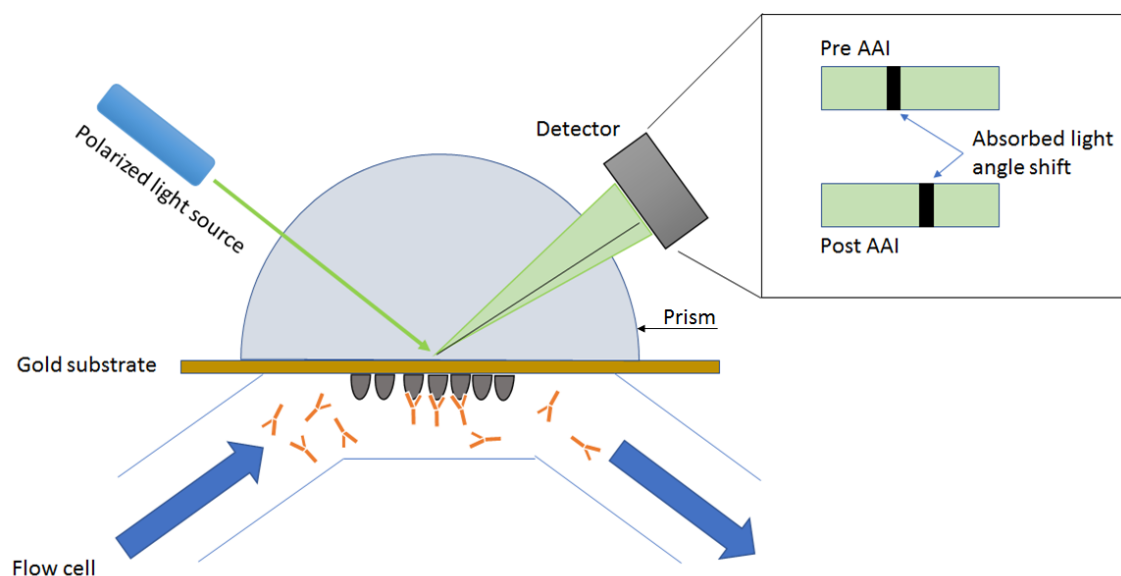
FIGURE 1.1: A schematic view of SPR; whereby the reflected light from a polarized light source contains an absorption band which shifts in position on interaction of binding molecules.

that uses up to four flow cells combined with a micro fluidics system to deliver analyte solutions to the ligand immobilized on the sensor surface. The response in a Biacore system is directly related to the change in mass concentration on the surface [37]–[39] .

Advantages of SPR include the ability to detect real time and transient binding kinetics and it is a label free approach to antigen antibody interaction. The detection surface offers the potential use of micro-arrays to increase AAI analysis throughput. However, disadvantages include the relatively complex surface preparation and antibody immobilization process, with only binary interactions detected. Care in data analysis is required as results can be easily misinterpreted [40].

1.3.3.3 Forster resonant energy transfer

In conventional confocal fluorescence microscopy, applying several antibodies labeled with individual fluorophores with each having separated excitation and emission spectra, optical filters can reveal the proximity of labels within cells or

tissue sections, revealing bulk information on AAI. However, the binding association can only be presumed because direct observation is beyond the diffraction limit of optical instruments [11]. By comparison, Forster Resonant Energy Transfer (FRET) is a process in which a radiationless energy transfer passes from a donor light sensitive molecule (fluorophore) to nearby receptor chromophor. The separation distance between fluorophore and chromophor is limited to approximately 10 nm, beyond which the energy transfer cannot occur and no fluorescent interaction is observed. Hence, by appropriate labeling of target antigens and antibodies, observation of donor fluorescence emission confirms close (<10nm) intermolecular association [41], [42]. The mechanism of fluorescence resonance energy transfer was first proposed by Theodore Forster in 1948 [43], a comprehensive history of the development is described by Clegg [44]. FRET has successfully identified physiological AAIs yet the variable stoichiometry between the two labeled molecules presents an added complexity to quantitative analysis [45].

Pros: Low cost and easy to use, it can also be real time in vivo.

Cons: FRET requires labeling of both interacting molecules.

1.3.3.4 Atomic force microscopy

The use of atomic force microscopy (AFM) to measure individual biomolecular interactions and AAI along with force spectroscopy of single molecules is expertly covered by the review of Willemsen *et al.* [46], which details the rise of AFM as an investigative tool to characterize AAI. A description of AFM therory and its application to this study is covered fully in Section 3.4.

1.3.4 Genetic methods for detection of AAI

1.3.4.1 Yeast 2 hybrid

The yeast 2 hybrid method was developed by Fields and Song in the late 1980's [47]. The system is based on the recombination of a transcription factor which only

occurs when two proteins of interest interact. A bait protein is fused with an independent DNA binding domain, a prey protein is fused with a activation domain, only when the two interact can transcription of the reporter gene occur. The interaction and recombination takes place within genetically modified yeast strains, where the transcription of the reporter gene leads to a phenotype that allows growth on a specific medium [48]. While this method is more appropriate for the detection of true PPI rather than the focus of AAI investigated in this thesis, some cross over is evident [49].

Pros: Simplicity, low cost, high throughput.

Cons: Occurrence of false negatives and false positives.

1.3.4.2 Tandem affinity purification

Tandem affinity purification (TAP) was originally developed in the late 1990's using yeast for the extraction and identification of AAIs [50]. The TAP method involves conjugating a TAP molecule to the target protein, which is then introduced into the host cell or organism. The TAP molecule is constructed in three parts, firstly a protein A domain, then a tobacco etch virus (TEV) protease and finally a calmodulin binding peptide (CBP). The TAP molecule is fused to the target protein through binding of CBP at the C terminus. Cells containing the TAP protein are lysed and the target protein with its associated AAIs are recovered in a two step affinity purification and elution process [51]. The first step removes the target protein complex by passing the cell lysate solution through an affinity column containing IgG coated agarose beads which attract the protein A of the TAP tag. The target protein is then released from the beads using the TEV protease, and incubated in a second affinity column containing calmodulin coated agarose beads which attract the CBP element of the TAP tag. The final elution from the calmodulin beads recovers the protein complex for further analysis.

Pros: TAP has been successfully used to identify AAIs and purify proteins in a wide range of organisms [52]. It is a relatively straightforward process and the

two step purification produces minimizes contaminants [51].

Cons: The TAP tag may inhibit certain binding interactions. Multiple wash steps may reduce the ability to monitor transient interactions.

1.3.5 Conclusion

Given the diverse array of AAI analysis tools there is currently no established gold standard for the evaluation of AAIs. Despite no gold standard, popular current techniques have individually and in combination provided considerable advancement in knowledge and improved understanding of AAI and PPI networks [1]. However none of the proposed AAI analysis tools would seem to answer a list of ideal features for analysis (Table 1.2). Based on the literature, ideal features for a AAI analysis tool would likely incorporate:

- Label free analysis: Enabling the evaluation of a wider range of proteins.

- Real time analysis: Allowing the monitoring of transient interactions for improved protein function analysis.

- Low Cost analysis: Allowing high throughput and low cost AAI investigation increasing the likely use towards diagnostics

- High speed analysis: Beneficial to both research and field based diagnosis.

- Field test application: For advanced diagnostics, analysis based on AAI detection in the field away from a full laboratory set up.

Given the restraints demonstrated for current AAI analysis methodologies, the current work focuses on the potential application of imaging ellipsometry to AAI analysis. Specifically this work investigates the novel features of the AIE which, unlike many existing methods to observe AAI, has the potential as an instrumentation system capable of quantitative characterization of AAIs, label free, low cost, high speed, in real time and with the potential of being utilized in field based diagnosis. All of which has considerable merit.

TABLE 1.2: Ideal features for AAI analysis; evaluation of a range of existing AAI techniques, comparing their applicability to the idealized features of a AAI process. Ticks indicate a process that fulfills the requirement and a cross those that do not.

Bio-chemical methods				
Feature	IP & co-IP	ELISA	Western	TAP
High speed	x	✓	x	x
High specificity	✓	✓	✓	✓
Real time	x	x	x	x
Label free	x	x	x	x
Low cost	✓	✓	✓	✓

Bio-physical methods				
Feature	AFM	FRET	SPR	MS
High speed	✓	✓	✓	x
High specificity	x	x	x	✓
Real time	x	✓	✓	x
Label free	✓	x	✓	✓
Low cost	x	✓	✓	x

1.4 Introduction to ellipsometry theory & practice

1.4.1 Explanation of ellipsometry theory

Ellipsometry measures the polarization state of light reflected from a substrate surface. The change in polarization is defined as an amplitude ratio, Ψ, and phase difference, Δ, these values respond very sensitively to nano-meter scale changes in the film thickness of any substrate over-layers.

1.4.1.1 The origins of ellipsometry

In a report on optics published by Nature in 1874 Spottiswoode described how the polarization of light can be achieved by passing light through a Nicol prism and then reflecting it [53]. It is Spottiswoode who for the first time described the element which first causes only polarized light to propagate as a polarizer and

the element (another polarizer) which is adjusted to determine the actual angle (or state) of polarization as an analyzer.

The change in state of polarized light, on interaction with a material, was observed and used by the German physicist Paul Drude in 1887 in his work on redefining the optical constants of crystals [54]. It was this work describing polarimetry that is used today to characterize optical properties of a material that has been subject to transmission, reflection or diffraction of electromagnetic waves.

It was Rothen who in 1945 introduced the term ellipsometry to specifically describe reflected light polarimetry of thin films in a publication describing an instrument which was initially developed to monitor the reaction between mono layers of antigens and antibodies [12]. The instrument was able, using the fundamental principals defined by Drude, to resolve film thicknesses to an accuracy of ± 0.03 nm.

1.4.1.2 The nature of polarized light

The content of this section relies on the description provided by Jenkins and White [11]. Light is an electromagnetic wave, consisting of both an electric field vector $\underline{E}$ and a magnetic field vector $\underline{M}$ which are perpendicular to each other and oscillate at a frequency (f) with wavelength (λ) in the relationship:

$$c = \lambda f \qquad (1.1)$$

Where c is the velocity of light.

The light wave propagates perpendicular to both the $\underline{E}$ and $\underline{M}$ vectors. It has been observed that the electric field vector $\underline{E}$ has a much greater interaction with matter than the magnetic field vector $\underline{M}$ and it is for that reason that the general convention of optics considers only the $\underline{E}$ field (Figure: 1.2).

A light wave can be described mathematically:

$$A = A_o sin(-\frac{2\pi}{\lambda}(z - vt) + \epsilon) \tag{1.2}$$

Where A is the value of the electric field strength at any point in time t and position z along the direction of travel, A_o is the maximum field strength or amplitude of the wave, λ is the wavelength of the light, v is the velocity of the propagating wave and ϵ is a phase angle to describe the offset of one wave from another when considering a superposition of waves.
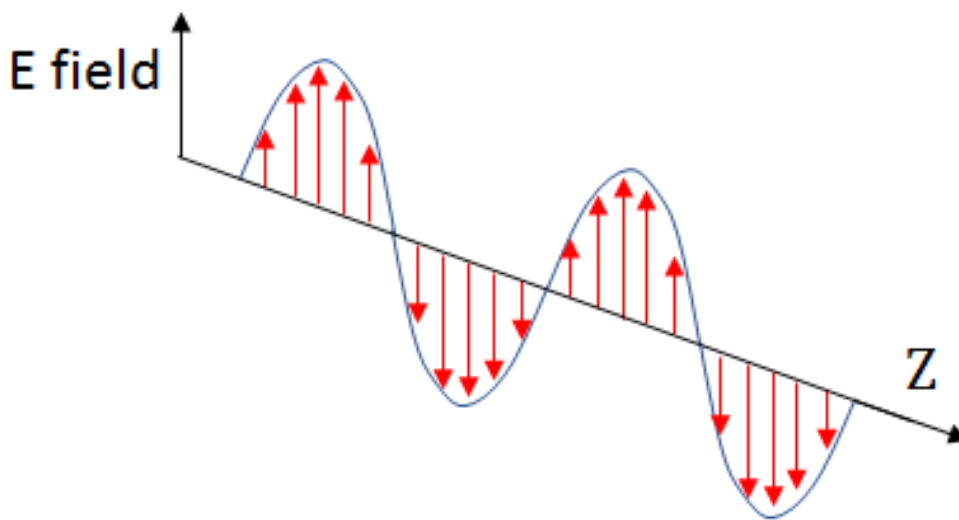
FIGURE 1.2: A schematic view of an electromagnetic wave; $\underline{E}$ field at a fixed point in time, propagating in the direction Z.

Considering two monochromatic (equal wavelength) light waves of equal amplitude propagating along the same path, with one orientated in the vertical plane and the other at 90 degrees to it. If their amplitudes are in phase, then from the vector nature of electromagnetic waves, their superposition will be seen as a light beam that is orientated and polarized at 45 degrees to the vertical (Figure 1.3A).

Similarly, if the two monochromatic, in phase light waves had different amplitudes their resultant vector would still be linearly polarized but at and angle proportional to the relative amplitudes. Should the amplitudes be equal but out of phase by 90 degrees the maxima of one coinciding with the minima of the other the resulting vector would have a constant amplitude but rotate circularly around
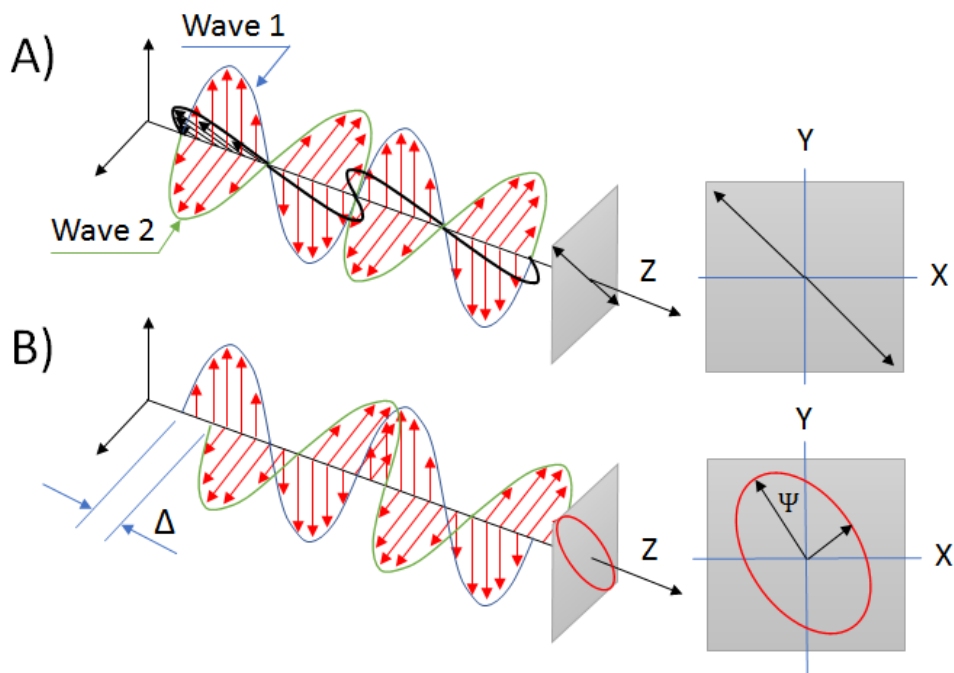
FIGURE 1.3: Considering two monochromatic light waves of equal amplitude propagating along the same path; A) Schematic view of two electromagnetic waves, in phase thus, combining to produce Linear Polarized light. B) The same two waves but 40 degrees out of phase, their vectors combining to produce elliptically polarized light.

the propagating axis. In most general cases the phase between waves is not zero or 90 degrees and the resultant light vector is a form of ellipse (Figure 1.3B). Linear and circular polarized light are specialized cases of the more general state of elliptically propagating light.

It is a fundamental of ellipsometry that upon reflection from a surface, light undergoes a shift in phase and amplitude of the two vector components parallel and perpendicular to the incident surface [55]. This change is, in most cases, not equal for each component and if for instance, the incident light is linearly polarized, there will be a shift from linear to elliptically propagating light at the point of reflection. The amount of ellipticity induced into the reflected light is a function of the optical properties of the sample under study and any thin films that may be present on it's surface. It is this change that forms the technique of ellipsometry and by which materials and thin films can have their optical and

mechanical properties characterized.

1.4.1.3   The ellipsometric co-ordinate system

The light beam that illuminates the sample surface is positioned at an oblique angle to the sample so as to cast a specular reflection. We can define a plane of incidence that contains both the incident and reflected beam of light and includes the normal to the reflective (sample) surface (Figure: 1.4).
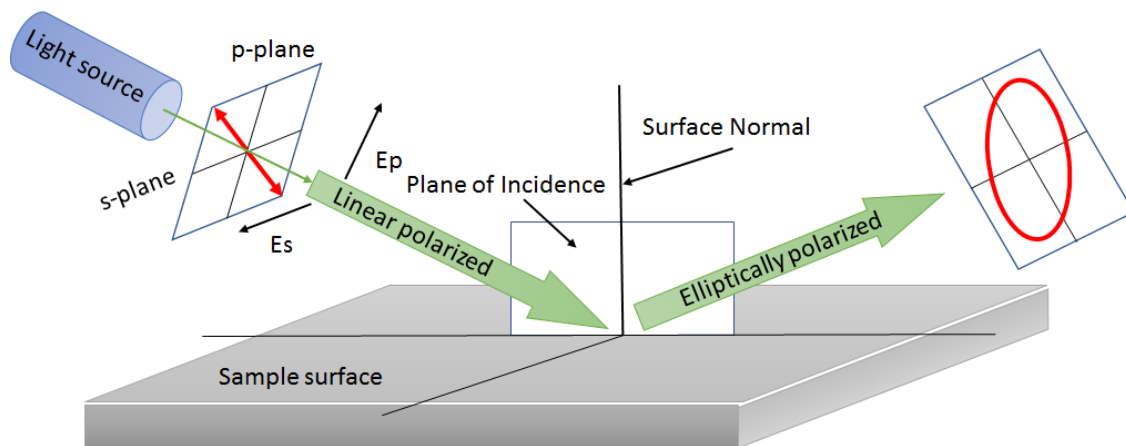
FIGURE 1.4: A schematic view of ellipsometry principals; demonstrating the plane of incidence, light matter interaction and it's effect on the polarization state of light. Ep defines the E field component in the p plane. Es defines the E field component in the s plane.

Plane polarized waves that are aligned with the plane of incidence are referred to as p-waves and those polarized perpendicular to the plane of incidence as s-waves, a convention introduced by Drude (s coming from the German Senkrecht or perpendicular)

1.4.1.4   Reflections at a surface

Before considering the reflection at a surface it is best to understand the complex index of refraction for light that enters the material under consideration. This term is made up of two parts n the index of refraction and k the extinction coefficient.

$$\widetilde{N} = n - ik \tag{1.3}$$

Where i is the imaginary number $\sqrt{-1}$. For dielectric materials such as diamond and glass the extinction co-efficient k = 0 because no light is absorbed in transmission.

The refractive index n is defined as:

$$n = \frac{c}{v} \tag{1.4}$$

Where c is the speed of light and v is the speed of light in the second medium into which the light passes.

The extinction co-efficient k is defined as:

$$k = \frac{\lambda}{4\pi}\alpha \tag{1.5}$$

Where α is the absorption co-efficient. In an absorbing medium the reduction in light intensity I *per* unit length Z is in direct proportion to I, that is:

$$\frac{dI(z)}{dz} = -\alpha I(z) \tag{1.6}$$

Which integrates to:

$$I(z) = I_0 e^{-\alpha z} \tag{1.7}$$

For a light beam interacting with a surface, at the point of incidence the light beam is divided and the law of reflection states that the angle of incidence is equal to the angle of reflection $\phi_I = \phi_R$, (Figure 1.5). The portion of incident light that is transmitted into the material is deflected to the angle ϕ_2, this deflection is governed by Snells Law:

$$\tilde{N}_1 \sin \phi_1 = \tilde{N}_2 \sin \phi_2 \tag{1.8}$$

For dielectric materials where the extinction co-efficient k = 0 the equation reduces to:

$$n_1 \sin \phi_1 = n_2 \sin \phi_2 \tag{1.9}$$

However in most cases for ellipsometry the first layer of the material interface is air and so $\tilde{N}_1 = n_1$, the second medium $\tilde{N}_2$ (the sample) is more often complex and k_2 is non zero.
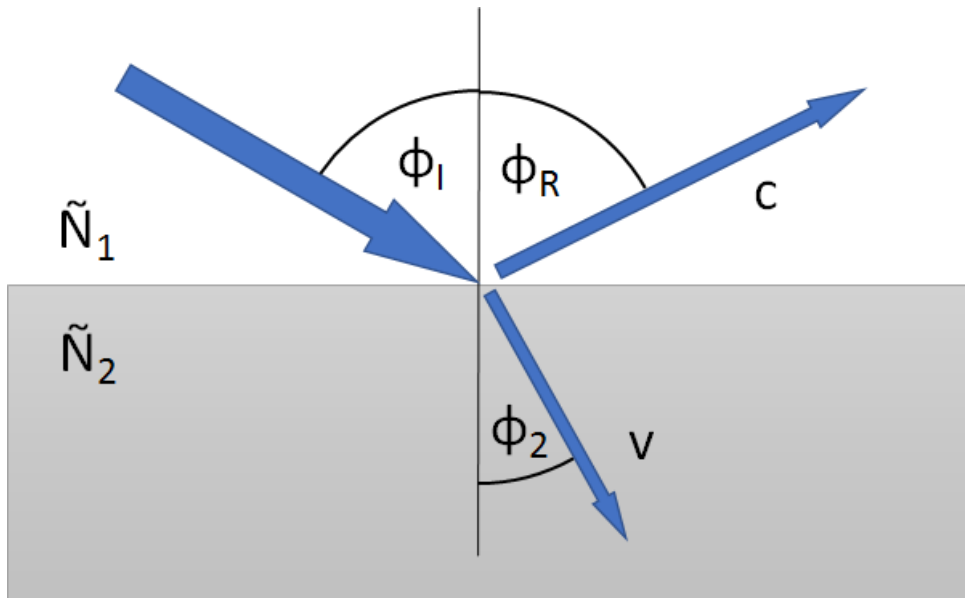
FIGURE 1.5: A schematic view of light matter interaction; with reflection from and transmission through the sample surface. $\tilde{N}_1$ = the complex refractive index of the first material. $\tilde{N}_2$ = the complex refractive index of the second material. c = the velocity of light in the first material. v = the velocity of light in the first material. $\phi_I = \phi_R$ = angle of incidence and reflection respectively. ϕ_2 = angle of refraction.

Having described the elements of complex refractive index n and k it should be noted that for any given medium these are optical constants that change as a function of wavelength. This dispersion can be approximated by the Cauchy co-efficients [55]:

$$n(\lambda) = n_1 + \frac{n_2}{\lambda^2} + \frac{n_3}{\lambda^4} \tag{1.10}$$

$$k(\lambda) = k_1 + \frac{k_2}{\lambda^2} + \frac{k_3}{\lambda^4} \tag{1.11}$$

1.4.1.5 Fresnel equations and Brewster's angle

Considering a light beam reflecting at the interface between two mediums (Figure 1.5) some light is reflected and some transmitted, the Fresnel reflection coefficient r is the amplitude ratio of the reflected light to the incident. Such that:

$$r^p = \frac{\widetilde{N}_2 cos\phi_1 - \widetilde{N}_1 cos\phi_2}{\widetilde{N}_2 cos\phi_1 + \widetilde{N}_1 cos\phi_2} \qquad r^s = \frac{\widetilde{N}_1 cos\phi_1 - \widetilde{N}_2 cos\phi_2}{\widetilde{N}_1 cos\phi_1 + \widetilde{N}_2 cos\phi_2} \tag{1.12}$$

It can be shown that the intensity of light is directly proportional to the square of it's amplitude [11].

$$I = \frac{c}{8\pi} A^2 \tag{1.13}$$

And so the reflectance R can be defined as the ratio of reflected intensity to the incident intensity. Considering a single interface:

$$R^p = |r^p|^2 \quad and \quad R^s = |r^s|^2 \tag{1.14}$$

As an example, considering an interaction between air as the first medium (n=1) and silicon dioxide as the second (n=1.54), the Fresnel equations as a function of angle are plotted (Figure 1.6 A) these being the ratios of the amplitudes of reflected light to the incident light. Plotting the ratio of reflected intensities to incident angle identifies the Brewster angle (Figure 1.6 B), which is the angle whereby reflected light is only *s* polarized.
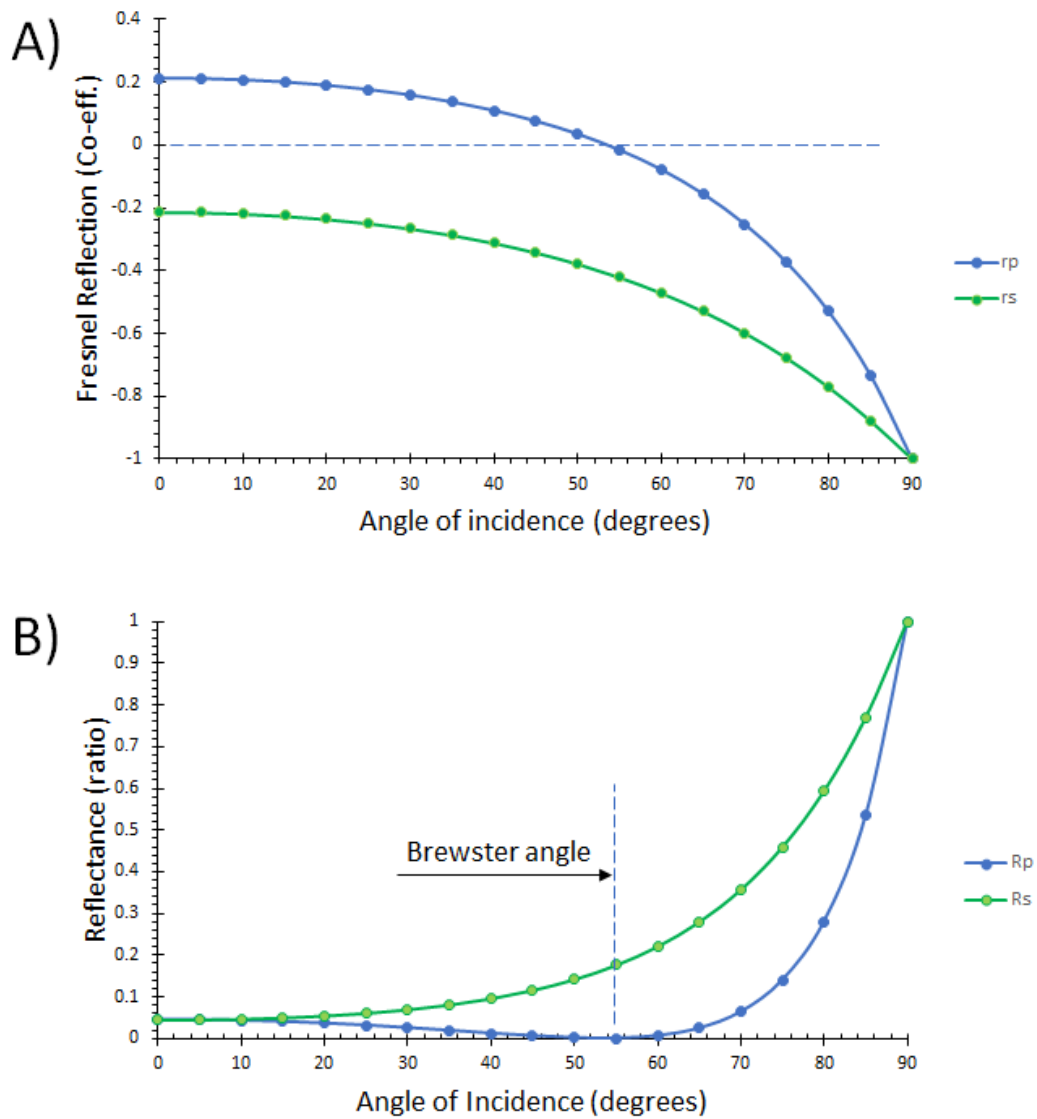
FIGURE 1.6: Fresnel plots for silicon dioxide with a refractive index $\widetilde{N} = 1.54 - 0i$: A) The Fresnel co-efficients r_p and r_s as a function of angle of incident light. B) The ratio of reflected intensities to incident intensities, R^p and R^s plotted as a function of angle.

When light enters a medium at an incident angle ϕ_1, that results in an angle of 90 degrees between the reflected and transmitted rays the specular reflected light is polarized in the s plane while the light transmitted is polarized in the p plane.

Geometrically as seen in Figure 1.5

$$\phi_1 + \phi_2 = 90^o \tag{1.15}$$

From Snell's law, (Equation 1.9):

$$n_1 \sin \phi_B = n_2 \sin(90^o - \phi_B) = n_2 \cos \phi_B \tag{1.16}$$

and hence

$$\tan \phi_B = \frac{n_2}{n_1} \tag{1.17}$$

Where ϕ_B is the polarization angle or Brewster angle after it's quantification in 1815 by Brewser [56], following Malus' discovery of reflective polarization in 1809. Historically this was a method by which polarized light was first created in a controlled way. The significance for ellipsometry being that if the incident light was already polarized in the p plane then no reflected light would propagate from the surface if incident at the Brewster angle.

Quite often, and as will be the current case, the reflection is that of a multiple interface (Figure 1.7). Here the co-efficients have to account for a transmitted light wave undergoing partial reflection from the interface between the second and third medium. Azzam and Bashara [57] derived the total reflected wave to be described by the total Fresnel co-efficients:

$$R^p = \frac{r^p{}_{12} + r^p{}_{23}exp(-i2\beta)}{1 + r^p{}_{12}r^p{}_{23}exp(-i2\beta)} \qquad R^s = \frac{r^s{}_{12} + r^s{}_{23}exp(-i2\beta)}{1 + r^s{}_{12}r^s{}_{23}exp(-i2\beta)} \tag{1.18}$$

Where subscript 12 denotes the Fresnel reflection co-efficient for the interface between materials 1 and 2, similarly 23 denotes the Fresnel reflection co-efficient

for the interface between materials 2 and 3. β is defined as the film phase thickness and is given by:

$$\beta = 2\pi(\frac{x}{\lambda})\tilde{N}_2 \cos \phi_2 \tag{1.19}$$

Where x is the film thickness of the surface layer.
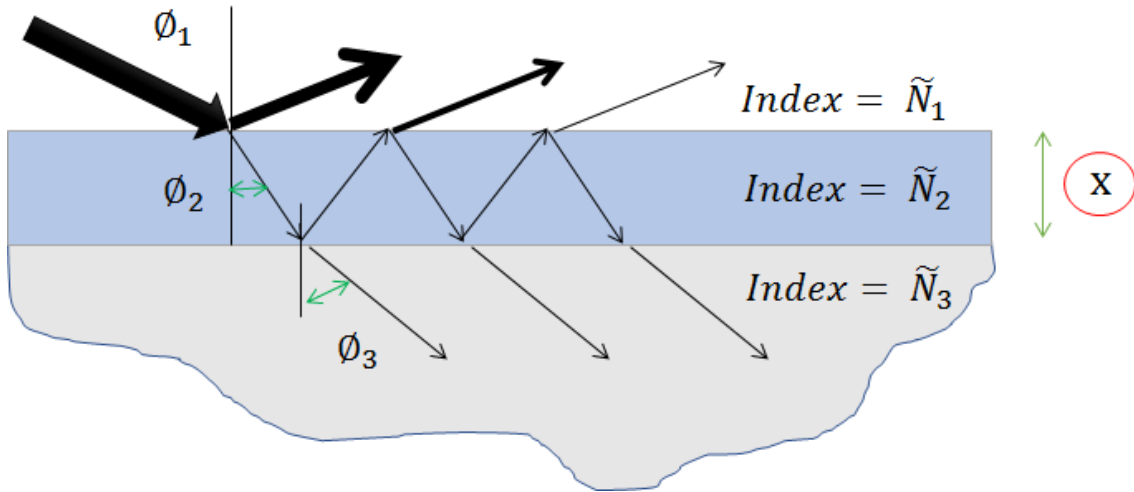
FIGURE 1.7: A schematic view of multiple reflections and transmissions from a bi-layer material; with different refractive indices, where dimension x is the film thickness of the over-layer. ϕ_1 = the angle of incidence, ϕ_2 = the angle of refraction in the over-layer and ϕ_3 = the angle of refraction in the substrate material.

As can be imagined for multiple interfaces Equation 1.14 becomes:

$$\Re^p = |R^p|^2 \quad and \quad \Re^s = |R^s|^2 \tag{1.20}$$

1.4.1.6 Ellipsometric parameters Psi and Delta

It has been observed that upon reflection the light wave incident on a surface undergoes a change in state [55], [57]. If we consider the initial phase between the two elements of the incoming wave (Figure 1.3 B) to be d_1 and the phase between the two elements of the reflected wave to be d_2 the change in the phase between the two components of the reflected light wave can be described by the term Delta; Δ or Del.

$$\Delta = d_1 - d_2 \tag{1.21}$$

Similarly the amplitude of the two incoming components may be changed on reflection, Equation 1.18 defines the amplitude of each component as a ratio of incoming to reflected light, these relative amplitudes defines the angle to which the reflected light (elliptical or linear) is orientated to our co-ordinate system. This angle is given the term Psi; Ψ such that:

$$\tan \Psi = \frac{|R_p|}{|R_s|} \tag{1.22}$$

We can then define the fundamental equation of ellipsometry:

$$\tan \Psi e^{i\Delta} = \frac{R_p}{R_s} \tag{1.23}$$

Because it is these two values that are measured by the ellipsometer, characterization details that are calculated for the sample are contained within the total reflection co-efficients R_p and R_s. A very common requirement is to calculate the thickness of the overlying thin film (x) and it can be seen from Equation 1.18 and 1.19 that with the term x appearing both denominator and numerator it is not possible to simply invert the Fresnel equations to provide an analytical answer to x. Instead it is necessary to construct an optical model and solve for x numerically.

1.4.2 Instrumentation

The original ellipsometer instrument by Rothen was a development of that used by Drude. Both Rothen and Drude adopted the terminology first introduced by Spottiswoode in that the arrangement of polarizer P , quarter wave plate compensator C , sample S and a second polarizer termed analyzer A (Figure 1.8).
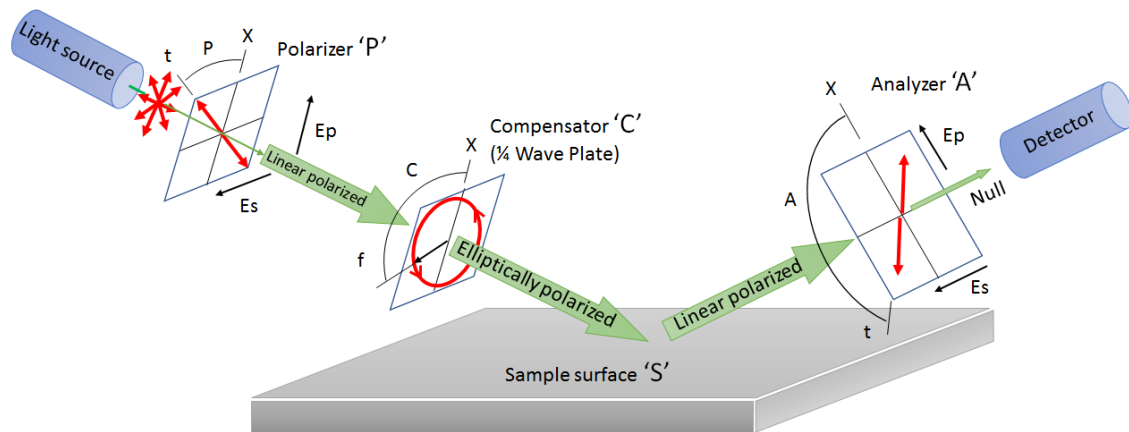
FIGURE 1.8: Schematic of a PCSA nulling ellipsometer.

1.4.2.1 Optical components

Light from a mono chromatic source such as a laser or filtered lamp is typically un-polarized. The beam can be passed through a polarizing filter P and all propagating light will be aligned with the axis of the polarizer. From here the light passes through an optical retarder, referred to within ellipsometry, as a compensator C. Compensators have a fast and a slow axis, the most typical being a quarter wave plate where by wave components traveling through the slow axis will be retarded 1/4 of a wavelength (a 90 degree phase shift) in comparison to the component traveling along the fast axis. This induces in the general case, a rotation in elliptically polarized light but in the specific case of linearly polarized light a change in output to circularly polarized light when set at 45 degrees to the axis of the polarizer P. The significance with this arrangement is that if the amplitude of the p and s waves are equal at the point of input, by manipulation of the axis of polarizer P and the angle of the compensator C relative to each other, any desired state of elliptical polarization can be produced. To achieve this, in early instruments, the components were placed in rotary mounts [55].

1.4.2.2 Nulling ellipsometry

As already stated, light upon reflection undergoes a change of state from the interaction with the surface, there may be a change in both phase and amplitude of

the wave components, whereby linearly polarized light can be deflected into an elliptical state on reflection. The combination of polarizer and compensator can therefore be adjusted in such a way as to generate an elliptically incident light ray that is on reflection from the sample surface, deflected into a purely linearly polarized light beam. If the now linearly polarized reflected light is passed through another polarizing filter, referred to as the analyzer A, when the analyzers axis is rotated into a position 90 degrees with respect to the axis of the reflected beam, no light will propagate. This is termed finding the null or just nulling. In practice adjusting three independent variables can prove troublesome. However, by setting the compensator at a fixed angle and rotating the polarizer until a minimum is found, followed by rotating the analyzer a null is achieved. This leads to a set of angles P, C and A that are a function of the fundamental equation of ellipsometry:

$$\tan \Psi e^{i\Delta} = \frac{R_p}{R_s} = f(P, C, A) \tag{1.24}$$

However, it is not simply a case of inverting the Fresnel equations and it is necessary to develop an optical model, in which the parameters are varied and solved numerically until the output from the model matches the values measured for Ψ and Δ. This is computationally heavy work and restricted the use of ellipsometry until the advent of readily available programmable computing in the 60's and 70's. [58]

1.4.2.3 Rotating element instruments

The limitations of a single wavelength (required by the compensator) and a single null point lead to two measurable real quantities Ψ and Δ which is only sufficient to define a complex index of refraction or the real index of refraction and single film thickness, or simply observe the relative change in a system [57]. To fully

characterize a complex material structure it is necessary to have more independently measurable data points. This can be achieved by taking data at multiple angles of incidence, changing the values of Ψ and Δ as described by the Fresnel equations (Figure 1.6). The polarizer and analyzer can be rotated in stages under microprocessor control adjusting each alternately until the minima is found. Alternatively multiple wavelength measurements can be taken leading to photometric spectroscopic ellipsometry. This requires the removal of the compensator, which will only operate reliably at one wavelength, and fixing the polarizer at 45 degrees. If only the analyzer is rotated the measured intensity will oscillate as a function of time and can be described [55]:

$$I(t) = I_o[1 + \alpha \cos 2A(t) + \beta \sin 2A(t)] \tag{1.25}$$

Where I_o is the average intensity with:

$$A(t) = 2\pi f t + A_c \tag{1.26}$$

Where A_c is a phase offset and f the angular frequency of rotation of the analyzer.

And the Fourier co-efficients α and β are described by:

$$\alpha = -\cos 2\Psi \tag{1.27}$$

$$\beta = \sin 2\Psi \cos \Delta_m \tag{1.28}$$

Where Δ_m is the phase difference between the two wave components p and s as measured at the analyzer. Both the above equations can be re-arranged to give measured values for Ψ and Δ:

$$\tan \Psi = \sqrt{\frac{1+\alpha}{1-\alpha}} \qquad and \qquad \cos \Delta_m = \pm\sqrt{\frac{\beta^2}{1-\alpha^2}} \tag{1.29}$$

1.4.2.4   Imaging ellipsometry

Taking the concept of a nulling instrument and replacing the detector with a focusing objective and a camera that can spatially resolve the sample surface produces an imaging ellipsometer. Rather than averaging the sample surface as a single element, any areas within the field of view that have different optical properties can be spatially resolved by signal intensity. If the polarizer, compensator and analyzer are set to give a null condition for the underlying substrate, any overlaid film will most likely cause a change in the optical parameters at that position and result in the null condition not being met. This leads to areas of brightness relating to the detail changes over the sample surface. These bright spots can themselves be nulled, with Ψ and Δ values individually mapped over the 2D surface [59].

The first practical imaging ellipsometer utilising a CCD detector was proposed as a proof of pricipal by Cohn *et al.* in 1988 [60]. The technique is described as dynamic imaging micro-ellipsometry (DIM) and offered an improvement over the slow scanning techniques using a photo diode that were previously proposed for evaluating spatially resolved film thickness [61]. Cohn's work led to the direct (radiometric) determination of Ψ and Δ adopted by the AIE and is described in full detail in Chapter 2.

The earlier work by Arwin on quantification of AAI using nulling ellipsometry [62], [63] was developed into a practical imaging ellipsometry apparatus with Jin and Arwin constructing a bio-sensor which recorded off null changes in a bio-film thickness in grey-scale. These changes in film thickness were then correlated to reference layers determined by spectroscopic ellipsometry or independent null measurements taken on selected sample areas [64].

Further improvements lead to advances in imaging ellipsometry for the detection of AAI including the covalent immobilization of proteins and the development of a micro fluid systems to present an array of proteins for detection of

AAI identifying bio-markers for hepatitis B in a label free way were reported by Wang *et al.* supporting the fabrication of a bio-sensor array [65]–[68]. Off null sampling by Chen *et al.* [69] which informed techniques to improve sample thickness sensitivity.

Research applications have included screening for AAI in infectious disease; detection of cytomegalovirus which is a cause of mental disability in newborns, was quantitatively assessed using imaging ellipsometry to rapidly detect AAI with cytomegalovirus antigen immobilized on silicon wafers and used to capture cytomegalovirus antibodies from serum samples. The results were in good agreement with ELISA and displaying high specificity and sensitivity [70].

Commercial products have been introduced to the market based on single wavelength imaging ellipsometry, such as those made by the Nanofilm company [59].

The detailed spacial resolution of imaging a sample surface would, at first instance seem to offer a significant leap forward combining both ellipsometry and microscopy. However, it is generally accepted that a major drawback for imaging ellipsometry is brought about by the need for an oblique viewing angle, with an inevitable limitation in the depth of field, so that only a narrow area of the sample is within focus. Manufactures of commercial equipment and researchers developing their own instruments [59], [64], [71] have sought to overcome this problem by by adopting a low magnification to increase the depth of field or by sequentially imaging the surface through a series of motorized steps. A digital imaging system then selects only the focused parts of each sequential image and reconstructs the whole surface from a series of individual segments. Poor focus at the edges of the image or reconstructed strips leads to a large circle of confusion and reduced lateral resolution [72]. Some attempts have been made to correct the issue with Jin *et al.* [71] describing tilting the image detector but no formal description has been given as to how this was related to the rest of the optical system.

Furthermore, imaging ellipsometry suffers from optical components that are not perfect and rotating elements used to measure the values of Ψ and Δ can cause deflection of the beam, leading to a movement between image frames. The movement between frames further complicates the image processing and frame registration. The time taken to accurately rotate optical components is finite and the need to repeat this process iteratively over a measurement cycle slows the process considerably, with acquisition times in the order of 10's of minutes [73] or even hours [74].

However, the AIE which was designed and built by Dr. Matt Gunn under the supervision of Prof. Tudor Jenkins has a novel approach to resolve the issue of image focus experienced with other imaging ellipsometers. The AIE introduces Scheimpflug optical geometry [75] which brings the whole of the sample imaged area into focus, the details of which are described in full in Chapter 2 Section 2.3.2. In addition the AIE employs a rapid method for calculation of Ψ and Δ values from the light intensity incident on each pixel in the imaging system. Both of these features make the AIE extremely well suited to the study of AAIs in a new and informative way.

1.5 Contact angle: substrate surface energy

1.5.1 Introduction

When investigating AAIs, whether single proteins or EVs, using imaging ellipsometry, it is necessary to present on a solid flat substrate, the proteins of interest suitably held, allowing the addition of analyte solutions and subsequent measurement using the AIE. Fabrication of a protein micro-array functioning as a bio-sensor to facilitate the AIE study of AAI requires chemical modification of the surface substrate, using chemical processes delivered in a liquid form. The interface between a liquid and solid is fundamentally influenced by the surface free

energy of interaction [76]. The area of contact is described by the balance of adhesive forces acting between the fluid droplet and the surface it sits upon, drawing the two together, and the cohesive forces of surface tension acting within the fluid, causing the droplet to form a sphere and resist contact with the surface [77]. In a pure liquid, each molecule is attracted to its near neighbours equally in all directions causing a zero net balanced force. At the exposed surface however, the molecules do not have an outward neighbour, resulting in an inward attraction and generation of an internal pressure, which induces the liquid to contract and reduce its surface area to maintain the lowest surface free energy [78].

To describe the interaction and balance of forces between cohesion and adhesion Young introduced a verbal description in 1804 [79] that was rapidly adopted and rendered mathematically as Equation 1.30:

$$\gamma^{sv} = \gamma^{sl} + \gamma^{lv} \cos(\theta) \tag{1.30}$$

Where γ^{sv}, γ^{sl} and γ^{lv} are the solid vapour, solid liquid and liquid solid interfacial tensions respectively. Equation 1.30 describes the surface energy of interaction between the two materials through the contact angle θ formed between the liquid vapor and solid liquid interfaces (Figure 1.9).

Contact angle is most typically measured by imaging the profile of a droplet as it sits statically on the solid substrate surface and calculating the angle formed between the liquid droplet and the supporting solid substrate at the tri-point of intersection. A range of alternative methods have been devised for alternatives to liquids, such as fibers and powders, and these are reviewed by Yuan and Lee [76].

1.5.2   Zisman theory

Quantitative determination of solid surface free energy values cannot be done directly. However using Young's equation (Equation 1.30) there is a correlation
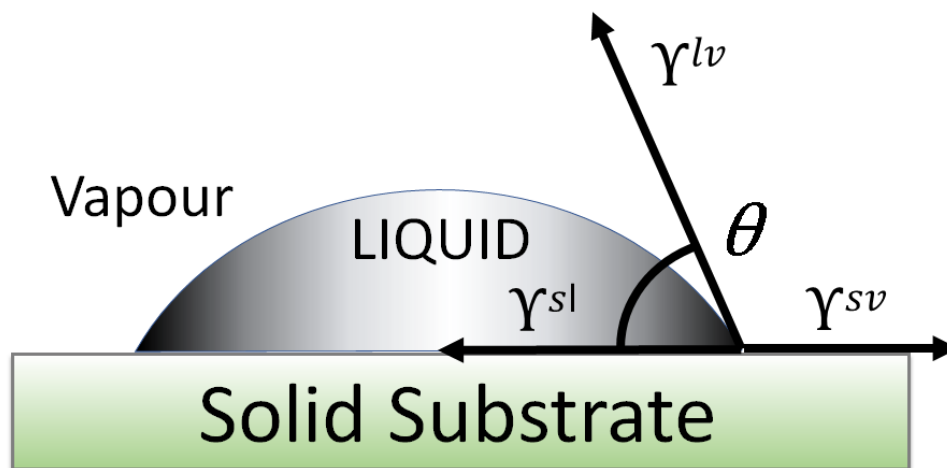
FIGURE 1.9: The principal of contact angle and its relationship to substrate surface energy; where γ^{sv}, γ^{sl} and γ^{lv} are the solid vapour, solid liquid and liquid solid inter-facial tensions respectively. High substrate surface energy enables the liquid to spread, increasing wettability and reducing the contact angle θ.

between the contact angle of a probe liquid and the inter-facial tensions. The work of Zisman determined that for a given surface, plotting the cosine of contact angle θ for a series of probe liquids with known surface tension, produces a linear trend (Figure 1.10). The point at which the trend line passes through $\cos\theta = 1$, and hence the contact angle = 0 degrees, represents a highest surface tension liquid that will completely wet the solid surface and, by Zisman theory, this is equal to the surface energy of the solid [80].

1.5.3 Owens / Wendt theory

However, Zisman's theory breaks down when polar interactions occur between the surface molecular structure and probe liquid, for instance when the solid surface is a hydrocarbon polymer. The Owens/Wendt theory [82] which comprises both a dispersive and polar component, describes a two parameter model for quantifying surface interactions.
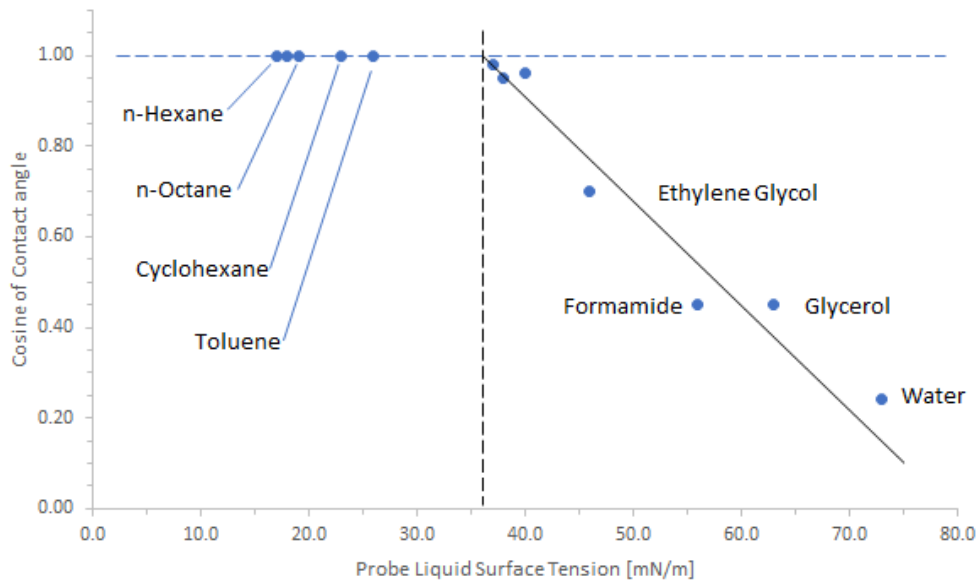
FIGURE 1.10: A representative example of a Zisman plot to determine surface energy of a solid substrate; multiple probe liquids are used including those that completely wet the surface. Reproduced using data from[81].

$$\frac{\sigma_L(cos\theta + 1)}{2\sqrt{\sigma_L{}^D}} = (\sqrt{\sigma_S{}^P} * \frac{\sqrt{\sigma_L{}^P}}{\sqrt{\sigma_L{}^D}}) + \sqrt{\sigma_S{}^D} \tag{1.31}$$

This model has the linear form $y = mx + c$.

$$y = \frac{\sigma_L(cos\theta + 1)}{2\sqrt{\sigma_L{}^D}} \tag{1.32}$$

$$m = \sqrt{\sigma_S{}^P} \tag{1.33}$$

$$x = \frac{\sqrt{\sigma_L{}^P}}{\sqrt{\sigma_L{}^D}} \tag{1.34}$$

$$c = \sqrt{\sigma_S{}^D} \tag{1.35}$$

Using data obtained from a test surface, commonly polytetrafluoroethylene,

determination of the polar and dispersive components for a series of probe solutions can be made. The sample surface to probe liquid contact angle data can be combined to the Owens/Wendt model and the trend line intersection with the y axis read to give a surface free energy value for dispersive component of the substrate, while regression of the line of best fit can be inverted in Equation 1.31 to give the polar component (Figure 1.11). This model is most applicable for substrates that are semi polar with a low surface charge.
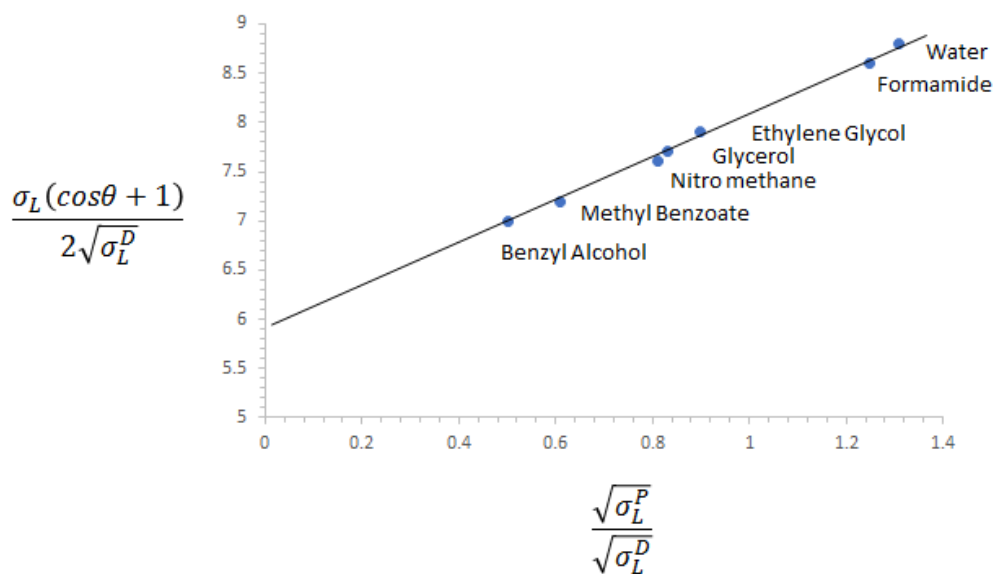
FIGURE 1.11: An example of an Owens/Wendt plot: to determine surface energy of a solid substrate, probe liquids of known polar and dispersive values, which form a measurable contact angle are used. [Reproduced using data from[81]]

The Owens/Wendt model leaves the choice of probe liquids open to the investigator and requires a number of data points (>5) to reliably assess the intersection point with the y axis, indicating the substrate surface free energy.

1.5.4 Fowkes theory

A significant simplification was proposed by Fowkes theory [83]. Which combines Young's equation with the Dupre definition of adhesion energy, such that:

$$I_{SL} = \sigma_S + \sigma_L - \sigma_{SL} \tag{1.36}$$

Where I_{SL} is the energy of adhesion between the solid substrate surface and the probe liquid.

Fowkes theory divides the Dupre definition of adhesive energy into two contributions of polar and dispersive components:

$$I_{SL} = 2 \left(\sqrt{\sigma_S{}^D \sigma_L{}^D} + \sqrt{\sigma_S{}^P \sigma_L{}^P} \right) \tag{1.37}$$

Where $\sigma_S{}^D, \sigma_L{}^D$ are the dispersive components of the solid and liquid respectively and $\sigma_S{}^P \sigma_L{}^P$ are the polar components of the solid and liquid.

The two equations combine with Young's to give:

$$\sqrt{\sigma_S{}^D \sigma_L{}^D} + \sqrt{\sigma_S{}^P \sigma_L{}^P} = \frac{\sigma_L (cos\theta + 1)}{2} \tag{1.38}$$

Using a probe liquid such as diiodomethane, which has no polar component ($\sigma_L{}^P = 0$ and $\sigma_L{}^D = \sigma_L$) the above equation reduces to:

$$\sigma_S{}^D = \frac{\sigma_L * (cos\theta + 1)^2}{4} \tag{1.39}$$

Hence $\sigma_S{}^D$ can be determined directly from contact angle measurements. Using a second probe liquid such as water, with well characterized dispersive and polar components, and having previously determined $\sigma_S{}^D$ this leaves only $\sigma_S{}^P$ as an unknown in Equation 1.38. The total substrate surface free energy is then determined to be:

$$\sigma_S = \sigma_S{}^D + \sigma_S{}^P \tag{1.40}$$

In this way Fowkes theory requires only two probe liquids; diiodomethane with $\sigma_L = \sigma_L{}^D = 50.8$ mN/m and de-ionized water with $\sigma_L{}^D = 26.4$ mN/m and $\sigma_L{}^P = 46.4$ mN/m. [84].

The van Oss theory [85] introduces a three component model. The dispersive element is kept with the polar term divided into acid and base components,

which can take account of surfaces containing ions such as chemical powders, dye pigments and paper. However, these factors extend beyond the scope of the current study.

The understanding of surface free energy that exists between the solid surface of a substrate and the range of chemical solutions used on it presents an opportunity to better control the assembly and function of a bio-sensor protein array. Principally through the correct volume application of the liquids which seek to modify the surface for the immobilization of proteins.

1.6 A target AAI for ellipsometry development

In order to develop ellipsometry, and the AIE, for the study of AAIs a suitable target AAI system was required. Ideally, the chosen system will be accompanied with a wide range of suitable molecular tools for the study of a selected AAI. Such tools would likely include recombinant and native proteins and antibodies targeted towards these proteins. Furthermore, supporting these tools would be a raft of molecular knowledge to allow the understanding of target AAIs. Finally, the chosen AAI to analyse using the AIE would ideally target a societal challenge. To this end, target AAIs from the parasitic helminth *Fasciola hepatica* conformed to these ideals and thus is the principle biological focus for the current AAI analysis.

1.6.1 The parasitic helminth *Fasciola hepatica*

F. hepatica is a parasitic trematode flatworm. The lifecycle of *F. hepatica* is complex involving two hosts [86] (Figure 1.12). Eggs are released from mature, hermaphroditic, adult fluke and pass through the host via the faeces, into the wider environment where they embryonate. The embryonated eggs hatch releasing miracidia which invade, principally, the amphibious freshwater snail *Galba truncatula* which act as an intermediary host. Development within the snail through generations of asexual development, through sporocystrs and rediae, finally results in the release of

free swimming cercariae. The cercariae encyst as infective metacercariae, onto aquatic vegetation or grasses at the water boundary. Upon mammalian ingestion of the infected vegetation the metacercariae excyst in the duodenum of the intestine and then follows a period of migration through the intestinal wall to the liver. The juvenile fluke develop to a patent (egg producing) stage in 8-9 weeks, whereupon they migrate to the bile ducts prior to excreting eggs, and thus, re-starting the cycle.
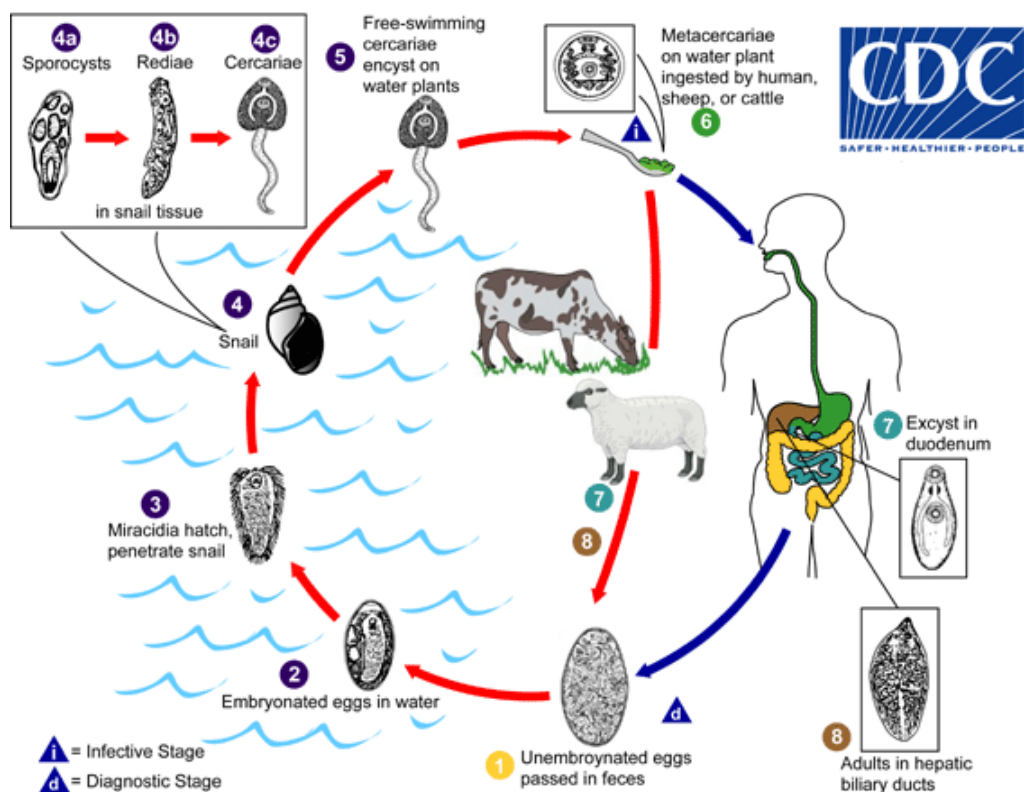
FIGURE 1.12: A schematic which indicates the complexity of the *Fasciola hepatica* lifecycle; outlining the development to the infective stage (1-6), juvenile development within the mamalian host (7) to maturity and diagnostic stage (8). Reproduced from the Center for Disease Control and Protection (CDC) [87].

The associated disease, fascioliasis has an acute stage, as a result of the migration of juveniles from the intestine to, and then progression through, the liver. Symptoms of acute infection include nausea, high temperature, internal bleeding and severe abdominal pain [87]. As the fluke mature and settle in the bile duct, a chronic stage occurs where long term inflammation of the liver causes

fibrosis and periodic blockage of the bile duct may occur. The WHO describes that the hosts symptoms at this stage can include: anemia, jaundice and intermittent abdominal pain. Long term inflammation can cause fibrosis of the liver tissues. With further complications being the possible occurrence of pancreatitis, gallstones and bacterial super-infections [4]

The WHO describes fascioliasis as a neglected parasitic disease [88]. Furthermore, the WHO estimates that between 2.4 and 17 million people in 70 countries worldwide are infected, with over 180 million at risk [89], [90]. It has been described as having the largest longitudinal, latitudinal and altitudinal distribution of any known disease [91]. Human infection normally manifests from the ingestion of contaminated freshwater plants such as watercress and water mint, yet it is also occasionally linked to the drinking un-boiled contaminated water [92].

A significant number of human infections occur in the Andes and the Middle East [93]. Far from what might be expected, in the light of modern healthcare, fascioliasis is seen as an emerging disease, with infections increasing following both man-made and environmental changes [89].

The human impact is highest in low income countries where diagnosis and record keeping can be poor, with hospital treatment often unavailable, presenting circumstances which may lead to under recording of already high incidence rates [90]. In the UK fascioliasis is recognised as a significant disease in animals. However, on average seven people are diagnosed by the National Health Service (NHS) England with the infection each year. This is investigated in more detail (Section 1.6.1.1).

The WHO published a report in 2015 [94] with a specific section dedicated to parasitic diseases and within that, infections caused by *Fasciola spp*, comprising *Fasciola hepatica* and *Fasciola gigantica*. The WHO Foodborne disease burden Epidemiology Reference Group (FERG) study of foodborne diseases identifies that more than 75% of the burden of four hazards (*Fasciola spp., Giardia spp.,* dioxins, and intestinal flukes) occurred among children under the age of five [94]. The

specific age distribution of fascioliasis as identified by FERG is presented (Figure 1.13).

Age distribution

AGE DISTRIBUTION (YEARS)	0-1	1-4	5-9	10-14	15-19	20-24	25-34	35-44	45-54	55-64	65-74	75-84	85+
G1 Mean	49.1	26.9	11.6	4.6	2.3	1.4	1.8	1.0	0.6	0.3	0.2	0.1	0.0
G2 Mean	19.5	33.1	29.5	10.4	4.3	1.4	1.0	0.4	0.2	0.1	0.0	0.0	0.0
G3 Mean	75.3	14.8	5.1	1.8	0.9	0.6	0.7	0.4	0.2	0.1	0.1	0.0	0.0
G4 Mean	21.9	52.6	16.1	1.3	0.5	0.7	1.5	1.3	1.1	0.8	0.7	0.7	0.7
G5 Mean	59.1	22.0	9.4	3.6	1.8	1.1	1.3	0.7	0.4	0.2	0.2	0.1	0.0

FIGURE 1.13: The age distribution of human infection with fascioliasis: as calculated by WHO FERG study 2007-2015. The five different age distributions (G1-G5) are a function of country specific data.

The more popular European vision of *F. hepatica* as a veterinary problem is also significant with the cost to livestock production estimated at $3 billion *per annum* from lost production and associated impacts [5]. Clinical infections in animals typically lead to weight loss, reduced fecundity, anemia, reductions in wool and milk yields, cases of high infection have been seen to lead to morbidity and increase in mortality [95]–[97]. Agricultural environmental controls typically take the form of land drainage and fencing which are expensive to deploy and maintain. These land management approaches are now proving a challenge even in more economically developed parts of the world as a result of climate change. Indeed, in a study looking climate change impacts on *F. hepatica* risk, Fox *et al.* predicts serious epidemics in Wales by 2050[97].

1.6.1.1 Human infections in the United Kingdom

In the United Kingdom *F. hepatica* infections are typically considered to be a veterinary concern. However, an analysis of hospital admittance data, available through the NHS hospital episode statistics, to evaluate how prevalent cases of fascioliasis are in the United Kingdom is presented in Tables 1.3 and 1.4. Diagnosis data is listed by ICD10 codes, a 3 digit general code eg. B66 for fluke

infections, then a more detailed 4 digit specific code is used when a more complete diagnosis is found, this is B66.3 for Fascioliasis. NHS digital England data are clear and have 4 digit codes that identify diagnosis very well. NHS Wales is less clear with a number of unspecified groupings eg. B83 (other helminthiasis) and any patient numbers under 3 are redacted. Scottish NHS online data is not listed by ICD codes and the diagnoses are grouped so broadly as to be unusable in this analysis.

TABLE 1.3: Yearly count of all fluke infections identified by ICD10 code B66; as diagnosed by NHS England for the years 2008-2018

	B66 Fluke infections				
Year	**All diagnoses**	**Main diagnosis**	**Male**	**Female**	**Mean age**
2017-18	12	7	7	5	51
2016-17	5	1	2	3	40
2015-16	14	4	9	5	61
2014-15	11	-	5	6	58
2013-14	11	2	8	3	58
2012-13	7	4	3	4	59
2011-12	9	-	3	6	52
2010-11	2	-	1	1	54
2009-10	3	-	2	1	31
2008-09	6	-	2	4	42

TABLE 1.4: Yearly count of Fascioliasis infections as identified by ICD10 code B66.3; as diagnosed by NHS England for the years 2008 to 2018

	B66.3 Fascioliasis infections				
Year	**All diagnoses**	**Main diagnosis**	**Male**	**Female**	**Mean age**
2017-18	7	4	5	2	51
2016-17	2	-	-	2	26
2015-16	6	4	3	3	52
2014-15	2	-	2	-	49
2013-14	3	1	3	-	57
2012-13	4	4	3	1	69
2011-12	9	-	3	6	52
2010-11	1	-	1	-	76
2009-10	2	-	1	1	17
2008-09	6	-	2	4	42

Within Tables 1.3 and 1.4 the term; all diagnoses, refers to the total number of instances that the ICD10 diagnosis code is recorded in any position on a finished consultant episode (FCE), if the code exists on the FCE more than once, it is counted more than once. For the term; main diagnosis, this is the total number of FCE with the ICD10 diagnosis code recorded in the primary position.

As can be seen from Tables 1.3 and 1.4 a small but stable numbers of annual infections are diagnosed each year in England. Unfortunately it would not appear possible to establish what portion of these diagnoses can be directly attributed to UK sourced infection and those that may be from refugees, migrant workers or visitors who may have been infected from overseas. Interestingly with only one or two exceptions, the yearly mean age would appear quite high, with an average over the 10 year period of recording being 51 years for all fluke infections and 49 years for fascioliasis specifically, with a standard deviation of 9.3 and 16.8 respectively. This would appear to be a substantially different distribution to that seen in the WHO study (Figure 1.13) which demonstrates 75% of cases occurring in those under five years. Further investigation of this age discrepancy may go some way to inform how the mechanism for infection may differ in the UK from the global average.

There is considerable potential for an increase in the UK and Europe in both human and animal infection rates. This arises from long term climate change and specifically for human infections, a more immediate threat due to unfamiliarity with the associated risks brought about by a rapid rise in urban food foraging [97]–[101]. As outlined by Mas-Comma *et al.* a significant number of plant species my contribute to infection over what is considered the traditional culprit, watercress. With *Taraxacum dens leonis* (dandelion leaves), *Valerianella olitora* (lamb's lettuce), and *Mentha viridis* (spearmint) being cited as sources of infection in France [89]. The activity of urban food foraging is something which has seen considerable growth in recent years [102] and looks set to increase with online content and apps promoting the activity, but providing little information of the

associated risks [103], [104].

1.6.1.2   Post infection control

In the absence of vaccines, the primary treatment for both animal and human infection is oral administration of the anthelmintic triclabendazole (TCBZ). This anthelmintic was introduced in the mid 1970's demonstrating a proven efficacy as a flukicide against both mature and juvenile ontogenic stages. However, a reduction in the potency of TCBZ was first observed in Australia during the mid 1990's [105]. Since this initial discovery of TCBZ resistance, further animal cases of resistance have been reported in a number of locations including South America, Europe and the Middle East [106]–[108].

Effectiveness in human cases was observed to be at 100% until recently, whereupon Cabada *et al.* have identified a number of human patients in Cusco-Peru that have failed repeated treatment courses with TCBZ [109]. This raises concerns that resistance to TCBZ may be emerging as a problem in the Andes, an area with high levels of human infection. Cabada *et al.* have also raised concerns regarding the preparedness to tackle resistant parasite infection and along with the WHO have called for more research into new medication and evaluation of resistance [89]. Therefore, continued dependence on TCBZ as a single, compromised anthelmintic is clearly not sustainable.

1.6.1.3   Post infection diagnosis

Diagnosis of suspected *F. hepatica* infection for both human and animal cases is traditionally based on faecal egg counting (FEC) via optical-microscopy identification of *F. hepatica* eggs in faeces. Unfortunately, FEC as a technique is unreliable [110], due in part to sporadic egg shedding [111] and occasionally from pseudo-fasciolaisis caused by consumption of food that contains eggs, which then pass through the individual unhindered and cause no harm [87]. However, most importantly from a medical point of view, egg shedding from mature adult

fluke, that are present in the host, only occurs at the chronic stage of infection, by which time much of the damage to the liver has already occurred. Therefore, early diagnosis is clearly a desirable option. However, at the moment there is only one commercially available clinical test for prepatent infections. This is an ELISA by DRG International marketed under the Bio-X brand name. This test was evaluated in cattle, obtaining a sensitivity of 98% and specificity of 96% at a cut-off value of 15% positivity [112] Valero *et al* in 2012 found similar results in a human study with sensitivity and specificity at 95.3% and 95.7% respectively [110].

While improvements are being made by researchers with their own in house optimization and the use of more specific antigens such as FhCathepsin-L1 [113] there is no gold standard for early stage clinical detection. This is despite the evidence for early antibody response to infection [110]. The merits for further research into this socially and economically important parasite is clear. There is a strong economic and social pressure to resolve both the current and the potential future issues associated with fasciolaisis caused by *F. hepatica*.

1.6.1.4   *Fasciola hepatica* **target AAIs**

With regard to this study there are, it would seem, two themes of investigation for assisting understanding of *F. hepatica* infection linked to AAIs. The first being that of improving understanding of key proteins within and released by *F. hepatica* and thus the interaction networks linked to these target proteins. The long term aim of such an approach would be to support the development of new chemotherapeutic compounds targeted to the disruption of the associated AAIs or to support the choice of a potential vaccine target. To this end, the sigma class glutathione transferase (FhGST-S1) has been identified as one of these key proteins [6], [114] with LaCourse and colleagues clearly stating the need for research on this protein. This is especially so given that FhGST-S1 is a recognized immune

modulator protein and therefore a key protein involved in the host-parasite inter-action, warranting further investigation as a potential vaccine candidate. In fur-ther support of investigation into FhGST-S1, many of the tools noted previously (Section 1.6) to aid AAI investigation are available for this protein. Both recom-binant, rFhGST-S1, and native, nFhGST-S1, are available [6], [115] alongside an antibody that has been used and tested in a number of research applications [6], [116]. In addition, FhGST-S1 has been subjected to increased investigation from initial discovery [117] to structure elucidation [118] including the recent discov-ery of FhGST-S1 within EVs [7], [116].

The second theme is the development of a detection technique capable of early clinical diagnosis for *F. hepatica* infection. Ideally, such a diagnostic would be a significant advancement over the current options including increased sensitivity and specificity. Development of such a diagnostic is clearly reliant on the dis-covery of key biomarkers. Whilst there are now recognized biomarkers for early stage infection and TCBZ stress already identified [114] these biomarkers are in their infancy and thus require investment to develop. However, if a diagnostic could be developed on AAI analysis which is adaptable to any AAI, this may offer excellent opportunities for future diagnostics.

Both approaches are very grand aims but tempered by the reality of having to start from humble beginnings and build a solid, reliable and repeatable method. To quote Hans Arwin in his review of ellipsometry and protein study "Good advice before undertaking analysis on layers of macromolecules is to take on a humble attitude and accept the fact that nature is very complex. One should always assume that each film is unique, requiring a start at square one." [119].

1.6.1.5 Extracellular vesicles; the key to ellipsometry based diagnostics

Following their discovery, not just in *F. hepatica* but more broadly, there is consid-erable emerging work on the role of EVs in the modulation of the host immune

response to parasite infection [120]–[124]. The International Society for Extracellular Vesicles (ISEV) endorses the term extracellular vesicles (EVs) as that used to describe 'particles naturally released from a cell which are delimited by a lipid bilayer and yet cannot replicate'. Given that EV sub-types and populations cannot have their genesis pathways easily assigned, inline with the ISEV recommendations the term EV will be used throughout this document to describe all such vesicles irrespective of physical characteristics or composition (Figure 1.14).
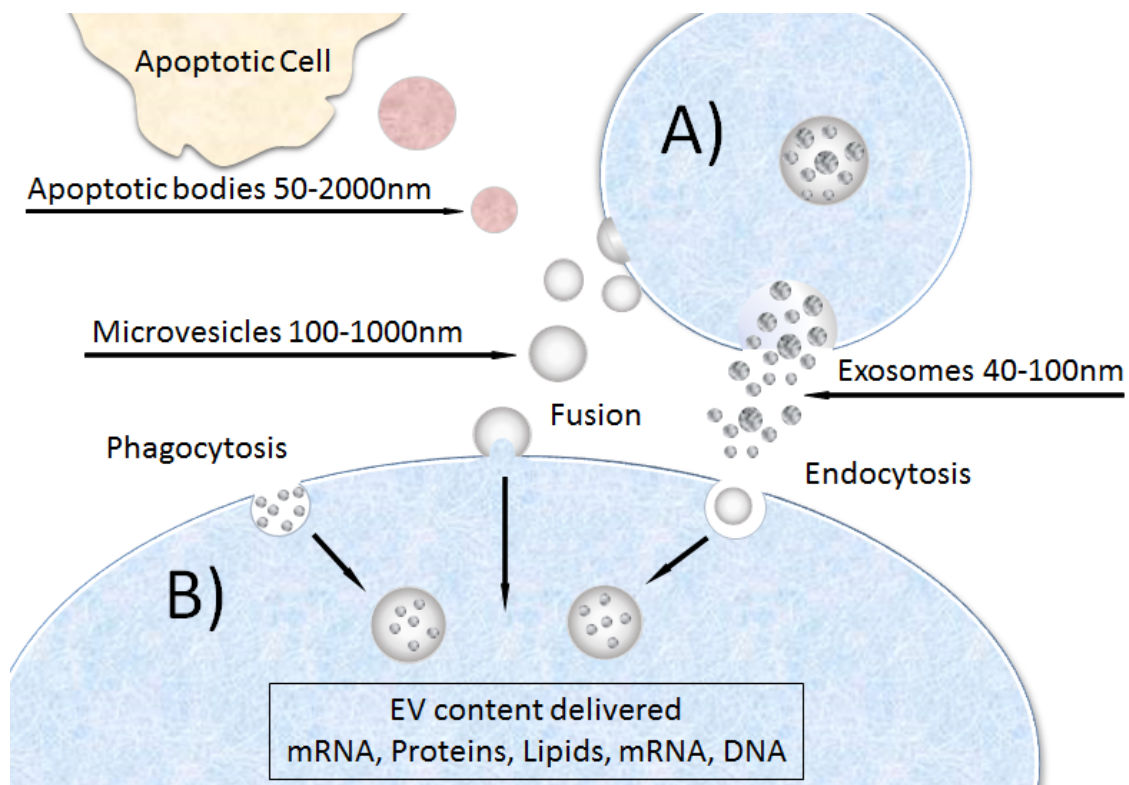
FIGURE 1.14: Schematic showing production of EVs which vary in size and content; A) Exosomes, microvesicles and apoptotic bodies are produced by normal, dying and diseased cells. B) EVs can be taken up by recipient cells in a range of ways including: Endocytosis, fusion, phagocytosis, which deliver the EVs content of proteins, lipids and a range of nucleic acids.

EVs have been isolated from easily accessible human and animal body fluids such as blood [125], urine [126] and saliva [127] or, as in the current work *in vitro* cultures of parasitic helminths including trematodes: *F. hepatica* [116], *Calicophoron daubneyi* [128]; Cestodes: *Anoplocephala perfoliata, Monezia expansa*

[Morphew, personal communication, 2019]; Nematodes: *Heligmosomoides poly-gyrus* [124] and *Ascaris suum*[129]. These helminth EVs are now known to contain cargo that includes proteins, lipids and a wide range of RNA species obtained from their source cells. They have also been shown to possess unique marker proteins on their surface, giving EVs significant potential as the source of disease bio-markers [10], [123], [130], [131]. For this study, these surface proteins have the potential to act as the binding agent, capturing the EV using a suitably selected antibody held on a prepared surface. Such an antibody-EV capture could then likely be detected using the AIE (Figure 1.15) [132].
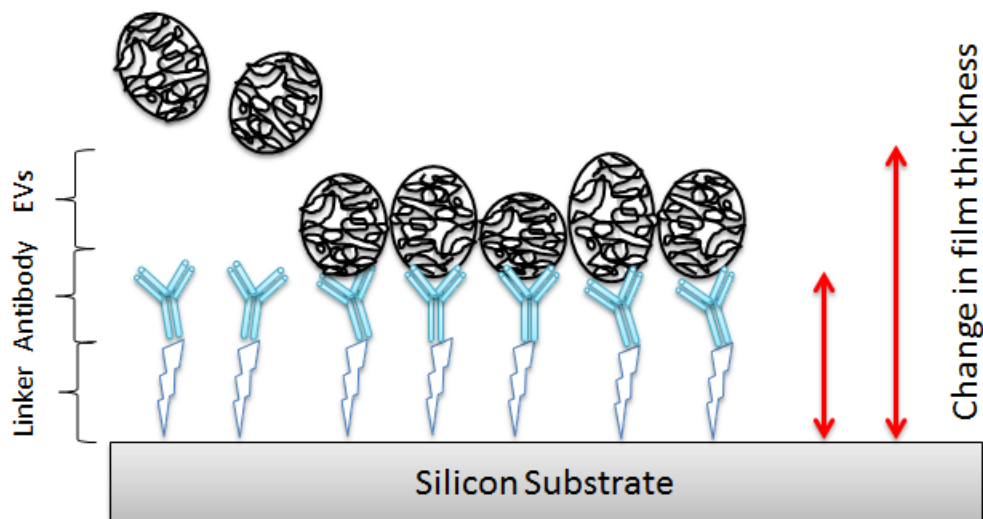
FIGURE 1.15: Schematic representation of EV capture and measurement; antibodies bound to the substrate surface (bio-sensor) capture the EVs from solution and hold them in place using affinity with their surface exposed antigens. Alternatively free protein could be captured from solution in a similar manner.

In their 2015 review of EVs as communicators in parasitic infections, Coakley *et al* [124] identified a range of literature that supports the role of EVs in influencing host cells and as such having a direct action on the progress and outcome of an infection. Mathivanan *et al.* further highlighted the role of EVs as a potential source of protein bio-markers that are reflective of the cellular origin [133]. In addition, it would seem clear that manipulation of the hosts innate immune

response to infection is a key function of parasite EVs [123], [132], [134]. Such a function is achieved by the uptake of the EVs by cells where upon they deliver their contents cargo of proteins, lipids and nucleic acids.

EVs as a potential source of vaccine candidates is exemplified by the work of delCacho *et al*, where by, chicken intestinal dendritic cells were incubated in vitro with antigens extracted from three strains of *Eimeria*. The EVs released by these cells were isolated and used as part of an immunization prior to infection. Compared to non-immunized but infected controls, chickens immunized with antigen-loaded *Eimeria* EVs were able to successfully improve symptoms and reduce the mortality rate of avian coccidiosis [135].

The relative newness of research into EVs has led to a range of methods that try to tackle the challenge of analyzing, characterizing and discriminating between the range of EV that constitute the larger population. To that end reference has been made during this process to the Journal of Extracellular Vesicles publication on minimal information for studies of extracellular vesicles 2018 (MISEV2018) [136]. This publication provides guidelines on terminology, outlines of protocols and steps to follow to identify specific EV related functional activity.

1.7   Immuno-gold labeling of EVs

A proven method to identify AAIs that can occur between antibodies and the surface exposed proteins of EVs is that of immuno-gold labeling.

Colloidal gold was first conjugated to salmonella antibody by Faulk and Taylor in 1971 [26], who used it in conjunction with TEM to identify the localization of antigens on salmonellae bacteria. Gold (^{197}Au) is an electron dense metal and as such scatters the electron beam of a TEM, producing a high contrast dark spot at the site of the gold particle. Samples for investigation are first incubated with a specific primary antibody that will bind with the antigen of interest. Following initial antibody binding, the sample is incubated with secondary antibody

which has been conjugated with colloidal gold nano particles and has a binding association with the primary antibody. Typically the primary antibody is synthesized by immunizing an animal, for example a rabbit, with the specific protein of interest and following an immune response, harvesting the polyclonal (heterogeneous mix) antibodies from whole serum. The secondary antibody is generated by immunizing a host animal of a different species to the primary (eg. a goat), with purified rabbit immunoglobulin G (IgG) which will generate in the goat, anti-rabbit IgG antibodies capable of binding to a wide range of rabbit molecules that will be present in the polyclonal primary antibody. Following incubation and contrast staining, observation of the prepared sample under TEM will show the gold nano particles as black spots, indirectly marking the original antigen of interest [28], [137].
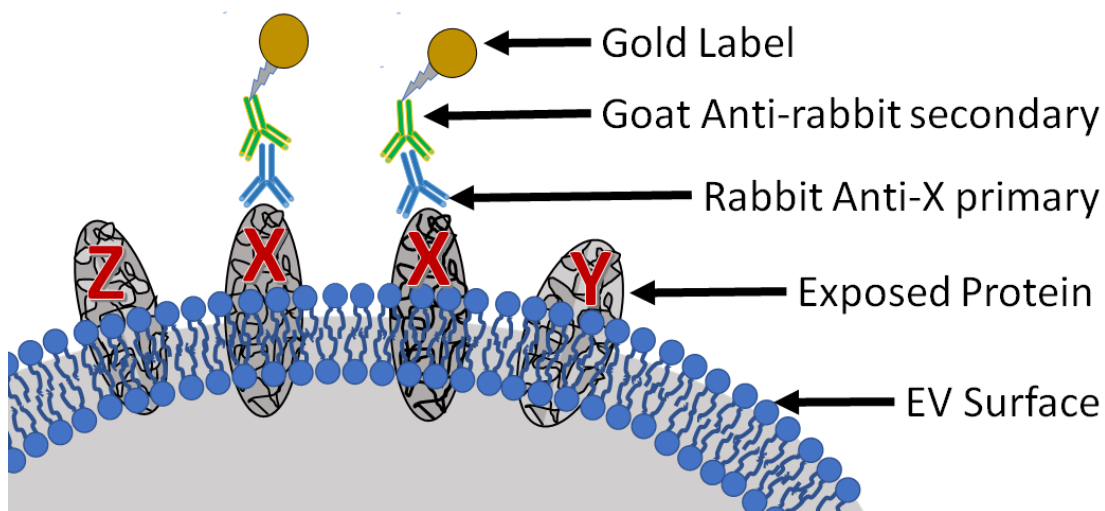
FIGURE 1.16: Schematic showing the principal of Immunogold labeling of surface exposed EV proteins; the differentiated proteins X,Y and Z are shown partially exposed from the EV lipid bi-layer. Protein X has an antigen / antibody binding affinity with the rabbit raised anti-X antibody. Incubation with an anti-rabbit secondary antibody, that is already conjugated to a gold tag, indirectly identifies the presence and position of protein X

1.8 Discussion

This study seeks to investigate the proposal that imaging ellipsometry and in particular the AIE offers the opportunity to develop an instrumentation system that provides all of the key desirable elements, combined with the necessary sensitivity and selectivity, appropriate for detailed AAI investigations.

The term ellipsometry was first coined by Rothen *et al.* in 1945 to describe an apparatus devised which was capable of determining the nano-meter scale thickness of thin films resulting from AAI. Arwin *et al.* demonstrated the principal and practicality of imaging ellipsometry in the area of studying AAI as early as 1993. Work from which Jin *et al.* have clearly demonstrated, on a number of occasions, that the technique has the necessary ability to act as a bio-sensor system with a sensitivity, selectivity and repeatability to equal any current AAI techniques [67], [71], [138]–[141]. However, some of the limitations currently experienced by groups that are conducting research into AAI using imaging ellipsometry is that the required geometric arrangement of an ellipsometer, results in an image with a narrow depth of field. This makes it necessary to index through samples slowing the measurement process. A key feature of the AIE is the Scheimpflug optical geometry, which allows the full field of view to be in focus and corrected for perspective. A second unique feature of the AIE is the rapid determination of the optical properties for ellipsometric parameters, the significance being that, unlike others utilizing imaging ellipsometry, no prior determination of the optical properties of proteins using spectroscopic ellipsometric methods is required. This offers the opportunity to measure a matrix of protein samples, presented on a protein micro-array, all at the same time, which can be applied to tackle key AAIs, thereby supporting diagnosis and control of *F. hepatica*.

1.8.1 Aims and objectives

Given that PPIs are a fundamental aspect to almost all biological processes and the AAI subset forms a backbone for infection diagnostics, the AIE could offer a novel approach to identification and analysis. This project has attempted to develop the AIE in such a way as to assess AAIs from the parasitic flatworm *Fasciola hepatica*. Specifically this thesis aims to:

- Develop the AIE in a way that optimizes it's application to observation of AAIs.

- Calibrate the AIE to a known standard.

- Develop equipment to construct protein micro-arrays, on a platform that makes maximum use of the novel features of the AIE.

- Identify and develop the tools to isolate model AAI systems from *F. hepatica*, for use in the protein micro-array.

- Conduct data analysis on AAI system results.

- Validate the combined system for diagnostic potential.

Chapter 2

Development of imaging ellipsometry

2.1 Outline of chapter general aims

This chapter introduces the AIE which was first designed and manufactured by Dr. Matt Gunn under the supervision of Prof. Tudor Jenkins, in 2007, with Dr. Dave Langstaff developing the LabView control software. A description is given of the precise operation of the AIE instrument both mathematically and mechanically, along with an explanation of the unique features of the instrument that make it particularly suited to the study of AAI. These unique features include the Scheimpflug optical arrangement, which makes sample observations and data gathering clearer and more refined. In addition, the direct calculation of ellipsometric parameters removes the need for any pre-evaluation of material characteristics using spectroscopic ellipsometry.

Developments undertaken during this study to specifically tackle the improved observation of AAIs, such as the revision of the light source and optics, are described in detail with the use of well characterized substrate materials, such as silicon, to calibrate and validate the instrument output. The results and analysis are documented which identify the development of the instrument and points of refinement that have fed back into the final operation of the instrument.

2.2 AIE introduction

As described earlier (Chapter 1 Section 1.4.1) ellipsometry measures the change in state of polarized light on reflection from a sample surface. It is a non-contact, non-destructive, label free method to determine the thickness and optical properties of thin films. Ellipsometers typically operate over a range of angles of incidence and at either a single photonic wavelength, using a monochromatic (laser) light source, or spectroscopically over a broad range of wavelengths [55]. The AIE is a single wavelength imaging ellipsometer which combines optical microscopy, novel data collection and Scheimpflug optical geometry to produce an instrument that can provide rapid, label free, real time determination of AAI through the observation of thin film thickness change.

2.2.1 The AIE instrument; initial starting parameters

The AIE is of a PCSA setup incorporating a polarizer P, compensator C, sample S and analyzer A (Figure 2.1). The mechanical positioning of the optical elements and motorized arms of the AIE are all under automated control in LabView (2015) software [142], with virtual instrument (VI) user interfaces and processing code developed by Dr.Dave Langstaff.

The optical light path of the AIE is demonstrated in Figure 2.2. Starting at the monochromatic laser, light is passed through a fixed polarizer (Edmund Optics : B47-216) to a quarter wave plate (Comar:133CM25), which produces a circularly polarized light output. The polarized light beam is then reflected into a second linear polarizer (Edmund Optics: B47-216) which is mounted in a rotary stage (Thorlabs: KM200B/M). The circular input into this second linear polarizer causes the linear output to be of constant intensity in whichever angle the rotary stage is positioned. From here the now linearly polarized light is passed through a Meadowlark liquid crystal variable retarder (LCVR) and liquid crystal polarization rotator (LCPR) device (Section 2.2.1.1). The narrow laser light emerges
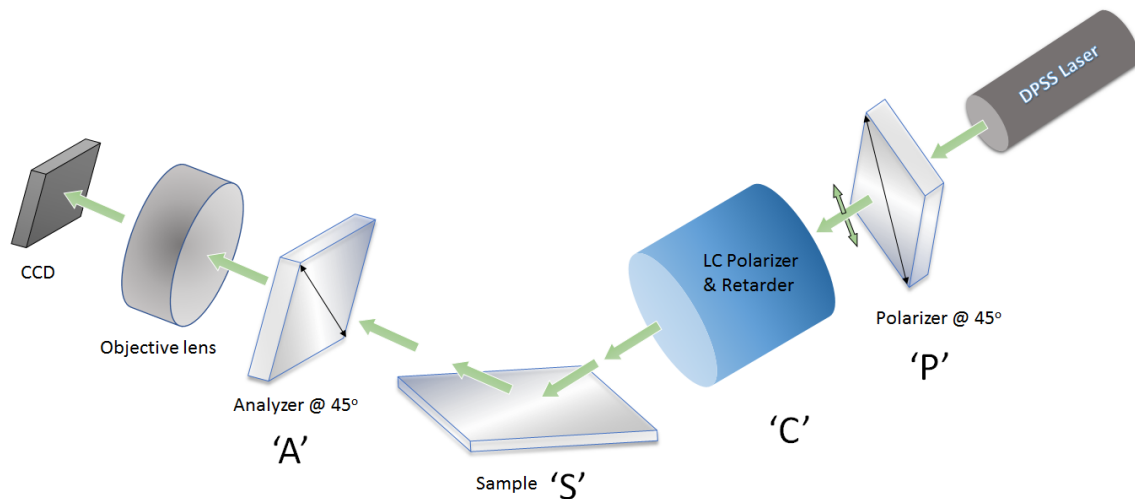
FIGURE 2.1: Schematic of the PCSA optical setup for the AIE: P polarizer, C compensator, S sample and A analyzer.

from the Meadowlark into a 15x beam expander (Thorlabs: BE015M-A) to fully illuminate the sample area. Light reflected from the sample is specularly reflected through a linear polarizer (analyser) mounted in a rotary stage and then collected by a lens (Schneider-Kreuznach Symmar macro 80mm f5.6) to focus the sample image onto a charge coupled device (CCD) camera (Pike F032B)[143] .
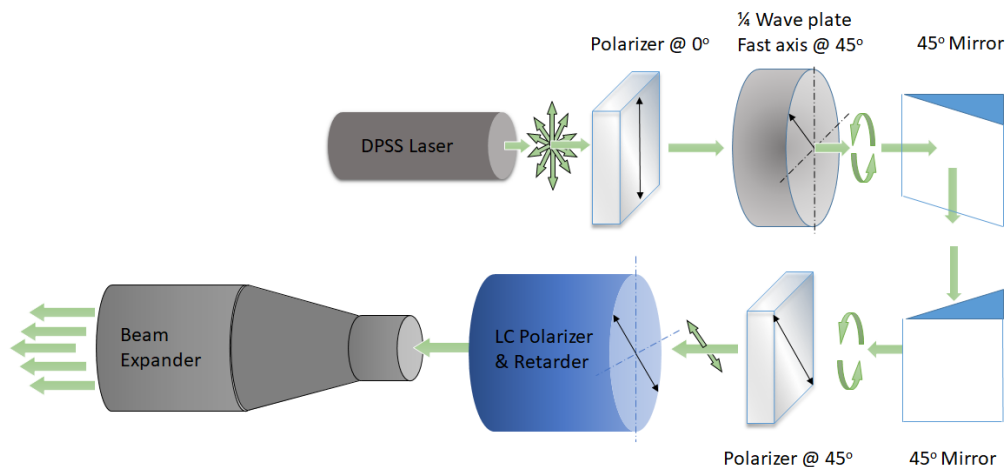
FIGURE 2.2: Schematic of the original light source setup for the AIE; indicating the relative complexity and sensitivity to alignment. The combined weight caused additional problems for correct positioning due to overloading of the arm positioning motor.

2.2.1.1 Liquid crystal polarization and retardance

Control of the polarization state for light projected onto the sample is mediated by a LCPR and LCVR from Meadowlark Optics. The LCVR utilizes a nematic liquid crystal element which produces a retardation of the incident linearly polarized laser light. This is achieved through an applied voltage which reorients the liquid crystal molecules changing the birefringence of the element in the fast and slow axis of propagation. The LCPR polarization rotation is achieved by a quarter-wave retarder converting the elliptical polarization formed by the LCVR, to linear polarization state. The rotation angle is equal to one-half the retardance change from the LCVR [144]. The significance of using this method of polarization control is two-fold. Firstly the response time for changes in polarization angle and retardance is in the order of micro seconds, and secondly no optical component is perfect, thus rotating optical elements can cause deflection of the optical beam which is particularly detrimental to an imaging system, and for rotating element imaging ellipsometers leading to the need for image registration in order to process the series of images necessary to extract ellipsometric data [59]. Therefore, the use of LCPR and LCVR eliminates the need for any rotating optical components.

2.2.1.2 Control system and computation

Control and positioning of all optical components is achieved through a LabView (2015) interface (Figure 2.3). Digital output from the LabView VI is encoded by Thorlabs Tcube motor drives to provide an analogue output to the positioning motors. Manipulation of the polarization state of output light is achieved by the Meadowlark unit which is integrated into the LabView VI, the number of individual LCVR LCPR steps are set at the VI interface. At each LCVR LCPR step, pixel by pixel intensity is captured from the CCD camera, this data is then

passed to the algorithm for direct calculation of Ψ and Δ which is subsequently presented as 2D and 3D full field maps for further analysis.
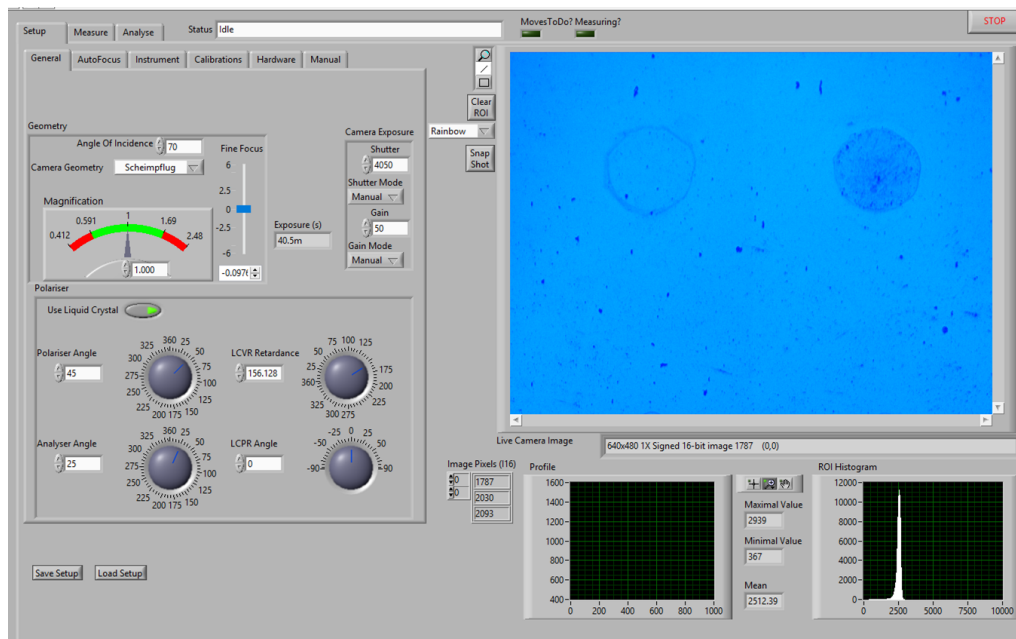
FIGURE 2.3: The LabView VI front panel; which presents the user interface for control of the initial AIE setup. Adjustments for incident light polarization state, optical magnification, camera settings, angle of incidence, fine focus and Scheimpflug optical geometry are all adjusted using the graphical user interface (GUI) to the left. The live camera feed is displayed to the right. Measurement and analysis settings are presented on different GUI, accessed through tabs (top left).

2.2.1.3 Scheimpflug optics

A significant technical challenge which has restricted the widespread adoption of imaging ellipsometry is the issues of sample focus, brought about by the oblique viewing angles required of ellipsometry [59], [72]. The inevitable limit to depth of field results in only a narrow area of the sample being in focus. The AIE overcomes these limitations by using a novel application of Scheimpflug's principal, which is an optical geometry that corrects for perspective distortion and focus across the whole of the sample area that is within the field of view. The positioning of the optics to achieve the Scheimpflug arrangement is calculated from

fundamental geometric principals (Section 2.3.2) and executed all within the Lab-View environment.

2.2.2   Optical parameters defining material properties: Ψ and Δ

A unique defining feature of the AIE is it's ability to calculate Ψ and Δ values spatially resolved over the imaging area using photon intensity data. This measurement algorithm was developed by Dr. Gunn following on from the work of Cohn, Wagner and Kruger [74], [145] (Section 2.3.1) who first applied the phrase, radiometric, to describe their approach which relies on the measurement of light intensity falling on the detector as the polarization state of the incident light is varied. The term radiometric is used here in a different context to that more popularly associated with the measurement of optical radiation power in space across the full optical spectrum. The algorithm to determine the sample parameters and the AIE automated motor control is all executed in LabView (2015) code written by Dr. Dave Langstaff. By contrast traditional, imaging ellipsometry relies on computing values of Ψ and Δ from the individual optical component angles required to achieve a null condition.

2.2.3   The AIE light source

The Meadowlark polarization and retardance device, like all birefringent compensators are able to operate effectively, only over a very narrow wavelength range. For imaging ellipsometers this typically requires the use of a monochromatic light source such as a laser [59]. The original AIE design, using a 532nm diode pumped solid state (DPSS) laser light provides a narrow spectral width and highly collimated beam and it was at this wavelength that the Meadowlark had been specified to operate. However, a problem that occurs as a result of the high coherence of the laser output is that it leads to significant interference fringes in

the refractive optics of the beam expander and focusing lens system reducing the resolution of collected images [72].

To overcome the issue of coherent interference and optimize the optical resolution of the AIE images, a range of options which could disrupt the laser coherence, were considered. These included, fiber optic cable bundles [146], A spinning ground glass disk [147] or an integrating sphere [148]. During the course of considering the performance to cost compromise for introducing de-coherence to the existing system. A failure of the DPSS laser optics focused attention on a complete redesign of the AIE illumination source. The cost of replacing the DPSS laser and adding a reliable mechanism to de-cohere the beam which would provide the equivalent illumination intensity of approximately 10mW over a beam expanded area of 50mm diameter [1963 mm^2] or $\approx 5.1 \mu$W per mm^2, was not insignificant.

An affordable, potential solution was the use of a high power light emitting diode (LED) which could be filtered at 532nm. However, such an approach required detailed investigation, to ensure sufficiency of illumination intensity over the narrow operating bandwidth, in addition to the difficulty in producing a high level of light beam collimation, given the large output area of the LED element.

2.3 Instrument development and methods

2.3.1 Radiometric determination of Ψ and Δ

The optical arrangement for radiometric imaging ellipsometry is the same as that already described (Section 2.2.1), with a standard, PCSA setup as shown (Figure 2.1) with the light passing from the analyzer through an objective lens and focused onto the detector of a CCD camera. The light intensity at each pixel of the CCD can be recorded for each of a series of instrument polarization settings. The Ψ and Δ values can be calculated from the intensity distributions and the

instruments settings and plotted as full field maps, which are referred to as ellipsograms.

The detailed description of how the algorithm is derived uses the Jones matrix and vector formalism of Azzam and Bashara [149] with the radiometric parameters defined by Cohn *et al.* [145]. For brevity here, a description of the key parameters used within the calculation is given. However, the full derivation from Dr. Gunn is included in the appendix.

$$
I_{PCSA} = I_O \cdot \left\{ \begin{array}{l} \cos^2(A) \cdot \tan^2(\Psi) \cdot [1 + \cos^2(2C) \cdot \cos(2(P - C))] \\[4pt] + \sin^2(A) \cdot [1 - \cos(2C) \cdot \cos(2(P - C)) + \cos(\Delta') \cdot \sin(2C) \cdot \sin(2(P - C))] \\[4pt] + \sin(2A) \cdot \tan(\Psi) \cdot [\cos(\Delta) \cdot (\sin(2C) \cdot \cos(2(P - C)) \\[4pt] + \cos(\Delta') \cdot \cos(2C) \cdot \sin(2(P - C))) - \sin(2(P - C)) \cdot \sin(\Delta) \cdot \sin(\Delta')] \end{array} \right\}
$$

$$(2.1)$$

If a total of N measurements are made for each polarization angle and phase retardance n (not to be confused with refractive index $\widetilde{N}$ and n), then the measured intensities of each pixel across the CCD can be recorded for each step n.

Setting the phase retardation to zero and the number of polarization angle steps to N equally divided between 0 and 180 degrees:

$$
\Delta' = 0 \qquad P_n = \frac{n \cdot \pi}{N} \qquad \text{for} \quad n = 1, 2, 3 \ldots N
$$

$$
I(P) = U + (V \cdot \cos(2P)) + (W \cdot \sin(2P)) \tag{2.2}
$$

Where:

$$
U = I_o(\cos^2(A) \tan^2 \Psi) + \sin^2(A) = \frac{1}{2\pi} \sum_{n=0}^{N} I(P_n) \tag{2.3}
$$

$$
V = I_o(\sin^2(A) - \cos^2(A) \cdot \tan^2 \Psi) = \frac{1}{\pi} \sum_{n=0}^{N} I(P_n) \cdot \cos(P_n) \tag{2.4}
$$

$$W = I_o\sin(2A) \cdot \tan\Psi \cdot \cos(\Delta) = \frac{1}{\pi} \sum_{n=0}^{N} I(P_n) \cdot \sin(P_n) \tag{2.5}$$

$$\tan(\Psi) = \tan(A)\sqrt{\left(\frac{U-V}{U+V}\right)} \tag{2.6}$$

$$\cos(\Delta) = \frac{W}{U} \cdot \frac{\cos^2(A) \cdot \tan^2(\Psi) + \sin^2(A)}{\sin(2A) \cdot \tan(\Psi)} \tag{2.7}$$

Setting the polarization angle to 90 degrees and varying the phase retardance steps to N equally divided between 0 and 360 degrees:

$$\Delta_n' = \frac{n \cdot 2\pi}{N} \qquad P_n = \frac{\pi}{2} \qquad \text{for} \quad n = 1, 2, 3 \ldots N$$

$$I(\Delta') = X + (Y \cdot \cos(\Delta')) + (Z \cdot \sin(\Delta') \tag{2.8}$$

Where:

$$X = I_o\left(\cos^2(A)\tan^2\Psi\right) + \sin^2(A) = \frac{1}{2\pi} \sum_{n=0}^{N} I(\Delta_n') \tag{2.9}$$

$$Y = I_o\left(\sin^2(A) - \cos^2(A) \cdot \tan^2\Psi\right) = \frac{1}{\pi} \sum_{n=0}^{N} I(P_n) \cdot \cos(\Delta_n') \tag{2.10}$$

$$Z = I_o\sin(2A) \cdot \tan\Psi \cdot \cos(\Delta) = \frac{1}{\pi} \sum_{n=0}^{N} I(P_n) \cdot \sin(\Delta_n') \tag{2.11}$$

And from this:

$$\tan(\Psi) = \tan(A)\sqrt{\left(\frac{X-Y}{X+Y}\right)} \tag{2.12}$$

$$\sin(\Delta) = \frac{-Z}{X} \cdot \frac{\cos^2(A) \cdot \tan^2(\Psi) + \sin^2(A)}{\sin(2A) \cdot \tan(\Psi)} \tag{2.13}$$

The radiometric intensities for each pixel of the CCD image are held as a matrix of values for each of the polarization and retardation steps (n) and the calculation of Ψ and Δ are determined through a processing algorithm executed in LabView.

2.3.1.1 Spectroscopic and radiometric comparison of silicon dioxide / silicon samples

The accuracy of radiometric data obtained from the AIE was investigated by comparing Ψ and Δ values to those obtained by a Sopra GESP-5 commercial spectroscopic ellipsometer. The GESP-5 is a rotating element instrument with high resolution double monochromator which collects specularly reflected light from a sample surface into a low noise photomultiplier. The angle of incidence can be set from 6 to 90 degrees from the vertical.

Calibration of the Sopra GESP-5 prior to use was achieved by standard operating procedure to determine the silicon dioxide (SiO_2) over layer on a silicon (Si) substrate using a calibration standard (Sopra SN:000920/056). SiO_2/Si samples are a classically used and well established method for the calibration of ellipsometric measurement systems [150], [151].

Measurements for a series of silicon wafers with thermally grown SiO_2 overlayers were obtained using the GESP-5. The spectroscopic data was fit, using Sopra Winelli software (version: 3.04), to a Cauchy extinction model using a Levenberg–Marquardt algorithm to determine the oxide layer thickness. Data was collected at an incidence angle of 60 degrees across a wavelength spectrum from 350 to 1000nm. Values for Ψ and Δ obtained at 532nm were then extracted for comparison with those of the AIE.

A further cross check of AIE Ψ and Δ values, compared to those obtained from the GESP-5 was conducted by measuring the same series of SiO_2/Si samples spectroscopically over a range of angles of incidence from 55 to 75 degrees. Values

for Ψ and Δ obtained at 532nm were once more extracted for comparison with those obtained by the AIE.

The measured SiO_2/Si samples were later used to inform a model of protein thickness (Chapter 5 Section 5.4.2).

2.3.1.2   Radiometric error estimation

The method for calculation of propagating errors through the system was constructed as described by Cohn *et al.* [74]. Uncertainties arise from three main sources. Firstly, the light source, with variations comprising of intensity and collimation deviation. Secondly, optical alignment errors, which include sample alignment and component positioning angle error. Thirdly, intensity measurement and computational errors and calculation rounding. CCD related errors are correlated to the light source and alignment so are considered separately.

An item of note is that the input light intensity is not required as part of the radiometric calculations, hence if the CCD gain is held constant during data acquisition no calibration of system gain is required. However, potential fluctuations in gain and input light intensity do contribute to random error. So to minimize ellipsometric error across the measured intensities, it is important to make maximum use of the camera dynamic range without saturation.

For electronic image sensors such as the AIE CCD, the signal-to-noise ratio (SNR) characterizes the quality of an image and hence influences the performance of the measurement system. Specifically, SNR refers to the ratio of the measured signal compared to the overall measured noise at any given pixel. The measured signal is the product of the photon flux, the quantum efficiency of the detector (in converting photons to electrons) and the integration time.

Typical sources of noise within electronic image sensors such as the AIE CCD are identified as; photon noise, often referred to as shot noise, which relates to the inherent variation of the incident photon flux, this variation is described by a Poisson distribution [152]. Read noise, predominately originates from the CCD

pre-amplifier and associated electronics which are used to quantifying the signal present on the CCD pixel. Dark noise, is a constant source of electrons that are generated predominantly by thermal energy within in the silicon layer of the CCD structure. However, the design and structure of the p-n junction combined with the doping levels used within the semi conductor also have some influence on the generation of dark noise [153]. Dark noise is independent of any photon flux incident on the CCD detector, however for current CCD detectors is considered to have a negligible effect on exposures of less than 1 second [154].

Therefore SNR can be expressed by the equation:

$$SNR_{\text{ccd}} = \frac{IQt}{\sqrt{IQt + Nd + Nr^2}} \qquad (2.14)$$

Where I is the incident photon flux, Q is the quantum efficiency of the detector (electron to photon ratio), t represents the integration time in seconds, Nd is the dark noise (electrons/pixel/sec) and Nr is the read noise in electrons. The Pike F-032 CCD camera used by the AIE quotes a SNR of upto 24dB.

Methods to increase SNR include binning of pixels, whereby the charge from adjacent pixels in a CCD is combined during readout to form a single larger pixel, and sub sampling which reduces detector read time while retaining the original image area and brightness. Both these options were rejected due to the inherent loss of resolution [155].

An error budget for the components that likely influence the radiometric results were compiled (Table 2.1) using manufacturer data and reasonable estimates where direct information was not available.

Following the principal of propagating uncertainty [156] the random error for Ψ and Δ as calculated by Equation A.23 for individual pixels can be evaluated by first estimating the relative error for the measured light input intensity dI, the relative error for alignment error dA and relative error for instrument response dM.

TABLE 2.1: Components error budget for the AIE; comprising of percentage error described by manufacturer specification or where necessary reasonable estimate (identified by *) for those elements that influence radiometric data values.

Item	Specification	Percentage error
Light Source		
Light intensity*	0.5 %	0.5
Collimation error*	1.6 Deg	0.4
Total		**0.64**
Optical Allignment		
Polarizer arm angle	0.2 Deg	0.22
Analyzer arm angle	0.2 Deg	0.22
Polarizer angle	0.1 Deg	0.1
Analyzer angle	0.1 Deg	0.1
Sample alignment*	1.0 Deg	1.0
Total		**1.06**
Measurement		
Calculation rounding	0.01%	0.01
Total		**0.01**

$$\frac{U\phi}{\phi} = \sqrt{(dI)^2 + (dA)^2 + (dM)^2} \tag{2.15}$$

Equation 2.15 can be combined with the error formula for standard deviation, which is appropriate for random errors with a normal distribution and applied to the number of polarization and retardation steps (N):

$$\sigma = \sqrt{\frac{1}{(N-1)} \cdot \sum_{i=1}^{N} (x - \bar{x})^2} \tag{2.16}$$

Where, for the all measurements taken during this study, $N = 25$

Hence:

$$\frac{U\phi}{\phi} = \sqrt{\frac{1}{(25-1)} \cdot 25 \cdot (0.64^2 + 1.06^2 + 0.01^2)} \tag{2.17}$$

Resulting in a component and alignment error of 1.26%

This error can then be combined with the SNR error of the CCD to give the overall combined error for Ψ and Δ which is estimated at 1.32%

2.3.2 Scheimpflug optical geometry

The Scheimpflug principal formally describes the optical geometry for the image plane, objective lens and subject plane to maximize the area of the image in focus and correct for perspective distortions introduced by an oblique viewing angle. To understand the influence of adjustment to the position of each element it is necessary to first consider the magnification of a single thin lens optical system. Which, is defined as [11, pg:54]:

$$M = -\frac{d_i}{d_s} \tag{2.18}$$

Where d_i is the distance from the lens plane to the image and d_s is the distance from the lens plane to the subject. The negative sign indicating that the image is inverted.

In reality the focusing objective of the AIE is not a thin lens and as such will suffer from aberrations. These aberrations include spherical, comma, astigmatism, distortion and chromatic: Spherical aberrations can arise from non-paraxial rays which focus at a different point to those of central rays. This is significantly increased in the situation of close working distances. However, reduction in non-paraxial rays can be achieved by reducing the aperture of the lens by means of a stop, or the use of non-spherical surfaces in the lens design. A full description of spherical aberration is given by Smith [157]. Coma derives it's name from the comet like appearance of an image formed of a point object projected off the lens axis. Coma can be corrected and minimized by a change in the curvature of the lens surface, this can be combined to minimize spherical aberration, such that any optical system free of both spherical aberration and coma is said to be aplanatic [11, pg:166]. This aplanatic arrangement can be found for any particular pair of conjugate points and describes the optimal design for a specific focusing objective. The focusing objective lens for the AIE is optimized for use at a 1:1 reproduction ratio as a macro lens with a focal length of 80mm. Astigmatism

for an optically symmetric system such as the AIE, arises from off axis objects where the vertical and horizontal components of the object are brought to focus at different points on the optical axis. Astigmatism can lead to considerable blurring of images at the edges of the field of view. Introduction and spacing of lens group elements can reduce and even eliminate astigmatism [11, pg:168]. Distortion is caused by the non uniform lateral magnification over the entire field of view. Distortion is typically introduced to an optical system by a stop, this can be a mechanical variable stop used to control light entry aiming to reduce spherical aberration and astigmatism or it can be formed as a result of the front optical elements acting as a stop for the rear positive elements within a complex lens group [11, pg:172]. Chromatic aberration is caused by dispersion, whereby the refractive index of the lens materials vary with wavelength. This leads to light of differing wavelength failing to focus at the same point. While the lens used by the AIE has apochromatic correction to reduce the effecs of chromatic aberration the use of a very narrow illumination wavelength (Section 2.3.3) removes any significant chromatic errors.

The focusing objective lens of the AIE (Schneider-Kreuznach Symmar macro 80mm f5.6) was selected with consideration that lenses are optimized for performance over a limited reproduction ratio (conjugate points) to minimize aberrations as described above. Experiments reported in this thesis were conducted at a 1:1 magnification with the lens stop fully open at f5.6. Distortion for this arrangement is reported as <0.1% positive (pincushion) [158].

2.3.2.1 Element alignment for Scheimpflug geometry

In an optical system where both the subject plane and the detector (image) plane can tilt relative to the lens axis (Figure 2.4), it can be observed from geometry that the magnification of the system can be linked to the angle of incidence (θ) and the tilt angle of the detector (α) such that:

$$M = -\frac{\tan \alpha}{\tan \theta} \qquad (2.19)$$
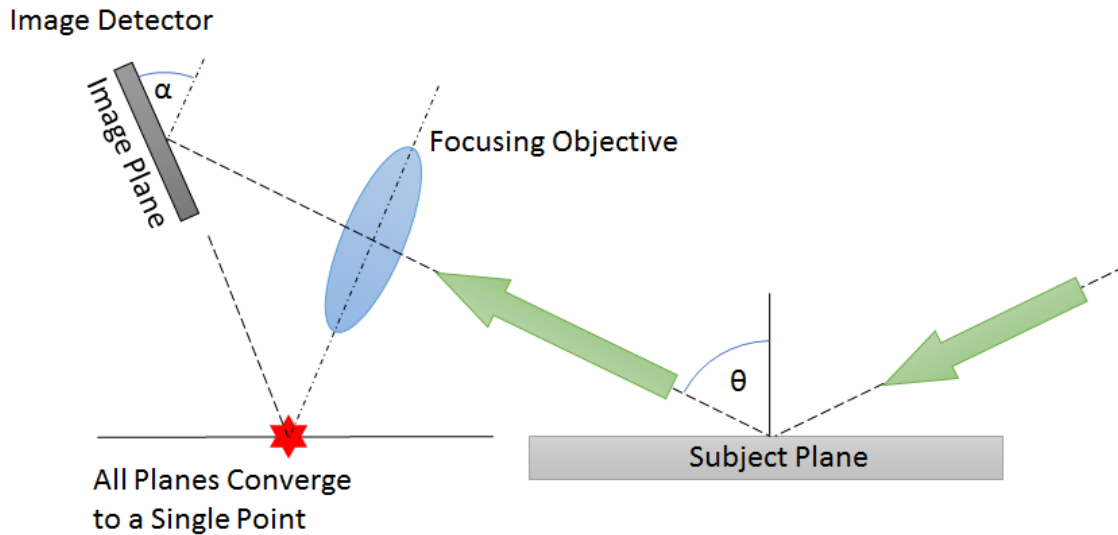
FIGURE 2.4: Schematic of the Scheimpflug principal; where the image, objective and subject planes all converge to a single point identified as a red star.

As can be seen in the schematic (Figure 2.4) if the detector plane tilt angle (α) is equal to the angle of incidence (θ) then the planes will all converge at a single point known as the Scheimpflug line. Here the plane of focus will be coincident with the detector plane and the image formed will appear as if the detector was looking straight down on, parallel to, the subject plane.

It can be noted from Equation 2.19 and Figure 2.4 that for large angles of incidence and magnifications, extending significantly from unity, the angle (α) required of the detector plane becomes prohibitive. However, a solution to this problem comes from the ability to vary the angle of the objective lens plane relative to the detector plane (Figure 2.5).

Application of the sine rule gives:

$$\frac{d_s}{\sin(\theta - \delta)} = \frac{x}{\sin(90 - \theta)} \qquad (2.20)$$

and
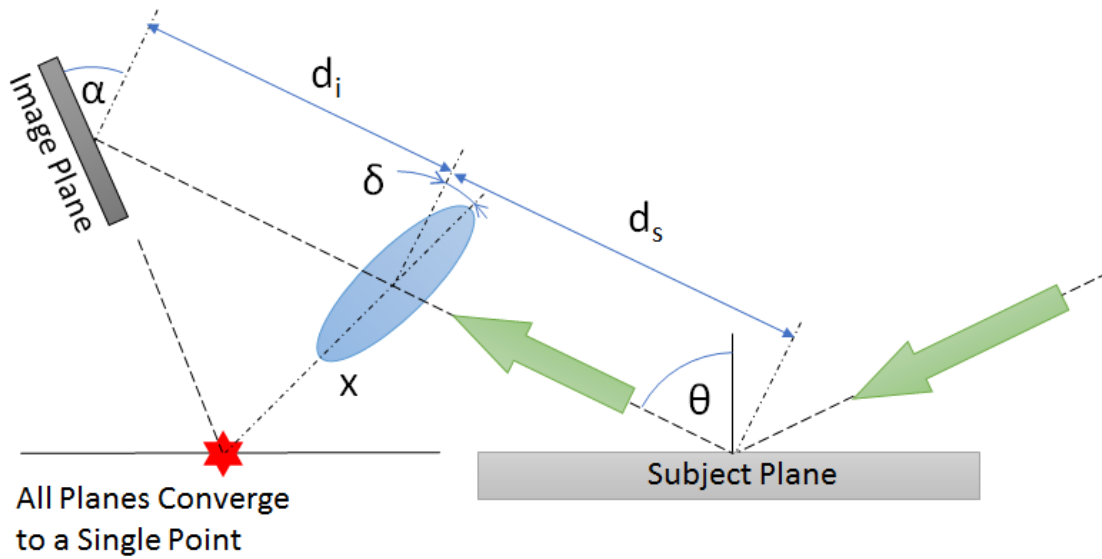
FIGURE 2.5: Schematic showing the Scheimpflug principal for large angles of incidence; highlighting how the Scheimpflug principal can be maintained by the additional inclination δ of the focusing objective. This then maintains the image, objective and subject planes ability to all converge to a single point, identified as a red star.

$$\frac{d_i}{\sin(\alpha + \delta)} = \frac{x}{\sin(90 - \alpha)} \tag{2.21}$$

Rearrangement and substitution into Equation 2.19 results in:

$$M = -\frac{\cos(\theta) \cdot \sin(\alpha + \delta)}{\cos(\alpha) \cdot \sin(\theta - \delta)} \tag{2.22}$$

This provides the mathematical basis which is encoded into the AIE lens control system.

2.3.3 LED light source

The high coherence of the original AIE laser light source led to issues of interference fringes within the AIE images (Section 2.2.3). To overcome these issues evaluation of LED light sources as a replacement for the DPSS laser were undertaken.

Evaluation involved calculating the delivered power of light over the narrow bandwidth of 531.20 - 532.78nm using the spectral profile of the LED, provided by the manufacturer. The delivered power reduction was brought about by the narrow band pass optical filter (Thorlabs: FL532-1) necessary to constrain the wavelength input to the Meadowlark unit. Code was written in SciLab which took the manufacturers normalized intensity spectrum and integrated the total area under the curve, divided the manufacturer specified LED total output wattage into this total area, then summed the portion under the curve within the filter band width specified, thus calculating a first order approximation of the energy adjusted output of the LED within the filtered wavelength of interest (Figure 2.6).

Optical models for the LED were evaluated using WinLens3D (version: 1.2.11) with a view to optimizing the relation between reducing beam divergence to a minimum and maximizing incident flux. The non point-source nature of any light source makes optical design something of a compromise (Figure 2.7), with the non-ideal output identified as chief rays A and B, these result from the physical width of the LED. This problem is particularly relevant to the collimation of light for the AIE because of the angular dependence of the ellipsometric values Ψ and Δ. WinLens3D allowed calculation of the numerical aperture for each optical arrangement considered, which when combined with the radial intensity distribution for the LED output, provided by the manufacturer, allowed further refinement of the anticipated incident flux for each design considered.

As such a 50mm diameter, 40mm focal length, aspheric condensor lens design (Thorlabs: ACL5040U-A) with a stop of 25mm diameter at a distance of 100mm was selected. When modeled, the beam divergence measured by the chief ray was 2.46 degrees, while providing an incident flux of $\approx 6.3\mu W$ per mm^2 when the radial intensity distribution for the LED was factored into the numerical aperture of the optical design. The original DPSS laser, by way of comparison, when passed through the beam expander (Thorlabs: BE015M-A) was estimated to have a beam divergence of ≈ 0.7 degrees and an illumination intensity of of $\approx 5.1\mu W$
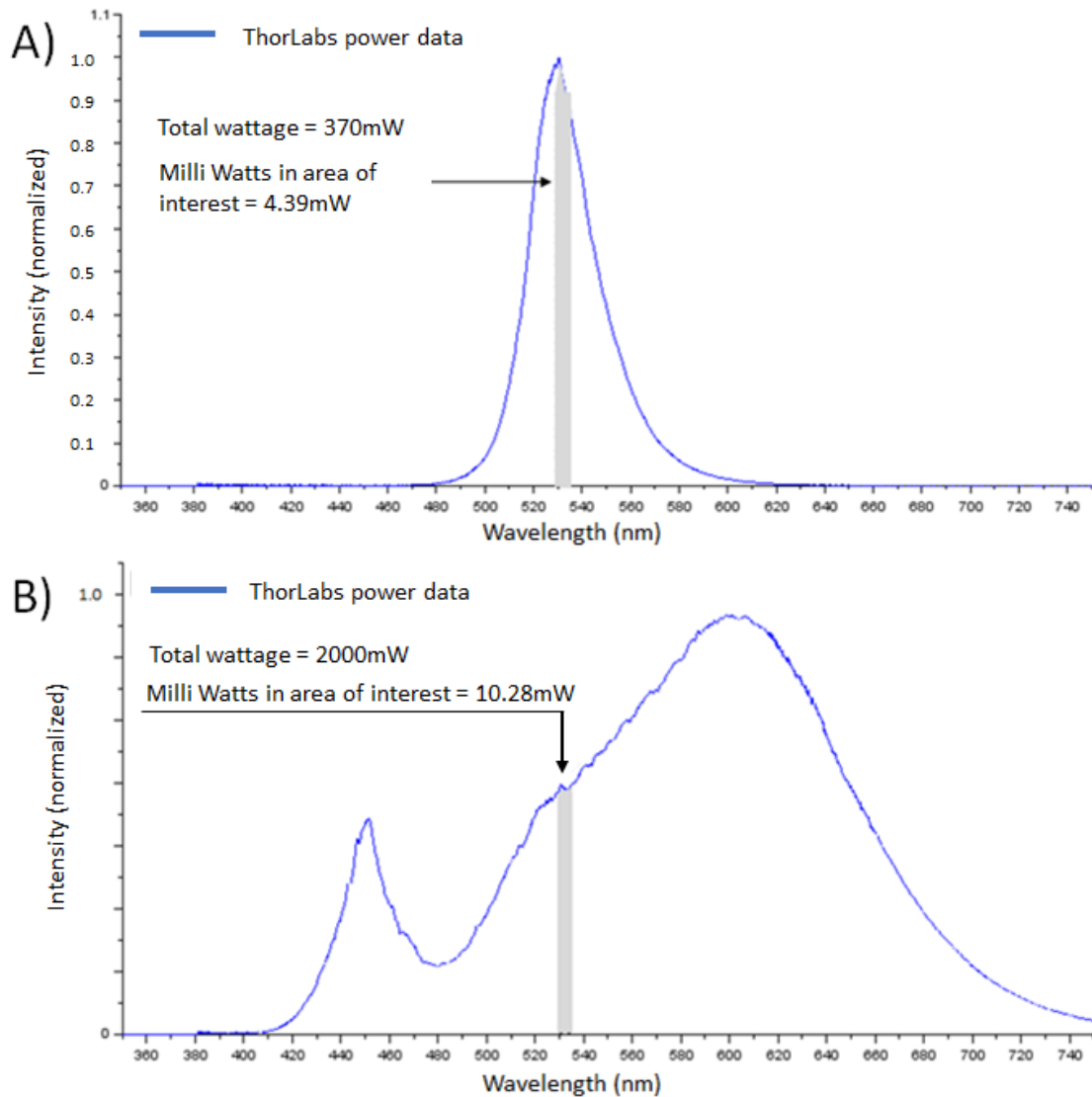
FIGURE 2.6: The spectral profile for two potential LED light sources; A) Thorlabs: M530F2 narrow wavelength 530nm 370mW LED, which has a power output of just under 4.4mW in the filtered spectral range shown as a gray band. B)Thorlabs: MWWHLP1 broad spectrum 2000mW LED, with a power output of just under 10.3mW delivered in the filtered range.

per mm^2 [159], [160]. An example of the chosen LED design evaluated using WinLens3D is presented (Figure 2.7).
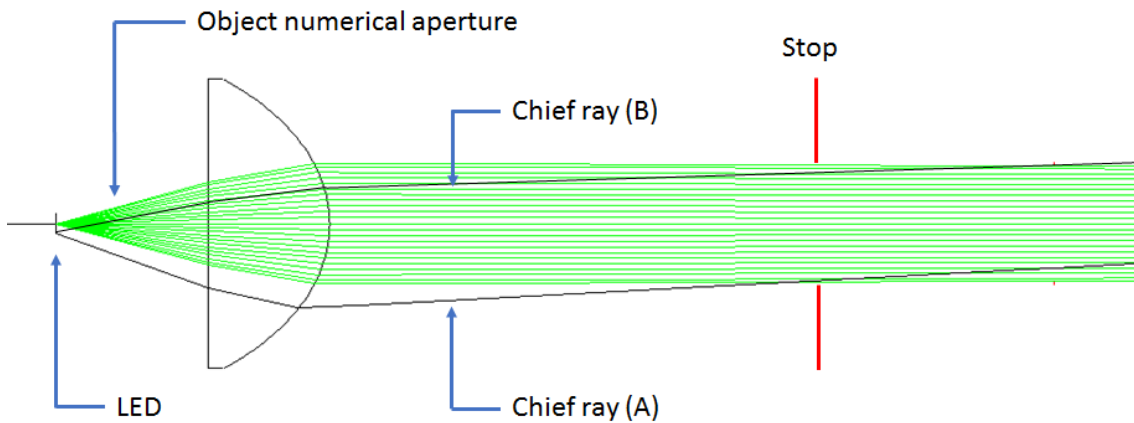
FIGURE 2.7: Example of WinLens 3d optical modeling: demonstrating the effect of a non point light source on the chosen optical design of an anti-reflection coated 50mm diameter, 40mm focal length aspheric condensor lens, with a 25mm diameter stop positioned at 100mm, identifying chief rays (A) and (B) which have a divergence of $\approx$ 2.5 degrees and 1.8 degrees respectively.

2.3.4 AIE optical resolution

The diffraction pattern formed by plane waves from a point source passing through a circular aperture is fundamental to the resolving power of an optical system. The problem of describing mathematically, the diffraction pattern of a point source from the perspective of optical performance was first solved by Airy in 1835 [161]. Airys description of a bright central spot surrounded by a series of fainter rings describes the best focused spot of light, that a diffraction limited optical system with a circular aperture can make. From the image intensity peak to the first minimum is called the airy disk. With the resolution of an optical instrument defined by it's ability to produce separate images of two objects in very close proximity [11, pg:329]. It is the diffraction pattern of adjacent airy disks and their superposition that sets the theoretical upper limit of resolution. Building on this work Abbe defined the limit of resolution for light illuminated microscopes in 1873 as being:

$$d = \frac{\lambda}{2n\sin(\theta)} \tag{2.23}$$

where d is the minimum resolvable distance, n is the refractive index of the lens, λ and θ are respectively the wavelength and half angle of the incident light [11,

pg:333]. From this $n\,sin(\theta)$ is termed the numerical aperture and represents the light gathering ability of the lens. The focal ratio or f number ($f\#$) is calculated as being:

$$f\# = \frac{focal\ length}{pupil\ diameter} \tag{2.24}$$

The Rayleigh criterion determines the minimum separation between two light sources that allows them to be resolved into two distinct objects [162]. If the central peaks of the two diffraction patterns are no closer than the radius of the first minimum of the airy disk (Figure 2.8) then the sum of the contributions at this point is given to be 0.811, which was chosen by Rayleigh at the time as the criterion for resolution of two diffraction patterns [11].
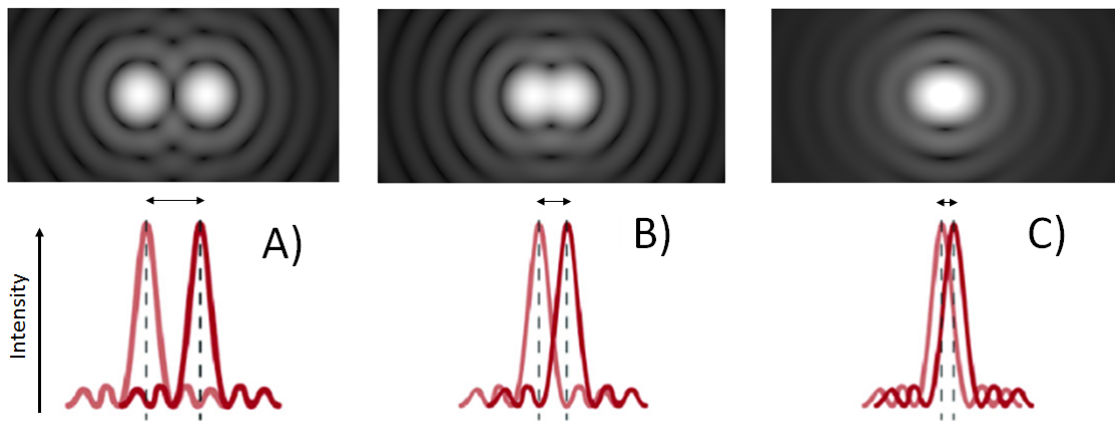
FIGURE 2.8: Airy disks and resolution; A) Two light sources are clearly resolvable as the first minimum of the airy disk are separated. B) Two light sources are just resolvable, the airy disks overlap but they are separated grater than the airy disk radius. C) The airy disks overlap less than the airy radius and the objects cannot be resolved into two separate images.

Following the Rayleigh criterion the minimum angle of resolution is given by:

$$sin\theta = 1.220 \cdot \frac{\lambda}{D} \tag{2.25}$$

Where, λ is the incident light wavelength and D is the diameter of the optical aperture. For the AIE lens, sensor and light source this combines with Equations 2.23 and 2.24 to give the minimum resolvable distance d for a given optical lens:

$$d = 1.220 \cdot \lambda \cdot f\# \tag{2.26}$$

Sparrow determined that the Rayleigh criterion was not intended as a measure of the actual limit of resolution, but rather as an index to describe the relative merit of different instruments of the time. The Sparrow criterion proposes that the condition for resolution of two objects occurs with what Sparrow describes as the undulation condition, whereby the central maximum just reduces. This produces a theoretical resolving power about 26 per cent greater than that obtained by the Rayleigh criterion [163].

With the advent of electronic photo multipliers and digital imaging technology such as CCD sensors, Rose applied the statistical probability of a noise signal fluctuating above the mean signal value such that a ratio of 5:1 signal to noise would provide only a $3 \cdot 10^{-7}$ (or 1 in 3 mega pixels) chance that the noise would exceed the mean signal value [164]. For the purpose of resolving objects on a 2D array through optical imaging it is necessary to ensure a SNR that exceeds the Rose criterion which can be described mathematicaly as:

$$SNR_{\mathrm{img}} = \frac{\mu_{\mathrm{s}}}{\sigma_{\mathrm{s}}} \tag{2.27}$$

Where μ_{s} is the signal mean value and σ_{s} is the signal standard deviation.

Currently a commonly used measure to compare the performance of optical systems is the modulation transfer function (MTF), which combines the concept of resolution as described above with that of image contrast which includes sensor generated noise. A typical test target consists of a series of alternating light and dark bars (called line pairs) of equal width, with several sets of patterns of reducing line spacing. When this type of pattern is imaged by a refractive optical system, diffraction and aberrations at the edge of each solid black / white line cause a blurring described as a line spread function (Figure 2.9) [165, pg:361].

The line spread function smooths the captured image and the effect on progressively finer line patterns is to reduce image contrast to a point where the detector system is no longer able to resolve illumination contrast and the pattern can no longer be defined [165, pg:366].
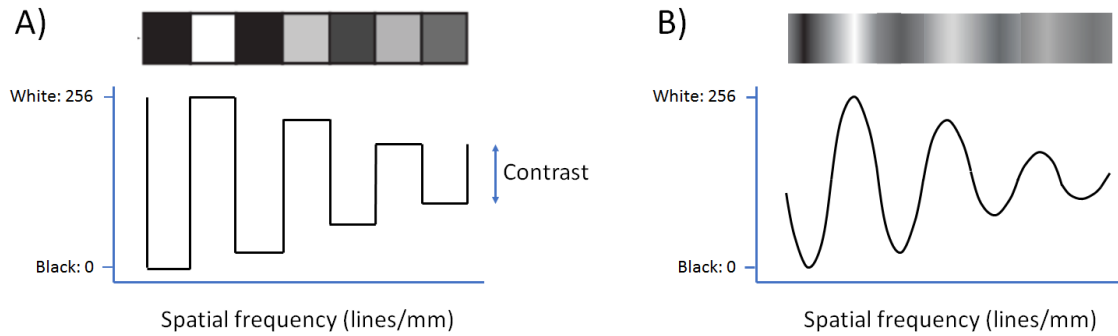
FIGURE 2.9: Contrast of a bar test target; A) The schematic representation of a physical set of line pairs displaying reduced contrast. B) The image formed of the line pairs presented in A when observed by a refractive optical system. When the detector system is no longer able to differentiate illumination contrast the pattern can no longer be resolved.

Contrast can be expressed as modulation and defined mathematically as:

$$C_i(\%) = \left(\frac{I_{\text{max}} - I_{\text{min}}}{I_{\text{max}} + I_{\text{min}}} \right) \tag{2.28}$$

Where I_{max} is the maximum image intensity and I_{min} is the minimum image intensity.

The MTF is by definition expressed as the contrast change observed in the image of the test target lines as a function of their spatial frequency. This gives:

$$MTF(v) = \frac{C_i}{M_o} \tag{2.29}$$

Where image contrast modulation C_i as a ratio of the object spatial modulation M_o can be plotted as MTF(v). The widespread adoption of MTF has thus led it to be an almost universal measure of an image systems performance [165, pg:369]. Plotting of the MTF as a function of the number of line pairs per millimeter characterizes the resolving performance of the optical system, whereby the

intersection of the MTF with the line describing the system limit of modulation detection defines the limit of resolution (Figure 2.10). Calculation of MTF from actual images is readily performed by ImageJ plugin Slanted Edge MTF and results were obtained in accordance with the recommended methods documented in the plugin bibliography.
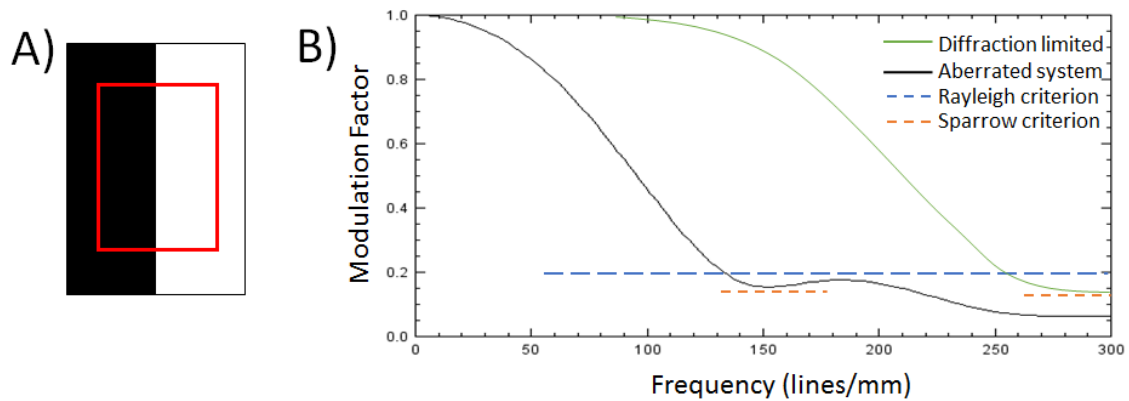
FIGURE 2.10: MTF limit of resolution; A) Simulated line pair with region of interest in red. MTF analysis is performed right to left over a chosen number of pixels in rows from top to bottom within the area of interest. B) MTF plot of the image region of interest, which shows a profile of a diffraction limited system in green and an aberrated non ideal optical system in black. Also shown is the Rayleigh criterion which is fixed at $\approx 0.2\%$ of MTF (blue dashed line) and Sparrow criterion which identified at the first minimum point of detectable change (red dashed lines).

The effects on a 2d array like the one imaged by the AIE are a combination of the factors discussed above, with lens $f\#$, illumination wavelength and Rayleigh (or Sparrow) criterion setting the upper limit of resolution. Influence on image contrast, which includes illumination intensity and collimation, along with the sample under investigation, further effect resolution. While lens aberrations and CCD sensor noise are additional factors that all combine in the final image.

The theoretical limit of resolution of the AIE optical system was calculated from Equation 2.26:

$$d = 1.220 \cdot 0.532 \cdot 5.6 = 3.63 \mu m \tag{2.30}$$

This is just less than half of the pixel size of the CCD sensor, which for a 1:1 magnification results in the image being limited by the sensor resolution under optimal contrast conditions.

The USAF1951 resolution target (Figure 2.11) is a common calibration standard for the quantification of optical system resolution and MTF [165], [166]. The target is comprised of carefully sized horizontal and vertical lines, termed elements, visualization of these discrete spatial frequencies allows the rapid manual estimation of resolution in line pairs *per* millimeter and detailed analysis of MTF. Six sets of elements are clustered into a group on the target. The manual estimation of system resolution is defined by the group and element numbers before the set of lines which cannot be seen distinctly and blur together. The resolution (R), described in the number of line pairs per millimeter which can be visualized, is calculated from Equation 2.31
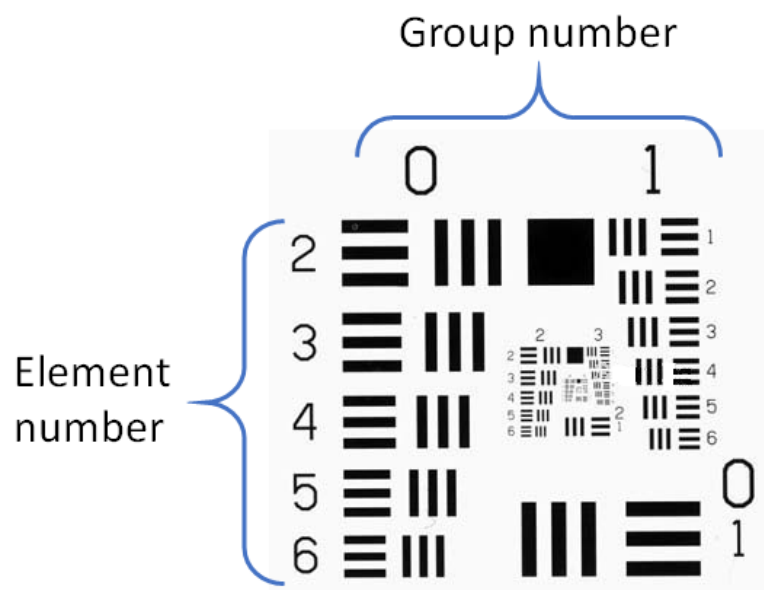
FIGURE 2.11: USAF1951 resolution target; as supplied by Edmund Optics. Visually finding the Group and Element which can just be resolved as distinctly separate lines, enables quantification of the resolving power of the optical system in line pairs per mm using formula 2.31.

$$R = 2^{\left(G_n + \frac{E_n - 1}{6}\right)} \tag{2.31}$$

where: G_n is the Group number and E_n is the Element number.

Changes to the optics of the AIE were checked and adjusted using the USAF 1951 target to ensure optimization of the system resolution. Final evaluation was conducted at a 60 degree angle of incidence in both standard and Scheimpflug optical geometry. Images were captured across the field of view and processed in ImageJ Slanted Edge MTF over an area of 64 pixels to produce image sensor scaled MTF plots in a lines *per* mm format.

2.3.5 AIE protein observations using null methods

Calibration standard BSA at a concentration of $200\mu g/ml$ (Sigma) was dispensed onto cleaned silicon wafers as $0.5\mu l$ droplets using a pipette. Droplets were covered and allowed to dry naturally at a room temperature of 18ºC on the lab bench. The samples were then visualized using the AIE at a 60 degree incident angle in Scheimpflug optical geometry, the retardance of input light and analyzer angle were adjusted to give a null background. Images were recorded in greyscale for analysis in ImageJ to determine pixel intensities, from which the model of Arwin *et al.* [63], [71] was applied, whereby the detected intensity relates to the thickness of the deposited layer as:

$$I = k \cdot d^2 \tag{2.32}$$

where I is the measured intensity, d^2 is the surface coverage and k is a constant of proportionality related to the protein layer. The value of k was determined by dividing the known amount of BSA in the spot by the square root of the integrated total intensity within the spot, obtained from image analysis using ImageJ. For a layer of protein adsorbed onto a silicon substrate, measured in air, the relation between the surface concentration and the protein layer thickness can be described as:

$$Sc \approx K \cdot d \tag{2.33}$$

where, Sc is surface concentration (ng/mm^2), d is the protein layer thickness (nm) and K approximates to 1.2 [67], [71], [167].

2.4 Results

2.4.1 Transparent substrate back reflection removal

To maximize the AIE optical resolution it was necessary to remove the back reflection from glass substrates, such as the USAF 1951 resolution target. This was done by placing a refractive index matching material under the transparent sample [168]. Examples of index matched and non index matched images are presented (Figure 2.12).
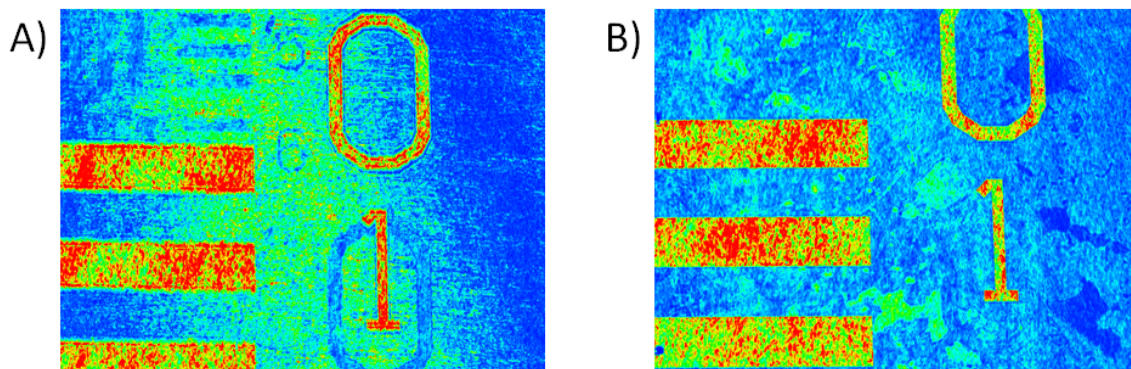
FIGURE 2.12: Imaging of the glass USAF 1951 resolution target using the AIE; A) Under laser illumination, without index matching and a back side reflection of the zero appearing around the number 1 B) Under laser illumination, with index matching material under the target, removing the back side reflection.

2.4.2 Evaluation of LED as an AIE light source

Modeling indicated that a collimated broad spectrum 2000mw LED light source (Thorlabs: MWWHLP1), filtered at 532nm, would provide an illumination intensity of ≈ 10.3mW, this translated over a 35mm diameter area of illumination to an intensity of $\approx 10.7\mu$W /mm^2 which reduced to $\approx 6.3\mu$W /mm^2 when the final design including the filter stop at 100mm and the LED radial intensity distribution was taken into consideration. This was higher than the DPSS laser ($\approx 5.1\mu$W

per mm^2) and hence sufficient to adequately illuminate sample surfaces such as silicon and glass. Other alternative LEDs that were evaluated, including single colour units such as the Thorlabs: M530L4 were not able to deliver sufficient irradiance ($\approx 2.7 \mu$W per mm^2) to make full use of the camera dynamic range, thereby risking an increase in system errors.
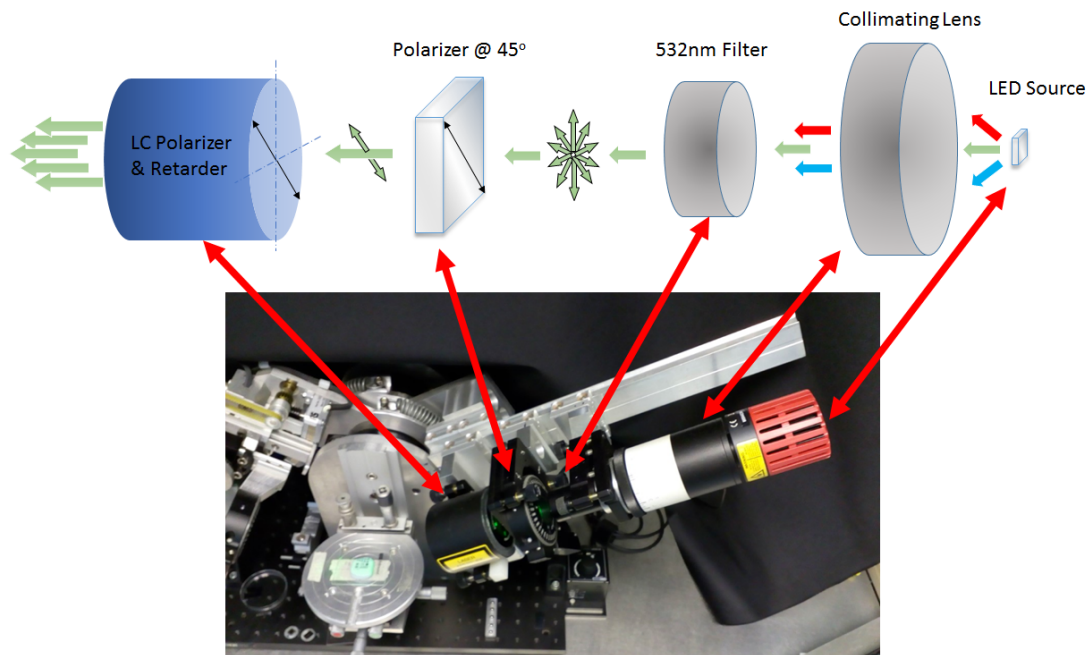
FIGURE 2.13: Schematic view of the LED set up; indicating from right to left, LED light source, aspheric condensing lens collimating the light beam, a 532nm narrow band pass filter, linear polarizer set at 45 degrees to provide input to the Meadowlark retarder and polarization rotator.

Therefore the light source chosen was a Thorlabs: MWWHLP1 LED which was collimated using an aspheric condensor lens 50mm diameter, 40mm focal length (ACL5040 AR coated) combined with a 25mm diameter 532nm filter (Thorlabs: FL532-1) set at a distance of 100mm. The light source and optical elements were positioned to give a minimum measurable spot size ($\approx$850mm diameter) at a distance of 8 meters, producing a numerical aperture (NA) of 0.10 and an estimated maximum chief ray divergence of $\approx$3.1 degrees. Which is in close agreement to the modeled value of 2.45 degrees. The full AIE setup is presented (Figure 2.13).

2.4.2.1 Comparison of signal to noise ratios for LED and laser illumination

A representative cross section through the ellipsogram measurement of an RCA1 cleaned silicon substrate chip with a 9nm overlayer of SiO_2, illuminated by the DPSS laser light source is presented (Figure 2.14). The standard deviation for 265 pixels across the surface was calculated to be: Δ = 3.26 deg [n=3] Ψ = 0.35 [n=3]. Applying the Rose criterion (Equation 2.27) gives a SNR of 57 for Δ and 64 for Ψ, which is an order of magnitude above the Rose threshold limit of 5.
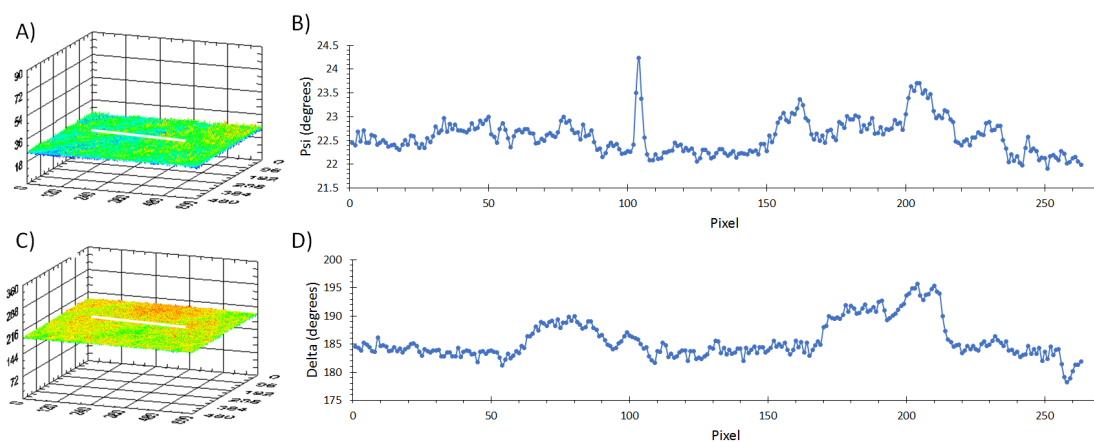
FIGURE 2.14: Representative ellipsograms of an RCA1 cleaned silicon chip; with a 9nm SiO_2 overlayer, illuminated at 70º by DPSS Laser light source, A) 2D plot of Ψ values across the sample. B) Plot of Ψ values along the line of interest, the white line in Figure A, presenting an indication of system noise over the surface. C) 2D plot of Δ values across the sample. D) Plot of Δ values along the line of interest, shown in white in Figure C.

RCA1 cleaned silicon substrate chip with a 9nm overlayer of SiO_2, illuminated by the LED light source is presented (Figure 2.15). Representative cross sections are included, from which the standard deviation for 360 pixels across the surface was calculated to be: Δ = 0.18 deg [n=12] Ψ = 0.05 [n=12]. Applying the Rose criterion (Equation 2.27) gives a SNR of 1018 for Δ and 460 for Ψ, which is almost two orders of magnitude above the Rose threshold limit of 5.
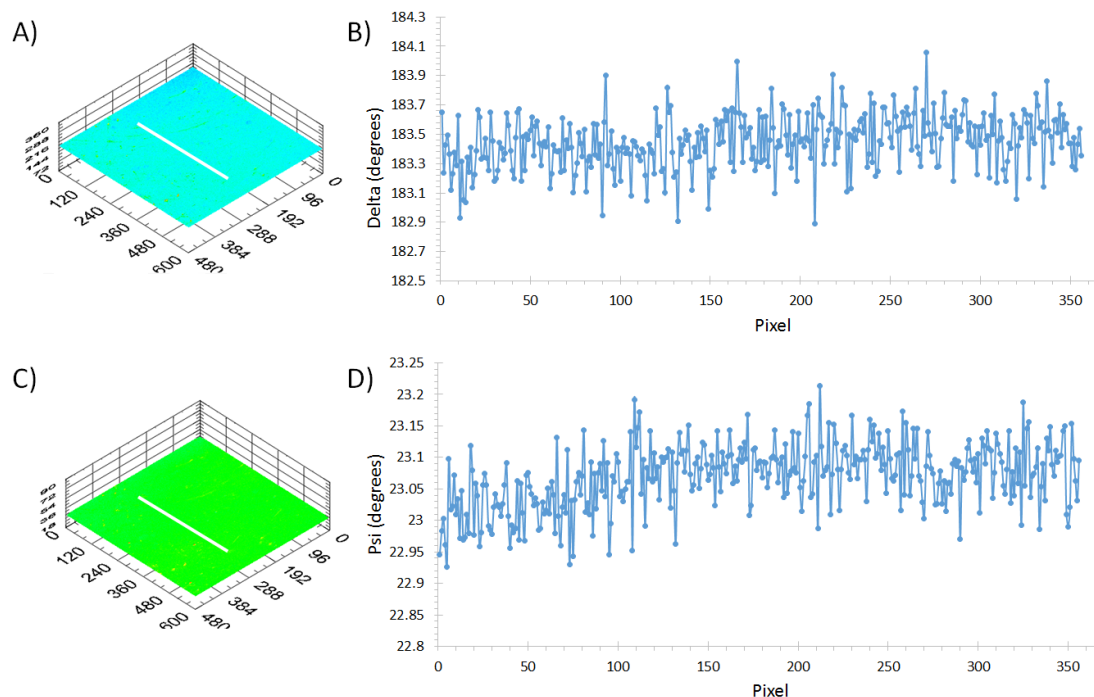
FIGURE 2.15: Representative ellipsograms of an RCA1 cleaned silicon chip with 9nm SiO$_2$ overlayer; illuminated at 70° by LED light source, A) 2D plot of Δ values across chip surface B) Plot of Δ values along the line of interest, the white line in Figure A, presenting an indication of system noise over the surface. C) 2D plot of Ψ values across chip surface. D) Plot of Ψ values along the line of interest, shown in white in Figure C.

2.4.3   AIE radiometric data collection absolute error

It was necessary to verify the AIE outputs and establish the absolute error between values for Ψ and Δ as calculated by the AIE, from radiometric intensity, and those values obtained from spectroscopic ellipsometry obtained by the GESP-5, for the same sample (Figure 2.16). Further comparisons were made using the same spectroscopically measured samples over a range of angles of incidence. Spectroscopic values for Ψ and Δ obtained at 532nm were extracted for comparison with those obtained by the AIE. A silicon substrate with at 9nm SiO$_2$ oxide over-layer was imaged at incident angles from 55 to 70 degrees with the AIE set to Scheimpflug optical geometry, ensuring the whole of the image was in focus across the CCD array. The mean values for Ψ and Δ were extracted from the ellipsograms and used as data points (Figure 2.17). Error bars are calculated from the error estimations described earlier (Section 2.3.1.2).
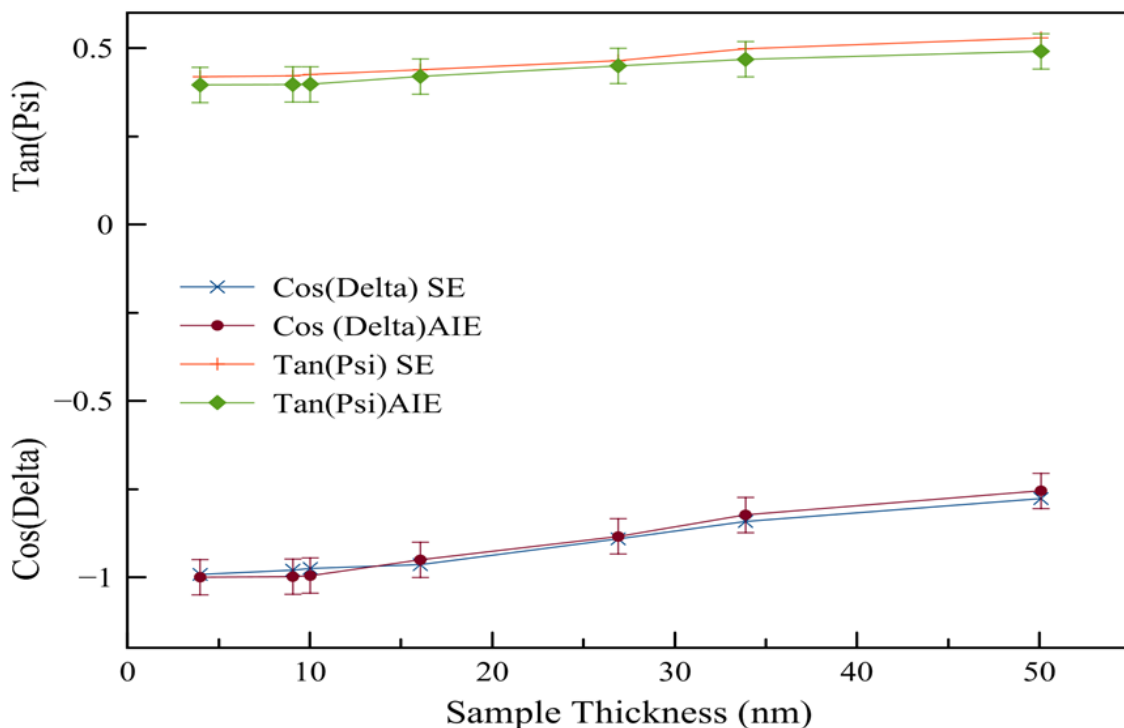
FIGURE 2.16: Comparison of AIE and GESP-5 Ψ and Δ sample determined values: for a series of thermally grown SiO_2 overlayers on crystalline Si substrate at an incident angle of 70 degrees.
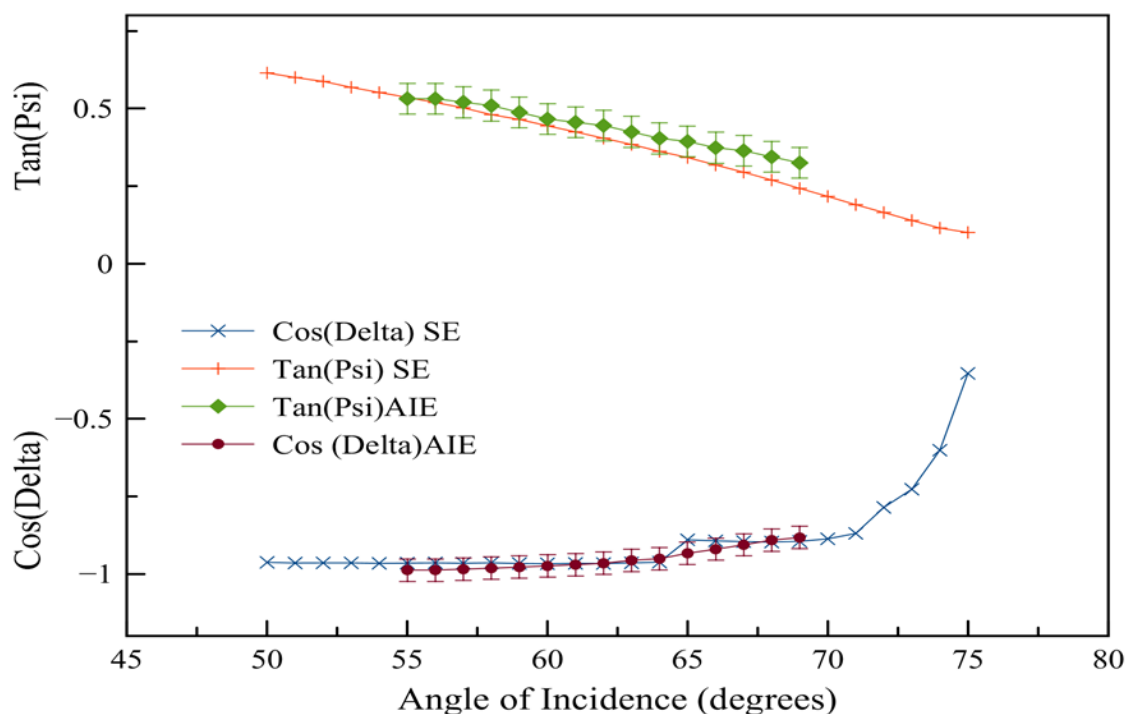
FIGURE 2.17: Comparing Ψ and Δ values obtained from GESP-5 spectroscopic ellipsometry and the AIE; Sopra GESP5 and the AIE, for silicon wafer with 9nm SiO_2 overlayer, at 532nm wavelength, from 50 to 75 degree angles of incidence.

2.4.4   Resolution under Scheimpflug optical geometry

The objective lens of the AIE is a Schneider-Kreuznach Symmar macro 80mm f5.6 giving an acceptance angle of just over 5 degrees at a 1:1 magnification. With such a lens it is possible possible to fix α equal to θ (Section 2.3.2.1) correcting the image perspective distortion, then adjust the objective lens tilt angle to maintain focus over a range of magnifications, to a maximum of 1.4 times at an incidence angle of 60 degrees.
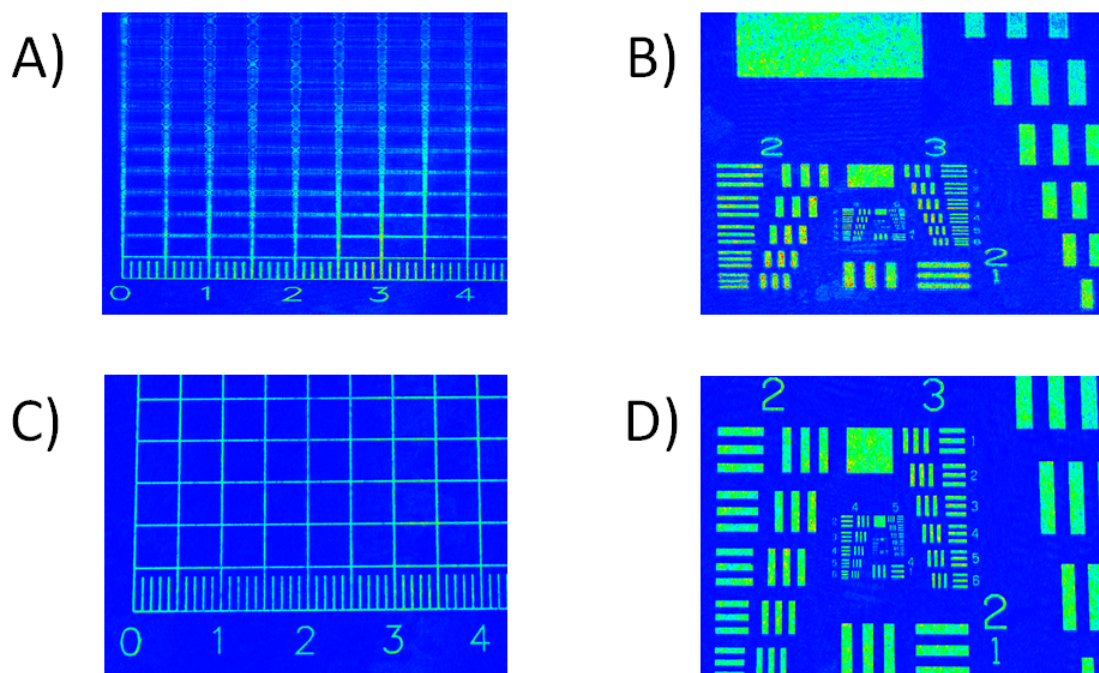
FIGURE 2.18: Representative reticule and target images captured via the AIE: A) & C) Calibration reticule (Edmund optics) and B) & D) USAF 1951 resolution target (Edmund optics). Imaged at 60 degrees under laser illumination using a conventional optical view A) & B) or using the embedded AIE Scheimpflug optics C) & D).

USAF1951 resolution target images can be observed in Figure 2.18, with the target illuminated using the laser light source and at a 60 degree oblique viewing angle, both standard (B) and Scheimpflug corrected (D) images are shown.

The resolution (R), described as the number of line pairs per millimeter which can be visualized, was calculated from MTF analysis of the USAF1951 target. The

MTF was conducted in ImageJ where the Slanted Edge MTF plugin was used over a 64 pixel area of interest (Figure 2.19).
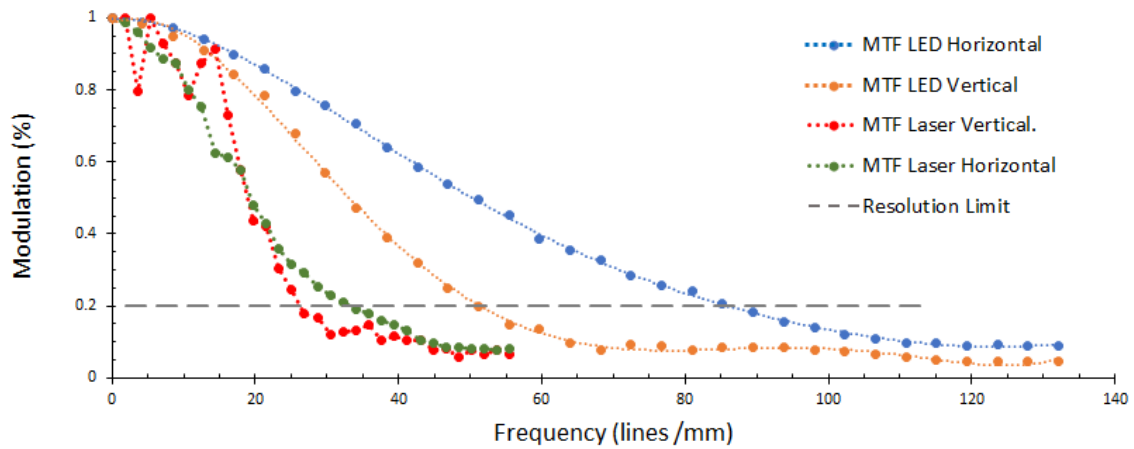
FIGURE 2.19: Representative MTF plots of images captured via the AIE: A USAF1951 target imaged under LED and then laser illumination at 60 degrees in Scheimpflug optical geometry, indicating both horizontal and vertical resolution.

Data from six MTF plots were averaged for each optical arrangement and the limit of resolution was chosen at the Rayleigh criterion. The resolution in μm was calculated as $1/R$ and is presented for variation in light source and optical geometry (Table 2.2). The error was calculated from the standard deviation of the measured data.

TABLE 2.2: Comparison of resolution determined using MTF analysis of USAF1951 target: for laser and LED light sources with both standard and Scheimpflug optical geometry, all at a 60 degree angle of incidence. Values are given in μm, [n=6].

	Laser		LED	
	Horizontal	**Vertical**	**Horizontal**	**Vertical**
Standard geometry	32.0 ($\pm$2.5)	115.1 ($\pm$9.3)	11.9 ($\pm$0.6)	99.2 ($\pm$7.7)
Scheimpflug geometry	31.3 ($\pm$2.5)	38.5 ($\pm$3.8)	11.8 ($\pm$0.6)	20.0 ($\pm$1.4)

2.4.5 AIE observation of proteins using null methods

Using null methods of ellipsometry proposed by Jin *et al.* it was possible to determine the surface coverage of a protein layer from image analysis of off null intensities, given the total protein content deposited is pre-known (Equation 2.32). Using calibration grade BSA (Sigma) produced the image shown (Figure 2.20), which can be seen to suffer from the coffee ring effect at the outer edges.
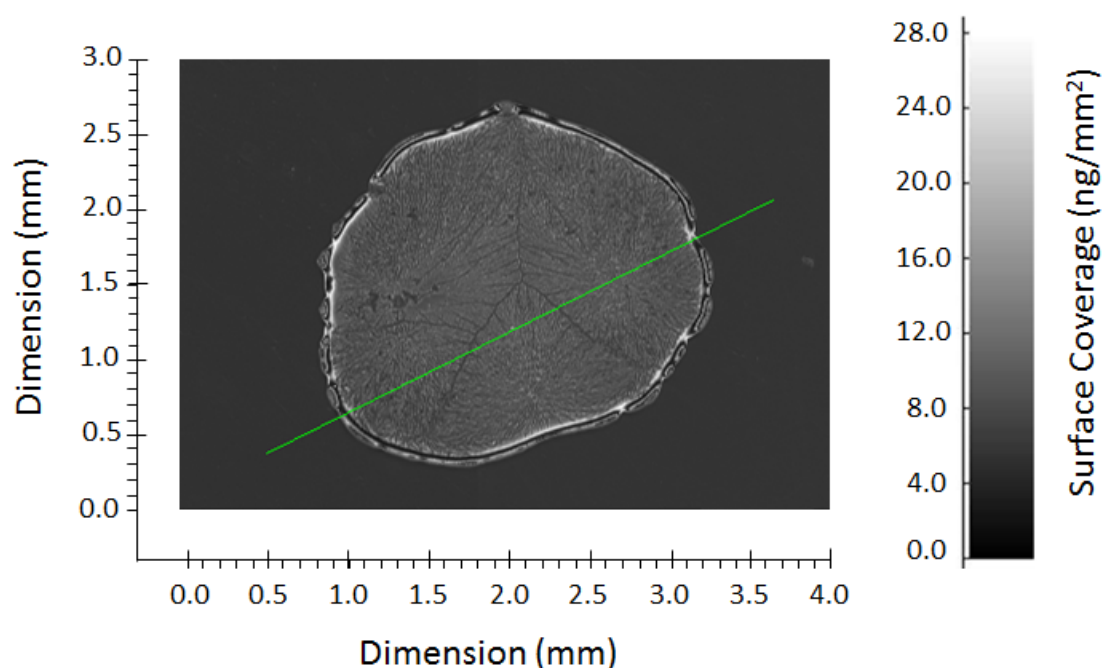
FIGURE 2.20: Representative null image of a 0.1μg Bovine Serum Albumin protein spot; imaged using the AIE with incident light polarization parameters adjusted such that the supporting substrate surface presents a null intensity. The Green line indicates a line of interest for intensity profile analysis (not shown).

The intensity of the image can be divided into three areas; firstly the solid substrate surface at 0.0 ng/mm^2, secondly the coffee ring periphery with values at 28.0 ng/mm^2 and finally the central portion of the spot which fluctuates from 8.0 to 16.0 ng/mm^2. Using Equation 2.33 the calculation of protein layer thickness across the center of the spot is seen to fluctuate from around 6 to 14nm and to peak at just over 23nm at the periphery. This would correspond with the BSA being distributed across the center of the spot between one and three layers

thick, then as a two to six multi-layer structure at the edges depending on protein orientation, given the BSA molecules description as a prolate ellipsoid 14 x 4 x 4nm [169].

2.5 Discussion

Ellipsometry measures the change in polarization state of reflected light and is a non-contact, non-destructive, label free method, which when applied to appropriate models is capable of determining the optical properties and thickness of thin films. The AIE combines the capabilities of ellipsometry with optical imaging to inform sample surface changes at a spacial resolution in the range of micro meters. The aim of this study was to develop and optimize the AIE to specifically observe AAI.

2.5.1 Radiometric discussion

The key feature of the radiometric approach is the ability to generate high speed determination of the change in polarization state of reflected light, Ψ and Δ, quickly and at a high spatial resolution. Typically, 25 polarization data points can be collected within 10 to 15 seconds, automatically passed to the LabView algorithm and presented immediately as an ellipsogram for further analysis.

However, despite this initial success, both reductions of absolute error and improvement for quantification of absolute error is necessary. This is particularly relevant in light of the need to develop accurate models for specific AAIs in an attempt to quantitatively determine thickness changes rather than the current method employed, observing relative change through the optical parameters Ψ and Δ.

2.5.2 Scheimpflug discussion

The oblique viewing angle required for ellipsometry produces issues for imaging ellipsometry as an efficient measurement technique. Previous methods to extract the in focus data, have required the use of scanning techniques that composite images together to produce an image of sufficient scale as to be informative. Thus additional processing procedures have incurred reduced resolution and increased data capture times [59], [72]. The application of fully automated Scheimpflug optical geometry on the AIE offers a significant step forward in ease of use and has particular benefits to the application of imaging of a compact bio-sensor array. The improvement provided by Scheimpflug geometry takes the resolution limit across the sample surface under LED illumination from $99.2(\pm7.7)\mu$m to $20.0(\pm1.4)\mu$m. This increase in optical resolution across the whole of the image area introduces the potential for imaging multiple protein spots in the form of an AAI micro-array.

2.5.3 LED light source

Changing the light source from a monochromatic laser to a broad spectrum LED coupled to a narrow band pass filter presented a number of significant benefits; Importantly the reduction in interference patterning improved horizontal image resolution from $31.3(\pm2.5)\mu$m to $11.8(\pm0.6)\mu$m, and reduced the standard deviation for data values across a optically constant surface by an order of magnitude, from 3.26 to 0.18 degrees for Δ and from 0.35 to 0.05 degrees for Ψ. The effect of which produced a significant overall improvement in observed image sharpness and ellipsogram quality despite an increase in the modeled beam divergence from $\approx$0.7 degrees for the laser to $\approx$2.5 degrees for the LED. Incident light flux is sufficient to ensure full illumination of the sample area, while utilizing the full dynamic range of the camera CCD, which further minimizes errors.

Removal of the DPSS laser light source and it's associated optical components, replaced by the more compact and simplified LED setup brought benefits in a simplified alignment procedure and a reduction in the overall weight on the polarizer arm of just under 1kg. This weight reduction saw an improvement in the reliability of the arm positioning motor to lift from 90º without overloading. This increase in reliability at the extremes of angular operation supported the work in extending the AIE functionality to include measurement of surface free energy through the observation of solid surface and liquid interface contact angle, something which is discussed in detail in Chapter 3.

2.5.4 Future development and improvements

The theoretical limit of resolution for a microscope was defined by Abbe [11, pg333] and is described by:

$$d = \frac{\lambda}{2n\sin(\theta)} \tag{2.34}$$

Where: $\sin(\theta) = 2\cdot$ Numerical Aperture (NA) and n for air = 1

So in our case, an $f5.6$ lens where $f\# = \frac{1}{2NA}$:

$$d = \frac{\lambda}{2NA} = \frac{532}{2NA} = 532 \cdot 5.6 = 2.98\mu m \tag{2.35}$$

The measured resolution of 11.8μm horizontal and 20.0μm vertical would by comparison indicate some room for improvement may be possible in optical alignments and light beam collimation to closer approach the theoretical limit. However, given the camera pixel cell size is 7.4μm [143], any optical improvement beyond this value would not be resolved. Currently, at a resolution of 11.8μm the camera is oversampling at a ratio of just over 1.6 which is lower than that required by the Nyquist-Shannon sampling theorem of 2 [170], [171]. Hence it is reasonable to assume that the camera CCD sensor is the current limit to resolution and an improvement would be gained by changing to a sensor with

smaller pixel size. The observation that the sensor is a limiting factor operating close to the Nyquist sampling limit raises the possibility that the laser illumination interference pattern seen on samples may have been caused by aliasing within the camera CCD sensor leading to a Moiré pattern formation [172] and this may warrant further investigation.

During the early part of this study the Sopra Gesp5 spectroscopic ellipsometer suffered a complete electronics failure which was unresolvable. This has limited the opportunity to directly compare AIE results to those of a calibrated spectroscopic system and has impacted on the ability to use the null methods described in literature to develop AAI models, due to their reliance on spectroscopic ellipsometry to fully quantify film growth [63]–[65], [67], [71]. Further quantification of AIE results and comparison to those obtained by spectroscopic ellipsometry would be of benefit in further refining and calibrating the optical output from the AIE.

Chapter 3

Experimental techniques supporting AIE development

3.1 Outline of chapter general aims

The aim of this chapter is to provide a description of how supplementary techniques such as contact angle measurement, AFM, and protein printing have been used to develop the concept and assembly of a bio-sensor protein array that can be measured by the AIE in a reliable and informative way.

For each technique, there is an introduction to their operation in broad terms and a summary of the research and technical literature that defines and justifies their place as a means to progress the overall aims of the study. It is shown how accurate and reliable protein arrays are a distinct advantage to imaging ellipsometry and the unique features of the AEI instrument.

Following the introduction, a description of the detail operation and methods used to quantify and cross check each supporting step is given, justifying the methods chosen. The results and analysis are documented, identifying the points of refinement and how developmental details have fed back into the final standard operating procedures.

3.2 Contact angle; a measure of surface free energy

3.2.1 Introduction and Young's equation

When investigating AAI using imaging ellipsometry, it is necessary to present the proteins of interest on a solid flat substrate. From the range of options available, primary consideration has been given to silicon as a substrate and thus as a platform for development. The choice of silicon as the supporting substrate is a logical one given that it is well characterized from an ellipsometry point of view, [173], [174], it is readily available in high purity with a highly polished surface and the literature describes a range of surface chemistry for the immobilization of proteins [67], [73]. However, one disadvantage to silicon is its low surface energy making it difficult to get a good wettability. Wetting is described by the balance of adhesive forces acting between the fluid droplet and the surface it sits upon, drawing the two together, and the cohesive forces of surface tension acting within the fluid, causing the droplet to form a sphere and resist contact with the surface [84].

By monitoring the surface free energy of the substrate at each stage of biosensor fabrication, observations can both confirm the successful change in surface chemistry and calculate the required volume of liquid to produce a spot covering the same surface area as wettability changes at each step of the process.

While the surface energy models described earlier (Section 1.5) can prove useful in evaluating different substrate surfaces as a supporting structure for a biosensor array, for the purposes of this work it is primarily the changes in surface free energy between each fabrication step, rather than absolute values, that determines the size of delivered volumes to produce maximum accuracy in bio-sensor spot size. Selecting a probe solution it is necessary to select one that has a higher surface free energy than that of the solid surface. In our case de-ionized water can cover the anticipated range of energy changes on the silicon substrate. When

using de-ionized water as a probe solution, surfaces are described as hydrophobic when the contact angle exceeds 90 degrees, indicating the likelihood of poor wetting and a surface with low free energy. By contrast, contact angles lower than 90 degrees are indicative of hydrophyilic surfaces which have good wetting and high surface energy [84].

The most common contact angle measurements are static, whereby a single measurement is taken of a static sessile drop just after it is deposited on the substrate surface. This type of measurement is widely used in the semiconductor industry to check initial surface cleanliness and monitor the production processes involving surface modifications. However, dynamic measurements involve tilting the sample or adding and removing liquid to establish the hysteresis in angle change. Hysteresis has been extensively studied and found to be related to surface roughness and/or material non homogeneity across the substrate surface [76], and can go some way to answering the influences of non ideal conditions in comparison to Youngs equation (Equation: 1.30), which assumes a great deal about the materials under study and idealizes the solid surface as perfectly flat, atomically smooth and chemically homogeneous.

The consideration of non ideal situations are significant when applied to the practical concerns of developing a reliable platform for the study of AAI. The principal of a bio-sensor array visualized by the AIE requires the proteins of interest to be bound securely to the solid substrate surface. The mechanism to do that is via modification of the substrate surface using molecules delivered in solution, each one of which will have their own interaction with the substrate based on surface free energy. The early literature describes protein adsorption onto a silicon substrate surface which has been made hydrophobic using silanization with dichlordimethylsilane [64]. Later work describes covalent bonding of protein and ligands to silicon surfaces through the use of 3-aminopropyltriethoxysilane (APTES) and glutaraldehyde. The alteration of surface chemistry is observed and confirmed in part by the change in contact angle of a probe solution (dH$_2$O) [73].

3.2.2   Methodology for using the AIE to study contact angles

The physical arrangement of components of the AIE is somewhat similar to that
of commercial drop shape analysis instruments (optical tensiometers) [175] in
that a collimated light source and imaging camera are mounted on goniometer
arms and can be positioned 180º to each other. Changing the light source on the
AIE from a laser to a filtered LED, as described earlier (Section 2.2.3), removed
the coherent source interference patterns observed in illumination and provided
significant improvement in the image acquisition quality for contact angle mea-
surements. The LED light output of the AIE is highly collimated and once the
camera is focused, provides high contrast and brightness, giving a sharp outline
to the sessile droplet under evaluation.

The methods used to capture contact angle information using the AIE were
developed specifically for this thesis using recommended practices for commer-
cial optical tensiometer instruments [176], [177].

3.2.2.1   Setup for image capture

The AIE was set with the camera at -90 degrees from the vertical and the light
source at 88 degrees. This slight off axis illumination provides back lighting of
the sessile drop without direct saturation of the camera CCD. The sample table
was set straight and level, adjustments for magnification and focus were made
based on droplet size. To avoid errors from sample droplet evaporation, droplets
of at least 100μL were deposited onto the test surface using a pipette held securely
above the sample surface and the images were captured within five seconds (Fig-
ure 3.1). Where possible droplets were placed on a new surface area for each of a
minimum five replicates. Images were captured by the AIE CCD camera at 640 by
480 pixel resolution in PNG format with no further processing prior to dropshape
analysis.
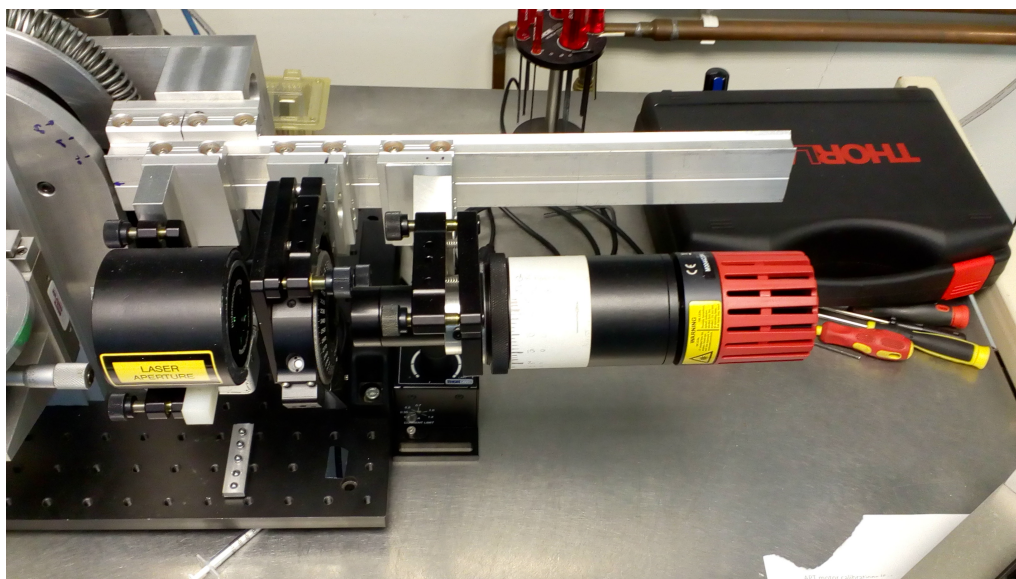
FIGURE 3.1: The AIE LED light source and camera set up; positioned at 88 and 90 degrees respectively in preparation to image the contact angle of sessile droplets.

3.2.2.2 Image processing

To measure the droplet contact angle a range of options were available, from simple geometric approximations such as the half angle method (Figure 3.2 A), to the mathematically rigorous Low-Bond Axisymmetric Drop Shape Analysis (LB-ADSA) available as a plugin analysis tool in ImageJ (Figure 3.2 B), which corrects for the polar and dispersive nature of the probe liquid.
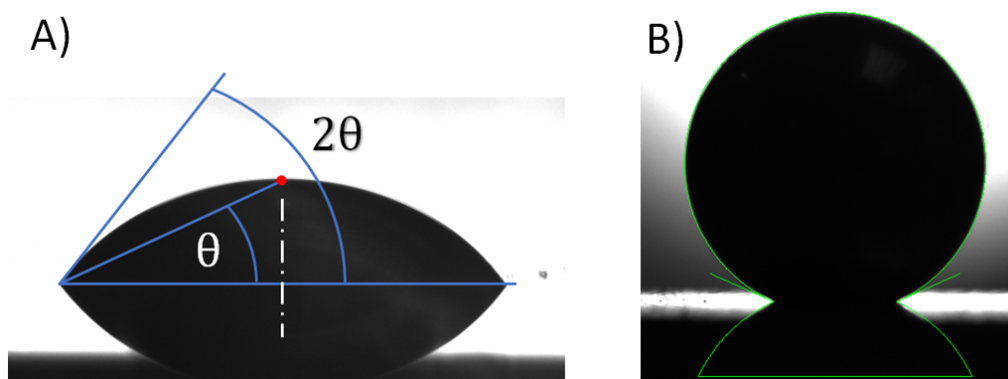
FIGURE 3.2: Representative images of contact angle image analysis; A) The half angle method; the angle from the highest mid point of the droplet is measured, then doubled. B) Representative image of LB-ADSA in process, parameters are adjusted to fit the green curve to the outline of the shape.

To reliably and consistently evaluate the accuracy of contact angle measurement for each image processing method, a calibration standard was required. To this end, 5mm diameter precision steel ball bearings were placed onto precision machined holes of 2, 3 and 4mm diameter, producing accurate, calculable contact angle values from the geometry of the arrangement such that when X < R:

$$\theta = \left(\frac{\pi}{2}\right) + \cos^{-1}\left(\frac{X/2}{R}\right) \tag{3.1}$$

Where, θ is the theoretical contact angle, R is the radius of the steel ball and X is the diameter of the hole.

To evaluate contact angles < 90 degrees a 5mm diameter ball bearing was pressed into a 5mm diameter hole leaving a known height protruding, the theoretical contact angle can be calculated, when Z < R, using the equation:

$$\theta = \left(\frac{\pi}{2}\right) - \sin^{-1}\left(\frac{R-Z}{R}\right) \tag{3.2}$$

Details of the five scenarios are presented graphically and physically (Figure 3.3).
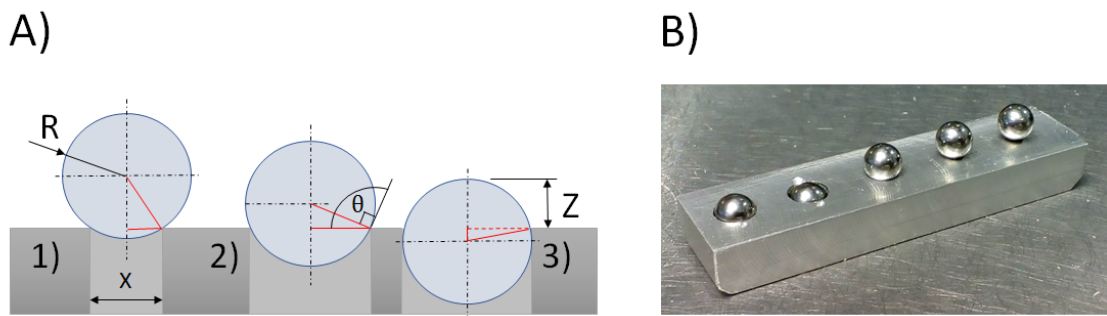
FIGURE 3.3: Detailing the contact angle calibration standard; A) Schematic representation of the method using precision ground steel balls to produce contact profiles of known angles. 1) X = 3mm, R = 2.5mm, hence θ = 143 degrees. 2) X = 4mm, R = 2.5mm, hence θ = 127 degrees, 3) Z = 2mm, R = 2.5mm, hence θ = 72.5 degrees. B) The physical components ready for imaging.

Images were captured using the AIE, setup as described in the previous section. The captured images (Figure 3.4) were all imported into ImageJ for analysis

where a choice of plugins were reviewed and assessed in a manner as described by Williams *et al*. [77]. Briefly, five separate images for each configurations was taken, each image was measured using three methods (Dropsnake, LB-ADSA, and half angle). Each analysis was performed using the guidance notes for each plugin [178]. The mean and standard deviation for each method was calculated and compared to the theoretical geometrically derived value.
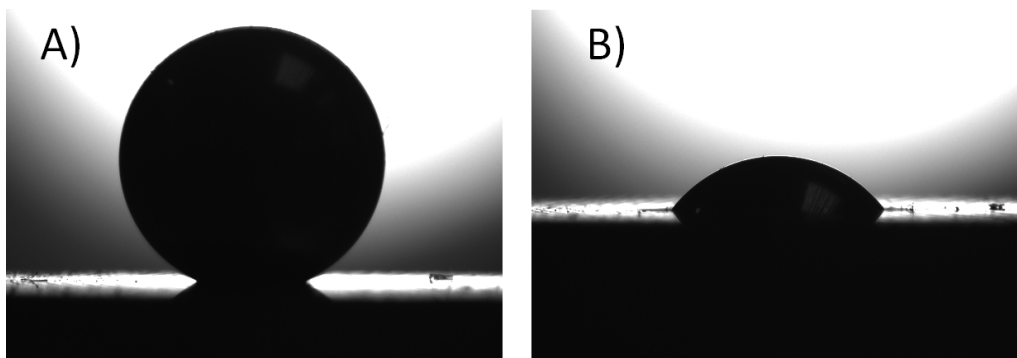
FIGURE 3.4: Representative captured images of steel calibration balls; demonstrating the two extremes of contact angle evaluation. A) Steel Ball R = 2.5mm sitting in a hole X = 2.0mm. B) Steel Ball R = 2.5mm protruding Z = 2.0mm. Images captured using the AIE.

Of the three methods, LB-ADSA was considered to be simple in operation, and where droplets are symmetric (as in this study), found to be closer to the theoretical target value, with a standard deviation from the mean that is almost an order of magnitude lower than that of the dropsnake method (Table 3.1). By comparison the standard deviation variations presented here for LB-ADSA and half angle measurements are in good agreement with similar analysis in literature [77], [78], [179]. Commercial instruments typically advertise an angular resolution of $\pm 0.1^{\circ}$ [176], [177].

TABLE 3.1: Showing the theoretical contact angle (TCA) and measured mean contact angle; for a 5mm diameter precision ground steel ball using three popular plugin methods for ImageJ analysis. Values are in angular degrees.

Mean Contact angle R = 2.500mm Ground Steel Ball (Std Dev) [n=5]			
x mm	**TCA**	**Dropsnake**	**LB-ADSA**	**Half angle**
2.00	156.42	152.7 (2.38)	155.7 (0.36)	156.2 (0.43)
3.00	143.13	141.6 (2.93)	142.2 (0.34)	143.1 (0.81)
4.00	126.87	127.0 (3.51)	124.3 (0.45)	123.8 (0.67)
Z = 2.00	78.46	72.9 (3.20)	77.8 (0.37)	78.5 (0.50)
Z = 1.00	53.13	53.3 (4.97)	53.5 (0.38)	53.1 (0.65)

3.2.3 Contact angle results

3.2.3.1 Silicon substrate preparation

The silicon that forms the substrate for the bio-sensor array was obtained from Dr. Dave Langstaff. They are highly polished 10mm by 10mm diced segments or chips, cut from a 100mm diameter crystalline silicon (c-Si) bulk p-type, 0.525mm thick wafer, in the <111> crystal plane.

The substrates were cleaned using the RCA-1 process [180], briefly the silicon chips were soaked in an oxidative solution of hydrogen peroxide H_2O_2 (30%), ammonium hydroxide NH_4OH (27%) and double distilled (dd) H_2O at a ratio of 1, 1, & 5 respectively, at a temperature of 75°C for 15 min. A standard operating procedure (SOP) for the RCA-1 process is included in the appendix.

The cleaned silicon chips were then prepared in the method of Wang and Jin [73], to covalently attach target proteins in readiness for immersion with analytical solutions. The protein attachment process involved an initial silanization of the silicon substrate surface, whereby, the RCA-1 cleaned silicon chips are immersed in a fresh solution of 5% v/v APTES, 5% v/v dH_2O and 90% v/v ethanol , for two hours at 18°C. Chips were then washed three times with flowing dH_2O followed by washing with 100% ethanol three times. Once washed, chips were dried under a gentle stream of nitrogen and then immediately reacted with a 2.5%

v/v solution of glutaraldehyde in phosphate buffer solution (PBS) buffer for two hours at 18°C. The surface was washed by placing the chip face down onto a 200μl droplet of dH$_2$O for 2min, repeated three times.

Capture antibodies were applied in solution to the prepared silicon chip surface by pipette. Either polyclonal anti-FhGST-S1 [6] diluted at 1:50 v/v with PBS or anti-α & β tubulin (Sigma) diluted at 1:50 v/v with PBS were deposited as 5mm diameter spots, covered and incubated at 18°C for 30 min, following which they were rinsed with PBS then dried under a gentle stream of nitrogen.

The assembled bio-sensor chips were exposed to droplets of analytical solutions containing FhGST-S1 [118] at 0.1mg/ml or EVs isolated from cultured *F. hepatica* excretory secretory products (Section 3.3) at 0.8mg/ml for 30 min at 18°C, rinsed with PBS then dried under a gentle stream of nitrogen.

At the end of each stage of fabrication, individual wafers were removed from the process ready for contact angle measurement (Table 3.2).

TABLE 3.2: Presenting the measured contact angle, using LB-ADSA: for PBS on modified silicon substrates.

Mean Contact angle of PBS (Std Dev) [n=10]	
Surface	**LB-ADSA**
RCA1 Clean	42.2 (1.1)
APTES	63.0 (0.8)
Gluteraldehyde	51.4 (1.7)
AntiGST-S1	78.5 (2.9)

3.2.4 Contact angle discussion

Studying AAI using imaging ellipsometry requires the proteins to be supported on a solid substrate. The surface free energy of the substrate has considerable influence on the way in which any solutions deposited on the substrate surface interact. By measurement of the contact angle a probe liquid makes between itself and the solid surface, an indication of the surface free energy is revealed.

Contact angle can be used to easily and reliably confirm changes in the solid substrates bulk surface chemistry brought about at each of the steps required to fabricate a bio-sensor; validating the success of each process. Furthermore, quantifying the contact angle at each stage informs the adjustment of the fluid volumes deposited to ensure each droplet rests on the surface with an equal area, producing a reliable and consistent bio-sensor array of over-layered elements. Combining the capability of contact angle measurement alongside the ellipsometric values for each stage of sample preparation, in one instrument, has some merit.

The use of a reliable fixed calibration standard to evaluate profile images captured by the AIE was done using a known size precision ground steel ball sitting on or in precision sized holes. This method produced a series of controllable, calculable contact angles which are unchanging in time. It was seen that images captured by the AIE and evaluated using the ImageJ LB-ADSA plugin, produced high quality, accurate contact angle values, measurable quickly and reliably.

The accurate measurement of contact angle will be useful in both quality control of solutions used in micro-array fabrication and analysis of alternative substrate suitability, and significantly can be done in conjunction with ellipsometry *in situ* using a single instrument. Ellipsometry unlike other techniques, such as SPR and TEM, can utilize a wide variety of substrate surfaces which is an area that warrants further investigation.

3.3   Isolation of protein and EVs

3.3.1   Introduction to EV isolation

The separation and concentration of EVs has no gold standard, this is due to the wide diversity of source material producing EVs as outlined in Chapter 1. Currently, differential ultra-centrifugation (DC) is the most widely used method of separating EVs from their source or culture medium [136], with size exclusion

chromatography (SEC) gaining ground as a simple, reliable and low cost route to EV isolation and enrichment [116].

The fundamentals of the ultra-centrifuge and separation of high molecular compounds was established in 1937 by Svedberg [181]. Modern application of this method takes the EV containing solution through a series of sequential centrifugation steps which progressively increase the centrifugal forces and time. Initially at low relative centrifugal forces (RCF), starting at 300 and rising to 10,000 times gravity (g), large particulates and debris sediment leaving the much smaller EVs as a colloid in solution. During these early stages the supernatant is retained and the pellet that forms, discarded. Later steps use centrifugation forces as high as 120,000 g to remove the EVs from suspension and pellet them for collection in an enriched state. These later stages are often repeated, the aim of which is to remove smaller particles of free protein from the pellet (containing EVs), by leaving the protein in suspension within the discarded supernatant [27].

Size exclusion chromatography by contrast, can separate EVs on the basis of their size as they pass through a filter medium packed into a column [182]. SEC media varies depending on application but typically consists of small spherical bead like particles that have a controlled distribution of pore sizes within them. Small molecules enter the pores and are retarded by having to follow a longer path to exit, while larger particles cannot enter the pores and follow a shorter path between the beads emerging from the bottom of the column sooner. The basic principal is that molecules of differing size pass through the column at different rates. So long as all the various molecules are loaded simultaneously then molecules of a similar size will elute together at the same time [183].

Recently Davis *et al* have evaluated DC and SEC methods for the isolation of EVs from the veterinary significant helminth *F. hepatica*. During which it became clear that some additional refinement of DC protocols could be beneficial to providing an improvement in EV isolation and purity. This could prove a more refined alternative to SEC to provide EVs for a biosensor based on the AIE.

3.3.2 EV isolation methods

The initial protocols for isolation and imaging of EVs using DC within veterinary parasitology group at AU were taken from a publication by a former AU colleague, Fanny Nowacki [184]. This and alternatives used by Théry *et al* [27] and Cwiklinski *et al* [7] to isolate EVs from culture fluids are detailed (Table 3.3).

TABLE 3.3: Comparison of differential centrifugation protocols for EV purification and analysis.

Step Description	Nowacki	Théry	Cwiklinski
Remove debris	500 g 2 min	300 g 10 min	300 g 10 min
Remove cells	700 g 20 min	2,000 g 10 min	700 g 30 min
Remove debris	-	10,000 g 30 min	1,500 g 45 min
Membrane filter	-	-	0.2 μm Ultrafilter
Pellet EVs	120,000 g 80 min	100,000 g 70 min	120,000 g 60 min
Remove protein	120,000 g 70 min	100,000 g 70 min	-

It can be seen that there are significant differences in the protocols. To investigate the significance of variation in run times and centrifuge steps a search of the literature revealed a paper by Livshits *et al* [185]. This paper proposes a mathematical model for the sedimentation of EVs undergoing centrifugation. The model balances archimedes buoyancy against gravitational sedimentation and Stokes viscous flow. Livshits *et al.* confirmed the accuracy of their model both experimentally and mathematically. To quantify and optimize the effects of DC protocol variations, the Livshits *et al.* model was taken and converted to a Microsoft Excel calculator. The Excel spreadsheet takes the fixed and variable parameters of each centrifuge step: rotor angle, minimum and maximum radius, spin speed, time of duration and sedimentation distance as a function of volume of fluid. Combined with the vesicle density, media viscosity and density, for each step of the process, it is possible to use the sedimentation model of Livshits *et al* to calculate the percentage of particles that will sediment into a pellet or remain as a colloid within the supernatant. By combining each of the steps within the

protocol sequentially the Excel spreadsheet, spin calculator, plots a figure that reflects the percentage of particles recovered, by size, in the final stage. A copy of the SOP for the DC isolation of *F. hepatica* EVs optimized using the Livshits model is enclosed in the appendix.

3.3.3 EV isolation results

TEM images of EVs isolated using the Nowaki protocol are presented (Figure 3.5). Looking critically for optimization and refinement, it can be seen that there is a significant amount of residual contaminating material which obscures clear, detailed observation of any EVs present.
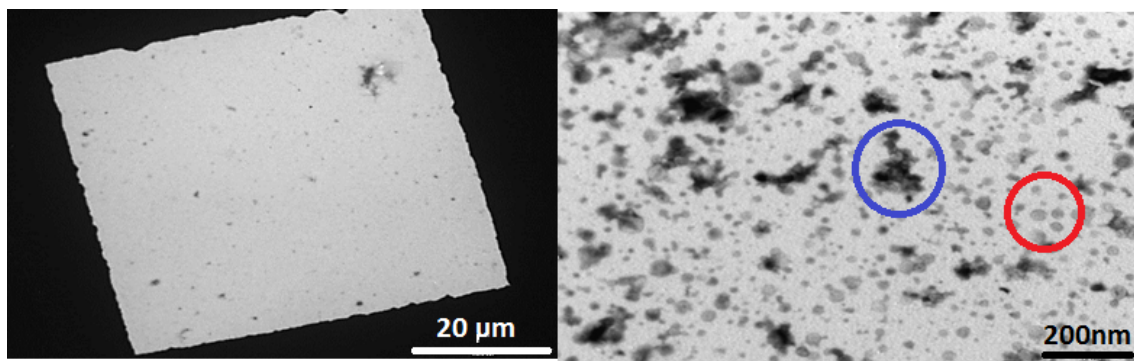
FIGURE 3.5: Representative TEM micrographs demonstrating EVs isolated using the Nowacki *et al.* protocol: Left, an image of the whole grid area. Right, close up image highlighting EVs in red and obscuring material in blue.

A graphical output from the spin calculator gives a quick and clear visualization of how changes made to the centrifuge protocol will impact on the size distribution of the particles collected in the final pellet. It can be seen (Figure 3.6), that using the Nowacki protocol predicts cellular debris up to 1000nm in diameter are likely to remain in the final pellet.

To evaluate the Théry protocol, a sample of *F. hepatica* culture fluid containing EVs was processed using the centrifuge protocol recommended by Théry *et al*[27]. TEM images were captured (Figure 3.7), where a clear reduction in background contamination can be seen.
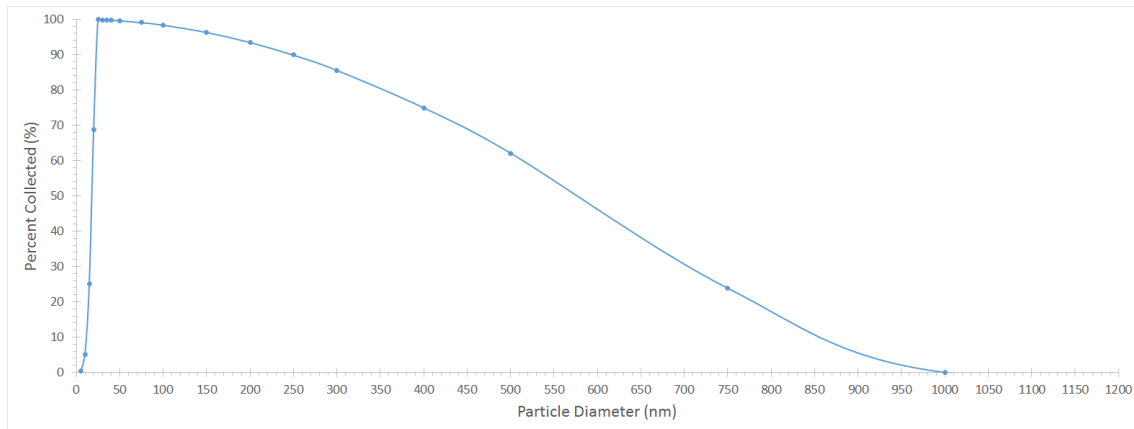
FIGURE 3.6: The percentage of EVs, by diameter, isolated from culture solution; as predicted by the Livshits *et al.* model when using the Nowacki DC protocol.
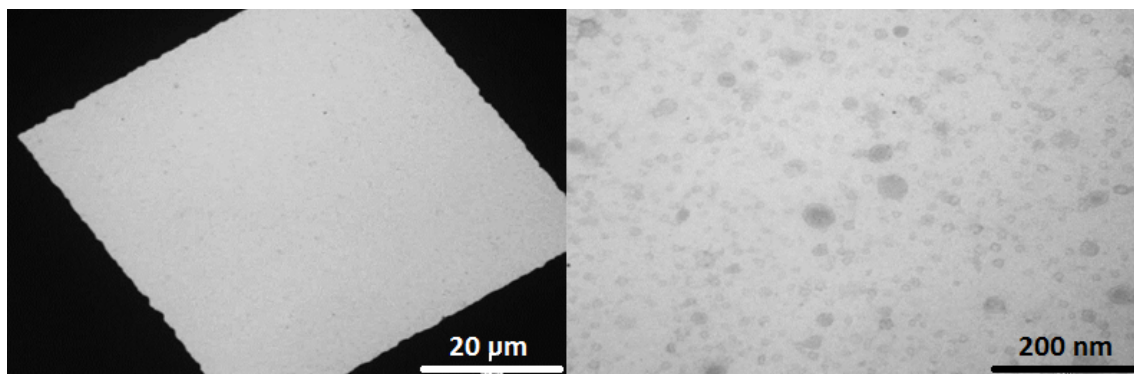
FIGURE 3.7: Representative TEM micrographs demonstrating EVs isolated using the Théry *et al.* protocol; Left, an image of the whole grid area. Right, a close up image identifying a large number of 30-50nm diameter EVs.

However, using this protocol as is, the Livshits model suggests EVs are isolated predominately in the range 30 to 120nm diameter, with an upper limit of 170nm on the maximum vesicle size (Figure 3.8).

3.3.4 EV isolation discussion

Using the AU veterinary parasitology groups initial Nowacki protocol it can be seen from the TEM micrographs (Figure 3.5) that the volume of residual contaminating material could have detrimental affects on downstream analysis. Particularly in trying to visualize gold imuno-labeling methods to identify surface
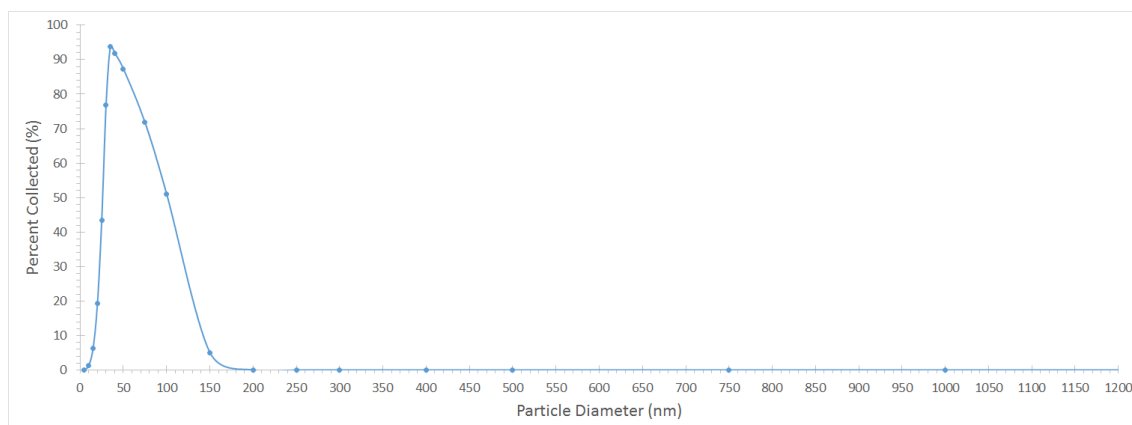
FIGURE 3.8: Graph representing the predicted EV size distribution
using the Théry DC protocol.

exposed proteins. The literature offers a number of alternative protocols, gener-
alized DC EV isolation methods like that of Théry or parasitic helminth tailored
protocols like that of Cwiklinski. While the reduction in contaminating and ob-
scuring material can be seen visually (Figure 3.7), the implications of making
adjustments to centrifugal force and time of duration for each of the individual
steps is difficult to quantify quickly and easily, without reference to some form of
predictive model.

By developing the model of sedimentation proposed by Livshits *et al.* into
an interactive Excel spin calculator, a quick and clear graphical output visualizes
directly, how even small changes made to the centrifuge protocol will impact the
size distribution of the particles collected in the final pellet.

Using the spin calculator, it predicts that the Nowacki protocol could produce
a final pellet which contains cellular debris up to 1000nm in diameter, something
which goes to explain the contaminating material seen in TEM micrographs. By
contrast similar analysis of the Théry protocol indicates that it will result in recov-
ering EVs in the range 30 to 170nm diameter, which has the potential to exclude
a significant portion of the whole EV population.

The use of the spin calculator now provides an opportunity to both target the
size range of EVs collected and to minimize centrifugation times to optimize the
process of isolating EVs for use with the AIE.

3.4 Atomic force microscopy

3.4.1 Introduction to AFM

In the process of developing a bio-sensor for the study of AAI it is necessary to chemically modify the surface of the supporting substrate (Section 3.2.3.1) in a sequence of steps to covalently attach proteins including antibodies to the substrate surface as preparation for exposure to likely interacting proteins. To monitor these changes, in addition to the bulk property study of surface free energy via contact angles (Section 3.2.2), AFM can quantify the substrate surface structure and it's attached components at a nano-meter scale [186], providing information that can inform the development and assembly of a bio-sensor protein array which can be measured by the AIE in a reliable and informative manner.

AFM is a subset of scanning probe microscopy (SPM) in which an almost atomically sharp probe tip, raster scans over a sample following the surface and mapping it out as a three dimensional profile.

3.4.1.1 The history of AFM

The origins of SPM can be traced back to stylus profilometers which have been in use, measuring macro surface roughness since their first commercial introduction in 1942 [187]. These early instruments suffered from probe bending caused by difficulty in coping with any large features present on the surface. This disadvantage was overcome to some extent by Becker in the 1950's by inducing the probe to oscillate above the surface and allowing the vibrating tip to make gentle contact with the surface [188]. In 1972 Young incorporated piezoelectric elements to position a non contact stylus probe and used electronic feedback to control the vertical Z height position over the surface. Thus maintaining a fixed distance above the surface by measurement of electron field emission and from the gathered data, producing a three dimensional map of the surface [189]. It was Binnig and Rohrer who in 1981 combined these features, and by improving the vibration

isolation of the instrument, they were able to monitor electron tunneling rather than the larger scale field emission of Young's instrument [190]. Binnig, Rohrer and co-workers had produced the first scanning tunneling microscope (STM). Success lay in the fact that electron tunneling is so closely related to distance that effectively only the last atom of the probe tip can tunnel. With feedback systems sensitive enough to precisely control the probe position and allow consistent tunneling, Binnig and Rohrer were able to directly image individual silicon atoms on a surface. The relative simplicity and incredible sensitivity of the invention led to their sharing of the 1986 Nobel prize for physics [191].

3.4.1.2   AFM theory of operation

Modern AFM instruments today have three basic elements, a piezoelectric control stage which moves the sample under the probe tip, a force transducer that provides the position of the tip in relation to the surface and finally a feedback control system that interprets the signal from the force transducer to maintain a constant force between the tip and the sample surface using the piezo control stage [192, pg:14]. In practice the probe tip is mounted onto or formed as part of a cantilever. A laser is reflected from the back of the cantilever onto a position sensitive photo detector (PSPD). The distance from the cantilever to the PSPD is designed to be large, forming an optical lever and as such a small movement of the probe tip produces a large deflection of the laser across the PSPD (Figure 3.9).

3.4.1.3   AFM topographic modes:

In contact mode, once the probe tip is brought into constant contact with the surface of the sample, the position of the laser spot on the PSPD provides feedback for movement of the piezos in X, Y and Z to maintain a constant cantilever deflection and hence contact force. This movement data is combined to produce a topographic map of the sample surface. In non-contact mode the cantilever is oscillated at resonant frequency and as the tip approaches the sample surface,
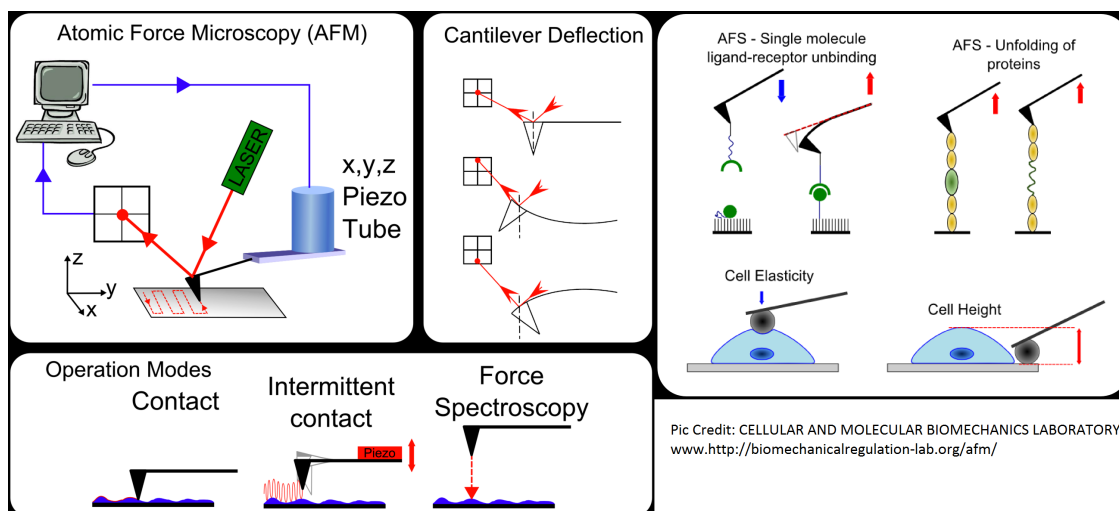
FIGURE 3.9: Schematic highlighting the wide range of operating modes and methods of operation of AFM. Reproduced from [193]

interaction with the electron field force induces a reduction in tip resonance and amplitude before contact with the surface occurs. The force transducer and feedback system adjusts the vertical Z height position of the cantilever to maintain a constant reduction in tip oscillation and hence a constant distance from the surface. The input signal to oscillate the cantilever can be compared with the output signal at the PSPD to give additional information about the structure of the surface under study, with a phase shift being observable between materials of different density and damping even when topographically flat. Between these two regimes is intermittent contact or tapping mode. Here, larger oscillation amplitudes are induced in the probe tip compared to non-contact made. As the tip comes into contact with the surface the feedback circuit adjusts the Z height position until a user set amplitude reduction is reached during each cycle of oscillation. The higher the amplitude reduction the firmer the tap and conversely the lower the amplitude reduction the softer the contact with the sample. The advantage of tapping mode is the removal of lateral forces present in contact mode and which can have detrimental effects on soft materials such as biological samples, or physically move less well adsorbed particles on the substrate surface [192, pg: 49-65], [130].

3.4.1.4 Non-topographic modes:

From the beginning, SPM has been used to gather more than just topographic information. Force spectroscopy involves the stage held static in X and Y, while the probe is moved in the Z direction towards the sample, deflection of the cantilever is measured as it approaches, contacts and then retracts. The gathered data produces force distance curves of the interaction, which display three key features: as the probe comes into close proximity to the surface, vann-der-Waal's forces attract the probe deflecting it downward, on contact with the surface the continued downward movement of the Z stage deflects the probe by the repulsive force of the sample, on retraction tip-sample adhesion produces an attractive deflection until separation returns the probe to its neutral position [192, pg: 64-66] [194]. An idealized force distance plot is presented (Figure 3.10).
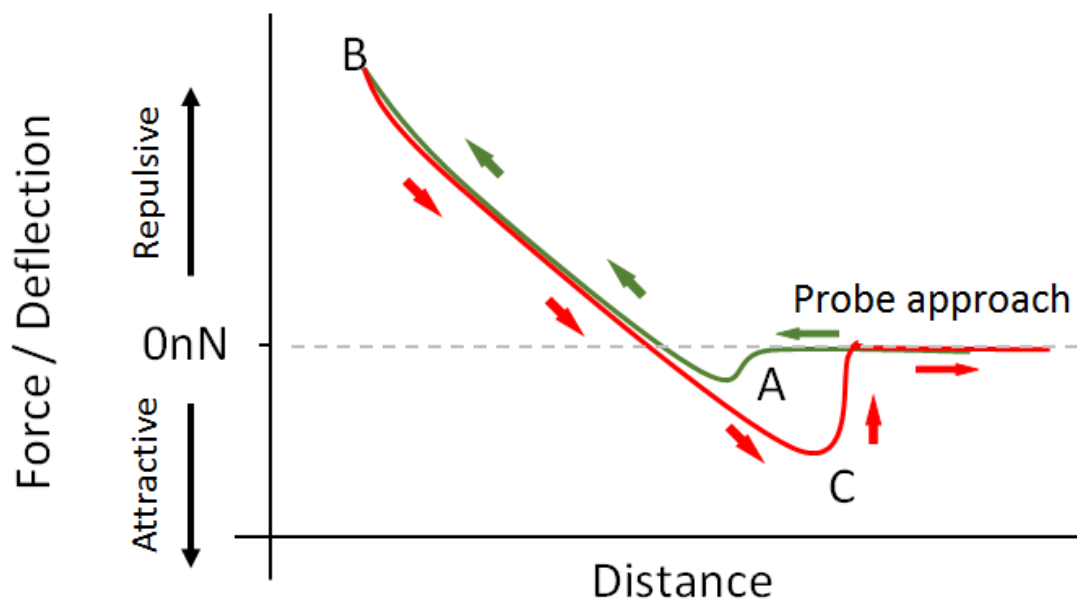
FIGURE 3.10: Schematic of a model force distance plot; as the probe approaches, point A, it is attracted towards the surface by vann-der-Waals forces. Once in contact, as the probe is moved further towards the surface, deflection is a function of both cantilever and surface rigidity, and reflected in the slope of the plot. At a user defined deflection, point B, the probe approach is reversed and at point C the retraction force overcomes probe-sample adhesion.

3.4.1.5 AFM of EVs

As outlined in Chapter 1 EVs have tremendous potential as disease bio-markers and targets for potential therapeutics [123], [132]. AFM offers two ways to improve bio-sensor and AIE development, through the ability to study the morphology of these nano (30-500nm) sized particles, and monitoring the substrate changes brought about by alteration of surface chemistry and component addition of the bio-sensor assembly.

AFM can provide insight into the distribution and surface arrangement of proteins. It makes an excellent accompaniment to ellipsometry which is able to evaluate the subsurface structure. As demonstrated by Finot *et al.* in their study of pulmonary surfactants, combining AFM and ellipsometry to provide better characterization of both morphology and thickness structure of surfactant films [195]. During the course of this study Gajos *et al* [125] have published work showing the successful immobilization and detection of platelet-derived EVs on silicon substrates using AFM and spectroscopic ellipsometry. In their recent review of AFM as a nanoanalytical tool for exosomes and EVs Sharma *et al* [130] highlights the unique ablity of AFM to quantify individual exosomes, and other EVs, yet simultaneously probing key EV parameters such as abundance, structure, biomechanics and biomolecular content. ISEV have recently published a revised minimal information for studies of extracellular vesicles 2018 (MISEV2018) [136] which gives guidance and outlines protocols to successfully document specific EV-associated functional activities. Thus, ISEV now recommends using TEM and/or AFM to check the quality of a prepared EV sample prior to any downstream functional analysis.

The object for this study was to establish the surface roughness of the silicon wafers that are to provide the platform for bio-sensor and AIE development. Then subsequently using AFM to monitor surface morphology through

each stage of the bio-sensor construction process, validating the integrity of using proteins or EVs as detection agents. Providing the opportunity to confirm ellipsometry results via direct surface measurement.

3.4.2 Methodology for using AFM

3.4.2.1 Silicon substrate preparation

The silicon chips that forms the substrate were cleaned using the RCA-1 process [180], and then prepared in the method of Wang and Jin [73], to covalently attach target proteins in readiness for immersion with analytical solutions as described earlier (Section 3.2.3.1). At each stage, chips were completely covered in process solution for the ascribed time, then washed using dH_2O and dried under a gentle stream of nitrogen in readiness for surface measurement using AFM.

3.4.2.2 AFM observations of EVs

To identify proteins exposed on the surface of *F. hepatica* EVs via MS, Dr. Rebekah Stuart provided EVs sourced from specific Aber, Italian and Miskin isolated strains of *F. hepatica*. Each strain of EVs were subdivided and left whole or using the method of Cwiklinski *et al.* trypsin shaved of their externally exposed protein peptides [7]. Observations to confirm the integrity of EVs post shave were done via TEM (described in detail in Chapter 4) and AFM. The use of AFM presented the opportunity for better understanding the mechanical and structural differences of EVs pre and post trypsin shaving using AFM force / distance spectroscopy.

Whole and shaved EV samples were diluted to 0.1mg/ml with ddH_2O and adsorbed onto freshly cleaved mica sheets (Agar Scientific AGG250-1) for two minutes and gently dried under a nitrogen stream. Samples were then scanned with a Park Systems XE100 AFM, using silicon probes (NT-MTD:NSG-01 & NSG-03PT) in both contact & non-contact mode. Topographic height and phase images

were scanned at 512 x 512 pixels at a rate of 1.5 Hz. Images were analysed using Gwyddion (version: 2.52). Force distance curves were analyzed using Park Systems XEI software (version: 1.8).

3.4.2.3 AFM evaluation of EV size distribution

In an attempt to measure the size distribution of isolated EVs the following method was applied. EV samples were adsorbed onto freshly cleaved mica sheets and scanned as described above. Gwyddion images were imported into ImageJ, grey-scaled and then progressively a threshold was applied to identify the peaks of individual EVs. Using the ImageJ particle analysis feature, the height and quantity data were passed to an Excel spreadsheet that models the AFM tip in a manor similar to that described by Sebaihi *et al.* [196]. Using this model, the influence of the AFM tip on the measured shape of the EVs can be de-convolved and a better estimate of the EVs spherical diameter can be obtained (Figure 3.11). The EV quantity and revised diameters can then be grouped and plotted as a distribution.
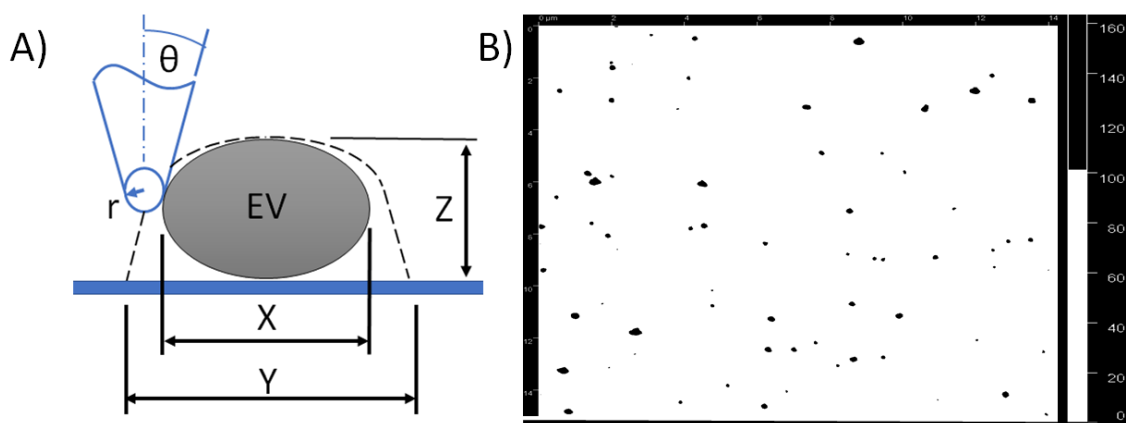
FIGURE 3.11: Schematic showing the principal of AFM tip model; A) AFM tip model, Y = apparent EV width, X = Corrected EV width. B) Example ImageJ thresholded image at Z = 100nm, with EVs over the threshold height identified as black spots for further particle analysis.

3.4.3 AFM results

Analysis of AFM micro-graphs show the surface of cleaned silicon chips were polished to a surface roughness average (RA) of 119 pico meters, or approximately 0.12 nm. Surface roughness values following the addition of other components as the the bio-sensor was fabricated are listed (Table 3.4) and presented visually (Figure 3.12).

TABLE 3.4: The substrate surface roughness for key stages of bio-sensor assembly and analysis.

Surface Roughness RA in pm [Std Dev] (n=5)			
RCA1 clean	**APTES**	**AntiFhGST-S1**	**FhGST-S1**
119 [9]	183 [15]	443 [45]	1637 [183]
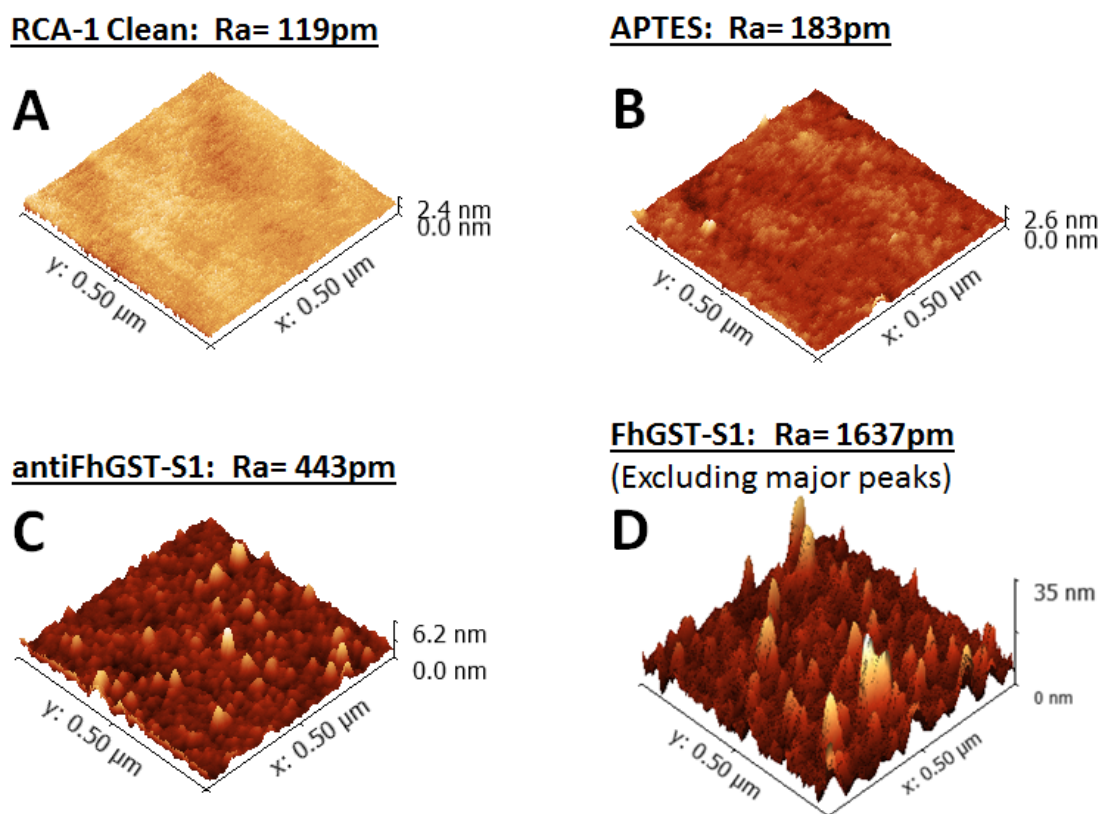
FIGURE 3.12: The surface topography of the silicon substrate at each step of bio-chip fabrication and evaluation; A) A cleaned substrate surface. B) Application of APTES as a linker. C) Covalent attachment of antiFhGST-S1 antibodies. D) Following exposure to an analyte containing FhGST-S1 protein.
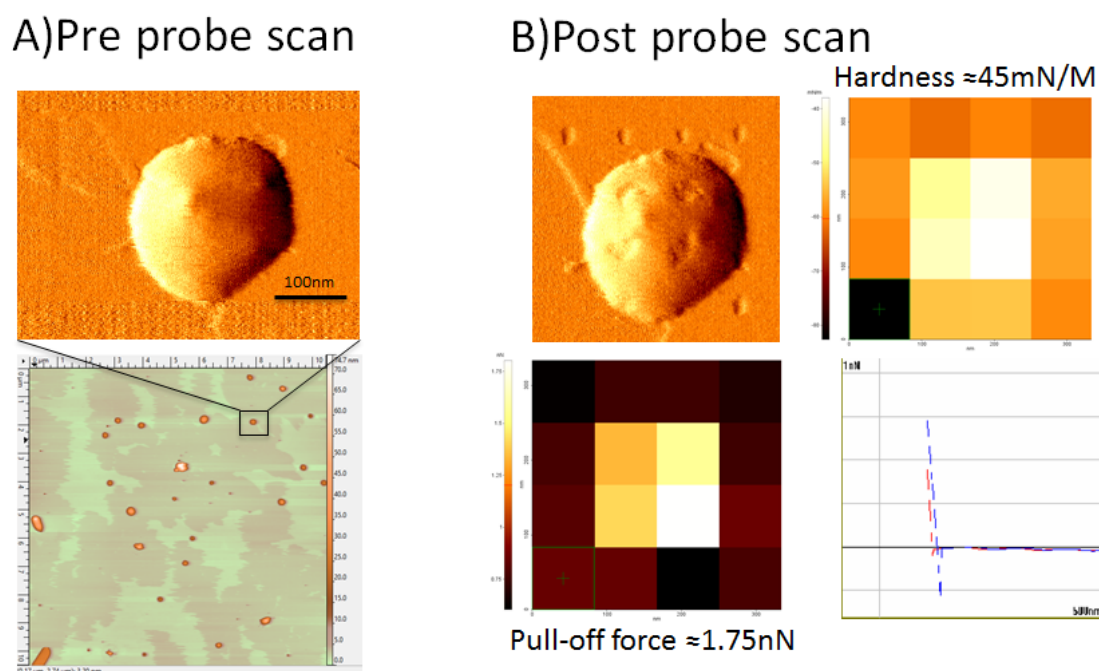
FIGURE 3.13: The surface topography of a single shaved Italian strain EV; A) Prior to force spectroscopy. B) Post force spectroscopy with hardness and peak pull off force grid maps along with a representative force-distance graph.

AFM micro-graphs reveal that the EVs which had been shaved of their exposed surface proteins, have a similar topography to the standard, natural EVs. However, force distance spectroscopy indicates that the peak pull off force experienced by the AFM tip for shaved EVs was ≈ 1.75nN which is around five times less that that for whole un-shaved EVs which had a pull off force of ≈ 8.00nN (Figure 3.13).

AFM was used as a supporting technique to provide information on the importance of EV purification for downstream analysis, comparing DC and SEC as mechanisms for the isolation of *F. hepatica* EVs. Assessment of EV morphology, post DC and SEC isolation was done using both AFM and TEM. Both techniques identified that EV structures were typically diverse in size and morphology [116]. Representative examples of non-contact mode micro-graphs, imaging EVs isolated by both DC and SEC are presented (Figure 3.14). The central graphs show individual EV topography from each isolation method. Such profiles identified
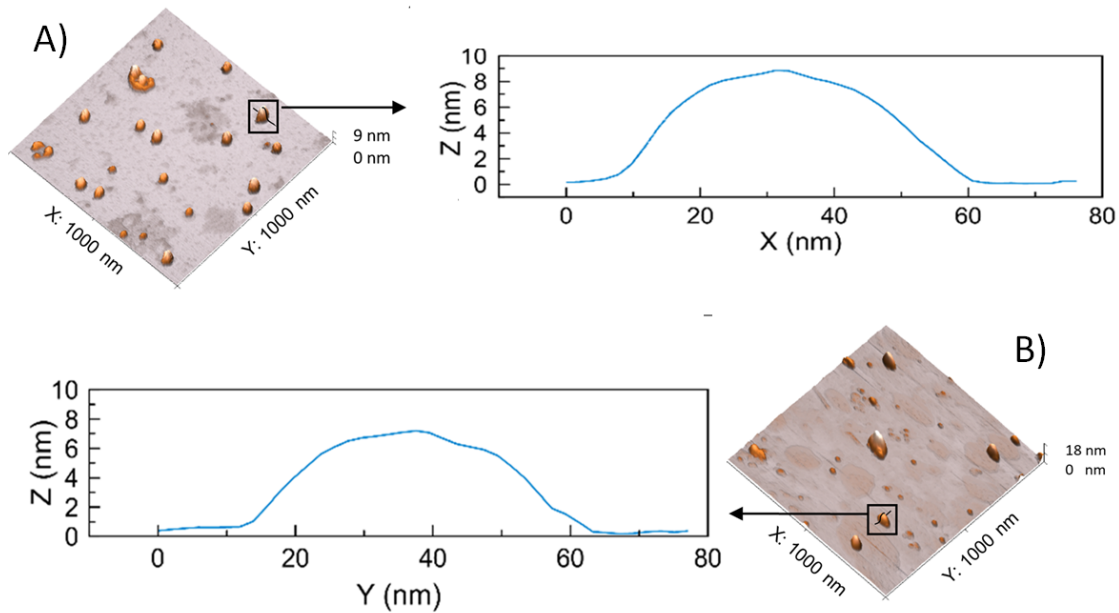
FIGURE 3.14: Representative AFM non-contact mode micro-graphs, demonstrating the topography of individual EVs: isolated by A) differential centrifugation and B) size exclusion chromatography purification methods.

that EV topographies were similar using both isolation methods, although SEC purified EVs were significantly smaller when analyzed using TEM at 76($\pm$44)nm, compared to DC isolated EVs 95($\pm$58)nm. Furthermore, DC purified EVs identified a vesicle sizes range of 505nm, compared to a SEC range of 285nm.

3.4.3.1 AFM evaluation of EV size distribution

The size distribution of *F. hepatica* EV samples isolated using SEC were analyzed by Izion Qnano tunable resistive pulse sensing (TRPS) by Davis *et al.* [116]. TRPS uses a nanopore membrane through which the EV containing solution is passed, changes in the impedance across the membrane as particles pass through are measured as a resistive pulse or blockade signal. The magnitude of the blockade is proportional to the particle volume and blockade frequency can be used to determine frequency. A full description of the fundamental principal is provided by Bayley *et al.*[197] and the means of quantitative sizing for TRPS is given by Vogel *et al.*[198]. Evaluation of particle size by Qnano is presented (Figure 3.15A),

along with analysis of AFM data for the same sample (Figure 3.15B).
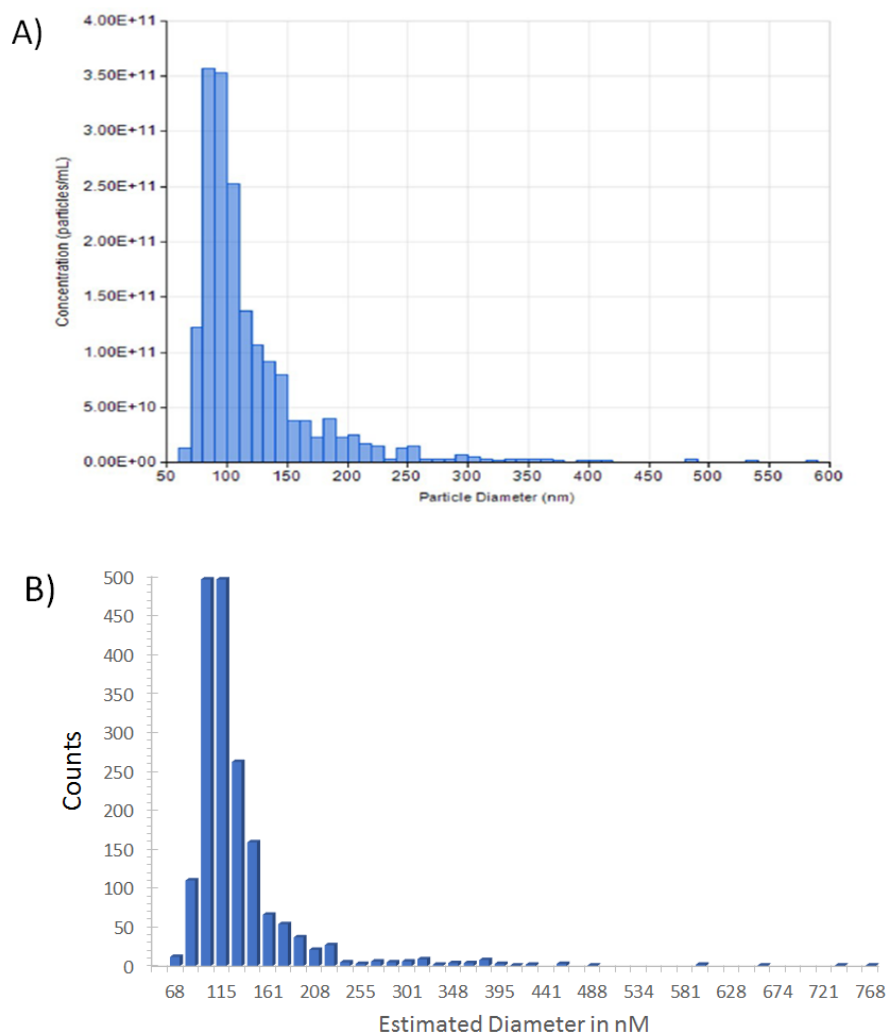
FIGURE 3.15: Comparison of EV size distribution; A) Size distribution of SEC isolated EVs analyzed by Izion Qnano TRPS, B) Size distribution of the same sample by image analysis of AFM topography data.

3.4.4 AFM discussion

AFM is ideally suited to monitor and quantify the substrate surface structure in three dimensions, supporting the process development necessary to construct a bio-sensor protein array which can be analyzed by the AIE in a reliable and informative way.

AFM analysis of the surface topography of silicon chips shows the progressive increase in surface roughness at each stage of the bio-sensor fabrication. The RA values are indicative of the average surface roughness and can be used to track the general surface morphology. The peak values, which change at each stage, correspond well with the structural size of the elements that are added to the substrate in solution. This provides some further evidence of the progressive assembly of the bio-sensor in line with the anticipated chemistry and biological function. For example, AFM of the silicon surface after the covalent attachment of antiFhGST-S1 shows a peak size of around 5nm, which following the addition of an analyte solution containing FhGST-S1, gives rise to peaks 20-25nm, in reasonable agreement with the x-ray resolved size of FhGST-S1 protein [118] and indicating antigen-antibody interaction.

AFM confirmed the integrity of EVs following their trypsin shaving of surface exposed peptides and identified a substantial difference between shaved and whole EVs with regard to the attractive forces between that AFM tip and EV surface.

In analyzing EVs isolated by both DC and SEC using AFM, it was seen that DC preparations did not suffer from excessive aggregation as has been seen by others [199]. Added to which, the improved isolation methods outlined in Section 3.3 suggests that DC isolation of EVs would be an acceptable method by which to prepare EV analyte solutions for use with the AIE.

AFM as a means of particle size and distribution determination would appear possible and would appear to offer a reasonable correlation to other methods such as TRPS, however the difficulty in obtaining high quality AFM data should not be underestimated. In addition the approximations required in the methods outlined are open to interpretation and user bias to an extent that the process was not relied upon to characterize further samples. However, in the absence of more established alternative further investigations may be warranted.

3.5 Printing of protein micro-arrays

3.5.1 Introduction to protein printing

The CCD detector size of the AIE is 4.7 x 3.6mm and at a 1:1 magnification this offers an opportunity to fabricate a protein micro-array which has a matrix of small, individual protein elements (spots) within the image area. Using the Scheimpflug optical arrangement (Section 2.2.1.3) the whole of the imaged area will be in focus and measurable simultaneously. Therefore the AIE represents a significant improvement over existing imaging ellipsometry techniques. Additional benefits of this micro-array are noted to be; low reagent and sample use, the detection of low abundance proteins and the potential for multiple detection elements on a single bio-sensor platform.

This bio-sensor, in conjunction with imaging ellipsometry can produce an assay with a sensitivity and reliability to validate interaction partners and, even offer fundamental information on protein, ligand and antibody interactions. The potential benefits and technical issues are clearly identified by Romanov *et al* [200].

There are many techniques currently promoted for the purpose of fabricating protein micro-arrays. However there are two prominent technologies; contact and non-contact printing, both of these having emerged from the more established DNA micro-array fabrication industry [201].

3.5.2 Piezo printing introduction

Drop on demand printing relies on a pressure pulse which is achieved by one of two ways. The most common is thermal printing, here a heating element creates a vapor pocket through rising temperature. The vapor is then allowed to collapse by removing the heating effect. This rapid expansion and collapse causes a pressure pulse that ejects a droplet of ink [200]. The second mechanism is piezoelectric

printing where the pressure pulse is generated by an electromechanical actuator within the ink reservoir. The idea of printing proteins using a piezo electric inkjet printer has a number of merits. Benefits include:

- No contact with the substrate which reduces the possibility of surface damage and artefacts influencing measurement.

- Precision placement of pico litre volumes.

- Reduction of the coffee ring stain effect [202], [203] which can be caused by having to use a large liquid volume to cover an area of interest.

- The lack of heating (which may cause denaturing of the proteins) compared to thermal inkjet processes.

- The pixel by pixel printing control which may be useful in producing a protein distribution that reduces steric hindrance.

The literature supports these advantages and outlines ways of modifying domestic printers for the purpose [200], [204]–[206].

These features makes the fabrication of a protein micro array by this method significantly attractive and thus investigations were made. An Epson R280 printer was purchased and fixtures to support the silicon wafers through the printing process were fabricated from acrylic by laser cutting using AutoLaser (version: 2.2.1) and ArtCam Pro (version: 7.0) software.

3.5.3   Piezo printing method of evaluation

Printing software defines the shape and size of the image to be printed and hence its area. For application to proteins it is necessary to correlate printed area to the dispensed volume. To that end, fluorescein was diluted with dH_2O into a 1 mM concentration, to produce a stock solution of fluorescent, printable liquid.

Using the fluorescein solution, a series of known volumes were manually dispensed as a thin film using a pipette, onto standard ISO536 80gsm paper. The
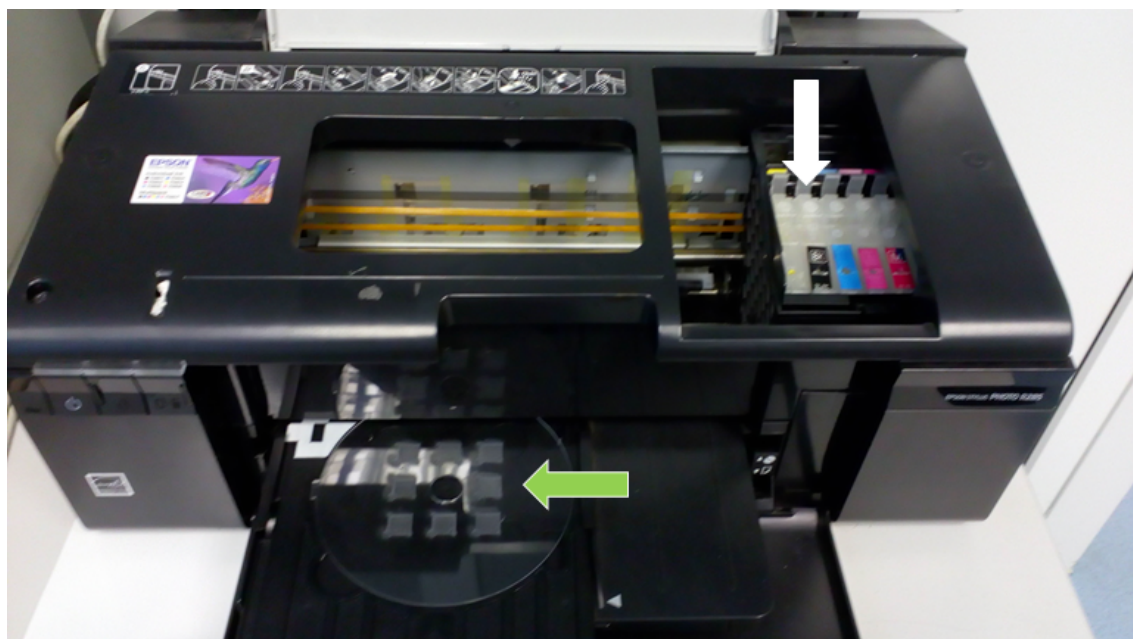
FIGURE 3.16: Epson R280 piezo printer used for protein printing; with refillable ink tanks identified (white arrow) and laser cut silicon chip holder highlighted (green arrow).

intensity of fluorescence was recorded using an integrating sphere by the method described by myself previously [148]. A series of known areas were then piezo printed by the Epson R280 onto standard ISO536 80gsm paper using the stock solution of fluorescein as an ink. The intensity of fluorescence of the printed paper areas were recorded using the same integrating sphere set up as for the manually pipetted volumes.

Following calibration using fluorescent liquid, the printing channel was thoroughly flushed using dH_2O. Protein printing was trialed using BSA (ThrmoFisher) diluted to 0.1mg/ml with dH_2O and a range of areas and shapes were printed onto silicon chips that had been RCA1 cleaned (Section 3.4).

3.5.4 Piezo printing results

Plotting the intensity of fluorescence for a series of dispensed volumes is presented (Figure 3.17) as blue diamonds. Regression of these values produced the

trend-line indicated in black and a model for extrapolation. The measured fluorescence intensity value, for each of the known areas piezo printed, was fitted to the regression model, and are identified as green triangles.
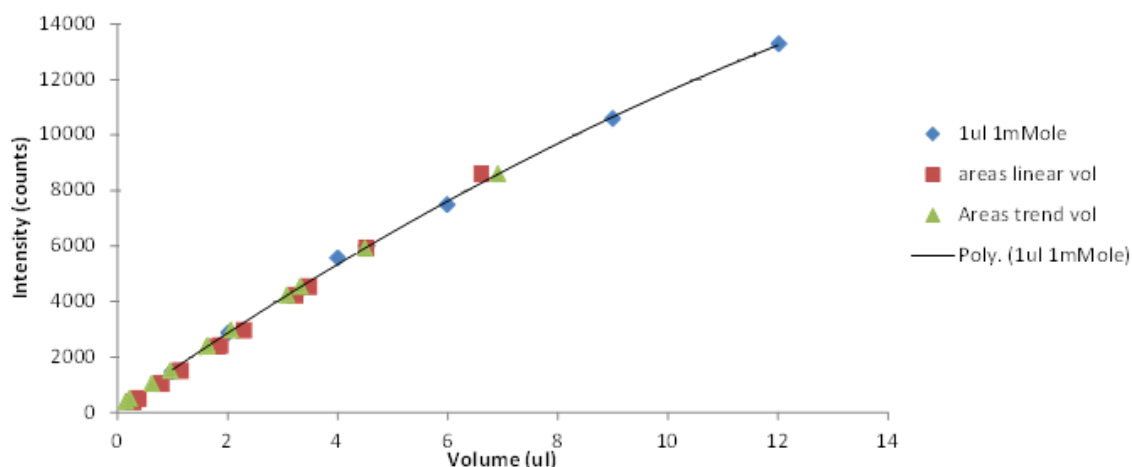
FIGURE 3.17: The relationship between fluorescent intensity and volume; fluorescence of known volumes, identified as blue diamonds, are regressed to produce the model (black line). Fluorescence of known areas are fitted to the model, presented as green triangles. An area to volume relationship can then be inferred.

From this, an approximate volume dispensed for area printed relationship can be extracted, which in the case of our printer on the black ink channel was 4 pl/mm^2. This compares well with the manufactures specification, which was discovered later to be 1.5 pl/pixel [207].

FIGURE 3.18: Images of piezo printed BSA on silicon: showing a 1mm diameter circle and three 0.8mm x 0.8mm squares of BSA, visualized using a simple prototype nulling imaging ellipsometer without Scheimpflug optics, and viewed from two angles.

An example of BSA printed onto silicon by piezo printing is presented (Figure 3.18). The 1mm diameter spot equates to an area of $0.785mm^2$ and an estimated delivered volume of 3.1 pl which at 0.1mg/ml equates to 0.31 pico grams (pg) of protein deposited. The 0.8mm x 0.8mm squares have an area of $0.64mm^2$ and hence approximately 0.26pg of BSA protein distributed into the printed area.

3.5.5 Discussion of piezo printing

A distinct advantage of piezo printing is the ability to deliver each micro droplet positioned sequentially on the surface covering the area as a thin film, encouraging rapid evaporation, reduction of coffee ring effect and hence even distribution of proteins. The method used to estimate the delivered volume to printed area cross checks well with the manufacturers specification and allows for a reasonable evaluation for the mass of protein distributed into any given area that is printed with a protein that is in solution. This method can be applied to determine the delivery volume of any of the other individual printer channels or indeed any other printer.

One of the disadvantages of non-contact printing is the volume of reagent held in the ink channels, which was found to be several milliliters, and the need to flush these reliably. Furthermore, blocked ink jet print heads are both common and frustrating to resolve. Indeed it was for these reasons that piezo printing using an Epson r280 was finally abandoned in favor of contact printing.

3.5.6 Contact printing introduction

In industry, fabrication of DNA micro arrays are almost exclusively done using contact printing methods, whereby a robot accurately places a pin, which holds the liquid sample material, onto the substrate surface [200].

Access to an unused Waters MicroMass ML2700, which is designed by the manufacturer to prepare samples for mass spectrometry, prompted initial trials

to place proteins onto silicon wafers. It was quickly realized that the control software was particularly inflexible in the shape and size of array available. Also the minimum pipetting volume was large at 2μl in comparison to 1.6 pico litres available for piezo printing. Despite these initial limitations, further investigations were undertaken.

3.5.7 Method of contact printing development

To reduce the scale and have full control over the layout of the array, the original control electronics were removed and replaced with StepperBee [208] modules to control the XYZ positioning stepper motors using a LabView programming interface. The individual motor movement control resulted in a positioning resolution for the X axis 0.45mm, Y axis 0.29mm and Z axis 0.10mm per step. Initial plans for a bespoke contact head to deliver solutions were abandoned after difficulties in both, controlling the head contact pressure onto the substrate and delivering repeatable, measured volumes of solution. To resolve these issues, a fourth axis drive was installed to deliver a more finely controlled quantity of solution through the existing pipette mechanism, with each individual motor control step delivering 0.1μl.
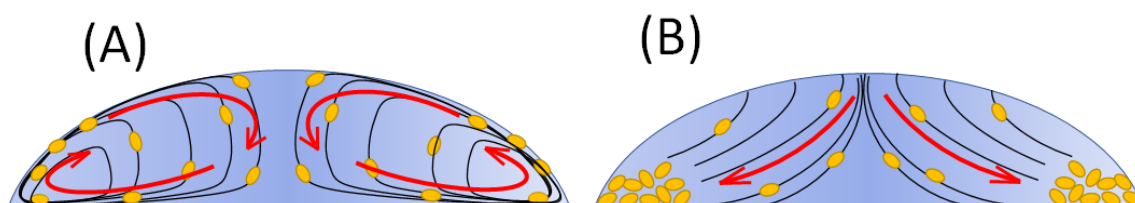
FIGURE 3.19: Schematic image showing Marangoni flow; A) Marangoni flow within the colloid liquid enhances particle distribution. B) Reduced or no Marangoni flow during evaporation risks formation of the coffee ring effect.

One issue that has significant impact on the visualization of this type of fabrication method is the coffee ring stain effect (Figure 3.19). Coffee rings form by the non-uniform distribution of a colloid material after it has dried, this problem is

a major cause of poor protein distribution and lack of consistency across protein arrays [200], [209]. The primary driver behind the coffee ring effect is pinning of the outermost contact point coupled with low levels of internal dynamic flow (the Maragnoni effect). For the effective assembly of a bio-sensor small spot sizes ($<$ 3 mm) will help to induce higher internal flow and reduce the coffee ring effect. [202], [203].

3.5.7.1   Calculations of overlap and target area

To optimize the fabrication of a protein array it was necessary to consider the variables that would influence the spot size and array pattern. Firstly if we assume a three step process of: linker, antibody and antigen, then it is necessary to create a spot size that will ensure an appropriate amount of overlap given the precision of the robot spotter in returning to the same spot 3 times.

The logic for calculating the optimum spot size based on the repeat-ability of spot centering was as follows.

- Calculate the standard deviation (σ) of variance from the target point.

- Use 3 times σ as a radius that will then contain 99.73% of all spot centers.

- Calculate the spot diameter that will overlap by a chosen % given a maximum distance center to center of the 3 spots, s = $Cos(30) * 3\sigma$.

- Using contact angles, calculate the volume needed to produce the desired spot size.

To establish the variability in spot center location, the robot was programmed to place a series of four spots in two rows using ink as a marker. The pipette tip was replaced and the sequence was repeated for a total of five times. Giving a total of 40 spots in a series of 8 groups each time an assessment of repeat-ability was taken. The results were photographed and spot center locations were measured using ImageJ.

It might be thought that to calculate the variability of the spot center positions the usual standard deviation formula (Equation 3.3) would be appropriate.

$$\sigma = \sqrt{\frac{1}{(n-1)} * \sum_{i=1}^{n} (x - \bar{x})^2} \tag{3.3}$$

However, because the positions of the spot centers are measured as a radius from the center of the enclosing circle the data has no mean from which the measured values can vary positively or negatively and as such it cannot be considered a normal distribution. Because all measured values from the mean are squared and all become positive it might be thought that $(x - \bar{x})^2$ can be substituted with $(r)^2$ where r is the distance from the center of the enclosing circle.

However, by using x,y position data for the spot center location each value can vary as a normal distribution positively or negatively around the datum of the enclosing circle center $\bar{x}$ and $\bar{y}$. Pooling the combined x, y data can be done using the formula:

$$\sigma = \sqrt{\frac{\sum_{i=1}^{n} \left((n_i - 1) * s_i^2\right)}{\sum_{i=1}^{n} (n_i - 1)}} \tag{3.4}$$

Which, because the number of x and y values are equal, can be reduced in this case to:

$$\sigma = \sqrt{\frac{(n_i - 1) * s_x^2 + (n_i - 1) * s_y^2}{2 * (n - 1)}} \tag{3.5}$$

Which simplifies further to:

$$\sigma = \sqrt{\frac{s_x^2 + s_y^2}{2}} \tag{3.6}$$

Substituting for s_x and s_y :

$$\sigma = \sqrt{\frac{\left(\sqrt{\frac{1}{(n-1)} * \sum_{i=1}^{n} (x - \bar{x})^2}\right)^2 + \left(\sqrt{\frac{1}{(n-1)} * \sum_{i=1}^{n} (y - \bar{y})^2}\right)^2}{2}} \tag{3.7}$$

Simplifying:

$$\sigma = \sqrt{\frac{1}{2(n-1)} * \sum_{i=1}^{n} (x-\bar{x})^2 * (y-\bar{y})^2} \tag{3.8}$$

Taking $\bar{x}$ and $\bar{y}$ as the center of the enclosing circle then $(x-\bar{x})^2 + (y-\bar{y})^2 = r_i^2$

Hence the adjusted measure for standard deviation of radial measurements from the center of the enclosing circle is:

$$\sigma = \sqrt{\frac{1}{2(n-1)} * \sum_{i=1}^{n} r_i^2} \tag{3.9}$$

A circle of radius 3σ, describes an area within which 99.73% of all spot centers will reside. The bio-sensor array will require three spots placed on top of each other, hence, the maximum spacing for three spot centers, takes the form of an equilateral triangle where the side length s represents a geometry that minimizes any potential overlap and describes the worst case scenario. It can be seen (Figure 3.20) that the distance s can be calculated from:

$$s = 2\cos(30) \cdot (3\sigma) \tag{3.10}$$
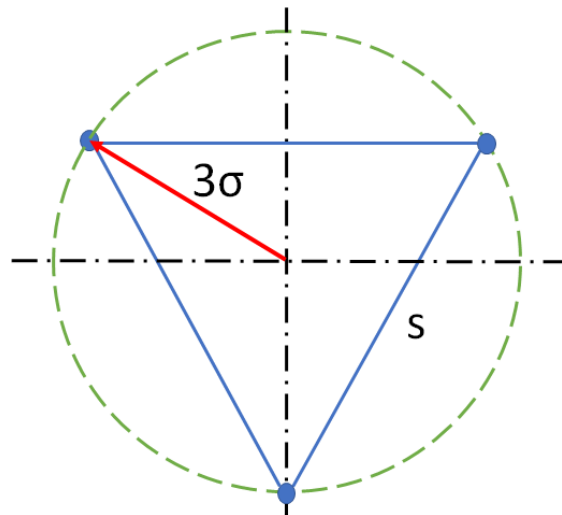
FIGURE 3.20: Identifying the maximum spacing for three spot centers; that minimizes overlap and represents the worst case scenario for a process with a position variability of 3σ.

3.5.7.2 Calculating the optimum spot size

Once the standard deviation of the spot center location is known, a spot diameter can be calculated that will produce the desired amount of overlap to ensure visualization by the AIE. Calculating the overlap formed by three overlapping circles first requires calculation of the intersection points to determine chord lengths and from that the areas of the three segments can be found and added to the central triangle area (Figure 3.21). The area of overlap cannot be determined analytically and requires numerical calculation using the value of center spacing (standard deviation σ) and chosen spot radius.

A simple engineering approximation was constructed. Taking r to be the radius of the spot, and 3σ as being three times the calculated standard deviation of the spot center point, as already described earlier (Equation 3.10) and represents a worst case scenario.
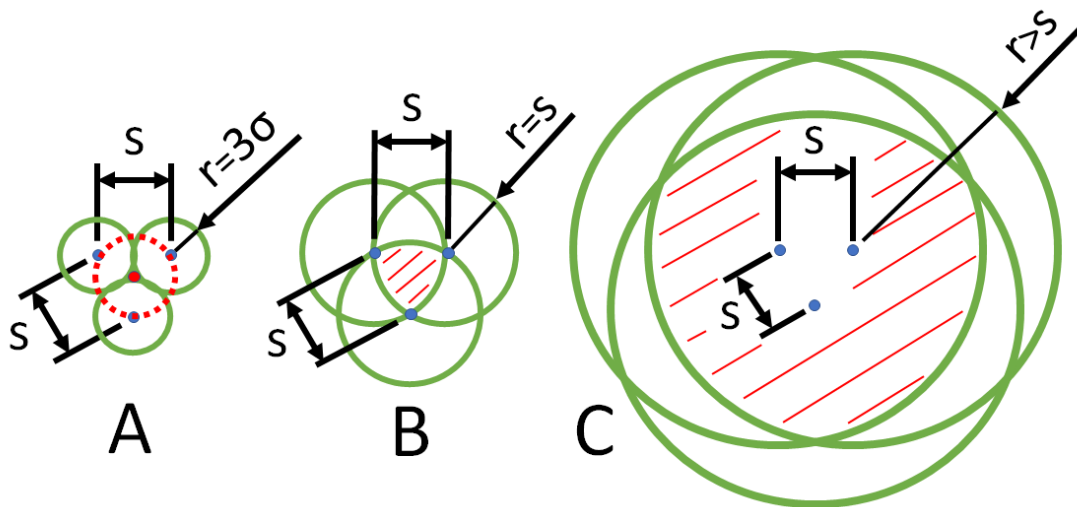
FIGURE 3.21: Schematic describing spot overlap for a given position scatter (s); A) Spots just fails to overlap B) The circle intersections coincide with the center point forming a Reuleaux triangle. C) As the radii become much larger than s the overlap will tend towards 100%

Three examples can be easily be established (Figure 3.21). Firstly, example A, when the spot radius r = 3σ. Here all three spots will just fail to overlap. Example B, When the spot radius r = s = $2\cos(30) \cdot 3\sigma$, here the spot radius is concurrent

with the intersection point, forming a Reuleaux triangle, giving an overlap of $\approx$ 22.4%. Finally example C, where the spot radius r becomes progressively larger in comparison to s and in this case it is easy to see that the overlap will tend towards 100%.

The ratio of maximum spot center spacing over spot radius (s/r) using the three points outlined can be plotted against overlap percentage and regressed to give a formula for the trend (Figure 3.22). This simple formula was checked using the full numerical solution at three additional points and the results were considered sufficiently accurate (within 5%) for the job of making a quick assessment of improvements as they occurred.
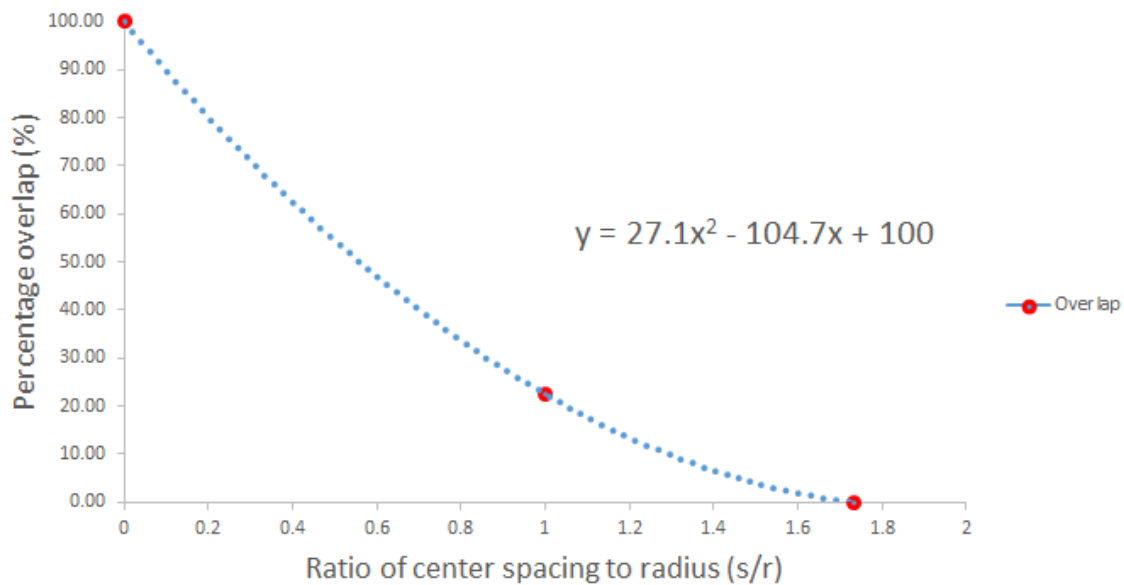
FIGURE 3.22: A model for estimation of spot overlap; the three known points and a regressed trend line resulting in the polynomial approximation used to estimate overlap for any given standard deviation to radius ratio.

So what can be observed is that to maintain an 80% overlap of all three spots the ratio of maximum spacing s to spot diameter r (s/r) needs to be 0.2 or less. For any other overlap percentages the graph in Figure 3.22 can be consulted and the model used to give an appropriate ratio of s/r from which the spot diameter can be calculated once the positioning error (3σ) is known and hence, using Equation 3.10, the value of s.

For most cases an overlap of 80% was considered appropriate and so the calculation of spot radius becomes:

$$r = \frac{2\cos(30) \cdot 3\sigma}{0.2} = \frac{\sqrt{3} \cdot 3\sigma}{0.2} \tag{3.11}$$

3.5.8 Results of contact printing

From the initial spot pattern spread as presented in Figure 3.23 example A, using Equation 3.9 the error can be calculated to be σ = 0.76mm, from Equation 3.10 s = 3.67mm and from the graph in Figure 3.22 an 80% overlap of spots will require s/r $\leq$ 0.2. Hence in this example the spot radius r = 3.67/0.2 = 18.4mm which is significantly out side the concept of a compact micro array of proteins, where two or more of these spots could be within the field of view of the ellipsometer.
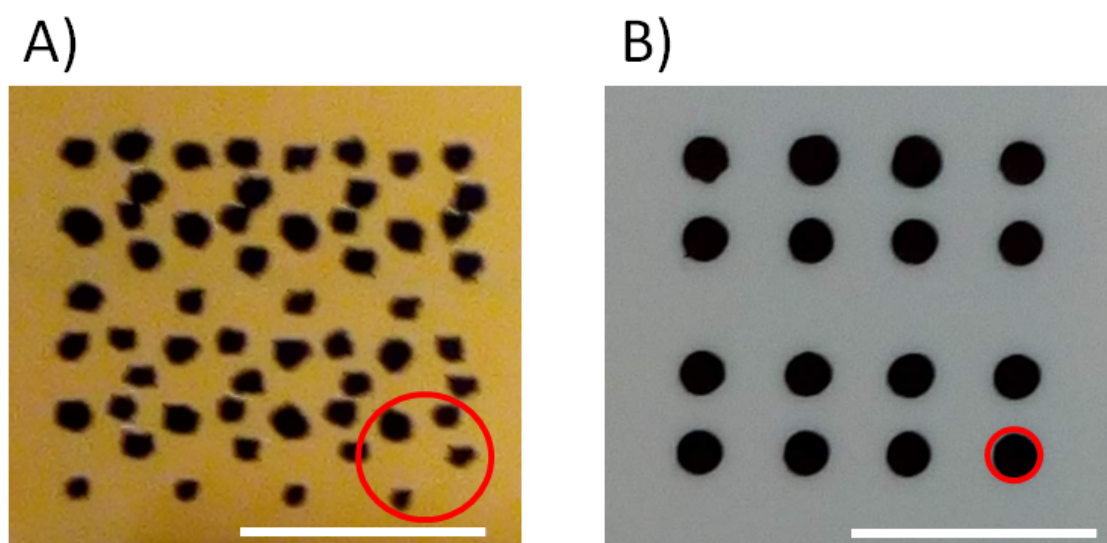
FIGURE 3.23: Results of spot size refinement: A) An early example of a 4 by 4 array, with five deposits at each target location, highlighting the poor repeatability of spot position. B) An example of an optimized 4 by 4 array, with five deposits at each location. In each case an enclosing circle is outlined in red. Scale bars are 5mm.

Each array was produced by picking up a pipette tip and depositing eight spots in two rows of four, removing the old tip replacing with a new one and then repeating the array pattern, depositing a total of five spots as a group in each of

the eight locations. It was quickly diagnosed that the group to group position of each spot was significantly more accurate than the spot on spot position within the group. This revealed that the major source of repeat-ability error was in the mounting of the pipette tips and not the xyz positioning accuracy of the robot. The pipette tips that were initially used had been taken from a bulk bag and placed in an accurately positioned tip rack, this allowed the robot to pick them up sequentially using a programmed control sequence. Measurement of the bulk bagged tips showed them to have a high degree of concentricity error that was contributing to the large amount of spot on spot deviation seen.

It's clear that the same pipette tip can not be used repeatedly because of the likelihood of cross contamination, so a wide range of bulk bagged, pre-racked and robot specific tips were selected and measured for concentricity error. The final selection was Star Labs Biomek FX E1076-4400 20μl which are pre-racked for use with an FX robotic pipette head. Modifications were made to the Walters pipette pickup head to enable the use of the final tip choice and following re pro-gramming of the control sequence, arrays were repeated to calculate the spot to spot center deviation 3σ and subsequent minimum spot radius. As presented in Figure 3.23 example B, significant improvements were observed and using Equation 3.9:

$$3\sigma = 0.06mm \tag{3.12}$$

For an 80% overlap of three spots, Equation 3.11 gives a minimum spot radius of:

$$r = \frac{0.16}{0.2} = 0.52mm \tag{3.13}$$

Hence the minimum spot diameter could now be reduced to $\approx$ 1.2mm.

3.5.9 Evaluation of volume and spot size

Once both the desired spot diameter is known and the contact angle the solution makes with the substrate has been determined, it is straight forward to calculate the volume of solution required to produce a spot diameter of the desired size using the appropriate equations describing the volume of a spherical cap (Figure 3.24). The results of the contact angle for each stage of the bio-sensor fabrica-

$$R = r/sin(\theta)$$
$$\theta = Contact\ angle$$
$$a = R\ cos(\theta)$$
$$h = R\text{-}a$$
$$V = \frac{\pi h}{6}(3r^2 + h^2)$$
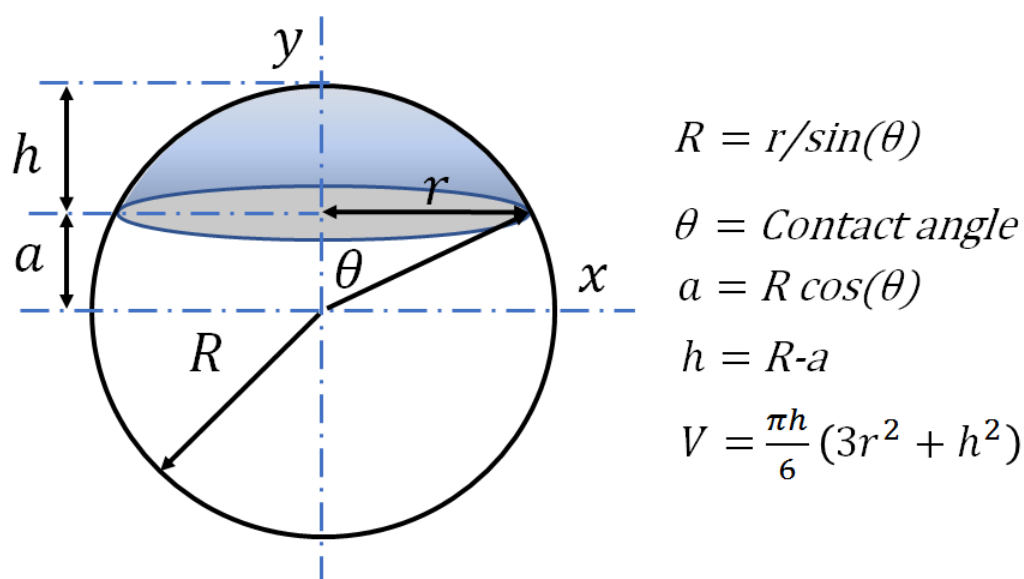
FIGURE 3.24: A schematic showing how the spherical cap volume V, relates to contact angle θ and spot radius r.

tion were used in combination with spherical cap volume to calculate a delivered volume required at each stage to produce a spot of 1.2mm diameter (Table 3.5).

TABLE 3.5: Hemispherical cap volumes of dH_2O; to produce a spot diameter of 1.2mm on silicon substrate with surface layer additions as indicated.

	Calculation of Spot Volume			
Material	Contact angle θ (deg)	Spot radius r (mm)	Sphere Radius R (mm)	Volume μL
Silicon	42	0.60	0.90	0.14
APTES	63	0.60	0.67	0.23
Gluteraldehyde	51	0.60	0.77	0.17
Protein	78	0.60	0.61	0.33

3.6 Discussion

The aim of this chapter was to provide a description of the diverse range of supplementary techniques that have helped to develop the concept of a protein micro-array and the fabrication process, in a way that maximizes the optical evaluation of AAI using the AIE.

3.6.1 Contact angle measurement

The AIE was easily adapted to take images suitable for contact angle measurement. Using ImageJ and the LB-ADSA plugin produced quick and accurate results for contact angle from the captured images. While the measurement of contact angle provided a simple means to monitor the surface chemistry change as the protein micro-array was being fabricated. With quantification of contact angle at each stage of the micro-array assembly informing understanding of the effects on deposited solutions, these result were then fed back to control the contact printer delivered volumes to improve the reliability and reproducibility of protein spot sizes.

3.6.2 Isolation of protein and EVs

Changes to the protocol for the DC isolation of *F. hepatica* EVs resulted in improved clarity of TEM micrographs, which brought particular benefits for downstream analysis, which is presented in detail in Chapter 4. The development of the sedimentation model proposed by Livshits *et al.* offers significant opportunity to further develop the refinement of EV isolation, with among other things, the potential to target specific EV size ranges. However, it is clear that independent confirmation of the sedimentation model is required, to that end further work to quantify the size distribution of EVs is necessary. Future experiments are proposed in which the Excel spin calculator prediction of EV size distribution is

compared to that as measured by direct quantitative technique for determination of nano scale particles, such as dynamic light scattering.

3.6.3   Atomic force microscopy

AFM has accurately monitored the substrate surface in 3D, informing the changes at each stage of bio-sensor assembly. In addition AFM analysis of EVs isolated by both SEC and DC techniques identified that the integrity of DC isolated EVs did not suffer from excess aggregation and indicates DC as an acceptable method by which an EV analyte solution can be prepared for use with the AIE. Investigations were made into the potential for using AFM as a means to quantify and qualify the accuracy of the Excel spin calculator in refining EVs from culture material. While some progress was made to de-convolve the effects of tip shape on EV topography refining the process and producing results in close agreement of those seen using TRPS, the process had no foundation in literature and was not considered reliable enough to characterize further samples.

3.6.4   Printing of protein micro-arrays

The piezo printer presented two key advantages, firstly the very low delivery volumes of around 4pl per mm^2 or 1.5pl per pixel. This delivered a thin film of solution over the substrate surface minimizing any coffee ring effects. The second related advantage is the flexibility in spot shape and size, which was almost unlimited. However, issues with print head blockage and the large volumes of reagent required lead to an abandonment in favor of contact printing.

The contact printer worked reliably once de-bugged and spots were reduced to a diameter of 1.2 mm, which allowed AIE visualization of two proteins spots consistently. Future developments using fine capillary pipette tips may provide improvements in further reducing the scale of the protein array.

Chapter 4

Selection of model antigen antibody interaction studies

4.1   Outline of the chapter general aims

The aim of this chapter is to describe the choice of AAI used within this study, and the developmental processes necessary to deliver them in a functional way for use by the AIE.

The introduction summarizes the literature that identifies the sigma class glutathione transferase (FhGST-S1) protein and EVs from the liver fluke *F. hepatica* as targets of interest given both the societal and economic pressures this particular parasite invokes. Highlighting how better understanding of these proteins can support the long term aims of diagnostic, vaccine and anthelmintic development.

The techniques used to advance development of a bio-sensor array are introduced. Following initial screening to identify novel binding partners by Western blotting, further investigations and observations from immuno-gold labeling and TEM, identify specific *F. hepatica* AAI.

The results section documents data collection and analysis identifying the points of refinement, developmental stages and how these provide a route to the selected proteins incorporated into a bio-sensor protein array for observation of AAI by the AIE.

4.2 Introduction

The work presented in this thesis focuses on two key areas; the development of the AIE to detect AAI, and the model proteins selected to support that very development. While straight forward off the shelf AAI systems such as BSA / anti-BSA could have been utilized a much more pertinent challenge comes with the prospect of developing the model AAI system using proteins from the parasite *F. hepatica*, which offers opportunity to develop improved understanding about a key parasitic infection.

The current gold standard for confirmation of *F. hepatica* infection is the FEC method [210], while excellent for diagnosis of high levels of infection in animals, this method has been shown to be insensitive on occasion in humans due to the sporadic nature of egg release which may be missed in low level infections [113]. In addition it fails to detect early stage acute infection by juvenile fluke migrating through the tissues when considerable damage is done. Only producing an egg positive result in the later chronic stage once fluke are mature and established within the bile ducts of the host and start shedding eggs. To resolve some of the problems associated with FEC some lab based alternatives have been developed.

A cELISA, which detects the presence of specific *F. hepatica* antigens found in host faeces is available for the early detection of *F. hepatica* infection from four weeks post infection [110], [112], [113], [211]. The cELISA method, typically relies on detection of *F. hepatica* cathepsin-L1 (FhCat-L1) antigens. Under experimental studies in sheep, it has been proven that FhCat-L1 cELISA has 100% sensitivity and specificity, even when sheep were only infected with a single fluke (Mezo et al., 2004). Given the lower sensitivity of FEC, (Charlier et al., 2008; Rapsch et al., 2006) compared to cELISA, the latter is potentially a convenient tool for the early diagnosis of *F. hepatica* infection in sheep. In addition, experimental evaluation of sera based cELISA have demonstrated it to have a sensitivity of 95.3% and 95.7% specificity in human fascioliasis cases [110]. Similarly, PCR of faecal samples is

also a promising tool for the detection of *F. hepatica* as early as two weeks post infection [212].

4.2.1 The role of the AIE

The opportunity of the AIE is twofold; as a potential diagnostic tool, detecting key bio-markers of infection via specific AAI, and in a long term developmental role supporting the understanding of AAIs and PPIs relating to key anthelmintic and vaccine candidates associated with *F. hepatica*. A number of key protein targets have been identified in *F. hepatica* that have vaccine, anthelmintic or combined interest.

TABLE 4.1: Presenting the target proteins relating to key vaccine and anthelmintic candidates.

	Protein					
	FhGST-S1	FhCatL1	FABp5	TGR	LAP	HDM
References	[6], [108], [114]	[7], [95]	[95]	[213]	[214]	[215]

Of particular note is FhGST-S1 which is documented to have an immunomodulatory function, which offers a significant opportunity as a vaccine candidate [6], [108], [114], [117]. One which is available for use as a recombinant protein and as a native protein [6], [115]. Additionally, a rabbit raised polycolonal antibody raised against FhGST-S1 [6] allows considerable avenues of investigation. A significant recent finding is the discovery that FhGST-S1 is a component of *F. hepatica* EVs [116].

It is likely that the EVs of *F. hepatica*, containing FhGST-S1 will play a key role in the future control of this parasite, whether through vaccine immunization or novel chemo-therapies. Originally described by Harding *et al.* in 1983 [216] and considered to be 'cellular garbage cans' removing unwanted cellular material, EVs have since been identified as important mediators for inter-cellular communication. Capable of delivering molecular signals, comprising of proteins, lipids and a wide range of RNA species [131]. In the case of parasitic diseases, EVs have

been shown to use this mechanism of inter-cellular communication to achieve modulation of immune responses [123]. Indeed Marcilla *et al.*'s summary of the data suggests that EVs are likely the principle trematode mechanism to export protein into the host, which gives them considerable potential to provide new diagnostic tools and therapies.

This particular focus is well evidenced during recent Innovate UK funded [217] AU Brophy-Morphew lab collaboration with Ridgeway Research Ltd. and Bio-check UK Ltd. to develop a pen-side diagnostic test to identify fascioliasis in sheep and cattle based upon EVs as a reactive agent (patent application currently in progress). This development work involved the complete characterization of the protein components, surface and cargo, by Dr. Rebekah Stuart [2018 unpublished] for key *F. hepatica* strains using proteomics; this work also involved exposing *F. hepatica* EVs to trypsin, causing proteolysis by catalyzing hydrolysis and cleaving the peptide bond at arginine or lysine points of the EVs surface exposed proteins, effectively shaving peptides from the surface. This was done using a modified version of the Cwiklinski *et al.* protocol [7]. Analysis of these shaved peptides by mass spectrometry (MS), has revealed the presence of 79 proteins, across all three strains tested, that are believed to be exposed beyond the lipid bi-layer of the EV surface, presenting a number of potential targets for a model AAI diagnostic system, observable using the AIE.

With regard to using the AIE, identification of EV surface exposed proteins which are receptive to specific *F. hepatica* antibodies presents a route to construct a diagnostic bio-sensor as presented earlier (Chapter 1 Figure 1.15). Therefore, the aim of the experimental work of this chapter was as follows:

- Optimise EV isolation.

- Optimise TEM visualization of EVs.

- Confirm anti-FhGST-S1 antibody interaction with EV surface proteins.

- Establish suitable positive and/or negative controls.

- Identify if *F. hepatica* EVs and/or FhGST-S1 protein are present in faecal samples from infected hosts. Raising the possibility that a diagnostic test may be feasible, using readily accessible EVs and the AIE.

4.2.2 EVs from *Fasciola hepatica* as a model AAI system

While it is has been shown in Chapter 2 that with suitable development the AIE has the potential to detect the change in polarization of incident light brought about by the mono layer interaction of antibody and antigen. If this were to prove difficult in practice when applied to *F. hepatica* specific proteins, an advantage of EV capture is their increased size compared to single proteins. While the bond strength between antibodies and EVs and hence ability to hold the EVs in place was unknown, the order of magnitude scale difference, the 5-15nm diameter of a protein compared to the 30-300nm diameter of an EV, makes them an attractive target for investigation alongside FhGST-S1.

4.2.3 Summary to introduction

The aim of this chapter's experimental work was to find and develop model AAI utilizing those proteins that would enable observations of interactions using the AIE and support the longer term aims of potential diagnostic, vaccine and anthelmintic development. Data from MS analysis by Cwiklinski *et al.* [7] and Dr. Stuart [2018 unpublished] from trypsin shaves of isolated *F. hepatica* EVs have identified a range of proteins that are exposed from the EV surface. This offers the potential of AAI detection of *F. hepatica* EVs as a diagnostic technique [218].

While the literature and the work both past and present of the Brophy-Morphew lab have identified key bio-markers of *F. hepatica* infection such as FhGST-S1, *F. hepatica* fatty acid binding protein -V (FhFABP-V) and FhCat-L1 no previous studies have shown if these proteins can be used in a label free, optical, bio-sensor format.

4.3 Materials and methods

4.3.1 Observations using TEM

Preparation for qualitatively visualizing the *F. hepatica* EV preparations by TEM was done initially as described by Nowacki *et al.*[184] and later to quantitatively record any immuno-gold labeling, the protocol of Théry *et al.* [27]. Describing the Théry *et al.* protocol briefly; isolated EVs were diluted in para-formaldehyde 4% v/v as a fixative, adsorbed onto formvar carbon coated TEM grids for 20 min, further fixed using glutaraldehyde 4% v/v, contrast stained for 5 minutes using a uranyl oxalate solution 4% v/v and then embedded in a final layer of methyl-cellulose.

Development of the protocols and points of refinement are described within the results (Section 4.4.1). In all cases, formvar-carbon coated copper grids (Agar scientific) were placed face down onto 10μl of EV-enriched sample solution prepared and allowed to adsorb in accordance with the specific protocol chosen.

All prepared grids were visualized on a JEOL 1010 transmission electron microscope operated at 80 kV. Images were recorded with a Kodak MegaPlus Model 1.4i camera, other than a file format change from jpeg to TIFF and the addition of scale bars, no further image processing was done. The full SOP is included in the appendix.

4.3.2 Immuno-gold labeling.

Immuno-gold labeling was done following the protocol of Théry *et al.* [27] modified by the replacement of BSA as non specific blocking agent and antibody diluent with caesin-thimerosal buffer (CTM-T) as described by Kenna *et al.* [219]. *F. hepatica* EVs were incubated with rabbit raised antibody, followed by anti-rabbit IgG with a colloidal gold tag attached (Sigma). Labeling was done using tags of either 5nm or 15nm nominal diameter. The full SOP is included in the appendix.

4.3.2.1 Quantification of labeling incidence and analysis.

The resultant immuno-gold label incidence for test and control samples was quantified from TEM micrographs of EVs prepared as described earlier (Section 4.3.1). Calculation of the gold label incidence involved 104 (minimum) to 572 (maximum) individual EVs which were counted for each sample. At least three grid areas were randomly selected for analysis, scanned and recorded in accordance with the recommendations of Lucocq [220] and Mayhew *et al* [137]. Labeling incidence were expressed as the number of gold particles on or within close proximity to the edge of EVs. Controls included counts of the background areas. Comparisons between samples were made by an independent means two-tailed t-test following Kaur and Raje [221] and computed using SPSS (version: 24.0) software.

4.3.3 *Fasciola hepatica* collection and culture

Six sheep were each experimentally infected with 200 *F. hepatica* metacercariae by Ridgeway Research Ltd. Twelve weeks post infection mature flukes were recovered from the livers immediately post slaughter. This process was repeated for each of three *F. hepatica* strains: Aber, Italian and Miskin. Once removed from the host livers the *F. hepatica* were maintained as previously described by Morphew et al [222]. Briefly, whole fluke from each individual liver were counted and thoroughly washed three times in PBS at 37ºC to remove host material and stimulate regurgitation of gut contents. The collected *F. hepatica* were then placed in *Fasciola* saline at 1 ml per fluke (Dulbecco's modified Eagle's medium (DMEM) (w/o NaHPO$_3$ and PO$_4$) plus 2.2 mM Ca (C$_2$H$_3$O$_2$), 2.7 mM MgSO$_4$, 61.1 mM glucose, 1 μM serotonin, 5 μg/mL gentamycin, 15 mM N-2-hydroxyethylpiperazine-N'-2-ethanesulfonic acid (HEPES), pH7.4) at 37ºC for 5 hours (including transport to the laboratory). All flukes remained alive after *in vitro* culture incubation. Post culture, flukes were removed from the media and snap frozen in liquid nitrogen.

Culture media was immediately frozen and stored at -80ºC, until further processing.

4.3.4 EV isolation

4.3.4.1 EVs isolated from *F. hepatica* culture media

EVs were isolated from the culture media by DC, originally using the protocols based on the method according to Nowacki *et al* [184] and Théry *et al* [27]. The SOP is provided in the appendix. Later modifications to the DC protocol were informed by the Excel spin calculator described in detail earlier (Section 3.3). Evaluation, optimization and points of refinement are described in the results (Section 4.4.1). Initial separations were done using an Eppendorf SW-A-4-81 centrifuge and later a Beckman Ultra XL with 50.2Ti rotor. The final pellet was resuspended in 100μl of PBS, transferred to 0.5ml ultra high recovery microcentrifuge tubes (StarLabs: E1405-2600) and frozen at -80ºC, until needed.

4.3.4.2 EVs isolated from host faecal material

Naive *F. hepatica* free ovine faecal samples were sourced via animals from an experimental infection study. The sample for evaluation was sourced by pooling 10 smaller 1 gram pellets obtained from individual sheep at Ridgeway Scientific Ltd., from experimental stock.

Spiked samples were prepared by adding 100μl of previously isolated Aber strain *F. hepatica* EVs at 0.85mg/ml (obtained from culture) to 10g of known *F. hepatica* free ovine faecal sample sourced as above from experimental stock at Ridgeway Scientific Ltd.

Wild ovine faecal samples were sourced from known *F. hepatica* egg positive faecal samples [223] 10 smaller 1g pellets were pooled together into a single 10g volume that was representative of a typical faecal collection.

All samples were processed by DC to isolate all EVs in a manner already described (Section 3.3.2). EVs were adsorbed onto TEM grids and incubated with rabbit raised anti-FhGST-S1 primary antibody followed by gold labeled anti rabbit IgG secondary, described in full later (Section 4.4.3). TEM grids were then contrast stained and imaged as described earlier (Section 4.3.1).

4.3.5 Sodium dodecyl sulfate polyacrylamide gel (SDS-PAGE) electrophoresis.

F. hepatica EV samples isolated as described above were thawed on ice then aliquated into ultra high recovery microcentrifuge tubes (StarLabs: E1405-2600). EVs within the tubes were lysed by immersion in a sonication bath for 30 seconds, then rested on ice for 30 seconds, this was repeated for a total of five times. Following lysis, samples were quantified for protein content using an Invitrogen Qubit fluorimeter as *per* the Qubit manufacturer's instructions [224]. The samples were mixed with loading buffer and rapidly heated to 95ºC for 5min. The resulting de-natured protein solution was then loaded into 7cm 12.5% tris/glycine polyacrylamide gels and run using the Protean III system (Bio-Rad). The gels were initially run at 70 volts, until the dye front passed through the stacking gel, at which point the voltage was increased to 150 volts and maintained until completion. Gels were fixed using a 40% (v/v) ethanol, 10% (v/v) acetic acid solution. Once fixed they were then stained with colloidal Coomassie Brilliant Blue (Sigma). Gels were imaged using a GS- 800 calibrated densitometer (Bio-rad)

4.3.6 Western blotting.

Samples were prepared and run on 1D SDS-PAGE gels as described above (Section 4.3.5). Proteins within the gel were then electrophoretically transferred across onto Hybond-C extra NCP (GE Healthcare). This was done using a Trans-Blot cell, immersed in transfer buffer [192 mM glycine, 25 mM trisHCL (pH 8.3), 20%

(v/v) methanol] running at 40 volts for two hours according to the method of Towbin *et al.* [15]. Transfer was visually assessed by staining the membrane with amido black [0.1% (w/v) amido black, 10% (v/v) acetic acid, 25% (v/v) iso-propanol] for one minute. Once confirmed, the membrane was then de-stained using 10% (v/v) acetic acid and 25% (v/v) isopropanol and subsequently washed three times in tris buffered saline (TBS) [100 mM tris-HCL (pH 7.5), 0.9% (w/v) sodium chloride] with 1% (v/v) tween20 tris buffered saline (TTBS). The membrane then had any remaining protein sensitive space blocked by immersion overnight in TTBS with 5% (v/v) skimmed milk powder) agitated by rocking and maintained at 4°C.

Following overnight blocking, membranes were incubated in primary antibody diluted according to each antibody used. Primary antibodies used for Western blotting were:

- Anti-FhGST-S1 at 1:20,000 [6],

- Anti-FhFABP-V at 1:2000 [116] which was commercially made (Lampire) from polyclonal antibodies to a purified recombinant FABP-V from *F. hepatica* expressed in bacteria and raised in rabbits,

- Anti-thioredoxin-glutathione reductase (Anti-FhTGR) at 1:2000, which was commercially made (Lampire) from polyclonal antibodies to a purified recombinant TGR from *F. hepatica* expressed in bacteria and raised in rabbits.

- α and β tubulin at 1:500, commercially purchased from Thermofisher Scientific.

- Anti-FhCat-L1 at 1:10,000 which was commercially made (Lampire) from polyclonal antibodies to a purified recombinant cathepsin L1 from *F. hepatica* expressed in bacteria and raised in rabbits.

All primary antibodies were diluted in TTBS with 1% (v/v) skimmed milk protein. Anti-FhGST-S1 and anti-FhCat-L1 primary antibodies are known to have

high specificity however, anti-FhFABP-V is known to be reactive to FABP I, FABP II, FABP III and FABP V [225].

With the primary antibody added the membrane was placed on a rocker for one hour at at 18ºC. The membrane was then washed three times for five minutes in TBS to remove any unbound antibody. The secondary antibody, anti-rabbit IgG (whole molecule) conjugated to alkaline phosphatase (Sigma) dilution 1: 30,000 in TTBS, was then added to the membrane and again rocked for one hour at at 18ºC. The membrane was then washed three times for five minutes in TBS as previously described, to further remove any free antibody. Following washing, any phosphatase which remained on the membrane as a result of binding with the primary antibody, and hence the antigen present within the lysed EV sample, was visualised by using a solution comprising, 33μl 5-bromo-4-chloro-3-indoyl phosphate (BCIP) [50mg/ml] and 330μl nitro blue tetrazolium (NBT) [10mg/ml] added to 10ml substrate buffer comprising of 0.1 M tris, 100mM sodium chloride, 5mM magnesium chloride, (pH 9.5). This detection solution was added to the membranes and rocked at 18ºC until either clear visualization of banding occurred or for a maximum of five minutes. The reaction was stopped by water washes and membranes were then scanned using a Bio-rad GS800 calibrated densitometer.

4.3.7   Trypsin shaving of EVs.

Cleaving of peptides from the surface of EVs, termed shaving, was performed and refined by Dr Stuart following the initial method described by Cwiklinski *et al.* [7]. Briefly, sequencing grade trypsin (Fisher Scientific) was added to isolated *F. hepatica* EVs at a final concentration of 50μg/ml for 20 min at 37ºC. The reaction was stopped by reducing the temperature of the solution to 4ºC. The treated EVs were condensed to a pellet by centrifugation at 100,000 g for 60 min at 4ºC, and the released peptides were recovered from the supernatant by vacuum drying,

followed by re-suspension in 20μl of 0.1% (v/v) formic acid in preparation for tandem MS.

Liquid chromatography tandem MS (Agilent 6550 iFunnel Q-TOF) coupled to a HPLC-Chip (1200 series, Agilent Technologies, Cheshire, UK) was used for peptide separations. Tandem mass spectrometry was performed in the 300–1700 Da range, at a rate of five spectra per second, on the five most intense ions in the precursor scan. Peak lists were generated with Mass Hunter Qualitative Analysis software (V B.06, Agilent Technologies) and exported as Mascot Generic Files. Analysis of sample data was processed following Morphew *et al* [114]. Briefly, for the overall list of proteins identified, only those with at least two unique peptides and present in at least 30 instances across three biological replicates (n = 3) were selected. Protein sequences were searched using BLAST2GO obtaining BLAST descriptions and gene ontology terms.

The pellet was resuspended in 100μl of PBS, transferred to 0.5ml ultra high recovery microcentrifuge tubes (StarLabs: E1405-2600) and frozen at -80°C, until needed.

4.4 Results

4.4.1 TEM visualization of EVs.

As described previously (Section 3.3) the initial protocols for isolation and imaging of EVs within AU were developed by a former research group colleague Fanny Nowacki [184]. A reduction in background contamination and improvements in TEM visualization of EVs were seen with the protocol of Théry *et al.* [27].
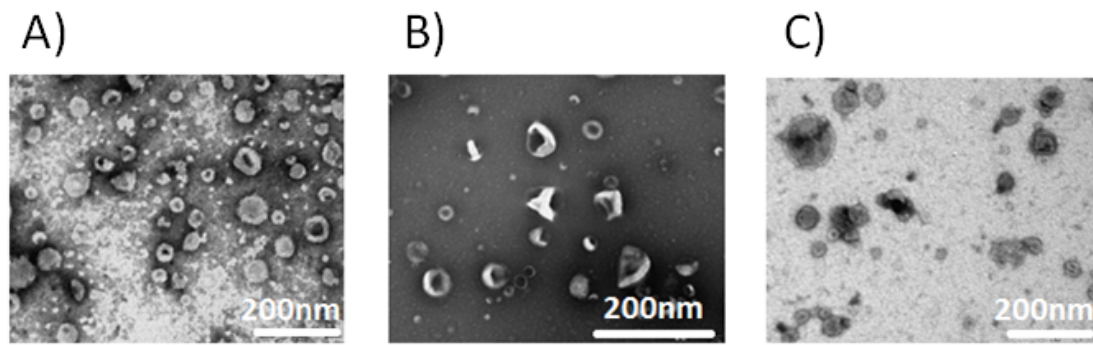
FIGURE 4.1: Three replicate TEM micro-graphs showing the variation in contrast staining; for *F. hepatica* EVs isolated and stained using the Nowacki method: 40min adsorb onto grid, 10 min uranyl acetate stain.

4.4.1.1   Contrast staining protocols.

Briefly, the initial stain protocol developed by Nowacki involves fixing EVs with a 4% (v/v) glutaraldehyde solution then allowing the prepared sample 40 min to adsorb onto formvar carbon coated TEM grids, followed by a contrast stain using 4% (v/v) uranyl acetate (PH 4) applied for 5-10 minutes (Figure 4.1).

However, while quick and simple, the Nowacki method produces reversed contrast across many of the grid squares (Figure 4.1 images A & B). This dark background staining makes the identification of gold label tags from the immuno-gold labeling process, which are seen as black spots, much more difficult, if not impossible, in large areas of the TEM grids. A search of the literature revealed the method of Théry & Clayton [27] gives the light background and contrast feature staining to the EVs that makes identification of gold tags in both the background and around target EVs much simpler and more accurate (Figure 4.2).

A SOP that compiles the protocol as concisely as possible from the reference source was constructed and is included in the appendix.
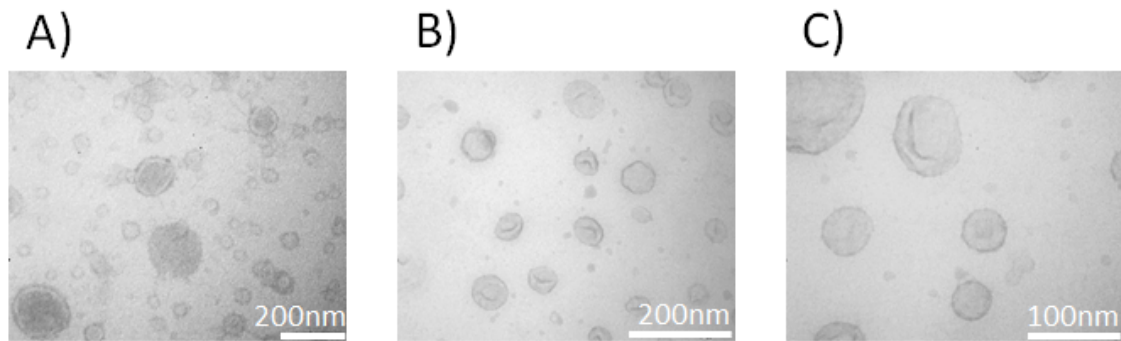
FIGURE 4.2: Representative TEM micro-graph showing EVs contrast stained using the Théry protocol; which produces good contrast and allows excellent EV definition across the whole grid area.

4.4.2 Western blotting of *Fasciola hepatica* antibodies on EVs

By using the Western blot method it was possible to evaluate that the culture obtained from *F. hepatica* helminths, refined by the process described earlier (Section 4.3.4) contains both proteins typically found in EVs generally and some that are specific to *F hepatica*. Antibodies targeting FhGST-S1, FhFABP-V, FhTGR, α & β tubulins and FhCat-L1 were used to probe lysed EVs. Following development, a visible reaction was observed relating to all antibodies used with the exception of FhCat-L1 which had only a faint response (Figure 4.3).

4.4.3 Immuno-gold labeling of EVs

Following the Western blot, some question remain; firstly, which of the proteins identified are expressed on the surface of EVs and which are contained within. Secondly, are any of the surface exposed proteins receptive to the antibodies identified in the Western blot, when the EVs are un-lysed. The use of immuno-gold labeling provides a means to help build a body of evidence that gains some insight into both of these questions. Once confirmed these specific AAI can then be utilized in a bio-sensor array and visualized by the AIE.

To answer these questions a series of experiments were conducted to optimize the amount of antibody present in the primary and secondary probing solutions.
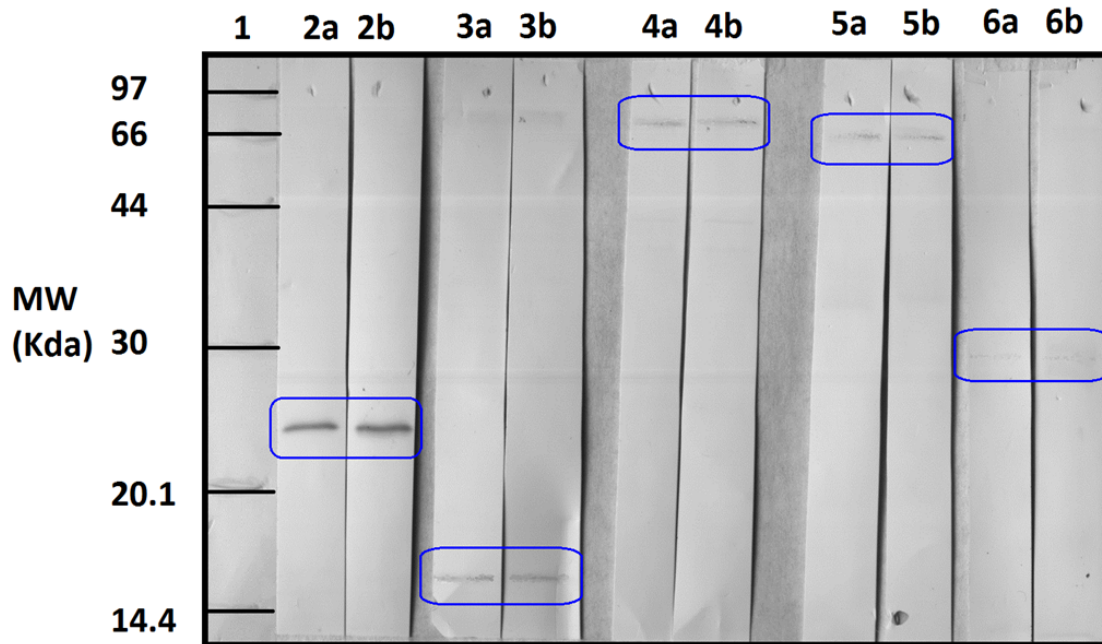
FIGURE 4.3: Western blot of *F. hepatica* EV proteins using target antibodies; analysis reveals the presence of FhGST-S1 (lanes 2a & 2b), FhFABP-V (lanes 3a & 3b, FhTGR (lanes 4a & 4b), α & β tubulins (lanes 5a & 5b), and faint recognition to FhCat-L1 (Lanes 6a & 6b). Lane 1 contains low molecular weight markers for size comparison. EV proteins were run on a 12.5% SDS-PAGE, transferred to NCP membrane and developed using BCIP and NBT.

Using TEM observations, the ideal was to use sufficient antibody to present a large enough number of binding opportunities but not overload the grid. Overloading which prevented all of the unbound antibodies from being removed during wash steps and allowed them to remain as false positives.

Initial trials were conducted using a series of serial dilutions and from this further refinements revealed that which was considered to be the optimum values for each antibody (Table 4.2).

During the early stages of immuno labeling experiments, a change was made to the protocol described by Théry [27]. Where by, use of BSA as a non specific binding site blocking agent was replaced with CTM-T. The object of using BSA within the protocol is for the BSA protein to attach to any areas on the EVs that will accept a non-specific partner. Thus, when the secondary, labeled antibody is added, the only available sites for it to bind are those provided by the specific

TABLE 4.2: The optimized antibody dilution ratio for immuno-labeling *F. hepatica* EVs.

Primary antibody	Dilution ratio	Conc. (mg/ml)
Anti-FhGST-S1	1:50	0.05
α & β tubulin	1:200	0.01
Anti-FhFABP-V	1:50	0.04
Anti-FhTGR	1:100	0.05
Anti-FhCathepsin-L1	1:50	0.06
Secondary antibody		
Anti-rabbit IgG 5nm	1:200	0.005
Anti-rabbit IgG 15nm	1:200	0.005

primary antibody. If left un-blocked these areas have the potential to accept the secondary gold labeled antibody directly and give a false positive result. The use of CTM-T has been seen to offer improvements in blocking performance over BSA without detriment and can in addition be used as an antibody diluent [219].

4.4.3.1 Antibody response to *Fasciola hepatica* EVs

The results of initial immuno-gold labeling investigations showed that anti-FhGST-S1 and anti-α & β tubulin had a considerable binding affinity with the surface of *F. hepatica* EVs and as a result further work was conducted to test the strain specific response, which is described fully (Section 4.4.3.2). Once the labeling process was suitably optimized the method of Kaur and Raje [221] was employed to quantify the proportion of EVs that were identified as tagged by the immuno-gold labeling process. Briefly, a minimum of three areas were selected at random from the overall TEM grid, in each chosen location the area was methodically scanned, where every recognizable EV was counted and then identified if it had one or more gold tags associated with it. Comparisons were then made to a control which had no primary antibody incubation. For anti-FhGST-S1 a total of 572 EVs were counted and 327 (57%) had one or more tags in contact or very close proximity to the edge of the EV (Table 4.3).

TABLE 4.3: The binding incidence for anti-FhGST-S1 immuno-labeled antibodies by *F. hepatica* EVs: n = number of EVs counted, $\bar{X}$ = mean, SD = standard deviation, t = t-test (distribution from null), p = p-value (significance level).

	Immuno-gold label binding incidence	
	Control	**a-FhGST-S1**
n	112	572
$\bar{X}$	0.0268	0.5719
SD	0.1615	0.6420
t		9.498
p		0.00001

4.4.3.2 Specific *Fasciola hepatica* strains tested against anti-FhGST-S1

Each of the three strains of *F. hepatica* EVs were incubated with rabbit raised anti-FhGST-S1, followed by anti-rabbit IgG with a 15nm colloidal gold tag attached (Sigma Aldrich: G7402). TEMs were counted in a manner as described to a total of 119 Miskin, 109 Italian and 125 Aber strain randomly selected EVs over multiple grid areas. In initial TEM observations following the use of anti-rabbit IgG with 15nm colloidal gold conjugated particles, a number of larger EVs were observed with multiple tags surrounding it. Whereas the smaller EVs (<30nm) were seen to be less prone to multiple labeling. This raised the possibility of steric hindrance from the relatively large tags in proportion to EVs in the smaller range of 30 to 50nm diameter.

Incubations were repeated using Italian strain *F. hepatica* EVs, with an anti-rabbit IgG with a gold tag of 5nm (Sigma Aldrich: G7277) (Figure 4.4). While somewhat more prolific in attachment the difficulty in TEM observation of 5nm gold tags should not be underestimated.

Experiments were repeated using each strain of *F. hepatica* EVs (Table 4.4), with TEM observation producing similar levels of AAI incidence (Figure 4.5).

The significance here is that despite the difficulties in TEM observation an increase in AAI occurrence on smaller EVs, present across all tested strains of *F. hepatica* EVs, strengthens the potential for FhGST-S1 use as a model system for the detection of *F. hepatica* infection using the AIE.
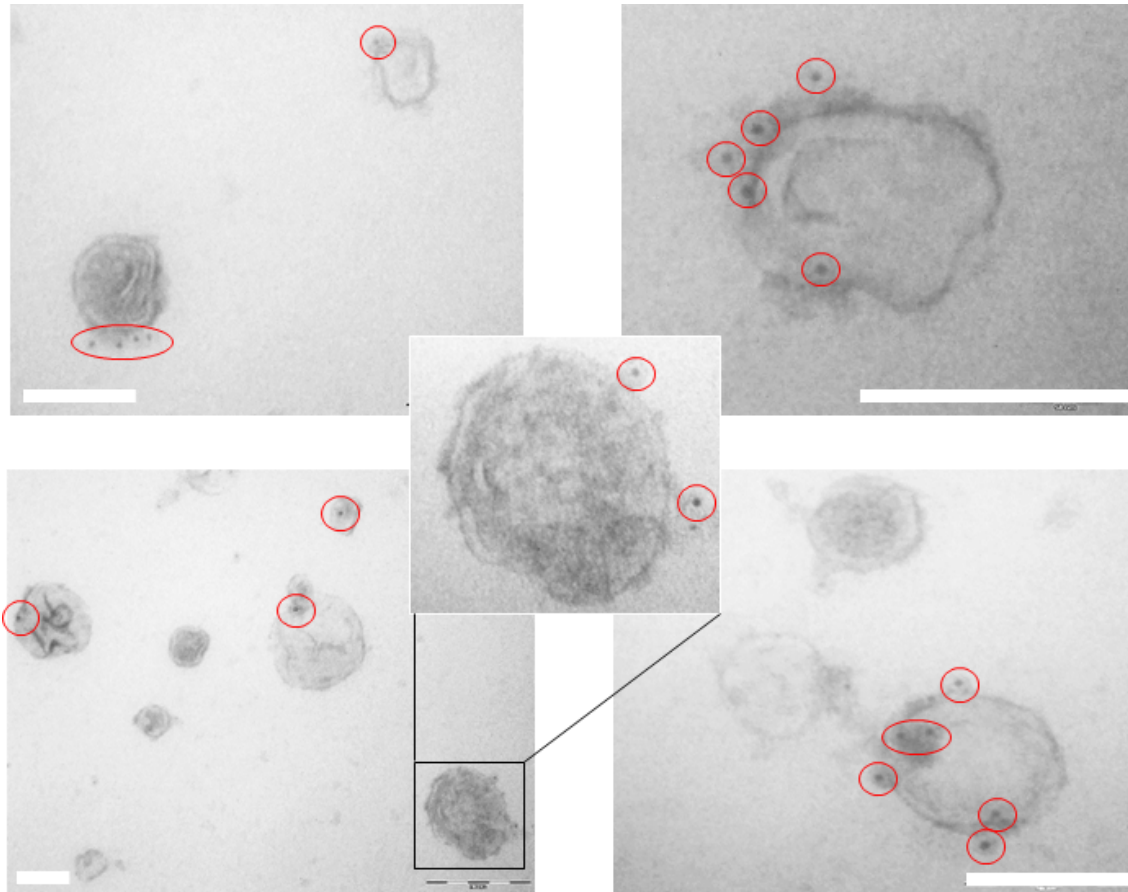
FIGURE 4.4: Representative TEM micro-graphs of Italian strain *F. hepatica* EVs; incubated with rabbit raised anti-FhGST-S1 primary antibody and 5nm gold labeled anti-rabbit IgG secondary antibody (outlined in red). The high incidence of AAI offers potential as a model system for detection using the AIE. Scale bars 100nm.

TABLE 4.4: The binding incidence for anti-FhGST-S1 immuno-labeled antibodies by *F. hepatica* EVs by strain expressed as a percentage.

Immuno-gold label binding incidence (%) [n = >100]	
Strain	**a-FhGST-S1**
Aber	57
Italian	52
Miskin	54

In all cases of immuno-gold labeling experiments a number of gold tags were seen in the background surrounding EVs on the grid areas. While the numerous wash steps during sample preparation aims to remove any free unbound gold antibody it was thought possible that the process may not be 100% effective.
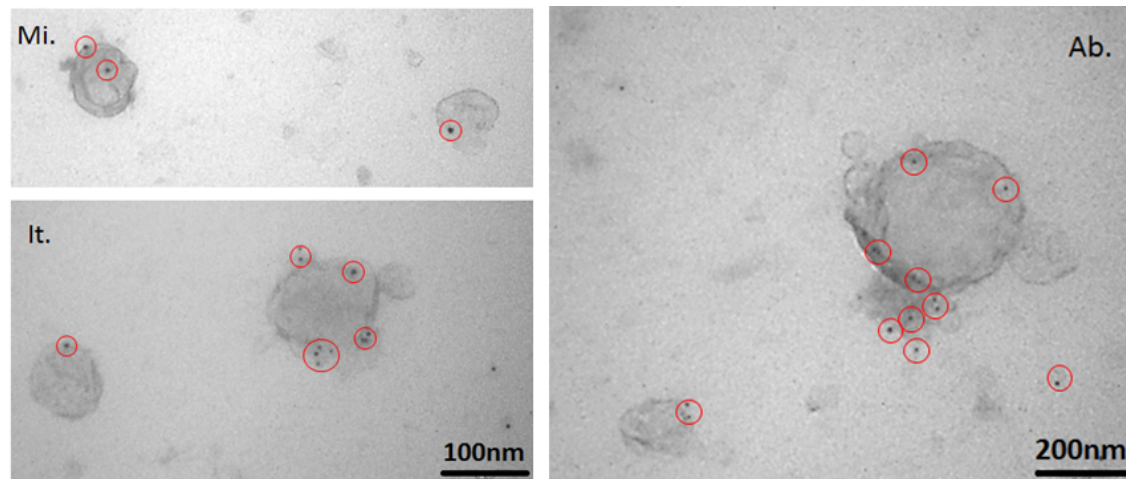
FIGURE 4.5: Representative TEM micro-graphs of Miskin, Aber & Italian strain *F. hepatica* EVs; labeled with rabbit raised anti-FhGST-S1 primary antibody and 5nm gold labeled anti-rabbit IgG secondary antibody (outlined in red). Indicating the presence of surface exposed FhGST-S1 across all strains of *F. hepatica* EVs evaluated.

In addition there remains the strong probability that ruptured EV content and segments of lumen remain in the sample solution following the differential centrifugation process of isolating EVs from culture media. The resulting free protein present within the sample solution and a possibility that the wash process may not be effective in completely removing unbound secondary gold labeled antibody, may go some way to explain the small number of background tags that were observed in almost all immuno-gold labeling experiments. During the course of immuno-labeling development biological replicates were in triplicate and technical replicates exceeded five.

4.4.3.3 Specific *Fasciola hepatica* strains tested against α & β tubulins

All three strains of *F. hepatica* EVs (Aber, Miskin and Italian) were incubated with rabbit raised anti α & β tubulin primary antibody followed by anti-rabbit IgG with a colloidal gold tag attached in the method of Théry *et al.* The SOP is presented in the appendix. Experiments were conducted using anti-rabbit IgG with a colloidal gold tag of both 15nm and 5nm diameter. As had been seen previously in the TEM micro-graphs using FhGST-S1 the 15nm gold tags were more

easily visualized. However by contrast, in the case of α & β tubulin primary antibody the large number of instances of association made the use of 5nm tags more readily visible on a high percentage of EVs.

The presence of tubulin protein was observed in the Western blot result, indicating that this protein is present somewhere within the whole *F. hepatica* EV content. As can be seen (Figure 4.6) Aber, Italian and Miskin strain *F. hepatica* EVs incubated using anti-α & β tubulins all show a substantial number of interactions on a high percentage of EVs (Table 4.5). Thus indicating that a substantial number of α & β tubulin proteins are exposed on the surface of *F. hepatica* EVs in a way that is receptive to an anti-α & β tubulin antibody. This finding combined with it's high incidence of AAI offers itself as a potential positive control for a model AAI system of detection using the AIE.

TABLE 4.5: The binding incidence for anti- α & β tubulin immunolabeled antibodies by *F. hepatica* EVs: n = number of EVs counted, $\bar{X}$ = mean, SD = standard deviation, t = t-test (distribution from null), p = p-value (significance level).

	Immuno-gold label binding incidence	
	Control	**Anti-α & β tubulin**
n	112	173
$\bar{X}$	0.0268	1.0462
SD	0.1615	1.2894
t		9.657
p		0.00001
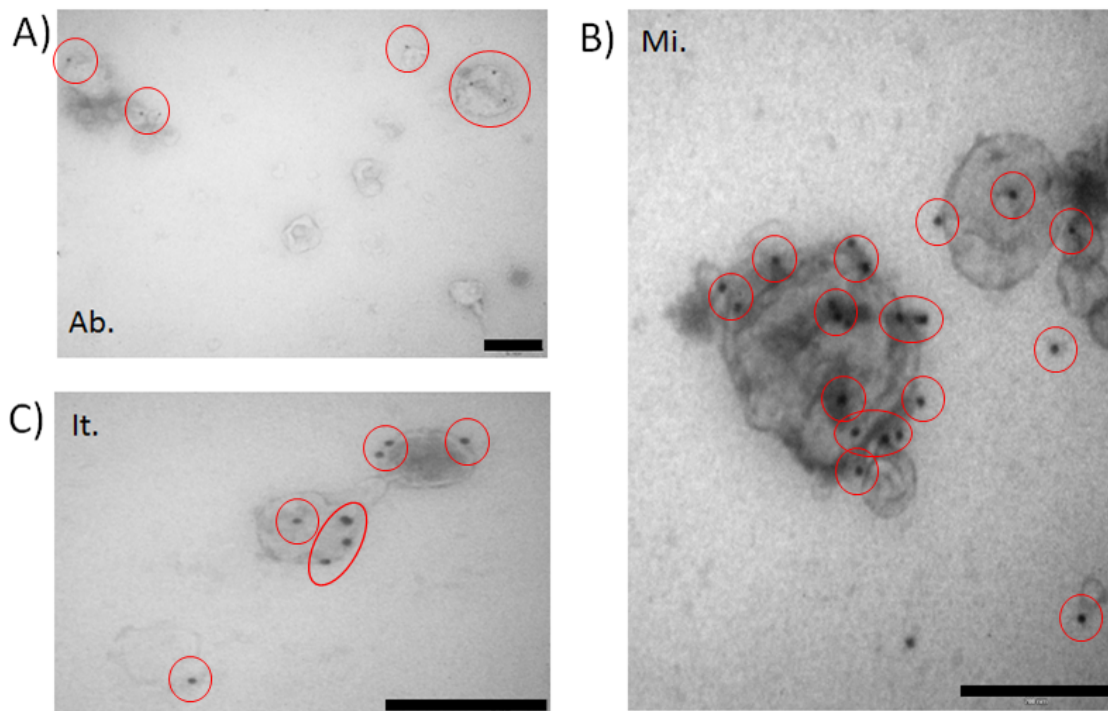
FIGURE 4.6: Representative TEM micro-graphs of labeled *F. hepatica* EVs; A) Aber strain, B) Miskin strain and C) Italian strain, labeled with rabbit raised anti-*α* and *β* tubulin primary antibody and a 15nm gold labeled anti-rabbit IgG secondary antibody. Images show the high incidence of AAI Scale bars 200nm.

4.4.3.4 Specific *F. hepatica* strain EVs, anti-FhCat-L1 and anti-FhFABP-V

Both anti-FhCat-L1 and anti-FhFABP-V are seen as reactive in the Western blot result, which indicates that these proteins are present somewhere within whole *F. hepatica* EV content. To identify if these proteins are surface exposed in a way that makes them receptive to antibody binding specific *F. hepatica* strains (Aber, Miskin and Italian) were incubated with rabbit raised anti-FhCat-L1 and anti-FhFABP-V primary antibody (as used in the Western blot experiment) followed by gold labeled anti-rabbit IgG secondary antibody (Figure 4.7).

TEM observations showed no significant numbers of gold labels clustering around EVs (Table 4.6). However, tags were visible as a random distribution in very small numbers in the background. What is important to state is that the images included here (Figure 4.7) represent the highest observed gold labels seen within TEM micro-graphs when subject to anti-FhCat-L1 or anti-FhFABP-V.

TABLE 4.6: The binding incidence for a-Cat-L1, a-FABP-V and a-TGR immuno-labeled antibodies by *F. hepatica* EVs: n = number of EVs counted, $\bar{X}$ = mean, SD = standard deviation, t = t-test (distribution from null), p = p-value (significance level)

	Immuno-gold label binding incidence			
	Control	**a-FhCat-L1**	**a-FABP-V**	**a-TGR**
n	112	141	155	123
$\bar{X}$	0.0268	0.0354	0.0322	0.0163
SD	0.1615	0.1849	0.1767	0.1265
t		0.4519	0.3076	-0.5658
p		0.3258	0.3793	0.2860

A)

B)
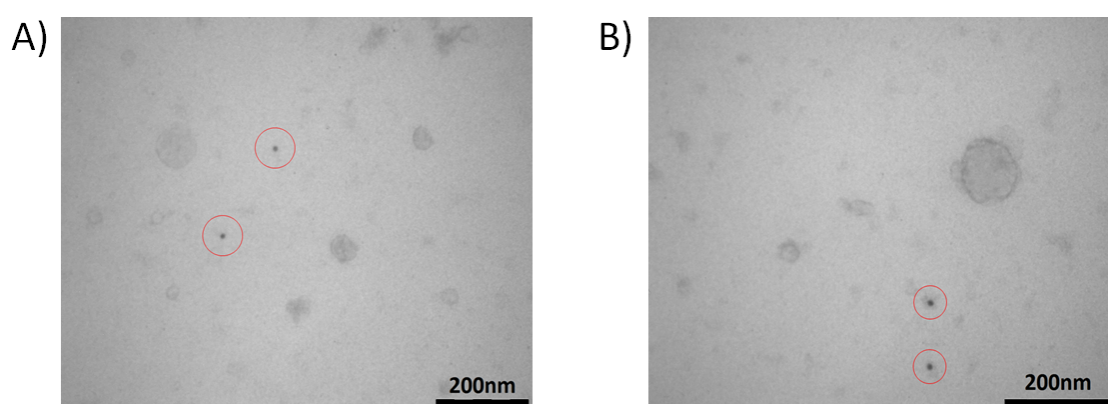
FIGURE 4.7: Presenting example TEM micro-graphs of anti-FhCatL1 and anti-FhFABP-V labeled *F. hepatica* EVs; A) Aber strain tested against anti-FhCat-L1. B) Miskin strain tested against anti-FhFABP-V. Both incubated with a rabbit raised primary antibody and then exposed to 15nm gold labeled anti-rabbit IgG secondary antibody. Images show the low incidence of AAI. Scale bars are 200nm as indicated.

4.4.3.5 Pre and post trypsin shave EVs

Dr. Stuart optimized the EV shaving process, where an exposure of EVs to trypsin in a 50μg/ml concentration at 37°C for 20 min was seen to provide a sufficient amount of cleaved peptides for reliable MS analysis whilst still leaving the EVs intact and of a typical morphology when viewed by TEM (Figure 4.8). MS data analysis indicated a total of 97 proteins for Aber, 135 for italian and 141 Miskin strains identified above significance (>30 occurrences) across three biological replicates in the shaved EV supernatant. From these 79 were common across all three strains with α tubulin occurring in the top 16 and FhGST-S1 identified within the

top 36 most abundant.
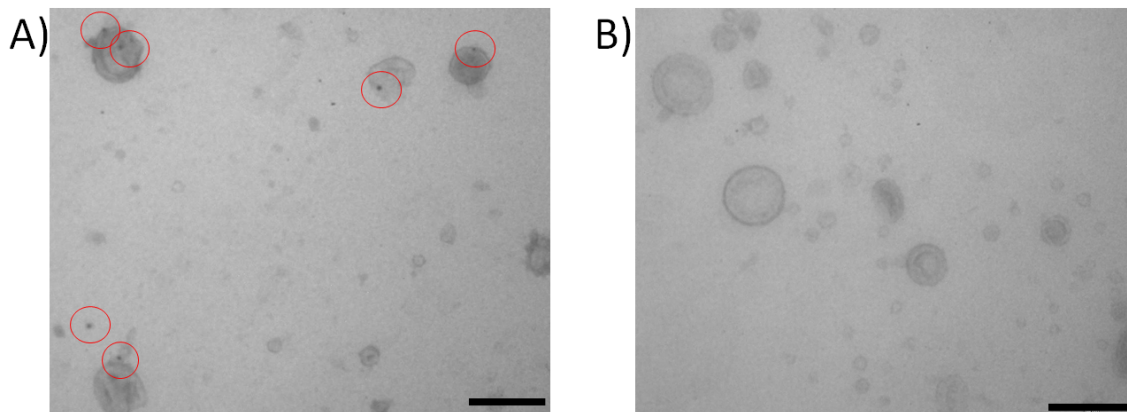
FIGURE 4.8: TEM micro-graphs of EVs pre and post trypsin shaving of surface exposed peptides; A) Miskin strain pre shave, incubated with rabbit raised anti-FhGST-S1 primary antibody and 15nm gold labeled anti-rabbit IgG secondary antibody (outlined in red). B) Miskin strain post shave, incubated with rabbit raised anti-FhGST-S1 primary antibody and 15nm gold labeled anti-rabbit IgG secondary antibody. Images indicate the consistency of EV integrity, morphology and lack of labeling post shave. Scale bars 200nm

To further investigate the surface exposed proteins post shave, trypsin shaved EVs were incubated with anti-FhGST-S1 primary and gold labeled rabbit IgG secondary as before. However, unlike whole EVs which had around 57% incidence of gold labeling, shaved EVs showed almost no gold labels in close proximity to the EVs (Table 4.7 and Figure 4.9).

TABLE 4.7: The binding incidence for anti-FhGST-S1 immuno-labeled antibodies by *F. hepatica* EVs pre & post shave: n = number of EVs counted, $\bar{X}$ = mean, SD = standard deviation, t = t-test (distribution from null), p = p-value (significance level)

Immuno-gold label binding incidence (anti-FhGST-S1)			
	Control	**Pre shave**	**Post shave**
n	112	572	105
$\bar{X}$	0.0268	0.5719	0.0381
SD	0.1615	0.6420	0.1914
t		9.498	-0.5327
p		0.00001	0.2973
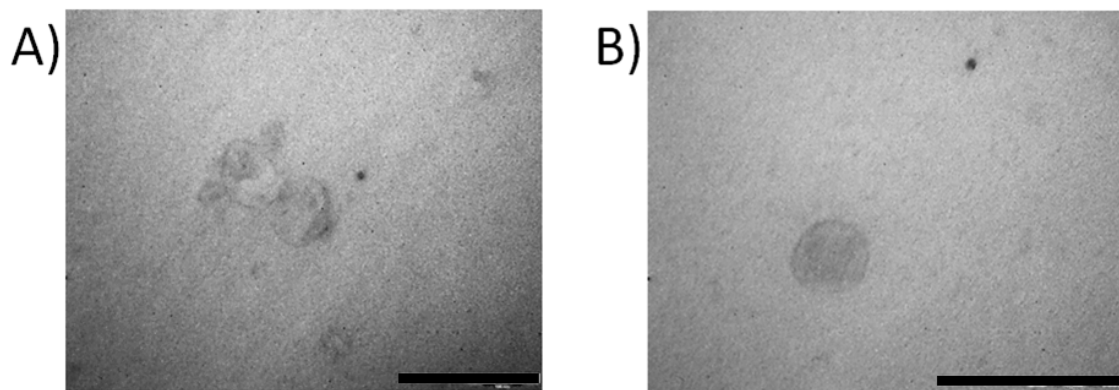
FIGURE 4.9: Representative example TEM micro-graphs of shaved Italian strain *F. hepatica* EVs; Subject to immuno-gold labeling by incubation with rabbit raised anti-FhGST-S1 primary antibody then 5nm gold labeled anti-rabbit IgG secondary antibody. In almost all cased no gold labels were seen, images shown here represent the only incidence of gold labels seen within the TEM micro-graphs. Scale bars 200nm

4.4.3.6 Faecal EV detection

To evaluate the possibility of detecting *F. hepatica* specific EVs in an infected hosts faecal sample using anti-FhGST-S1 as a positive bio-marker of infection, a series of simple tests were conducted. The aim of these tests were to isolate EVs from three faecal sample types. Firstly, *F. hepatica* free ovine faeces, secondly, *F. hepatica* free ovine faeces that were spiked with a known quantity of *F. hepatica* EVs and finally from an ovine faecal sample with a known *F. hepatica* infection.

Counts for the presence of gold labels were conducted as described in the methods (Section 4.4.3). The known *F. hepatica* negative sample was compared to the negative control used in all other counts. While both the *F. hepatica* EV spiked and *F. hepatica* EV known positive infection samples, were compared to the *F. hepatica* negative sample (Table 4.8).

The aim of the first experiment was to confirm that using anti-FhGST-S1 immuno-gold labeling on a known *F. hepatica* infection free faecal sample would not produce a false positive result. A sample was prepared as described in the methods section, comprising a group of known uninfected (egg negative) faecal samples pooled into a volume typical of a faecal collection of 10 grams. EVs were isolated

TABLE 4.8: The binding incidence for anti-FhGST-S1 immuno-labeled antibodies by *F. hepatica* faecal EVs: n = number of EVs counted, $\bar{X}$ = mean, SD = standard deviation, t = t-test (distribution from null), p = p-value (significance level)

	Control	Fh Negative	Fh Spiked	Fh Positive
Immuno-gold label binding incidence				
n	112	104	119	118
$\bar{X}$	0.0268	0.0481	0.1008	0.2034
SD	0.1615	0.2139	0.3011	0.4231
t		-0.9264	1.4819	3.3669
p		0.1776	0.0699	0.00045

from the sample in a manner already described earlier (Section 3.3.2). Isolated EVs were adsorbed onto TEM grids and incubated with rabbit raised anti-FhGST-S1 primary antibody followed by gold labeled anti rabbit IgG secondary as described earlier (Section 4.4.3). TEM grids were then contrast stained and imaged as described previously (Section 4.3.1). In all *F. hepatica* negative cases the number of gold labels observed on any TEM grid was low. Typically no gold labels were seen in, on or around any isolated EVs and the images included here represent examples of the maximum extent of observation (Figure 4.10).

FIGURE 4.10: Representative TEM images of EVs isolated from an uninfected (egg negative) host faecal sample; incubated with rabbit raised anti-FhGST-S1 primary then immuno-gold labeled (5nm) anti rabbit IgG secondary. This negative control is confirmed by the very low occurrence of gold tags (outlined in red) suggesting a lack of FhGST-S1 proteins both on the surface of EVs or as a free protein. Images shown represent the maximum incidence of gold tags seen. Scale bars 200nm

The second experiment sought to establish if it was possible to detect the presence of *F. hepatica* EVs which have been deliberately added to an uninfected (egg negative) hosts faecal sample. The object being that by homogenizing a faecal sample and subjecting it to DC, would the isolated EVs retain sufficient quality and quantity to be identifiable by immuno-gold labeling as presented earlier (Section 4.4.3.2).

The spiked sample was prepared as described in the methods (Section 4.3.4.2 and EVs isolated in a manner already described (Section 3.3.2). EVs were adsorbed onto TEM grids and incubated with rabbit raised anti-FhGST-S1 primary antibody followed by gold labeled anti-rabbit IgG secondary as described (Section 4.4.3). TEM grids were then contrast stained and imaged as described previously (Section 4.3.1). A small number of gold labels were seen in close proximity to EVs (Figure 4.11), however this was not statistically significant (Table 4.8).
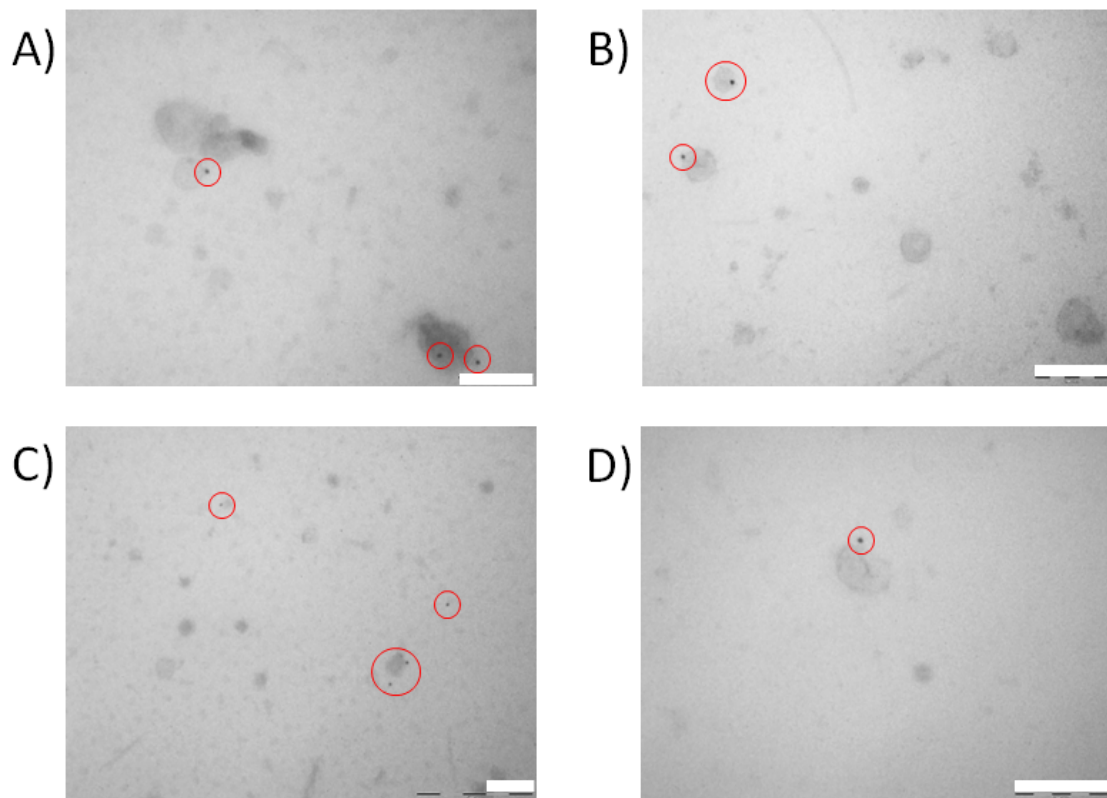
FIGURE 4.11: Representative TEM images for EVs isolated from *F. hepatica* negative ovine faeces spiked with *F. hepatica* EVs; incubated with rabbit raised anti-FhGST-S1 primary then gold labeled (15nm) anti rabbit IgG secondary.

Given encouragement from the first two results on *F. hepatica* negative EVs and spiked EVs the object of the third sample was to establish if it is in fact possible to detect the presence of *F. hepatica* EVs in naturally infected host faecal samples. The wild sourced sample was prepared as described in the methods (Section 4.3.4.2) and EVs isolated via DC as described earlier (Section 3.3.2). EVs were adsorbed onto TEM grids and incubated with rabbit raised anti-FhGST-S1 primary antibody followed by gold labeled anti rabbit IgG secondary as described (Section 4.4.3). TEM grids were then contrast stained and imaged (Section 4.3.1). It was observed (Figure 4.12) that a significant number of gold tags were in close proximity to EVs isolated from the sample and also present in the background. A specific quantified count as per the anti-FhGST-S1 test on cultured *F. hepatica* EVs (Section 4.4.3.2) is given (Table 4.8).
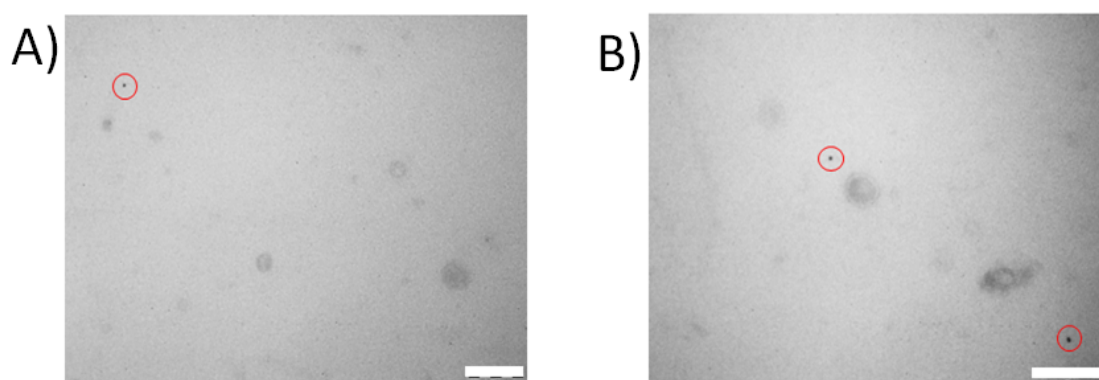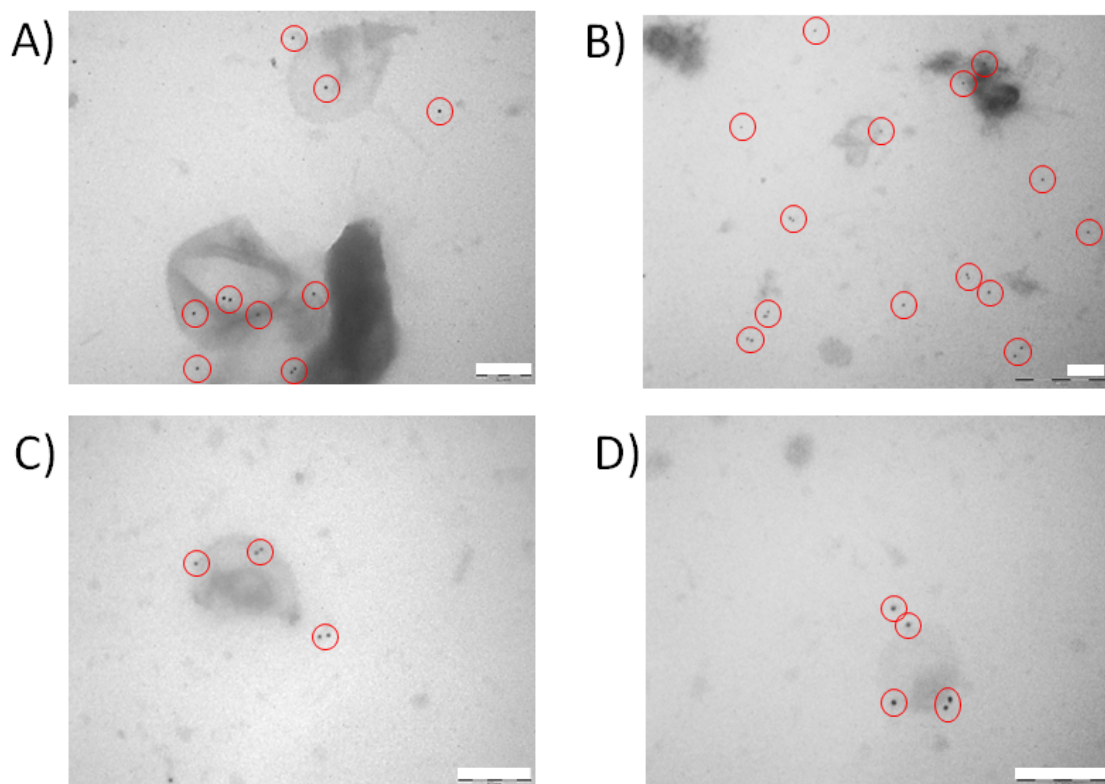

FIGURE 4.12: Representative TEM images of EVs isolated from an egg positive host; incubated with rabbit raised anti-FhGST-S1 primary then gold labeled (15nm) anti rabbit IgG secondary. Gold tags indicating the presence of FhGST-S1 on the surface of some EVs and as free protein in the background (outlined in red). Scale bars 200nm.

4.5 Discussion

4.5.1 TEM observation of EVs

The MISEV2018 guidelines for characterization of EVs recommends that two different but complementary techniques are used to provide images of single EVs at high resolution such as TEM and AFM [136]. With both close up and wide field images to be provided. In seeking to comply with the requirements it was clear that improvements on the existing methods of TEM visualization methods were needed.

Following developments in EV isolation from *F. hepatica* culture media via DC, as described in Chapter 3, a significant amount of material that was seen to previously contaminate TEM grids, obscuring detailed observation of EVs was removed from the final purified solution. Contrast staining of EVs adsorbed for visualization onto TEM grids was initially performed to the existing AU lab protocol of Nowacki *et al.*, which had been developed and used for *Schistosoma mansoni* EVs. By this method there was a considerable variation in contrast over the whole grid, producing a dark background to such an extent that observation and analysis of immuno-gold labeling was severely compromised. A second concern came with the lack of long term stability of the EVs on the TEM grids once prepared. It was necessary to complete all imaging within 48 hours otherwise significant degradation of the EVs was seen. Despite these drawbacks, for a qualitative assessment of EVs the Nowacki method had some merit, mainly from being quick and simple to execute.

For detailed and consistent observations of *F. hepatica* EVs the protocol of Théry *et al.* proved superior in almost all respects, with a TEM image clarity and contrast that allowed for the easy identification of immuno-gold labeling tags. The addition of a final layer of methyl-cellulose encapsulates the EVs on the TEM grid and maintains their integrity for a period which, in the words of Théry extends to several years.

Rikkert *et al.* have recently presented a comparison of nine EV contrast staining methods and reviewed four in detail, to evaluate operator led bias in evaluation of EV quality and quantity [226]. One of the recommended methods is very similar to the Nowacki stain protocol and non are as extensive and time consuming as the Théry protocol. Future work would involve a quantitative assessment of the other methods recommended by Rikkert *et al.* to compare and contrast with that of Théry *et al.* for the observation of *F. hepatica* and other EVs. During the course of this study, work on EVs from parasites such as *Schistosoma mansoni, Calicophoron daubneyi* and *Anoplocephala perfoliata* have highlighted the need to adjust protocols to suit the particular subject, with EVs from *Schistosoma mansoni* proving particularly difficult to image clearly by the Théry protocol.

4.5.2 Identification of suitable antibodies

The work of Cwiklinski *et al* and Dr. Stuart has identified 79 proteins as being exposed in part on the surface of *F. hepatica* EVs, all of which have potential as candidates for use in a AAI bio-sensor. It has been shown that several of these proteins released by *F. hepatica* have the ability to influence the host immune cells [215]. Some of these proteins have been identified as suppressing the hosts natural inflammatory response and have been seen to be packaged within EVs released by *F. hepatica*, these include, FhCat-L1, FhFABP and FhGST-S1 [7]. The result of Western blotting has reaffirmed that α & β tubulin, FhCat-L1, FhFABP and FhGST-S1 are all present within lysed *F. hepatica* EVs. Interestingly an unexpected response to TGR was seen and only a very faint recognition of FhCat-L1 which both warrant further investigation.

From the point of view of this study, a key result of the work by Dr. Stuart was the discovery of FhGST-S1 as one of the proteins which is present on the surface of *F. hepatica* EVs. This particular protein found in *F. hepatica* and *F. gigantica* offers itself as a key bio-marker of infection and a potential vaccine candidate [6], [227].

4.5.3 Immuno-gold labeling to qualify antibody choice

Western blotting has confirmed the presence of proteins, within *F. hepatica* EVs, using *F. hepatica* specific antibodies. The mass spectrometry results of Dr. Stuart and Cwiklinski *et al.* indicate that some of these proteins, such as α and β tubulin, FhCatL1, FhFABP and FhGST-S1 are exposed on the surface of *F. hepatica* EVs. This raises the question of whether the proteins are exposed in a way in which antibodies can interact with a binding affinity. Thereby increasing the potential of using these antibodies as part of an AAI process to capture *F. hepatica* EVs in a way that can be detected by the AIE.

4.5.3.1 Immuno-gold labeling; tubulin

The response to incubation with anti-α & β tubulin across all strains was very high with almost all EVs seen to have gold tags on or in very close proximity ($\bar{X}$ = 1.046, SD = 1.289) a significant increase compared to the control (t(173) = 9.657, p = 0.00001). This immuno-gold labeling result is in contrast to Cwiklinski's MS analysis, where tubulins fail to reach the top 50 most abundant identified proteins.

The presence of antibody binding tubulin protein on the surface of *F. hepatica* EVs, while not being a specific bio-marker of infection, would prove useful for deployment as a positive control in a bio-sensor application, due to its presence in typical host EVs [10], [127]. However, alternative positive control antibodies for future investigation could include other cytoskeletal proteins such as, tetraspannin-CD63 or heat shock protein-70 (HSP-70), which are commonly associated with mammalian EVs [228], [229]

4.5.3.2 Immuno-gold labeling; Cat-L1, FABP-V

Despite mass spectrometry results of shaved *F. hepatica* EVs indicating the presence of both FhCat-L1 and FhFABP-V proteins as being surface exposed, by both

Dr. Stuart and Cwiklinski *et al.*[7], TEM observations of immuno-gold labeling using anti-FhCat-L1 ($\bar{X}$ = 0.035, SD = 0.185) did not indicate a statistical increase compared to the control (t(141) = 0.452, p = 0.326). And anti-FhFABP-V ($\bar{X}$ = 0.032, SD = 0.177) also did not indicate any significant increase compared to the control (t(155) = 0.308, p = 0.379). This is something which may warrant further investigation given the somewhat contradictory finding of Cwicklinski *et al.*, who found significant immuno-gold labeling identification following incubation with anti-FhCat-L1 antibody. However, one possible explanation is that Cwiklinski's observations were made on cross section of EVs, which were present within cross sections of whole flukes embedded in agar resin and microtome cut into ultra thin sections. This apparent contradiction may be an indication that the protrusion of the FhCat-L1 protein through the EV lipid membrane is simply not one which presents the appropriate elements for antibody affinity binding.

4.5.3.3 Immuno-gold labeling; FhGST-S1

TEM observations of strain specific immuno-gold labeling of *F. hepatica* EVs using anti-FhGST-S1 antibody has indicated a significant incidence of binding which was approximately equal across all three tested strains ($\bar{X}$ = 0.572, SD = 0.642) when compared to a control (t(572) = 9.498, p = 0.00001) . The interaction of the anti-FhGST-S1 antibody offers a clear route to an EV capture based bio-marker of infection.

For the purposes of this study identifying surface exposed proteins on EVs by using an antibody that is a bio-marker of *F. hepatica* infection can support the construction of a bio-sensor of the style described earlier (Figure 1.15). Where antibodies supported on a substrate can capture from solution EVs that are released from the infecting parasite into the hosts blood, urine or faeces for example. These specific AAI can then be observed by the AIE to see if detection of interaction is possible, with the longer term aim of developing a label free, real time, low cost

and high speed diagnostic test. The literature supports FhGST-S1 as being of importance in identifying the potential pathway to a vaccine or as bio-markers of infection [6], [8], [108], [115].

4.5.4 *Fasciola hepatica* EV shaving

Pre and post shave EVs are seen to have similar morphology under TEM, indicating that the process that was developed, cleaves surface exposed peptides without significant damage to the EV membrane, thereby minimizing the release of EV contents cargo. The immuno-gold labeling of shaved *F. hepatica* EVs using anti-FhGST-S1 antibodies ($\bar{X}$ = 0.038, SD = 0.191) produced no significant incidence of labeling compared to the control ($t(105)$ = -0.533, p = 0.297). This finding further supports the identification of FhGST-S1 and α & β tubulin as surface exposed and antibody receptive proteins on EVs released by *F. hepatica*. Additionally, shaved EVs subject to immuno-gold labeling qualitatively showed a reduction in the number of gold tags seen in the general background. This could possibly be explained by the additional centrifuge steps used to remove peptides for MS analysis, with the smaller peptides remaining suspended as a colloid within the supernatant, reducing the amount of free protein from the isolated EV pellet. Or alternatively, that the trypsin cleavage of proteins occurred to such an extent that any free protein was unable to affinity bind to the antibodies.

The idea that trypsin shaving, aimed at targeting EVs, also cleaves any free protein which has been co-isolated within the EV containing solution, into peptide fragments small enough to reduce antibody affinity binding, is not unreasonable. The implication being that a proportion of the background gold tags seen in immuno-gold labeling of whole EVs are not simply there from surviving the washing steps to remove unbound tags but are in fact affinity binding to free proteins within the sample solution.

Future work would seek to qualify the exact cause and quantify the extent

of this issue and may be of benefit in understanding the extent to which a bio-marker such as FhGST-S1 is available within a host.

4.5.5   Faecal EV evaluation

The results of TEM immuno-gold labeling of EVs isolated from faecal collection, has provided an indication that EVs can be isolated from faecal materials. *F. hepatica* free faecal EVs were statistically similar ($\bar{X} = 0.048$, SD $= 0.214$) to the negative control (t(104) $= -0.926$, p $= 0.178$). The sample spiked with *F. hepatica* was also not found to be statistically different ($\bar{X} = 0.101$, SD $= 0.301$) to the negative faecal sample (t(119) $= 1.482$, p $= 0.069$). However, it was close and this may simply be a function of not having added sufficient EVs to the experimental sample to generate a sufficient level of significance. Wild sourced *F. hepatica* positive faecal sample was seen to have a highly significant number of immuno-gold labeling incidence ($\bar{X} = 0.203$, SD $= 0.423$) when compared to the *F. hepatica* negative faecal sample (t(118) $= 3.367$, p $= 0.00045$).

Significantly, this indicates that the EVs of *F. hepatica* can be differentiated from those of the host using anti-FhGST-S1 antibody. The long term implication of this means the possibility of using *F. hepatica* EVs easily recovered from a host faecal sample as a bio-marker of infection and potentially using the AIE to observe AAI as a label free, highly specific diagnostic.

4.5.6   Implications for AIE

The investigations within this chapter demonstrate the previously unseen evidence that the protein FhGST-S1 and α & β tubulins are present on the surface of EVs isolated from the excretory and secretory products of *F. hepatica* and are exposed in a way that is receptive to the binding of anti-FhGST-S1 and anti-tubulin antibodies. There's some preliminary evidence that both *F. hepatica* EVs and FhGST-S1 protein may survive into the host faeces. This has been observed

physically in this study and is supported technically by crystallographic study of the FhGST-S1 protein structure [118]. On that basis a trial bio-sensor could be constructed using the proteins identified in this study as a model AAI for evaluation using the AIE. The bio-sensor could have an α & β tubulin positive control spot which will detect host EVs (and tubulin) along with an anti-FhGST-S1 spot which would detect a positive *F. hepatica* infection.

What has been established is a suitable model AAI system using anti-FhGST-S1 which could be printed onto a suitable substrate using the printing techniques identified in Chapter 3, probed with EV analyte solutions and then observed using the AIE to detect AAIs.

Chapter 5

AIE observations of AAI

5.1 Outline of chapter general aims

This chapter presents the combination of all the previous developments made during this thesis to date. The introduction briefly recaps the process development stages that have led to the fabrication of a bio-sensor using a model AAI system selected from the helminth parasite *F. hepatica*. Following the introduction a description of the methods used to fabricate the protein array and optimize the AIE observations are documented. Examples of AAI as observed with the AIE are demonstrated following the application of an analyte solution containing protein or EVs specific to *F. hepatica*.

5.2 Introduction to AIE observation of AAI

This current work has has focused on two key themes; firstly the development of the AIE to optically detect AAIs and secondly the selection of appropriate model protein(s) that can be used to confirm the effectiveness of the AIE in achieving the first aim. Therefore, this chapter describes the culmination of these two themes, combined with the process development steps that have enabled the fabrication of a first generation protein micro-array to present proteins in a way that maximizes the novel approach of the AIE for observation of AAI in a reliable and informative way.

As a key protein for *F. hepatica*, FhGST-S1 has been identified as being present on the surface of EVs released by *F. hepatica* (Chapter 4). In addition the literature confirms FhGST-S1 as a significant excretory/secretory product produced by this parasitic helminth, with an important recognized role in modulating the host immune response to infection [6], [108], [114], [117]. Such modulation, likely not solely attributed to FhGST-S1, promotes the survival and longevity of the infection. Therefore, the observation of, and improved characterization of FhGST-S1 AAIs using a recombinant or native protein or whole intact EVs expressing FhGST-S1 at their surface as an analyte would likely produce potential benefits in the areas of disease diagnostics and chemotheraputic advances.

To observe the FhGST-S1 AAI, production of a protein micro-array has been achieved using the robot spotting process, fabricated following the research and developments that are described in Chapter 3. This fabrication method presents anti-FhGST-S1 antibody on a solid substrate, ready for combination with analyte solutions and was developed on previously established methods [67]. The protein micro-array approach, in conjunction with the AIE therefore presents the proteins as a bio-sensor which can be observed and measured at high speed, label free, with the further advantages of high spatial resolution and ease of use.

To further improve observation of AAIs in general, the optimization of the AIE setup parameters must be considered, with attention given to maximizing the measured differences between the pre and post analyte observations. In order to achieve the optimized AIE setup, the AIE must be applied to model AAI, in this case FhGST-S1.

To evaluate the AAI film thickness directly from AIE calculation of ellipsometric parameters, consideration was given to constructing a comparison model. The refractive index of SiO_2 at the AIE observation wavelength of 532nm is 1.46 [230], similarly the refractive index of thin protein layers is described in literature, as ranging from 1.35 to 1.6 [231], depending on the observation wavelength. The work of Arwin *et al.* states the refractive index of adsorbed protein layers to

be 1.5 [63], with Voros describing the refractive index to be 1.48 and having a clear dependence on molecule size [231]. This suggested that with similar optical properties a direct comparison could be made between SiO_2 and adsorbed protein thickness, as a coarse first approximation.

On a substrate such as silicon with a high refractive index, at an angle of incidence close to the pseudo- Brewster angle the elipsometric phase angle Δ is very sensitive to changes in refractive index and thickness change, while the amplitude Ψ is considered to be almost independent of the layer parameters [71].

Therefore, the experiments presented in this chapter aimed to monitor the FhGST-S1/antibody AAI using an optimized AIE setup on a silicon based protein microarray.

5.3 Materials and methods

5.3.1 Bio-sensor silicon substrate preparation

The bio-sensor for visualization using the AIE was prepared onto silicon chip substrates, cleaned using the RCA-1 process [180] and prepared for covalent linking of antibodies by the method of Wang and Jin [73], described earlier in full (Section 3.2.3.1). Briefly this covalent linking involved immersion of the silicon chip in APTES 5% v/v dH_2O and 90% v/v ethanol, immediately followed by reaction with 2.5% v/v glutaraldehyde in PBS.

5.3.2 Bio-sensor antibody capture preparation

Post glutaraldehyde activation of the silicon chip a polyclonal anti-FhGST-S1 antibody [6] diluted at 1:50 with PBS (0.05mg/ml) was applied in solution to the prepared silicon chip surface.

5.3.3 Protein and EV analyte solutions

Analyte solutions of recombinant FhGST-S1 protein were supplied by Cutress *et al.* [118] and prepared at 0.2mg/ml in PBS. *F. hepatica* EV analyte solutions were prepared as described earlier (Section 4.3.4), at a concentration 0.4mg/ml in PBS.

5.3.4 Protein micro-array fabrication

Following RCA-1 cleaning and immersion in APTES to silanize the SiO_2 surface, the next stages in fabrication of a protein array were completed using the robot contact printer (Chapter 3), to deliver consistent spot on spot positioning of the protein array solutions.

The arrays were prepared as four rows of four spots, giving a total of sixteen elements (Figure 5.1). Glutaraldehyde was applied to the silanized silicon chip surface as a deposited volume of $0.17\mu l$ producing target spot diameter of 1.2mm. Following washing with dH_2O, polyclonal anti-FhGST-S1 antibodies were then applied in solution to the silicon chip surface at a deposited volume of $0.33\mu l$ again producing a bio-sensor spot of 1.2mm diameter positioned over the previously prepared glutaraldehyde spot. Full details of the process are described previously (Section 3.5.6).
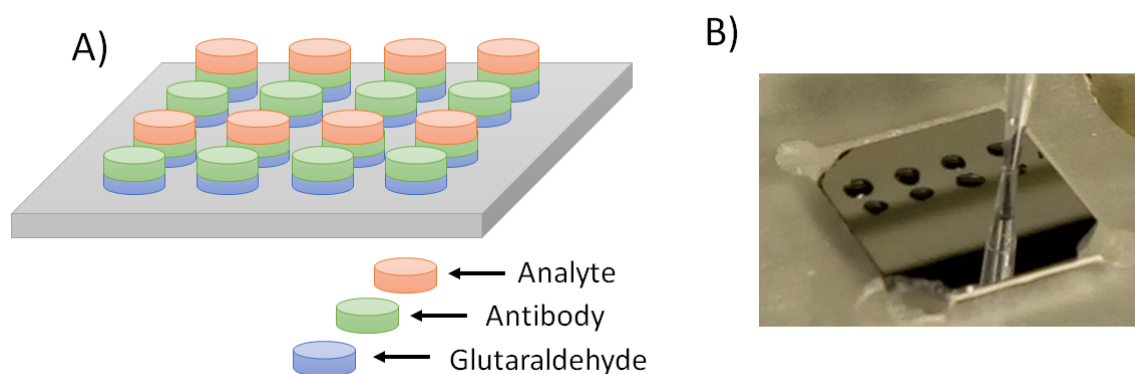

FIGURE 5.1: Presenting the proposed protein array; A) Schematic representation of the protein array assembly, indicating the protein array 4 by 4 layout with all 16 spots incubated with antibody (anti-FhGST-S1) and then 8 subject to analyte solutions (rFhGST-S1 or whole, intact *F. hepatica* EVs) to test for changes in thickness representing the AAI. B) An image of the process in operation.

5.3.5 AIE optimization of settings for AAI analysis

A series of parameter changes were investigated to optimize the AIE for AAI observations. A silicon chip was cleaned and prepared with a covalently linked anti-FhGST-S1 antibody spot, as described earlier (Section 5.3.4), allowing observation of both the antibody layer and supporting substrate surface. The observation angle of incidence was varied between 35 and 80 degrees in 1 degree increments. For each angle of incidence the analyzer angle was varied from 25 to 70 degrees, incident flux onto the sample was kept constant. The camera shutter and gain were adjusted as required in each case, to make full use of the camera dynamic range and thus maximize system sensitivity. AIE ellipsograms were collected for each parameter setting and values recorded for the measured difference between substrate and antibody layer, for both Ψ and Δ. The number of data points for the radiometric calculation of Ψ and Δ was determined by the number of polarization and retardation steps applied to the input light source by the Meadowlark unit. For consistency, the number of steps was set at 25 for all measurements.

5.3.6 Protein film thickness evaluation

The thickness of a series of thermally grown SiO_2 layers over a crystalline silicon substrate were measured using a Sopra GESP-5 spectroscopic ellipsometer (Chapter 2 Section 2.3.1.1). The SiO_2 layers were then evaluated using the AIE at settings optimized for AAI observations. Lines of interest were selected across the surface at randomized locations and the profile of Δ values extracted to Excel where the mean and standard deviations for each SiO_2 layer were calculated. A plot of Δ values against SiO_2 layer thickness was regressed to generate a comparative model. For each stage of the protein micro-array fabrication and incubation of analyte solutions, AIE measurement of Δ values were compared to the model and an estimate of adsorbed layer thickness was calculated.

5.4 Results

5.4.1 AIE setup optimization

A series of parameter changes were investigated to optimize the AIE set up conditions for AAI observations. The angle of incidence has significant influence on the absolute values of Ψ and Δ (as was presented in Figure 2.15), with particular sensitivity for change in Δ around the pseudo-Brewster angle, which for a 4nm SiO_2 overlayer with a refractive index of n=1.46 at 532nm [230] is 76.1 degrees [232]. Single degree increments were made in the angle of incidence and at each step single degree adjustment of the analyzer angle from 35° to 55° were made to improve signal to noise ratio as proposed by Cohn *et al.* [145]. A small extract centered around the optimum (highlighted in blue) is presented (Table 5.1). For the specific application of this thesis the optimized settings were observed to be at 70° incident angle and 40° analyzer angle. Therefore, all AAI observations subsequently reported here were recorded at these settings.

TABLE 5.1: Summary of data indicating the Psi and Delta measured difference; between the silicon substrate surface and a covalently attached anti-FhGST-S1 antibody layer, in degrees. All measurements taken at single degree increments, with the same incident light flux, adjustments to shutter speed and camera gain were made to give full use of the camera dynamic range.

Incidence Angle (deg)	Analyzer Angle (degrees)									
	35		40		45		50		55	
	Δ	Ψ	Δ	Ψ	Δ	Ψ	Δ	Ψ	Δ	Ψ
60	2.5	0.4	3.0	0.4	3.0	0.5	3.0	0.5	2.5	0.7
65	4.0	0.6	4.0	0.8	3.5	0.8	7.0	0.8	6.0	0.8
70	4.0	0.8	**8.0**	**1.2**	7.5	1.2	6.0	1.1	6.0	1.2
75	3.5	0.6	4.0	1.0	4.0	0.8	4.5	0.8	5.0	0.6

5.4.2 Protein layer thickness estimation

To approximate protein film thickness from the ellipsometric parameter Δ a simple comparison was made to the Δ values obtained for a series of thermally grown

SiO$_2$ layers over a crystalline silicon substrate (Figure 5.2 A). SiO$_2$ layers were selected to span the anticipated range observed by the AIE for AAIs. Plotting Δ values obtained by the AIE against the known SiO$_2$ layer thickness, produced a series of data points that were regressed to provide a comparative model, which had an R^2 value of 0.996 (Figure 5.2 B).

For each stage of the protein micro-array fabrication process and incubation with analyte solutions, the AIE measurement of Δ values were compared to the model and an evaluation of adsorbed layer thickness was calculated (Table 5.2).
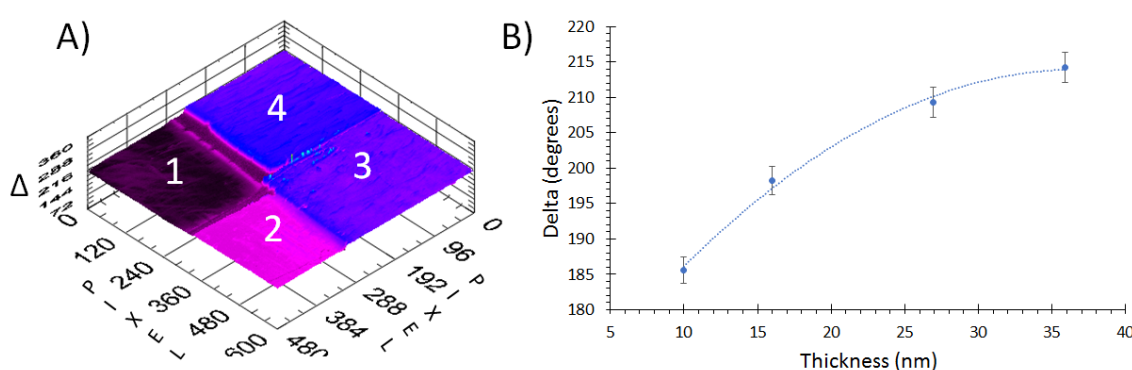
FIGURE 5.2: Presenting the development of a protein film thickness model; based on the AIE Δ values obtained for known thickness SiO$_2$ layers. A) Representative AIE ellipsogram indicating Δ values for a series of thermally grown SiO$_2$ layers. 1) 10.0 nm 2) 16.0 nm 3) 26.9 nm 4) 35.9 nm the thicknesses were determined by spectroscopic ellipsometry. B) Plotting Δ values obtained by the AIE against the known SiO$_2$ layer thickness, regressed to produce a comparative model. R^2 = 0.9957

5.4.3 Bio-sensor exposure to analyte solutions

Given the low signal to noise from analyzing silicon substrate chips with a 4nm overlayer of native SiO$_2$ it was now key to evaluate the AIE with analyte solutions representing AAIs. Representative AIE ellipsograms (Figure 5.3) detail bio-sensors pre an post exposure to FhGST-S1 protein analyte solution. Post analyte incubation indicates a clear difference in the mean Δ values, identifying an increase in film thickness, generated by AAI binding affinity between the immobilized anti-FhGST-S1 antibody and FhGST-S1 protein drawn from the analyte

solution. The high spatial resolution of the AIE indicates increased changes at the spot edges.

FIGURE 5.3: Representative ellipsograms of a bio-sensor prepared with anti-FhGST-S1 antibody; A) 2D Δ values; 1) Post incubation with FhGST-S1 protein analyte. 2) Pre incubation, anti-FhGST-S1 antibody only. B) 2D Ψ values; 1) Post incubation with FhGST-S1 protein analyte. 2) Pre incubation, anti-FhGST-S1 antibody only. C) Plot of Δ values along the white line of interest in A.

After establishing observable differences between FhGST-S1 AAIs based on the recombinant protein, whole intact EVs were also assessed. AIE ellipsograms of bio-sensors pre an post *F. hepatica* EV analyte solution were recorded (Figure 5.4). There is a clear change in Δ measurements between the spots that have been subjected to an EV analyte solution and those that have not.
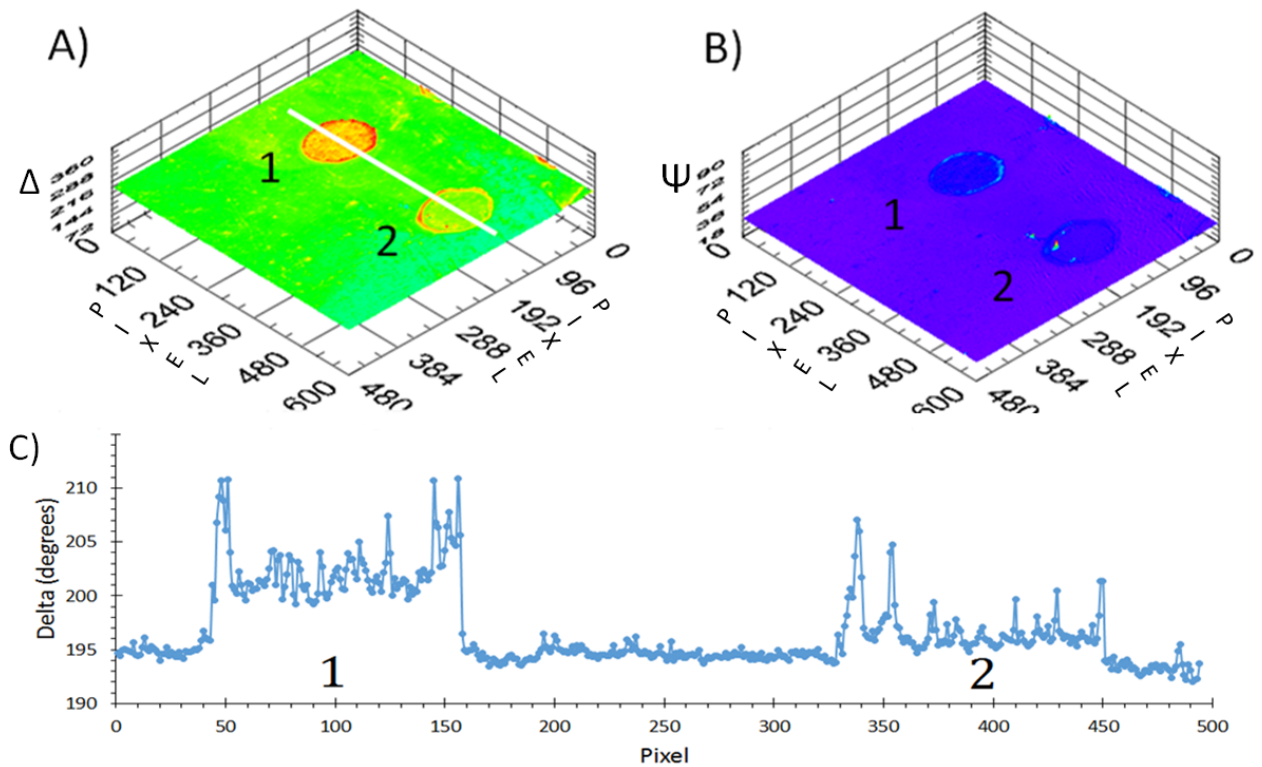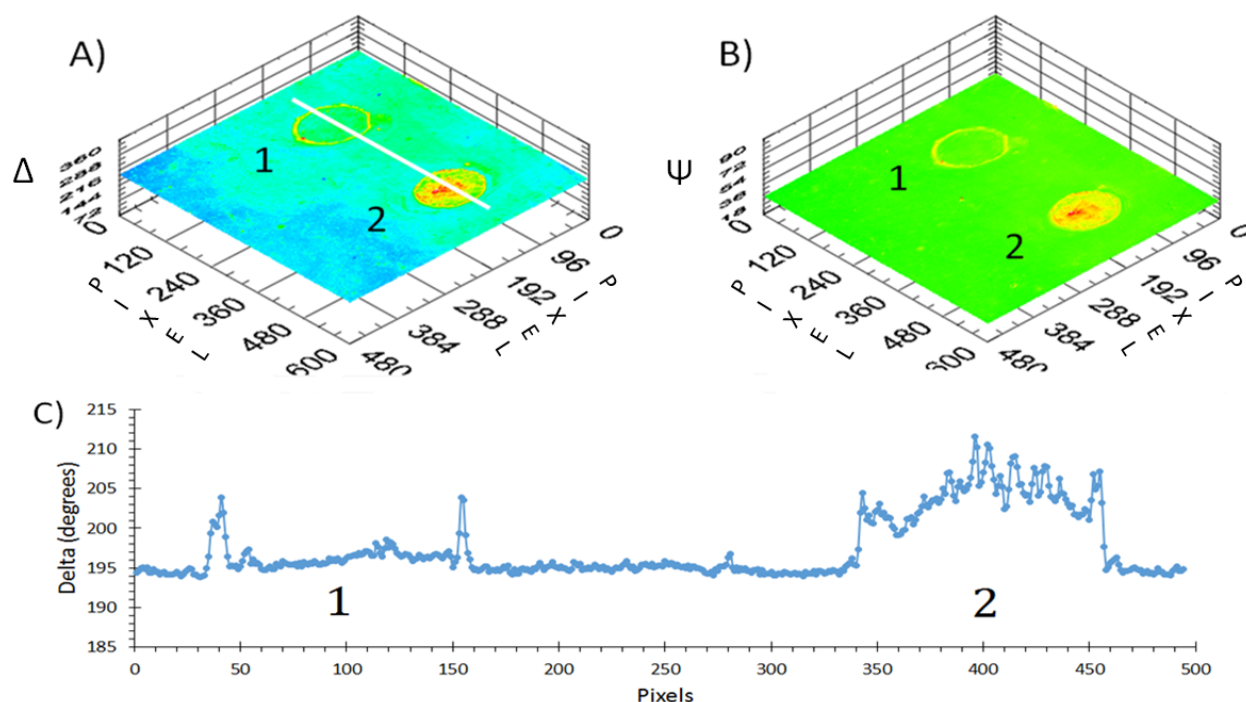
FIGURE 5.4: Representative ellipsograms of a bio-sensor prepared with anti-FhGST-S1 antibody: A) 2D Δ values; 1) Pre analyte incubation, anti-FhGST-S1 antibody only. 2) Post incubation with *F. hepatica* EV analyte. B) 2D Ψ values; 1) Pre incubation, anti-FhGST-S1 antibody only. 2) Post incubation with *F. hepatica* EV analyte. C) Plot of Δ values along the white line of interest in A.

The mean Ψ and Δ values measured over each of the bio-sensor surfaces as it is constructed (Table 5.2), were extracted from ellipsograms of the whole bio-sensor surface as data points through a line of interest passing across the protein spots laid down onto the silicon chip bio-sensor surface.

TABLE 5.2: The mean and standard deviation [SD] values for Ψ and Δ over the surface of the bio-sensor spots at each stage of fabrication; as indicated (n=12). Glu = Gluteraldehdye; a-FhGST-S1 = anti-FhGST-S1 antibody; FhEVs = whole intact EVs from in vitro culture of *F. hepatica*. nm = the estimated total film thickness.

	RCA1	APTES	Glu	a-FhGST-S1	FhGST-S1	FhEVs
Ψ	23.1 [0.05]	23.5 [0.07]	24.1 [0.05]	26.2 [0.68]	28.3 [0.87]	27.7 [1.02]
Δ	183.5 [0.18]	184.8 [0.26]	189.5 [0.19]	197.1 [2.03]	204.9 [2.53]	207.8 [3.57]
nm	8.8± 0.37	9.3±0.39	11.7±0.49	16.0±0.67	21.6±0.91	24.2±1.02

5.5 Discussion

5.5.1 The AIE optimized set Up

While the absolute calibration values for Ψ and Δ are seen to be in reasonable agreement with model values (Figure 2.17), it is the relative local values that are significant to the determination of AAIs. The key variables on optimizing the signal to noise ratio for AAI observation includes the angle of incidence, analyzer angle, shutter and camera gain [74], [145]. All of which were observed to influence the background noise level and the degree of separation observed between the supporting substrate and the protein overlayers. Once cleaned, the high purity crystalline silicon chips have been shown to have a very low surface roughness of just under 0.12nm (Section 3.4.3) making them ideal for use in determining the AIE system noise and resolution. Data of the individual pixel values over lines of interest across the silicon chip's surface as measured by the AIE produced base line values with standard deviation of 0.18 degrees for Δ which represents a 0.05% variance over the full dynamic measurement range of 360 degrees. Standard deviation for Ψ is 0.05 degrees which represents 0.055% variance over the full dynamic measurement range of 90 degrees (Section 2.4.2.1). This high SNR offers excellent opportunity to investigate other thin film AAI applications.

5.5.2 Pre and post analyte observations

Given that the AIE has been shown to have excellent sensitivity in calculating relative difference for both Ψ and Δ values, the aim was to assess monitoring of AAIs. The high spatial resolution of the AIE clearly identifies high levels of variation across the bio-sensor protein array both before and after analyte incubation (Figures 5.3 and 5.4). Pre analyte and in particular post analyte incubation, it can be observed that there are peaks at the periphery of the array spots with Δ values rising sharply by approximately eight degrees, which potentially indicates

that there is some significant buildup of material is occurring at the edges of the spot, a coffee ring effect [203]. However, despite the edge effects, what can be clearly observed for Δ angles is a progression of the mean value relative differences between each stage of the fabrication process and these are highlighted in Table 5.2. The standard deviation values presented in Table 5.2 were calculated to include the edge effect peaks. However, selecting out the edge effect and calculating data across the spot central area reduces the standard deviation values by approximately 10%. Further refinements of the array fabrication process to reduce delivered volumes and spot diameter by the use of smaller diameter pipette tips, could increase Marangoni flow within the droplet [203], and coupled to improved washing steps, may help to reduce the effects seen at the edges of the array spots. Despite this initial success it is clear that further investigation is required to fully optimise array production. This does however highlight the success of the AIE.

5.5.3 Estimation of protein film thickness

The estimation of over-layer film thicknesses start at just under 9nm for the RCA-1 cleaned silicon chip substrate and this is in good agreement with the value as determined by spectroscopic ellipsometry. Measurement of cleaned silicon substrate incubated with APTES increases layer thickness by an estimated 0.5nm which is less than the 2.0nm reported by others as a typical mono-layer thickness for silanes formed by this method [233], [234]. The addition of glutaraldehyde was estimated to increase the film layer to a total thickness of 11.7nm representing an increase of 1.4nm which is in good agreement with reports by Gunda *et al.* of 0.9($\pm$0.83)nm [233]. Immobilization of anti-FhGST-S1 to the substrate surface was estimated to increase the thickness of the total film layer by 4.3nm which is in excellent agreement with the literature [67], [73], [233], [235]. Incubation of the prepared protein array with an analyte containing rFhGST-S1 further increased

the observed layer by 5.6nm which in line with the approximate dimensions 4.6 x 5.3 x 5.0nm described [118]. The incubation of anti-FhGST-S1 antibody spots with FhEVs generated an estimated increase from the anti-FhGST-S1 antibody layer of 8.2nm which is significantly less than that which would be expected by the capture of EVs with a typical size of 10-400nm [10]. However, the shape of the model indicates a loss in sensitivity beyond 25nm which is in line with previous observations [63], [71], and a revised model based on Ψ values may prove more accurate for estimation of EV based AAIs. Errors indicated (Table 5.2) are an estimation from the propagating error estimation calculated for the AIE absolute error (Section 2.3.1.2) and the fit of data to the comparison model. Those estimates do not take into account the suitability of the model used.

5.5.4 Significance to the overall theme

The results of incubating *F. hepatica* EVs onto anti-FhGST-S1 antibodies that have been immobilized as a micro-array onto a silicon substrate would appear to produce a change in ellipsometric values that are measurable by the AIE. Which, given the earlier work of Chapter 4 in identifying the binding association between anti-FhGST-S1 and exposed proteins on the surface of *F. hepatica* EVs would seem to indicate an AAI and capture of EVs in the form of a bio-sensor. This indicates the potential for future development of the FhGST-S1/EV/anti-FhGST-S1 antibody AAIs and the possibility of an optical diagnostic test. In a similar manner, the incubation of FhGST-S1 protein onto the protein micro-array, produces changes in ellipsometric values measurable by the AIE, and again this would appear to indicate AAI. While substantial work is still required to further refine the process and improve consistency of results, the initial indications are positive in being able to detect AAIs in a high speed and label free way.

5.5.5 Further work and areas of weakness

There clearly remains a great deal of future work to further clarify the details of what has already been done. The most basic improvements would be a series of experiments to understand the sensitivity and specificity of the observed AAI processes, as is the case for alternative diagnostics. This would give some further insight to the resolution of the AIE in detecting changes in antigen antibody interaction over a much larger data set. Combined with further refinements in the protein micro-array fabrication, such as those used for nucleotide micro arrays [236], to remove coffee ring effects [202], may lead to a bio-sensor capable of capturing and detecting *F. hepatica* EVs from faecal samples. This is especially pertinent given the identification of EVs purified from infected faeces that can be labeled with anti-FhGST-S1 antibody (Chapter 4 Section 4.4.3.6).

One major area that has not been fully addressed and requires further refinement and development is the model to determine absolute quantitative values for film thickness. While the use of SiO_2 as a proxy for protein film thickness produces results that are in agreement with the literature for thin layers upto 25 nm, it is not clear whether this approach can be extended to gain improved quantitative determination of EV AAIs, interactions which could range from 10-400nm in scale.

However, despite some areas of weakness it would appear that the AIE is able to detect AAI in principal, further development of the system has some merit and holds potential for improvement.

Chapter 6

Conclusion

6.1 Conclusions

6.1.1 Thesis summary by chapter

Chapter 1: This thesis embodies the result of investigations into the use of imaging ellipsometry as a novel detection method for observations of AAIs. Given that AAIs are an important mechanisim in the detection of infection the development of suitable observational techniques is vital to the improved understanding of AAI and the complex processes with which they are involved. At present there are a wide range of techniques for investigating AAIs all with particular merits and disadvantages. However, a novel instrument for observing AAI is the AIE, which unlike many existing methods has now been demonstrated to optically monitor the mechanism in a non-contact, non-destructive and label free manner. The novel optical geometry and data gathering features of the AIE produces rapid calculation of ellipsometric parameters at high spatial resolution, making it ideally suited to the observation of both stable and transient AAIs [237], which could lead to real time simultaneous multiple detection for fascioliasis and other diseases.

Chapter 2: Detailed development and optimization of the AIE to observe AAI has lead to the implementation of an LED light source, resulting in an improvement in the spatial resolution by 10% and reduction in measurement noise by just

under an order of magnitude to less than 0.05% variance over the full dynamic measurement range. This has resulted in the ability to resolve AAIs spatially by this technique in a detail previously not observed.

Chapter 3: Through the course of this thesis, supplementary techniques such as CA measurement, EV isolation, AFM and protein printing have been employed to develop the concept and assembly of a protein micro-array that can be employed as a bio-sensor to observe AAI in a way that maximizes the strengths of the AIE instrument as a disease diagnostic instrument. Whereby, the Scheimpflug optical geometry places the whole of the imaged area in focus and the radiometric data gathering directly calculates the change in polarization state, resulting in direct evaluation and analysis of multiple AAI location spots. Protein printing and contact angle studies have informed the positioning techniques and delivered sample volumes required to reliably assemble covalently immobilized antibody spots into a micro-array, ready for incubation with analyte solutions for diagnostic disease detection. EVs isolated from *F. hepatica* culture have been refined for use in analyte solutions, through the use of a novel interactive Excel based sedimentation model.

Chapter 4: To exemplify and assess the AIE a case study was conducted incorporating key protein targets cultured from the zoonotic parasite *F. hepatica*. In keeping with current research this thesis has confirmed that *F. hepatica* releases excretory and secretory products which contain essential proteins and EVs [7], [95]. Importantly, this thesis presents these excretory and secretory components as potential bio-markers to monitor infection. Following initial Western blot screening to determine novel binding partners, refinements in the isolation of *F. hepatica* excretory and secretory products facilitated further investigations and TEM observations of immuno-gold labeling which has identified AAI between an anti-FhGST-S1 antibody and surface exposed FhGST-S1 present on *F. hepatica* EV. Which, given EVs role as immuno-modulators is something which has the

potential to inform future research on *F. hepatica* drug resistance and vaccine development. This discovery has also provided a system that has the potential to act as a bio-sensor protein array for the observation of AAIs by the AIE in the form of a diagnostic test of infection. The tantalizing identification of *F. hepatica* EVs purified from host faeces offers some strong indication that EVs remain sufficiently intact following passage through the host gastrointestinal tract and are in a sufficient concentration to offer their potential use as a bio-marker of infection, in what would be a simple and effective way.

Chapter 5: The combined progress of the initial AIE and target AAI optimisation has culminated in the form of a protein micro-array assembled using the model AAI system (FhGST-S1) selected from *F. hepatica* which was then optically detected using the AIE at high speed, label free, with the advantage of high spatial resolution and ease of use. The results of incubating the protein micro-array with an analyte solution show a clear measurable change in ellipsometric values that indicate the FhGST-S1 AAI in the form of a bio-sensor. With the detected change in film thickness in good agreement with the protein size as described in literature.

6.1.2 Practical applications / implications and future work

The research and development conducted as part of this thesis has been highly interdisciplinary, which has involved investigations in the fields of parasitology, materials physics, instrumentation, and engineering. These investigations by their very nature have posed significantly more questions than they have resolved. From these considerations a number of potential developments and future experiments are briefly presented in this final section.

6.1.2.1 Hybridization with existing techniques

An early objective that has not been achieved is the element of studying AAI in real time. A liquid cell allows the observation of the sample surface while immersed in analyte solution [119], [238], this offers the potential to monitor the antibody capture of antigens in real time with the potential to study the binding kinetics of association and disassociation. The use of a liquid cell offers the further opportunity for hybridization of the AIE with existing ELISA diagnostics. Utilizing the detection antibodies from established commercially available ELISA kits, there is the potential to deconstruct these kits and use the antibodies in a protein micro-array, capable of being visualized by the AIE, to detect this diagnostic AAI in a one step label free way. An example is Bio-X Diagnostics S.A. Belgium, which offers a wide range of diagnostic ELISA including one for the identification of fascioliasis. Diagnosis is achieved using polyclonal antibodies in a standard sandwich ELISA arrangement, which captures coproantigens from faecal material [239]. Other examples of diagnostic ELISA for parasitic infections include, Schistosoma [240] and visceral leishmaniasis [241], [242]. Going beyond parasitism, a wide range of commercial ELISA diagnostic kits are available with over 1000 products available from a single source [243]. Available tests include, Alzheimer's disease [244], HIV [245] and Hepatitis B [246]. Employing antibodies from ELISA which have in literature well established specificity and sensitivity would be a key avenue for investigation with the AIE.

6.1.2.2 Novel opportunities for field use

Work by Roda *et al.* [247] and my own experience is inspirational in the use of 3d printing to produce prototypes and even functional instruments for low cost use in research or field based tests [148]. The availability of proven multi-screen diagnostic polyclonal antibodies developed for ELISA based tests, could be combined with developments in optical components for ellipsometry which allow

instruments with solid state components and no moving parts, an approach that is perfect for ruggardisation into field based detection units [248].

6.1.2.3 Surface Evolver: A model of EV structure

EVs are now recognized as a key aspect of cell biology across a wide range of fields. EVs are known to facilitate cell to cell communication and have received attention for their role in disease progression [123], [124], [131]. Through the use of multiomic approaches (principally proteomics, lipidomics and glycomics) progress is being made to understand the structure and content of EVs yet this current knowledge falls short of developing new EV based tools [131], [228]. In addition, one element that is as yet undefined is a model that represents the structural and mechanical properties of EVs, properties that cannot be easily determined with current approaches [196]. This study has very briefly investigated the structural rigidity and surface attractive forces of EVs and it is proposed that further work based upon the use of AFM and structural modeling software, such as Surface Evolver, can inform a better understanding of EV structure, which will lead to an improvement in the downstream applications of EVs in diagnostics and infection control approaches. An early evaluation is presented (Figure 6.1).
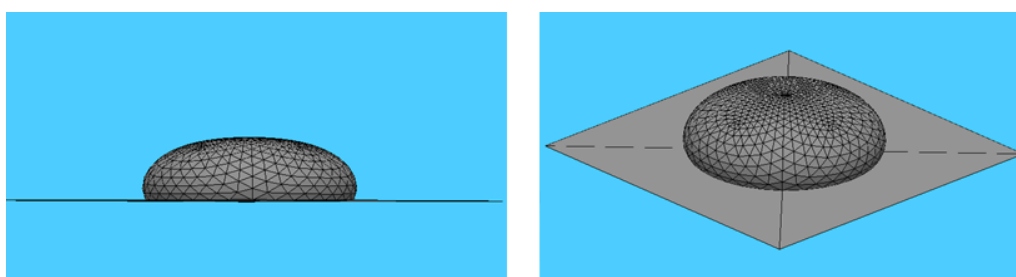

FIGURE 6.1: Example of an EV modeled using Surface Evolver; the shape is evolved from a spherical droplet using surface energies and gravitational forces to develop the external topography. In this example attempt was made to reproduce the structure of an isolated EV on a mica substrate, equivalent to the morphology observed when measured by AFM.

6.1.2.4 Discovery of novel AAIs and PPIs

A future opportunity for investigation using the AIE would be the immobilization of a known protein, such as FhGST-S1, as a micro-array which could than be incubated with known purified proteins to investigate potential binding partners, or alternatively an analyte mixture such as a cell lysate. Confirmation of AAIs / PPIs would be obtained with data directly from the AIE, subsequent identification of binding partners could be achieved by trypsin digestion of the micro-array spot, followed by MS of the resulting peptides.

6.2 An Overview

Climate change, anthelmintic resistance and the current lack of a vaccine are set to facilitate the increase of fascioliasis across the globe, with unprecedented levels of risk in parts of the UK with the threat of serious epidemics in Wales by 2050 [97]. The potential for more targeted deployment of anthelmintics and better understanding of disease development at a farm level may go some way to improve the longevity of TCBZ, the sole anthelmintic effective against juvenile *F. hepatica* and this could be achieved by a rapid AAI pen-side diagnostic. Use of the AIE as an optical means to observe AAI in a high speed, label free way that is highly spatially resolved has considerable merit.

References

[1] A. G. Ngounou Wetie, I. Sokolowska, A. G. Woods, U. Roy, J. A. Loo, and C. C. Darie, "Investigation of stable and transient protein-protein interactions: Past, present, and future", *Proteomics*, vol. 13, no. 3-4, pp. 538–557, 2013, ISSN: 16159853. DOI: 10.1002/pmic.201200328.

[2] T. Berggård, S. Linse, and P. James, "Methods for the detection and analysis of protein-protein interactions", *Proteomics*, vol. 7, no. 16, pp. 2833–2842, 2007, ISSN: 16159853. DOI: 10.1002/pmic.200700131.

[3] R. J. Goldberg, "A theory of antibody - antigen reactions: Theory for reactions of multivalent antigen with bivalent and univalent antibody", *Journal of the American Chemical Society*, vol. 74, no. 22, pp. 5715–5725, 1952. DOI: 10.1021/ja01142a045.

[4] The World Health Organization, *Fascioliasis*, 2016. [Online]. Available: https://www.who.int/foodborne{_}trematode{_}infections/fascioliasis/en/.

[5] T. W. Spithill, P. M. Smooker, J. L. Sexton, E. Bozas, C. A. Morrison, J. Creaney, and J. C. Parsons, *Development of vaccines against Fasciola hepatica*, J. Dalton, Ed. Wallingford UK: CABI, 1999, pp. 377 –409, ISBN: 9780851992600.

[6] E. J. LaCourse, S. Perally, R. M. Morphew, J. V. Moxon, M. Prescott, D. J. Dowling, S. M. O. Neill, A. Kipar, U. Hetzel, E. Hoey, and R. Zafra, "The sigma class glutathione transferase from the liver fluke *Fasciola hepatica*", *PLOS Neglected Tropical Diseases*, vol. 6, no. 5, 2012. DOI: 10.1371/journal.pntd.0001666.

[7] K. Cwiklinski, E. de la Torre-Escudero, M. Trelis, D. Bernal, P. J. Dufresne, G. P. Brennan, S. O'Neill, J. Tort, S. Paterson, A. Marcilla, J. P. Dalton, and M. W. Robinson, "The extracellular vesicles of the helminth pathogen, *Fasciola hepatica* : Biogenesis pathways and cargo molecules involved in parasite pathogenesis", *Molecular & Cellular Proteomics*, vol. 14, no. 12, pp. 3258–3273, 2015, ISSN: 1535-9476. DOI: 10.1074/mcp.m115.053934.

[8] R. M. Morphew, H. A. Wright, E. J. LaCourse, D. J. Woods, and P. M. Brophy, "Comparative proteomics of excretory-secretory proteins released by the liver fluke *Fasciola hepatica* in sheep host bile and during *in vitro* culture ex host", *Molecular & Cellular Proteomics*, vol. 6, no. 6, pp. 963–972, 2007, ISSN: 1535-9476. DOI: 10.1074/mcp.M600375-MCP200.

[9] J. M. J. M. Berg, J. L. Tymoczko, L. Stryer, and L. Stryer, *Biochemistry*, 5th. W.H. Freeman, 2002, ISBN: 0716730510.

[10] G. Raposo and W. Stoorvogel, "Extracellular vesicles: Exosomes, microvesicles, and friends", *The Journal of Cell Biology*, vol. 200, no. 4, pp. 373–383, 2013, ISSN: 0021-9525. DOI: 10.1083/JCB.201211138.

[11] F. A. Jenkins and H. White, *Fundamentals of Optics*, 4th. McGraw Hill, 2001, vol. 1, ISBN: 9781259002298.

[12] A. Rothen, "The ellipsometer, an apparatus to measure thicknesses of thin surface films", *Review of Scientific Instruments*, vol. 16, no. 2, p. 26, 1945, ISSN: 00346748. DOI: 10.1063/1.1770315.

[13] J. J. Bass, D. J. Wilkinson, D. Rankin, B. E. Phillips, N. J. Szewczyk, K. Smith, and P. J. Atherton, "An overview of technical considerations for Western blotting applications to physiological research", *Scandinavian Journal of Medicine and Science in Sports*, vol. 27, no. 1, pp. 4–25, 2017, ISSN: 16000838. DOI: 10.1111/sms.12702.

[14] B. T. Kurien and R. H. Scofield, "Western blotting", *Methods*, vol. 38, no. 4, pp. 283 –293, 2006, ISSN: 1046-2023. DOI: 10.1016/j.ymeth.2005.11.007.

[15] H. Towbin, T. Staehelint, and J. Gordon, "Electrophoretic transfer of proteins from polyacrylamide gels to nitrocellulose sheets: Procedure and some applications.", *Proceedings of the National Academy of Sciences of the United States of America*, vol. 76, no. 9, pp. 4350–4354, 1979. [Online]. Available: https://www.pnas.org/content/pnas/76/9/4350.full.pdf.

[16] M. G. Sumi, A. Mathai, C. Sarada, and V. V. Radhakrishnan, "Rapid diagnosis of tuberculous meningitis by a dot immunobinding assay to detect mycobacterial antigen in cerebrospinal fluid specimens", *Journal of Clinical Microbiology*, vol. 37, no. 12, pp. 3925–3927, 1999, ISSN: 0095-1137. DOI: 10.1128/JCM.37.12.3925-3927.1999.

[17] M. Fearon, "The laboratory diagnosis of HIV infections", *Canadian Journal of Infectious Diseases*, vol. 16, no. 1, pp. 26 –30, 2005, ISSN: 1046-2023. DOI: 10.1155/2005/515063.

[18] B. Kim, "Western blot techniques", in *Methods in Molecular Biology*, V. Espina, Ed., vol. 1606, Humana Press, New York, 2017, pp. 133 –139, ISBN: 978-1-2939-6986-0. DOI: 10.1007/978-1-4939-6990-6_9.

[19] C. Corona, E. V. Costassa, B. Iulini, M. Caramelli, E. Bozzetta, M. Mazza, R. Desiato, G. Ru, and C. Casalone, "Chapter Eleven - Phenotypical variability in bovine spongiform encephalopathy: Epidemiology, pathogenesis, and diagnosis of classical and atypical forms", in *Prion Protein*, ser. Progress in Molecular Biology and Translational Science, G. Legname and S. Vanni, Eds., vol. 150, Academic Press, 2017, pp. 241 –265. DOI: 10.1016/bs.pmbts.2017.06.015.

[20] K. R. Rupprecht, R. K. Nair, L. C. Harwick, J. Grote, G. S. Beligere, S. D. Rege, Y.-Y. Chen, Z. Lin, and J. R. Fishpaugh, "Development of a dot-blot assay for screening monoclonal antibodies to low-molecular-mass drugs", *Analytical Biochemistry*, vol. 407, no. 2, pp. 160 –164, 2010, ISSN: 0003-2697. DOI: 10.1016/j.ab.2010.08.003.

[21] L. Trinkle-Mulcahy, S. Boulon, Y. W. Lam, R. Urcia, F. M. Boisvert, F. Vandermoere, N. A. Morrice, S. Swift, U. Rothbauer, H. Leonhardt, and A. Lamond, "Identifying specific protein interaction partners using quantitative mass spectrometry and bead proteomes", *Journal of Cell Biology*, vol. 183, no. 2, pp. 223–239, 2008, ISSN: 00219525. DOI: 10.1083/jcb.200805092.

[22] K. Markham, Y. Bai, and G. Schmitt-Ulms, "Co-immunoprecipitations revisited: An update on experimental concepts and their implementation for sensitive interactome investigations of endogenous proteins", *Analytical and Bioanalytical Chemistry*, vol. 389, no. 2, pp. 461–473, 2007, ISSN: 16182642. DOI: 10.1007/s00216-007-1385-x.

[23] E. Phizicky and S. Fields, "Protein-Protein interactions: Methods for detection and analysis", *Microbiological Reviews*, vol. 59, no. 1, pp. 94–123, 1995. [Online]. Available: https://mmbr.asm.org/content/mmbr/59/1/94.full.pdf.

[24] Thermo Fisher Scientific, *Co-Immunoprecipitation (Co-IP) - UK*. [Online]. Available: https://www.thermofisher.com/uk/en/home/life-science/protein-biology/protein-biology-learning-center/protein-biology-resource-library/pierce-protein-methods/co-immunoprecipitation-co-ip.html (visited on 09/22/2019).

[25] A Hyatt and T Wise, *Immunocytochemistry and In Situ Hybridization in the Biomedical Sciences*, 1st ed., J Beesley, Ed. Birkhauser, 2001, vol. 33, pp. 73–107, ISBN: 9781461201397. DOI: 10.1016/s0031-3025(16)34564-0.

[26] W. Page Faulk and G. Malcolm Taylor, "An immunocolloid method for the electron microscope", *Immunochemistry*, vol. 8, no. 11, pp. 1081–1083, 1971, ISSN: 00192791. DOI: 10.1016/0019-2791(71)90496-4.

[27] C. Théry, S. Amigorena, G. Raposo, and A. Clayton, "Isolation and characterization of exosomes from cell culture supernatants and biological fluids", *Current Protocols in Cell Biology*, vol. 30, no. 1, pp. 3.22.1–3.22.29, 2006, ISSN: 19342500. DOI: 10.1002/0471143030.cb0322s30.

[28] J. A. Ramos-Vara, "Technical aspects of immunohistochemistry", *Veterinary Pathology*, vol. 42, no. 4, pp. 405–426, 2005, ISSN: 03009858. DOI: 10.1354/vp.42-4-405.

[29] P. Webster, H. Schwarz, and G. Griffiths, "Chapter 3: Preparation of Cells and Tissues for Immuno EM", in *Introduction to Electron Microscopy for Biologists*, ser. Methods in Cell Biology, vol. 88, Academic Press, 2008, pp. 45–58. DOI: https://doi.org/10.1016/S0091-679X(08)00403-2.

[30] S. Aydin, "A short history, principles, and types of ELISA, and our laboratory experience with peptide/protein analyses using ELISA", *Peptides*, vol. 72, pp. 4–15, 2015, ISSN: 18735169. DOI: 10.1016/j.peptides.2015.04.012.

[31] "ELISA Protocol (General Guidelines) - UK", [Online]. Available: https://www.thermofisher.com/uk/en/home/references/protocols/cell-and-tissue-analysis/elisa-protocol/general-elisa-protocol.html.

[32] J. Kool, N. Jonker, H. Irth, and W. M. A. Niessen, "Studying protein-protein affinity and immobilized ligand-protein affinity interactions using MS-based methods", *Analytical and Bioanalytical Chemistry*, vol. 401, no. 4, pp. 1109–1125, 2011, ISSN: 16182642. DOI: 10.1007/s00216-011-5207-9.

[33] A. L. Rockwood, M. M. Kushnir, and N. J. Clarke, *2 - Mass Spectrometry*, N. Rifai, A. R. Horvath, and C. T. Wittwer, Eds. Elsevier, 2018, pp. 33–65, ISBN: 9780128160633. [Online]. Available: http://www.sciencedirect.com/science/article/pii/B9780128160633000025.

[34] K. Mitsui, Y. Handa, and K. Kajikawa, "Optical fiber affinity biosensor based on localized surface plasmon resonance", *Applied Physics Letters*, vol. 85, no. 18, pp. 4231–4233, 2004, ISSN: 00036951. DOI: 10.1063/1.1812583.

[35] S. Underwood and P. Mulvaney, "Effect of the solution refractive index on the color of gold colloids", *Langmuir*, vol. 10, no. 10, pp. 3427–3430, 1994, ISSN: 15205827. DOI: 10.1021/la00022a011.

[36] M. M. Miller, A. A. Lazarides, and N. Carolina, "Sensitivity of metal nanoparticle surface plasmon resonance to the dielectric environment", *Physical Chemistry B*, vol. 109, pp. 21 556–21 565, 2005. DOI: 10.1021/jp054227y.

[37] GE Healthcare, "Biacore™ Assay Handbook", GE Healthcare, Tech. Rep., 2002, p. 129. [Online]. Available: http://publications.rwth-aachen.de/record/56938.

[38] P. Torreri, M. Ceccarini, P. Macioce, and T. C. Petrucci, "Biomolecular interactions by surface plasmon resonance technology", *Annali dell'Istituto Superiore di Sanita*, vol. 41, no. 4, pp. 437–441, 2005, ISSN: 00212571. [Online]. Available: https://pubmed.ncbi.nlm.nih.gov/16569911/.

[39] M. Malmqvist, "BIACORE: An affinity biosensor system for characterization of biomolecular interactions", *Biochemical Society Transactions*, vol. 27, no. 2, pp. 335–340, 1999, ISSN: 03005127. DOI: 10.1042/bst0270335.

[40] K. Retra, H. Irth, and J. E. van Muijlwijk-Koezen, "Surface plasmon resonance biosensor analysis as a useful tool in FBDD", *Drug Discovery Today: Technologies*, vol. 7, no. 3, e181–e187, 2010, ISSN: 17406749. DOI: 10.1016/j.ddtec.2010.11.012.

[41] B. Wallace and P. J. Atzberger, "Förster resonance energy transfer: Role of diffusion of fluorophore orientation and separation in observed shifts of FRET efficiency", *PLOS One*, vol. 12, no. 5, S. D'Auria, Ed., e0177122, 2017, ISSN: 1932-6203. DOI: 10.1371/journal.pone.0177122.

[42] B. Herman, J. Lakowicz, T. Fellers, and M. Davidson, *Fluorescence resonance energy transfer (FRET) microscopy - Introductory concepts — Olympus Life Science*. [Online]. Available: `https : / / www . olympus - lifescience . com / en / microscope - resource / primer / techniques / fluorescence / fret / fretintro/` (visited on 09/22/2019).

[43] T. Förster, "Zwischenmolekulare energiewanderung und fluoreszenz", *Annalen der Physik*, vol. 437, no. 1-2, pp. 55–75, 1948. DOI: `10 . 1002 / andp . 19484370105`.

[44] R. Clegg, *The history of FRET: from conception through the labors of birth*, 3rd ed. Springer, 2006, pp. 1–45. [Online]. Available: `http://photobiology. info/PDF/HistoryofFRET.pdf`.

[45] D. W. Piston and G. J. Kremers, "Fluorescent protein FRET: the good, the bad and the ugly", *Trends in Biochemical Sciences*, vol. 32, no. 9, pp. 407–414, 2007, ISSN: 09680004. DOI: `10.1016/j.tibs.2007.08.003`.

[46] O. H. Willemsen, M. M. Snel, A. Cambi, J. Greve, B. G. De Grooth, and C. G. Figdor, "Biomolecular interactions measured by atomic force microscopy", *Biophysical Journal*, vol. 79, no. 6, pp. 3267 –3281, 2000. DOI: `10.1016/S0006-3495(00)76559-3`.

[47] S Fields and O Song, "A novel genetic system to detect protein-protein interactions", *Nature*, vol. 399, pp. 655–656, 1989, ISSN: 0028-0836. DOI: `10. 1038/340301a0`.

[48] A. Brückner, C. Polge, N. Lentze, D. Auerbach, and U. Schlattner, "Yeast two-hybrid, a powerful tool for systems biology", *International Journal of Molecular Sciences*, vol. 10, no. 6, pp. 2763–2788, 2009, ISSN: 14220067. DOI: `10.3390/ijms10062763`.

[49] O Vielemeyer, C Nizak, A. J. Jimenez, A Echard, B Goud, J Camonis, J. C. Rain, and F Perez, "Characterization of single chain antibody targets through

yeast two hybrid", *BMC Biotechnology*, vol. 10, no. 59, p. 59, 2010. DOI: 0.1186/1472-6750-10-59.

[50] G. Rigaut, A. Shevchenko, B. Rutz, M. Wilm, M. Mann, and B. Seraphin, "A generic protein purification method for protein complex characterization and proteome exploration", *Nature Biotechnology*, vol. 17, no. 10, pp. 1030–1032, 1999, ISSN: 10870156. DOI: 10.1038/13732.

[51] O. Puig, F. Caspary, G. Rigaut, B. Rutz, E. Bouveret, E. Bragado-Nilsson, M. Wilm, and B. Séraphin, "The tandem affinity purification (TAP) method: A general procedure of protein complex purification", *Methods*, vol. 24, no. 3, pp. 218–229, 2001, ISSN: 10462023. DOI: 10.1006/meth.2001.1183.

[52] X. Xu, Y. Song, Y. Li, J. Chang, H. Zhang, and L. An, "The tandem affinity purification method: An efficient system for protein complex purification and protein interaction identification", *Protein Expression and Purification*, vol. 72, no. 2, pp. 149–156, 2010, ISSN: 10465928. DOI: 10.1016/j.pep.2010.04.009.

[53] W Spottiswoode, "Polarisation of light", *Nature*, vol. 9, no. 226, pp. 323–326, 1874. DOI: org/10.1038/009323d0.

[54] P. Drude, "Ueber die gesetze der reflexion und brechung des lichtes an der grenze absorbirender krystalle", *Annalen der Physik*, vol. 268, no. 12, pp. 584–625, 1887, ISSN: 1521-3889. DOI: 10.1002/andp.18872681205.

[55] H Tompkins, *A User's Guide to Ellipsometry*, 3rd. San Diego: Academic Press, 1993, p. 260, ISBN: 9780486450285.

[56] D. Brewster, "On the laws which regulate the polarisation of light by reflexion from transparent bodies", *Philosophical Transactions of the Royal Society of London*, vol. 105, pp. 125–159, 1815.

[57] R. M. A. Azzam and N. M. Bashara, *Ellipsometry and polarized light*, Paperback. Amsterdam; New York: North-Holland, 1987, p. 539, ISBN: 9780444870162.

[Online]. Available: https://www.worldcat.org/title/ellipsometry-and-polarized-light/oclc/15742574.

[58]   D. Gonçalves and E. A. Irene, "Fundamentals and applications of spectroscopic ellipsometry", *Quimica Nova*, vol. 25, no. 5, pp. 794–800, 2002, ISSN: 01004042. DOI: 10.1590/S0100-40422002000500015.

[59]   NanoFilm Ltd., *Principles of nulling and imaging ellipsometry*. [Online]. Available: https://www.accurion.com/imaging-ellipsometry/technology/principles-of-imaging-ellipsometry.pdf (visited on 10/06/2019).

[60]   R. Cohn, J. Wagner, and J Kruger, "Dynamic imaging microellipsometry - Theory, system design and feasibility demonstration", *Applied Optics*, vol. 27, no. 22, pp. 4664–4671, 1988, ISSN: 0003-6935. DOI: 10.1364/AO.27.004664.

[61]   K Sugimoto, S Matsuda, Y Ogiwara, and K Kitamura, "Microscopic ellipsometric observation of the change in passive film on 18cr-8ni stainless steel with the initiation and growth of pit", *Journal of The Electrochemical Society*, vol. 132, no. 8, pp. 1791–1795, 1985, ISSN: 0013-4651. DOI: 10.1149/1.2114219.

[62]   H. Arwin and I. Lundstrom, "A reflectance method for quantification of immunological reactions on surfaces", *Analytical Biochemistry*, vol. 145, no. 1, pp. 106 –112, 1985, ISSN: 003-2697. DOI: 10.1016/0003-2697(85)90334-3.

[63]   H. Arwin, S. Welin-Klintstrom, and R. Jansson, "Off-null ellipsometry revisited: Basic considerations for measuring surface concentrations at solid / liquid interfaces", *Journal of Colloid and Interface Science*, vol. 156, no. 2, pp. 377 –382, 1993, ISSN: 0021-9797. DOI: 10.1006/jcis.1993.1125.

[64] G. Jin, P. Tengvall, I. Lundström, and H. Arwin, "A biosensor concept based on imaging ellipsometry for visualization of biomolecular interactions.", *Analytical biochemistry*, vol. 232, no. 1, pp. 69–72, 1995, ISSN: 0003-2697. DOI: 10.1006/abio.1995.9959.

[65] Z. H. Wang, G. Jin, "A label-free multisensing immunosensor based on imaging ellipsometry", *Analytical Chemistry*, vol. 75, no. 22, pp. 6119–6123, 2003, ISSN: 00032700. DOI: 10.1021/ac0347258.

[66] Z. H. Wang and G. Jin, "Feasibility of protein A for the oriented immobilization of immunoglobulin on silicon surface for a biosensor with imaging ellipsometry", vol. 57, pp. 203–211, 2003. DOI: 10.1016/S0165-022X(03)00109-X.

[67] Z. H. Wang, G. Jin, "Silicon surface modification with a mixed silanes layer to immobilize proteins for biosensor with imaging ellipsometry", *Colloids and Surfaces B: Biointerfaces*, vol. 34, no. 3, pp. 173–177, 2004, ISSN: 09277765. DOI: 10.1016/j.colsurfb.2003.12.012.

[68] Z. H. Wang, Y. H. Meng, P. Q. Ying, C. Qi, and G. Jin, "A label-free protein microfluidic array for parallel immunoassays", *Electrophoresis*, vol. 27, no. 20, pp. 4078–4085, 2006, ISSN: 01730835. DOI: 10.1002/elps.200500956.

[69] Y. Chen, Y. Meng, and G. Jin, "Optimization of off-null ellipsometry for air/solid interfaces", *Applied Optics*, vol. 46, no. 35, pp. 8475–8481, 2007, ISSN: 1559-128X. DOI: 10.1364/AO.46.008475.

[70] H. Sun, C. Qi, Y. Niu, T. Kang, Y. Wei, G. Jin, X. Dong, C. Wang, and W. Zhu, "Detection of cytomegalovirus antibodies using a biosensor based on imaging ellipsometry", *PLOS One*, vol. 10, no. 8, pp. 1–12, 2015, ISSN: 19326203. DOI: 10.1371/journal.pone.0136253.

[71] G. Jin, R Jansson, and H Arwin, "Imaging ellipsometry revisited: Developments for visualization of thin transparent layers on silicon substrates",

Review of Scientific Instruments, vol. 67, no. 8, pp. 2930–2936, 1996, ISSN: 00346748. DOI: 10.1063/1.1147074.

[72] L. Asinovski, D. Beaglehole, and M. T. Clarkson, "Imaging ellipsometry: Quantitative analysis", *Physica Status Solidi (A) Applications and Materials Science*, vol. 205, no. 4, pp. 764–771, 2008, ISSN: 18626300. DOI: 10.1002/pssa.200777855.

[73] Z. H. Wang, G. Jin, "Covalent immobilization of proteins for the biosensor based on imaging ellipsometry", *Journal of Immunological Methods*, vol. 285, no. 2, pp. 237–243, 2004, ISSN: 00221759. DOI: 10.1016/j.jim.2003.12.002.

[74] R. F. Cohn, J. W. Wagner, and J. Kruger, "Dynamic imaging microellipsometry: Theory, system design, and feasibility demonstration", *Applied Optics*, vol. 27, no. 22, p. 4664, 1988, ISSN: 0003-6935. DOI: 10.1364/ao.27.004664.

[75] H. M. Merklinger, "View camera focus and depth of field part II", *View Camera Magazine*, vol. 7, pp. 56–58, 1996.

[76] Y. Yuan and T. R. Lee, "Contact angle and wetting properties", in *Surface Science Techniques*, B. G., Ed., Springer, 2013, pp. 3–34, ISBN: 9783642342424. DOI: 10.1007/978-3-642-34243-1_1.

[77] D. L. Williams, A. T. Kuhn, M. A. Amann, M. B. Hausinger, M. M. Konarik, and E. I. Nesselrode, "Computerised measurement of contact angles", *Galvanotechnik*, vol. 101, no. 11, pp. 2502–2512, 2010, ISSN: 00164232.

[78] A. F. Stalder, T. Melchior, M. Müller, D. Sage, T. Blu, and M. Unser, "Low-bond axisymmetric drop shape analysis for surface tension and contact angle measurements of sessile drops", *Colloids and Surfaces A: Physicochemical and Engineering Aspects*, vol. 364, no. 1, pp. 72 –81, 2010, ISSN: 0927-7757. DOI: https://doi.org/10.1016/j.colsurfa.2010.04.040.

[79] T. Young, "An essay to the cohesion of fluids", *Philoshopical Transaction of the Royal Society of London*, pp. 65–87, 1804, ISSN: 09628436. DOI: 10.1098/rstl.1805.0005.

[80] W. Zisman, *Relation of the equilibrium contact angle to liquid and solid constitution*, 1st, F. M. Fowkes, Ed. 1964, vol. 43, pp. 1–51, ISBN: 0841200440. DOI: 10.1021/ba-1964-0043.ch001.

[81] Krüss Ltd., "So you want to measure surface energy?", Tech. Rep., 1999, pp. 1–8. [Online]. Available: www.kruss.de.

[82] D. K. Owens and R. C. Wendt, "Estimation of the surface free energy of polymers", *Journal of Applied Polymer Science*, vol. 1, no. 19, pp. 1741–1747, 1969, ISSN: 10974628. DOI: 10.1002/app.1969.070130815.

[83] F. Fowkes, "Determination of interfacial tensions, contact angles and dispersion forces in surfaces by assuming additivity of intermolecular interactions in surfaces.", *The Journal of Physical Chemistry*, vol. 66, no. 2, p. 382, 1961.

[84] R. J. Good and K. L. Mittal, *Contact angle, wettability and adhesion*, 3rd, K. L. Mittal, Ed. Utrecht: VSP, 1993, p. 971, ISBN: 906764157X. [Online]. Available: https://www.worldcat.org/title/contact-angle-wettability-and-adhesion/oclc/872661651.

[85] C. J. Van Oss, R. J. Good, and M. K. Chaudhury, "The role of van der Waals forces and hydrogen bonds in "hydrophobic interactions" between biopolymers and low energy surfaces", *Journal of Colloid And Interface Science*, vol. 111, no. 2, pp. 378–390, 1986, ISSN: 00219797. DOI: 10.1016/0021-9797(86)90041-X.

[86] S. Andrews, *The life cycle of Fasciola hepatica*, 3rd, J. P. Dalton, Ed. Wallingford: CABI, 1999, pp. 1–30.

[87] Centers for Disease Control, "Fasciola - Resources for health professionals", Centers for Disease Control, Tech. Rep., 2019. [Online]. Available: https://www.cdc.gov/parasites/fasciola/health{_}professionals/index.html (visited on 09/21/2019).

[88] World Health Organization, "Fascioliasis: infection with the "neglected" neglected worms", W.H.O., Tech. Rep., 2013. [Online]. Available: https://www.who.int/neglected{_}diseases/integrated{_}media/integrated{_}media{_}fascioliasis/en/.

[89] S. Mas-Coma, M. D. Bargues, and M. A. Valero, "Human fascioliasis infection sources, their diversity, incidence factors, analytical methods and prevention measures", *Parasitology*, vol. 145, no. 13, pp. 1665–1699, 2018, ISSN: 0031-1820. DOI: 10.1017/S0031182018000914.

[90] World Health Organization, "Human fascioliasis: review provides fresh perspectives on infection and control", W.H.O., Tech. Rep., 2018. [Online]. Available: https://www.who.int/neglected_diseases/news/fascioliasis-review-provides-new-perspectives-infection-control/en/ (visited on 09/21/2019).

[91] S. Mas-Coma, M. A. Valero, and M. D. Bargues, "Chapter 2 Fasciola, Lymnaeids and human fascioliasis, with a global overview on disease transmission, epidemiology, evolutionary genetics, molecular epidemiology and control", *Advances in Parasitology*, vol. 69, no. 09, pp. 41–146, 2009, ISSN: 0065308X. DOI: 10.1016/S0065-308X(09)69002-3.

[92] World Health Organization, "Estimates of the global burden of foodborne diseases", W.H.O., Tech. Rep., 2018. [Online]. Available: https://apps.who.int/iris/bitstream/handle/10665/199350/9789241565165{_}eng.pdf?sequence=1.

[93] T. Furst, J. Keiser, and J. Utzinger, "Global burden of human food-borne trematodiasis: A systematic review and meta-analysis", *The Lancet Infectious Diseases*, vol. 12, no. 3, pp. 210–221, 2012, ISSN: 14733099. DOI: `10.1016/S1473-3099(11)70294-8`.

[94] World Health Organization. Foodborne Disease Burden Epidemiology Reference Group, *W.H.O. estimates of the global burden of foodborne diseases*, p. 254, ISBN: 9789241565165.

[95] N. J. Beesley, C. Caminade, J. Charlier, R. J. Flynn, J. E. Hodgkinson, A. Martinez-Moreno, M. Martinez-Valladares, J. Perez, L. Rinaldi, and D. J. Williams, "Fasciola and fasciolosis in ruminants in Europe: Identifying research needs", *Transboundary and Emerging Diseases*, vol. 65, no. April 2017, pp. 199–216, 2018, ISSN: 18651682. DOI: `10.1111/tbed.12682`.

[96] J. C. Boray, *Chemotherapy of infections with Fasciolidae, In Immunology, Pathobiology and Control of Fasciolosis*, Boray, Ed. Rahway, NJ, USA: MSD AGVET, 1997, pp. 83–97.

[97] N. J. Fox, P. C. L. White, C. J. McClean, G. Marion, A. Evans, and M. R. Hutchings, "Predicting impacts of climate change on *Fasciola hepatica* risk", *PLOS One*, vol. 6, no. 1, pp. 19–21, 2011, ISSN: 19326203. DOI: `10.1371/journal.pone.0016126`.

[98] A. B. Arrington, S. A. Diemont, C. T. Phillips, and E. Z. Welty, "Demographic and landscape-level urban foraging trends in the USA derived from web and mobile app usage", *Journal of Urban Ecology*, vol. 3, no. 1, 2017, ISSN: 2058-5543. DOI: `10.1093/jue/jux006`.

[99] The Telegraph, *Foodie foraging trend fuels sharp rise in the flouting of picking bans*. [Online]. Available: `https://www.telegraph.co.uk/news/2018/10/18/foodie-foraging-trend-fuels-sharp-rise-flouting-picking-bans/` (visited on 06/23/2019).

[100] M. Nyman, "Food, meaning-making and ontological uncertainty: Exploring 'urban foraging' and productive landscapes in London", *Geoforum*, vol. 99, pp. 170–180, 2019, ISSN: 0016-7185. DOI: 10.1016/J.GEOFORUM.2018.10.009.

[101] C. Shackleton, P. Hurley, A. Dahlberg, M. Emery, H. Nagendra, C. M. Shackleton, P. T. Hurley, A. C. Dahlberg, M. R. Emery, and H. Nagendra, "Urban Foraging: A ubiquitous human practice overlooked by urban planners, policy, and research", *Sustainability*, vol. 9, no. 10, p. 1884, 2017, ISSN: 2071-1050. DOI: 10.3390/su9101884.

[102] The Telegraph, *Foodie foraging trend fuels sharp rise in the flouting of picking bans*, 2018. [Online]. Available: https://www.telegraph.co.uk/news/2018/10/18/foodie-foraging-trend-fuels-sharp-rise-flouting-picking-bans/ (visited on 09/21/2019).

[103] Fallingfruit.org, *Falling fruit foraging app*. [Online]. Available: https://fallingfruit.org/ (visited on 09/21/2019).

[104] The Woodland Trust, *Foraging guidelines*. [Online]. Available: https://www.woodlandtrust.org.uk/visiting-woods/things-to-do/foraging/foraging-guidelines/ (visited on 09/21/2019).

[105] D. Overend and F. Bowen, "Resistance of *Fasciola hepatica* to triclabendazole", *Australian Veterinary Journal*, vol. 72, no. 7, pp. 275–276, 1995, ISSN: 17510813. DOI: 10.1111/j.1751-0813.1995.tb03546.x.

[106] G. P. Brennan, I. Fairweather, A. Trudgett, E. Hoey, McCoy, M. McConville, M. Meaney, M. Robinson, N. McFerran, L. Ryan, C. Lanusse, L. Mottier, L. Alvarez, H. Solana, G. Virkel, and P. M. Brophy, "Understanding triclabendazole resistance", *Experimental and Molecular Pathology*, vol. 82, no. 2, pp. 104–109, 2007, ISSN: 00144800. DOI: 10.1016/j.yexmp.2007.01.009.

[107] A. J. Wolstenholme, I. Fairweather, R. Prichard, G. Von Samson-Himmelstjerna, and N. C. Sangster, "Drug resistance in veterinary helminths", *Trends in Parasitology*, vol. 20, no. 10, pp. 469–476, 2004, ISSN: 14714922. DOI: 10.1016/j.pt.2004.07.010.

[108] P. M. Brophy, N. Mackintosh, and R. M. Morphew, "Anthelmintic metabolism in parasitic helminths: Proteomic insights", *Parasitology*, vol. 139, pp. 1205–1217, 9 2012. DOI: 10.1017/S003118201200087X.

[109] M. M. Cabada, M. Lopez, M. Cruz, J. R. Delgado, V. Hill, and A. C. White, "Treatment failure after multiple courses of triclabendazole among patients with fascioliasis in Cusco, Peru: A case series.", *PLoS neglected tropical diseases*, vol. 10, no. 1, e0004361, 2016, ISSN: 1935-2735. DOI: 10.1371/journal.pntd.0004361.

[110] M. Adela Valero, M. Victoria Periago, I. Pérez-Crespo, E. Rodréguez, M. Jesús Perteguer, T. Gárate, E. M. González-Barberá, and S. Mas-Coma, "Assessing the validity of an ELISA test for the serological diagnosis of human fascioliasis in different epidemiological situations", *Tropical Medicine and International Health*, vol. 17, no. 5, pp. 630–636, 2012, ISSN: 13602276. DOI: 10.1111/j.1365-3156.2012.02964.x.

[111] S. Mas-Coma, R. Anglés, J. G. Esteban, M. D. Bargues, P. Buchon, M. Franken, and W. Strauss, "The Northern Bolivian Altiplano: A region highly endemic for human fascioliasis", *Tropical Medicine and International Health*, vol. 4, no. 6, pp. 454–467, 1999, ISSN: 13602276. DOI: 10.1046/j.1365-3156.1999.00418.x.

[112] M. R. Salimi-Bejestani, J. W. McGarry, S. Felstead, P. Ortiz, A. Akca, and D. J. L. Williams, "Development of an antibody-detection ELISA for *Fasciola hepatica* and its evaluation against a commercially available test", *Research in Veterinary Science*, vol. 78, no. 2, pp. 177–181, 2005, ISSN: 00345288. DOI: 10.1016/j.rvsc.2004.08.005.

[113] B. Gonzales Santana, J. P. Dalton, F. Vasquez Camargo, M. Parkinson, and M. Ndao, "The diagnosis of human fascioliasis by enzyme-linked immunosorbent assay (ELISA) using recombinant cathepsin L protease", *PLOS Neglected Tropical Diseases*, vol. 7, no. 9, 2013, ISSN: 19352727. DOI: 10.1371/journal.pntd.0002414.

[114] R. M. Morphew, N. Mackintosh, E. H. Hart, M. Prescott, E. J. LaCourse, and P. M. Brophy, "In vitro biomarker discovery in the parasitic flatworm *Fasciola hepatica* for monitoring chemotherapeutic treatment", *EuPA Open Proteomics*, vol. 3, pp. 85–99, 2014, ISSN: 2212-9685. DOI: 10.1016/j.euprot.2014.02.013.

[115] J. Duncan, D. Cutress, R. M. Morphew, and P. M. Brophy, "Purification of native sigma class glutathione transferase from *Fasciola hepatica*", *Molecular and Biochemical Parasitology*, vol. 222, no. 2010, pp. 45–50, 2018, ISSN: 18729428. DOI: 10.1016/j.molbiopara.2018.04.006.

[116] C. N. Davis, H. Phillips, J. J. Tomes, M. T. Swain, T. J. Wilkinson, P. M. Brophy, and R. M. Morphew, "The importance of extracellular vesicle purification for downstream analysis: A comparison of differential centrifugation and size exclusion chromatography for helminth pathogens", *PLOS Neglected Tropical Diseases*, vol. 13, no. 2, e0007191, 2019. DOI: 10.1371/journal.pntd.0007191.

[117] G. Chemale, R. Morphew, J. V. Moxon, L Morassuti, E. J. LaCourse, J. Barrett, D. A. Johnston, and P. M. Brophy, "Proteomic analysis of glutathione transferases from the liver fluke parasite , *Fasciola hepatica*", *Proteomics*, vol. 6, pp. 6263–6273, 23 2006. DOI: 10.1002/pmic.200600499.

[118] K. Line, M. N. Isupov, E. J. LaCourse, D. J. Cutress, R. M. Morphew, P. M. Brophy, and J. A. Littlechild, "X-ray structure of *Fasciola hepatica* sigma class glutathione transferase 1 reveals a disulfide bond to support stability in gastro-intestinal environment", *Scientific Reports*, vol. 9, no. 1, p. 902,

2019, ISSN: 20452322. DOI: 10.1038/s41598-018-37531-5. [Online]. Available: www.nature.com/scientificreports.

[119] H Arwin, "Spectroscopic ellipsometry and biology: recent developments and challenges", *Thin Solid Films*, vol. 313–314, no. 0, pp. 764–774, 1998, ISSN: 00406090. DOI: 10.1016/s0040-6090(97)00993-0.

[120] M. E. Kuipers, E. N. N. 't Hoen, A. J. van der Ham, A. Ozir-Fazalalikhan, D. L. Nguyen, C. M. de Korne, R. I. Koning, J. J. Tomes, K. F. Hoffmann, H. H. Smits, and C. H. Hokke, "Dc-sign mediated internalisation of glycosylated extracellular vesicles from *Schistosoma mansoni* increases activation of monocyte-derived dendritic cells", *Journal of Extracellular Vesicles*, vol. 9, no. 1, p. 1 753 420, 2020. DOI: 10.1080/20013078.2020.1753420.

[121] B. Fromm, V. Ovchinnikov, E. Høye, D. Bernal, M. Hackenberg, and A. Marcilla, "On the presence and immunoregulatory functions of extracellular microRNAs in the trematode *Fasciola hepatica*", *Parasite Immunology*, vol. 39, no. 2, 2017, ISSN: 13653024. DOI: 10.1111/pim.12399.

[122] E. de la Torre-Escudero, A. P. Bennett, A. Clarke, G. P. Brennan, and M. W. Robinson, "Extracellular vesicle biogenesis in helminths: More than one route to the surface?", *Trends in Parasitology*, vol. 32, no. 12, 2016, ISSN: 14715007. DOI: 10.1016/j.pt.2016.09.001.

[123] A. Marcilla, L. Martin-Jaular, M. Trelis, A. de Menezes-Neto, A. Osuna, D. Bernal, C. Fernandez-Becerra, I. C. Almeida, and H. A. del Portillo, "Extracellular vesicles in parasitic diseases", *Journal of Extracellular Vesicles*, vol. 3, no. 1, p. 25 040, 2014. DOI: 10.3402/jev.v3.25040.

[124] G. Coakley, R. M. Maizels, and A. H. Buck, "Exosomes and other extracellular vesicles: The new communicators in parasite infections", *Trends in Parasitology*, vol. 31, no. 10, pp. 477–489, 2015, ISSN: 14714922. DOI: 10.1016/j.pt.2015.06.009.

[125] K. Gajos, A. Kamińska, K. Awsiuk, A. Bajor, K. Gruszczyński, A. Pawlak, A. Żądło, A. Kowalik, A. Budkowski, and E. Stępień, "Immobilization and detection of platelet-derived extracellular vesicles on functionalized silicon substrate: Cytometric and spectrometric approach", *Analytical and Bioanalytical Chemistry*, vol. 409, no. 4, pp. 1109–1119, 2017. DOI: 10.1007/s00216-016-0036-5.

[126] T. Pisitkun, R. F. Shen, and M. Knepper, "Identification and proteomic profiling of exosomes in human urine", *PNAS*, vol. 101, no. 36, pp. 13 368–13 373, 2001, ISSN: 00149446. DOI: 10.1073/pnas.0403453101.

[127] Y. Ogawa, Y. Miura, A. Harazono, M. Kanai-Azuma, Y. Akimoto, H. Kawakami, T. Yamaguchi, T. Toda, T. Endo, M. Tsubuki, and R. Yanoshita, "Proteomic analysis of two types of exosomes in human whole saliva", *Biological and Pharmaceutical Bulletin*, vol. 34, no. 1, pp. 13–23, 2011, ISSN: 09186158. DOI: 10.1248/bpb.34.13.

[128] K. M. Huson, C. Wild, C. Fenn, and M. W. Robinson, "Optimized conditions for the in vitro excystment of *Calicophoron daubneyi* metacercariae", *Parasitology*, vol. 145, no. 8, pp. 1015–1019, 2018, ISSN: 0031-1820. DOI: 10.1017/S0031182017002220.

[129] T. Tzelos, J. B. Matthews, A. H. Buck, F. Simbari, D. Frew, N. F. Inglis, K. McLean, A. J. Nisbet, C. B. A. Whitelaw, D. P. Knox, and T. N. McNeilly, "A preliminary proteomic characterisation of extracellular vesicles released by the ovine parasitic nematode, *Teladorsagia circumcincta*", *Veterinary Parasitology*, vol. 221, pp. 84–92, 2016, ISSN: 18732550. DOI: 10.1016/j.vetpar.2016.03.008.

[130] S. Sharma, M. LeClaire, and J. K. Gimzewski, "Ascent of atomic force microscopy as a nanoanalytical tool for exosomes and other extracellular vesicles", *Nanotechnology*, vol. 29, no. 13, p. 132 001, 2018. DOI: 10.1088/1361-6528/aaab06.

[131] B. Thébaud and D. J. Stewart, "Exosomes, cell garbage can, therapeutic carrier, or trojan horse?", *Circulation*, vol. 126, no. 22, 2012. DOI: `10.1161/CIRCULATIONAHA.112.146738`.

[132] P. D. Robbins and A. E. Morelli, "Regulation of immune responses by extracellular vesicles", *Nature Reviews Immunology*, vol. 14, no. 3, pp. 195–208, 2014, ISSN: 1474-1733. DOI: `10.1038/nri3622`.

[133] S. Mathivanan, H. Ji, and R. J. Simpson, "Exosomes: Extracellular organelles important in intercellular communication", *Journal of Proteomics*, vol. 73, no. 10, pp. 1907–1920, 2010, ISSN: 18743919. DOI: `10.1016/j.jprot.2010.06.006`.

[134] A. H. Buck, G. Coakley, F. Simbari, H. J. McSorley, J. F. Quintana, T. Le Bihan, S. Kumar, C. Abreu-Goodger, M. Lear, Y. Harcus, A. Ceroni, S. A. Babayan, M. Blaxter, A. Ivens, and R. M. Maizels, "Exosomes secreted by nematode parasites transfer small RNAs to mammalian cells and modulate innate immunity", *Nature Communications*, vol. 5, no. 1, p. 5488, 2014, ISSN: 2041-1723. DOI: `10.1038/ncomms6488`.

[135] E. del Cacho, M. Gallego, S. H. Lee, H. S. Lillehoj, J. Quilez, E. P. Lillehoj, and C. Sánchez-Acedo, "Induction of protective immunity against *Eimeria tenella*, *Eimeria maxima*, and *Eimeria acervulina* infections using dendritic cell-derived exosomes", *Infection and Immunity*, vol. 80, no. 5, J. H. Adams, Ed., pp. 1909–1916, 2012, ISSN: 0019-9567. DOI: `10.1128/IAI.06413-11`.

[136] C. Théry and K. W. Witwer, "Journal of Extracellular Vesicles Minimal information for studies of extracellular vesicles 2018 (MISEV2018): a position statement of the International Society for Extracellular Vesicles and update of the MISEV2014 guidelines", ISSN: 2001-3078. [Online]. Available: `https://www.tandfonline.com/loi/zjev20`.

[137] T. M. Mayhew, C. Mühlfeld, D. Vanhecke, and M. Ochs, "A review of recent methods for efficiently quantifying immunogold and other nanoparticles using tem sections through cells, tissues and organs", *Annals of Anatomy - Anatomischer Anzeiger*, vol. 191, no. 2, pp. 153 –170, 2009, ISSN: 0940-9602. DOI: https://doi.org/10.1016/j.aanat.2008.11.001.

[138] G. Jin, Y. Meng, L. Liu, Y. Niu, S. Chen, Q. Cai, and T. Jiang, "Development of biosensor based on imaging ellipsometry and biomedical applications", *Thin Solid Films*, vol. 519, no. 9, pp. 2750–2757, 2011, ISSN: 00406090. DOI: 10.1016/j.tsf.2010.12.175.

[139] C. Huang, J. Li, Y. Tang, Y. Chen, and G. Jin, "Detection of duck hepatitis virus serotype1 by biosensor based on imaging ellipsometry", *Current Applied Physics*, vol. 11, no. 3, pp. 1–5, 2010, ISSN: 1567-1739. DOI: 10.1016/j.cap.2010.08.004.

[140] C. Huang, Y. Chen, C. Wang, W. Zhu, H. Ma, and G. Jin, "Detection of alpha-fetoprotein through biological signal amplification by biosensor based on imaging ellipsometry", *Thin Solid Films*, vol. 519, no. 9, pp. 2763–2767, 2011, ISSN: 00406090. DOI: 10.1016/j.tsf.2010.11.064.

[141] C. Huang, J. Li, Y. Tang, C. Wang, C. Hou, D. Huo, Y. Chen, and G. Jin, "Biosensor based on imaging ellipsometry for serotype-specific detection of *Riemerella anatipestifer*", *Materials Science and Engineering C*, vol. 31, no. 7, pp. 1609–1613, 2011, ISSN: 09284931. DOI: 10.1016/j.msec.2011.05.018.

[142] National Instruments Ltd., *What is labview?* [Online]. Available: http://www.ni.com/en-gb/shop/labview.html?cid=Paid{_}Search-129008-United{_}Kingdom-Google{_}ESW1{_}labview{_}exact{\&}gclid=EAIaIQobChMI9ufolc3z5AIVwbTtCh0-mwtGEAAYASAAEgI4kPD{_}BwE (visited on 09/28/2019).

[143] Pike Ltd., *F-032 fast vga camera - allied vision*. [Online]. Available: https://www.alliedvision.com/en/products/cameras/detail/Pike/F-032.html (visited on 09/28/2019).

[144] Meadowlark Ltd., *High speed liquid crystal variable retarder*. [Online]. Available: https://www.meadowlark.com/high-speed-liquid-crystal-variable-retarder-p-141?mid=2 (visited on 09/28/2019).

[145] R. F. Cohn, "Evaluation of alternative algorithms for dynamic imaging microellipsometry", *Applied Optics*, vol. 29, no. 2, p. 304, 1990, ISSN: 0003-6935. DOI: 10.1364/ao.29.000304.

[146] Q. Wang and M. K. Giles, "Coherence reduction using optical fibers", *Free-Space Laser Communications V*, vol. 5892, 58920N, 2005. DOI: 10.1117/12.620375.

[147] A. Gatti, M. Bache, D. Magatti, E. Brambilla, F. Ferri, and L. A. Lugiato, "Coherent imaging with pseudo-thermal incoherent light", *Journal of Modern Optics*, vol. 53, no. 5-6, pp. 739–760, 2006, ISSN: 09500340. DOI: 10.1080/09500340500147240.

[148] J. Tomes and C. Finlayson, "Low cost 3D-printing used in an undergraduate project: An integrating sphere for measurement of photoluminescence quantum yield", *European Journal of Physics*, vol. 37, no. 5, p. 055501, 2016, ISSN: 13616404. DOI: 10.1088/0143-0807/37/5/055501.

[149] R. M. A. Azzam and N. M. Bashara, *Ellipsometry and polarized light*. North-Holland, 1987, p. 539, ISBN: 0444870164.

[150] J Vanhellemont, H. Maes, M Schaekers, A Armigliato, H Cerva, A Cullis, J Desande, H Dinges, J Hallais, V Nayar, C Pickering, J. Stehle, J Vanlanduyt, C Walker, H Werner, and P Salieri, "Round-robin investigation of silicon-dioxide on silicon reference materials for ellipsometry", *Applied Surface Science*, vol. 63, no. 1-4, pp. 45–51, 1993, ISSN: 0169-4332. DOI: 10.1016/0169-4332(93)90062-G.

[151] J. A. Woollam, J. N. Hilfiker, C. M. Herzinger, R. A. Synowicki, and M. Liphardt, "Metrology standards with ellipsometers", *AIP Conference Proceedings*, vol. 449, no. 1, pp. 352–356, 1998. DOI: 10.1063/1.56818.

[152] L Mandel, "Fluctuations of photon beams: The distribution of the photoelectrons", *Proceedings of the Physical Society*, vol. 74, no. 3, pp. 233–243, 1959. DOI: 10.1088/0370-1328/74/3/301.

[153] R. Hui, "Chapter 4 - photodetectors", in *Introduction to fiber-optic communications*, R. Hui, Ed., Academic Press, 2020, pp. 125 –154, ISBN: 978-0-12-805345-4. DOI: https://doi.org/10.1016/B978-0-12-805345-4.00004-4.

[154] J. Unger, S. Hajisharif, and J. Kronander, "Chapter 2 - unified reconstruction of raw hdr video data", in *High dynamic range video*, F. Dufaux, P. L. Callet], R. K. Mantiuk, and M. Mrak, Eds., Academic Press, 2016, pp. 63 –83, ISBN: 978-0-08-100412-8. DOI: https://doi.org/10.1016/B978-0-08-100412-8.00002-4.

[155] Pike Ltd., *Pike f-032 camera technical manual*. [Online]. Available: https://cdn.alliedvision.com/fileadmin/content/documents/products/cameras/Pike/techman/Pike_TechMan_01.pdf (visited on 09/30/2019).

[156] BIPM, IEC, IFCC, ISO, and IUPAC, "Evaluation of measurement data – An introduction to the GUM and related documents", no. July, 2009. [Online]. Available: http://www.bipm.org/en/publications/guides/gum.html.

[157] T. Smith, "Spherical aberration in thin lenses", *Scientific Papers of the Bureau of Standards*, vol. 18, no. 3, pp. 559–586, 1922, ISSN: 0096-6231. DOI: https://dx.doi.org/10.6028/nbsscipaper.127.

[158] Schneider-Kreuznach, *Symmar Macro -80mm F5.6*. [Online]. Available: https://schneiderkreuznach.com/application/files/8815/2845/6566/Makro-Symmar-5.6-80.pdf (visited on 10/06/2019).

[159] Thorlabs Inc., *DJ532-40 532nm DPSS laser specification*. [Online]. Available: https://www.thorlabs.com/drawings/a2f1c9b4e9581bfd-93F3ACB0-A617-73CC-C2E8C5D24E297140/DJ532-40-SpecSheet.pdf (visited on 12/06/2019).

[160] Thorlabs Inc.., *BE15M-A optical beam expander*. [Online]. Available: https://www.thorlabs.com/catalogpages/Obsolete/2015/BE15M-A.pdf (visited on 12/06/2019).

[161] G. Airy, "On the diffraction of an object-glass with circular aperture", *Transactions of the Cambridge Philosophical Society*, vol. 5, no. 3, pp. 283–291, 1835. DOI: https://archive.org/details/transactionsofca05camb.

[162] Lord Rayleigh F.R.S., "Investigations in optics", *Philosophical Magazine and Journal of Science*, vol. 8, no. 49, pp. 261–274, 1879. DOI: 10.1080/14786447908639684.

[163] C. M. Sparrow, "On spectroscopic resolving power", *The Astrophysical Journal*, vol. 44, pp. 76–86, 1916. DOI: 10.1086/142271.

[164] A. Rose, *Optical physics and engineering*, W. L. Wolfe, Ed. Springer, 1974, p. 10, ISBN: 9780306307324. [Online]. Available: https://archive.org/details/visionhumanelect01rose/page/10/mode/2up.

[165] W. J. Smith, *Modern Optical Engineering*, 3rd, S. S. Chapman, Ed. McGraw Hill, 2007, p. 366, ISBN: 9780071593755. [Online]. Available: https://spie.org/Publications/Book/781851.

[166] Edmund Optics, *Testing and Targets*. [Online]. Available: https://www.edmundoptics.co.uk/resources/application-notes/imaging/testing-and-targets/ (visited on 09/29/2019).

[167] M. Stenberg and H Nygren, "A receptor-ligand reaction studied by a novel analytical tool - the isoscope ellipsometer", *Analytical Biochemistry*, vol. 127, no. 1, pp. 183–192, 1982, ISSN: 10960309. DOI: 10.1016/0003-2697(82)90163-4.

[168] D. J. Hayton and T. E. Jenkins, "On the frustration of back-surface reflection from transparent substrates in ellipsometry", *Measurement Science and Technology*, vol. 15, no. 2, 2004, ISSN: 09570233. DOI: 10.1088/0957-0233/15/2/N01.

[169] A. K. Wright and M. R. Thompson, "Hydrodynamic structure of bovine serum albumin determined by transient electric birefringence", *Biophysical Journal*, vol. 15, no. 2, pp. 137–141, 1975, ISSN: 00063495. DOI: 10.1016/S0006-3495(75)85797-3.

[170] C. E. Shannon, "Communication in the presence of noise", *Proceedings of the IRE*, vol. 37, no. 1, pp. 10–21, 1949, ISSN: 0018-9219. DOI: 10.1109/JRPROC.1949.232969.

[171] D. Lüke, "Origins of the sampling theorem", *IEEE Communications Magazine*, vol. 37, no. 4, pp. 106–108, 1999, ISSN: 01636804. DOI: 10.1109/35.755459.

[172] C. A. Sciammarella, L. Lamberti, and F. M. Sciammarella, "High-accuracy contouring using projection moiré", *Optical Engineering*, vol. 44, no. 9, pp. 1–12, 2005. DOI: 10.1117/1.2044847.

[173] J. T. Zettler, M. Weidner, and A. Röseler, "On the characterization of silicon dioxide and silicon nitride by spectroscopic ellipsometry in the Vis and IR Regions", *Physica Status Solidi (a)*, vol. 124, no. 2, pp. 547–555, 1991, ISSN: 1521396X. DOI: 10.1002/pssa.2211240222.

[174] G. Jungk and T. Grabolla, "Spectroscopic ellipsometry on silicon-oxide films on silicon", *Thin Solid Films*, vol. 335, no. 1-2, pp. 253–257, 1998, ISSN: 00406090. DOI: 10.1016/S0040-6090(98)00814-1.

[175] Krüss Ltd., *Drop Shape Analyzer: DSA30*. [Online]. Available: https://www.kruss-scientific.com/products/drop-shape/dsa30/drop-shape-analyzer-dsa30/ (visited on 10/06/2019).

[176] Attension, Ltd., *Optical tensiometer user guide*. [Online]. Available: `https://supertec.com.ar/archivos/346_archivo.pdf` (visited on 05/06/2020).

[177] Attension Ltd., *Optical tensiometer user manual*. [Online]. Available: `https://www.manualslib.com/manual/1359167/Attension-Theta.html` (visited on 05/06/2020).

[178] ImageJ, *Plugins*. [Online]. Available: `https://imagej.nih.gov/ij/plugins/` (visited on 10/06/2019).

[179] D. Biolè, M. Wang, and V. Bertola, "Assessment of direct image processing methods to measure the apparent contact angle of liquid drops", *Experimental Thermal and Fluid Science*, vol. 76, pp. 296 –305, 2016, ISSN: 0894-1777. DOI: `https://doi.org/10.1016/j.expthermflusci.2016.04.006`.

[180] W. Kern and D. Puotinen, "Cleaning solutions based on hydrogen peroxide for use in silicon semiconductor technology.", *RCA Review*, vol. 31, pp. 187–206, 1970. [Online]. Available: `http://garfield.library.upenn.edu/classics1983/A1983QD90200001.pdf`.

[181] T. Svedberg, "The ultra-centrifuge and the study of high-molecular compounds", *Nature*, vol. 139, no. 3529, pp. 1051–1062, 1937, ISSN: 0028-0836. DOI: `10.1038/1391051a0`. [Online]. Available: `http://www.nature.com/articles/1391051a0`.

[182] H. G. Barth, "The early development of size exclusion chromatography: A historical perspective", *LCGC Europe*, vol. 26, pp. 224–232, 4 2013. [Online]. Available: `http://www.chromatographyonline.com/early-development-size-exclusion-chromatography-historical-perspective-0`.

[183] R. R. Burgess, "A brief practical review of size exclusion chromatography: Rules of thumb, limitations, and troubleshooting", *Protein Expression and Purification*, vol. 150, pp. 81–85, 2018, ISSN: 10465928. DOI: `10.1016/j.pep.2018.05.007`.

[184] F. C. Nowacki, M. T. Swain, O. I. Klychnikov, U. Niazi, A. Ivens, J. F. Quintana, P. J. Hensbergen, C. H. Hokke, A. H. Buck, and K. F. Hoffmann, "Protein and small non-coding rna-enriched extracellular vesicles are released by the pathogenic blood fluke schistosoma mansoni", *Journal of Extracellular Vesicles*, vol. 4, no. 1, p. 28 665, 2015. DOI: 10.3402/jev.v4.28665.

[185] M. A. Livshits, E. Khomyakova, E. G. Evtushenko, V. N. Lazarev, N. A. Kulemin, S. E. Semina, E. V. Generozov, and V. M. Govorun, "Isolation of exosomes by differential centrifugation: Theoretical analysis of a commonly used protocol", *Nature Publishing Group*, vol. 32, no. 4, 2015. DOI: 10.1038/srep17319.

[186] P. Ying, Y. Yu, G. Jin, and Z. Tao, "Competitive protein adsorption studied with atomic force microscopy and imaging ellipsometry", *Colloids and Surfaces B: Biointerfaces*, vol. 32, no. 1, pp. 1–10, 2003, ISSN: 09277765. DOI: 10.1016/S0927-7765(02)00133-9.

[187] Taylor-Hobson Ltd, "Exploring surface texture a fundamental guide to the measurement of surface finish 7th Edition", Tech. Rep., 2011, p. 98. [Online]. Available: https://www.taylor-hobson.com/-/media/ametektaylorhobson/files/learningzone/exploringsurfacetexture2014.pdf?la=en.

[188] H. Becker, *Apparatus for measuring surface irregularities*, 1955. [Online]. Available: https://patentimages.storage.googleapis.com/48/31/a1/40b97b4fb33216/US2728222.pdf.

[189] R. Young, J. Ward, and F. Scire, "The Topografiner: An instrument for measuring surface microtopography", *Review of Scientific Instruments*, vol. 43, no. 7, pp. 999–1011, 1972, ISSN: 0034-6748. DOI: 10.1063/1.1685846.

[190] G. Binning, H. Rohrer, C. Gerber, and E. Weibel, "Surface studies by scanning tunneling microscopy", vol. 49, no. 1, p. 6196, 1975. [Online]. Available: https://journals.aps.org/prl/pdf/10.1103/PhysRevLett.49.57.

[191] NobelPrize.org, *The nobel prize in physics 1986*. [Online]. Available: https://www.nobelprize.org/prizes/physics/1986/summary/ (visited on 08/07/2019).

[192] P. Eaton and P. West, *Atomic Force Microscopy*. Oxford University Press, Oxford England, 2010, p. 248, ISBN: 9780199570454. [Online]. Available: https://books.google.co.uk/books?id=VB0UDAAAQBAJ.

[193] BioLab, *AFM — Cellular and Molecular Biomechanics Laboratory*. [Online]. Available: http://biomechanicalregulation-lab.org/afm (visited on 10/06/2019).

[194] C. McAllister, M. A. Karymov, Y. Kawano, A. Y. Lushnikov, A. Mikheikin, V. N. Uversky, and Y. L. Lyubchenko, "Protein interactions and misfolding analyzed by AFM force spectroscopy", *Journal of Molecular Biology*, vol. 354, no. 5, pp. 1028–1042, 2005, ISSN: 00222836. DOI: 10.1016/j.jmb.2005.10.012.

[195] E. Finot, L. Markey, F. Hane, M. Amrein, and Z. Leonenko, "Combined atomic force microscopy and spectroscopic ellipsometry applied to the analysis of lipid-protein thin films", *Colloids and Surfaces B: Biointerfaces*, vol. 104, pp. 289–293, 2013, ISSN: 09277765. DOI: 10.1016/j.colsurfb.2012.12.013.

[196] N. Sebaihi, B. De Boeck, Y. Yuana, R. Nieuwland, and J. Pétry, "Dimensional characterization of extracellular vesicles using atomic force microscopy", *Measurement Science and Technology*, vol. 28, no. 3, p. 034 006, 2017, ISSN: 13616501. DOI: 10.1088/1361-6501/28/3/034006.

[197] H. Bayley and C. R. Martin, "Resistive-pulse sensing - from microbes to molecules", *Chemical Reviews*, vol. 100, no. 7, pp. 2575–2594, 2000, ISSN: 00092665. DOI: 10.1021/cr980099g.

[198] R. Vogel, G. Willmott, D. Kozak, G. S. Roberts, W. Anderson, L. Groenewegen, B. Glossop, A. Barnett, A. Turner, and M. Trau, "Quantitative sizing of nano/microparticles with a tunable elastomeric pore sensor", *Analytical Chemistry*, vol. 83, no. 9, pp. 3499–3506, 2011, ISSN: 0003-2700. DOI: 10.1021/ac200195n.

[199] R. Linares, S. Tan, C. Gounou, N. Arraud, and A. R. Brisson, "High-speed centrifugation induces aggregation of extracellular vesicles", *Journal of Extracellular Vesicles*, vol. 4, no. 1, p. 29 509, 2015, PMID: 26700615. DOI: 10.3402/jev.v4.29509.

[200] V Romanov, S. N. Davidoff, A. R. Miles, D. W. Grainger, B. K. Gale, and B. D. Brooks, "A critical comparison of protein microarray fabrication technologies", *Analyst*, vol. 139, no. 6, pp. 1303–1326, 2014, ISSN: 0003-2654. DOI: 10.1039/c3an01577g.

[201] P. Angenendt, "Progress in protein and antibody microarray technology", *Drug Discovery Today*, vol. 10, no. 7, pp. 503–511, 2005, ISSN: 13596446. DOI: 10.1016/S1359-6446(05)03392-1.

[202] Y. Li, Q. Yang, M. Li, and Y. Song, "Rate-dependent interface capture beyond the coffee-ring effect", *Scientific Reports*, vol. 6, p. 24 628, 2016, ISSN: 2045-2322. DOI: 10.1038/srep24628.

[203] H. Hu and R. G. Larson, "Marangoni effect reverses coffee-ring depositions", *Journal of Physical Chemistry B*, vol. 110, no. 14, pp. 7090–7094, 2006, ISSN: 15206106. DOI: 10.1021/jp0609232.

[204] P. Yager, *Adapting an Epson R280 printer to print protein solutions*. [Online]. Available: http://docplayer.net/15568053-Adapting-an-epson-r280-printer-to-print-protein-solutions.html (visited on 03/06/2020).

[205] K. Abe, K. Kotera, K. Suzuki, and D. Citterio, "Inkjet-printed paperfluidic immuno-chemical sensing device", *Analytical and bioanalytical chemistry*, vol. 398, pp. 885–893, 2 2010. DOI: 10.1007/s00216-010-4011-2.

[206] D. J. Cohen, R. C. Morfino, and M. M. Maharbiz, "A modified consumer inkjet for spatiotemporal control of gene expression", *PLOS One*, vol. 4, no. 9, pp. 3–10, 2009, ISSN: 19326203. DOI: 10.1371/journal.pone.0007086.

[207] Epson, "Ultra Hi-Definition R280 Photo Printer", Tech. Rep. [Online]. Available: https://files.support.epson.com/pdf/r280{_}{_}/r280{_}{_}sl.pdf (visited on 11/07/2019).

[208] PC Control Ltd, *Stepper Bee USB adaptor board for motor control from a PC.* [Online]. Available: https://www.pc-control.co.uk/stepperbee{_}plus{_}info.htm (visited on 10/06/2019).

[209] R. Chen and M. Snyder, "Yeast proteomics and protein microarrays", *Journal of Proteomics*, vol. 73, no. 11, pp. 2147–2157, 2010, ISSN: 18743919. DOI: 10.1016/j.jprot.2010.08.003.

[210] World Health Organization, "Identification of intestinal parasites. Bench aids for the diagnosis of intestinal parasites," W.H.O., Tech. Rep., 2012, p. 23. [Online]. Available: https://apps.who.int/iris/bitstream/handle/10665/37323/9789241544764{_}eng.pdf?sequence=1.

[211] M. Mezo, M. González-Warleta, and F. M. Ubeira, "Optimized serodiagnosis of sheep fascioliasis By Fast-D protein liquid chromatography fractionation of *Fasciola hepatica* excretory–secretory antigens", *Journal of Parasitology*, vol. 89, no. 4, pp. 843–849, 2003, ISSN: 0022-3395. DOI: 10.1645/ge-74ri.1.

[212] D. Robles-Perez, J. M. Martinez-Perez, F. A. Rojo-Vazquez, and M. Martinez-Valladares, "The diagnosis of fasciolosis in feces of sheep by means of a PCR and its application in the detection of anthelmintic resistance in sheep flocks naturally infected", *Veterinary Parasitology*, vol. 197, no. 1-2, 277–282, 2013, ISSN: 0304-4017. DOI: {10.1016/j.vetpar.2013.05.006}.

[213] G. Maggioli, F. Silveira, J. M. Martín-Alonso, G. Salinas, C. Carmona, and F. Parra, "A recombinant thioredoxin-glutathione reductase from *Fasciola hepatica* induces a protective response in rabbits", *Experimental Parasitology*, vol. 129, no. 4, pp. 323–330, 2011, ISSN: 00144894. DOI: 10.1016/j.exppara.2011.09.013.

[214] D. Acosta, M. Cancela, L. Piacenza, L. Roche, C. Carmona, and J. F. Tort, " *Fasciola hepatica* leucine aminopeptidase, a promising candidate for vaccination against ruminant fasciolosis", *Molecular and Biochemical Parasitology*, vol. 158, no. 1, pp. 52–64, 2008, ISSN: 01666851. DOI: 10.1016/j.molbiopara.2007.11.011.

[215] J. P. Dalton, M. W. Robinson, G. Mulcahy, S. M. O'Neill, and S. Donnelly, "Immunomodulatory molecules of *Fasciola hepatica*: Candidates for both vaccine and immunotherapeutic development", *Veterinary Parasitology*, vol. 195, no. 3-4, pp. 272–285, 2013, ISSN: 03044017. DOI: 10.1016/j.vetpar.2013.04.008.

[216] C. Harding, J. Heuser, and P. Stahl, "Receptor-mediated endocytosis of transferrin and recycling of the transferrin receptor in rat reticulocytes.", *The Journal of Cell Biology*, vol. 97, no. 2, pp. 329–339, 1983, ISSN: 0021-9525. DOI: 10.1083/JCB.97.2.329.

[217] UKRI, *Improving diagnostics of liver and rumen fluke livestock parasites utilising exosome-like vesicles*, 2018. [Online]. Available: https://gtr.ukri.org/project/AE03441A-4158-45E1-928E-5E7DD7B2D550 (visited on 09/11/2019).

[218] A. V. Vlassov, S. Magdaleno, R. Setterquist, and R. Conrad, "Exosomes: Current knowledge of their composition, biological functions, and diagnostic and therapeutic potentials", *Biochimica et Biophysica ACTA-General Subjects*, vol. 1820, no. 7, pp. 940–948, 2012, ISSN: 0304-4165. DOI: 10.1016/j.bbagen.2012.03.017.

[219] J. G. Kenna, G. N. Major, and R. S. Williams, "Methods for reducing non-specific antibody binding in enzyme-linked immunosorbent assays", *Journal of Immunological Methods*, vol. 85, no. 2, pp. 409–419, 1985, ISSN: 00221759. DOI: 10.1016/0022-1759(85)90150-4.

[220] J. Lucocq, "Chapter 4: Quantification of structures and gold labeling in transmission electron microscopy", in *Introduction to Electron Microscopy for Biologists*, ser. Methods in Cell Biology, vol. 88, Academic Press, 2008, pp. 59 –82. DOI: https://doi.org/10.1016/S0091-679X(08)00404-4.

[221] R. Kaur and M. Raje, "A solid-phase method for evaluation of gold conjugate used in quantitative detection of antigen by immunogold-labeling electron microscopy", *Journal of Immunological Methods*, vol. 279, no. 1, pp. 33 –40, 2003, ISSN: 0022-1759. DOI: https://doi.org/10.1016/S0022-1759(03)00254-0.

[222] R. M. Morphew, T. J. Wilkinson, N. Mackintosh, V. Jahndel, S. Paterson, P. Mcveigh, S. M. Abbas Abidi, K. Saifullah, M. Raman, G. Ravikumar, J. La-Course, A. Maule, and P. M. Brophy, "Exploring and expanding the fatty-acid-binding protein superfamily in *Fasciola* species", *Journal of proteome research*, vol. 15, pp. 3308–3321, 9 2016. DOI: 10.1021/acs.jproteome.6b00331.

[223] R. A. Jones, H. W. Williams, S. Dalesman, S. Ayodeji, R. K. Thomas, and P. M. Brophy, "The prevalence and development of digenean parasites within their intermediate snail host, *Galba truncatula* , in a geographic area where the presence of *Calicophoron daubneyi* has recently been confirmed", *Veterinary Parasitology*, vol. 240, pp. 68–74, 2017, ISSN: 03044017. DOI: 10.1016/j.vetpar.2017.03.021.

[224] Thermo Fisher Scientific, "User guide: Qubit protein assay kits", Tech. Rep. [Online]. Available: https://assets.thermofisher.com/TFS-Assets/LSG/manuals/Qubit{_}Protein{_}Assay{_}UG.pdf.

[225] A. Sirisriro, R. Grams, S. Vichasri-Grams, P. Ardseungneon, V. Pankao, A. Meepool, K. Chaithirayanon, V. Viyanant, P. Tan-Ariya, E. S. Upatham, and P. Sobhon, "Production and characterization of a monoclonal antibody against recombinant fatty acid binding protein of *Fasciola gigantica*", *Veterinary Parasitology*, vol. 105, no. 2, pp. 119 –129, 2002, ISSN: 0304-4017. DOI: 10.1016/s0304-4017(02)00007-9.

[226] L. G. Rikkert, R Nieuwland, L. W. M. M. Terstappen, and F. A. W. Coumans, "Quality of extracellular vesicle images by transmission electron microscopy is operator and protocol dependent", *Journal of Extracellular Vesicles*, vol. 8, 1 2018, ISSN: 2001-3078. DOI: 10.1080/20013078.2018.1555419.

[227] R. Zafra, R. A. Pérez-écija, L. Buffoni, I. L. Pacheco, A. Martínez-Moreno, E. J. LaCourse, S. Perally, P. M. Brophy, and J. Pérez, "Early hepatic and peritoneal changes and immune response in goats vaccinated with a recombinant glutathione transferase sigma class and challenged with *Fasciola hepatica*", *Research in Veterinary Science*, vol. 94, no. 3, pp. 602–609, 2013, ISSN: 00345288. DOI: 10.1016/j.rvsc.2012.10.026.

[228] C. Lässer, S. C. Jang, and J. Lötvall, "Subpopulations of extracellular vesicles and their therapeutic potential", *Molecular Aspects of Medicine*, vol. 60, pp. 1–14, 2018, ISSN: 18729452. DOI: 10.1016/j.mam.2018.02.002.

[229] J. Sotillo, M. Pearson, J. Potriquet, L. Becker, D. Pickering, J. Mulvenna, and A. Loukas, "Extracellular vesicles secreted by *Schistosoma mansoni* contain protein vaccine candidates", *International Journal for Parasitology*, vol. 46, no. 1, pp. 1–5, 2016, ISSN: 00207519. DOI: 10.1016/j.ijpara.2015.09.002.

[230] I. H. Malitson, "Interspecimen comparison of the refractive index of fused silica", *Journal of the Optical Society of America*, vol. 55, no. 10, p. 1205, 1965, ISSN: 0030-3941. DOI: 10.1364/josa.55.001205.

[231] J. Vörös, "The density and refractive index of adsorbing protein layers", *Biophysical Journal*, vol. 87, no. 1, pp. 553–561, 2004, ISSN: 00063495. DOI: 10.1529/biophysj.103.030072.

[232] H. Arwin and I. Lundström, "A reflectance method for quantification of immunological reactions on surfaces", *Analytical Biochemistry*, vol. 145, no. 1, pp. 106–112, 1985, ISSN: 10960309. DOI: 10.1016/0003-2697(85)90334-3.

[233] N. S. K. Gunda, M. Singh, L. Norman, K. Kaur, and S. K. Mitra, "Optimization and characterization of biomolecule immobilization on silicon substrates using (3-aminopropyl) triethoxysilane (APTES) and glutaraldehyde linker", *Applied Surface Science*, vol. 305, pp. 522–530, 2014, ISSN: 01694332. DOI: 10.1016/j.apsusc.2014.03.130. [Online]. Available: http://dx.doi.org/10.1016/j.apsusc.2014.03.130.

[234] B. J. Nehilla, K. C. Popat, T. Q. Vu, S. Chowdhury, R. F. Standaert, D. R. Pepperberg, and T. A. Desai, "Neurotransmitter analog tethered to a silicon platform for neuro-BioMEMS applications", *Biotechnology and Bioengineering*, vol. 87, no. 5, pp. 669–674, 2004, ISSN: 00063592. DOI: 10.1002/bit.20171.

[235] Y. Niu and G. Jin, "Surface modification methods to improve behavior of biosensor based on imaging ellipsometry", *Applied Surface Science*, vol. 281, pp. 84–88, 2013, ISSN: 0169-4332. DOI: 10.1016/j.apsusc.2013.05.077.

[236] S. Lucchini, A. Thompson, and J. C. D. Hinton, "Microarrays for microbiologists", *Microbiology*, vol. 147, no. 2001, pp. 1403–1414, 2001.

[237] J. R. Perkins, I. Diboun, B. H. Dessailly, J. G. Lees, and C. Orengo, "Transient protein-protein interactions: Structural, functional, and network properties", *Structure*, vol. 18, no. 10, pp. 1233–1243, 2010. DOI: 10.1016/j.str.2010.08.007.

[238] Woolam Ltd., *RC2 Specifications*. [Online]. Available: `https://www.qd-latam.com/downloads/28/RC2{\_}Spec{\_}Sheet{\_}2015.pdf` (visited on 10/05/2019).

[239] BioX Ltd., *Bio k 201 - monoscreen agelisa Fasciola hepatica / indirect sandwich, double wells - en*. [Online]. Available: `https://www.biox.com/en/bio-k-201-monoscreen-agelisa-fasciola-hepatica-indirect-sandwich-double-wells-p-257/` (visited on 10/04/2019).

[240] K. Hancock and V. C. Tsang, "Development and optimization of the FAST-ELISA for detecting antibodies to *Schistosoma mansoni*", *Journal of Immunological Methods*, vol. 92, no. 2, pp. 167–176, 1986, ISSN: 00221759. DOI: `10.1016/0022-1759(86)90162-6`.

[241] M. G. Pappas, R. Hajkowski, and W. T. Hockmeyer, "Dot enzyme-linked immunosorbent assay (Dot-ELISA): a micro technique for the rapid diagnosis of *Visceral leishmaniasis*", *Journal of Immunological Methods*, vol. 64, no. 1-2, pp. 205–214, 1983, ISSN: 00221759. DOI: `10.1016/0022-1759(83)90399-X`.

[242] M. Z. Islam, M. Itoh, S. M. Shamsuzzaman, R. Mirza, F. Matin, I. Ahmed, A. K. Shamsuzzaman Choudhury, M. Akram Hossain, X. G. Qiu, N. Begam, M. Furuya, J. L. Leafasia, Y. Hashiguchi, and E. Kimura, "Diagnosis of *Visceral leishmaniasis* by enzyme-linked immunosorbent assay using urine samples", *Clinical and Diagnostic Laboratory Immunology*, vol. 9, no. 4, pp. 789–794, 2002, ISSN: 1071412X. DOI: `10.1128/CDLI.9.4.789-794.2002`.

[243] Thermo Fisher Scientific, *ELISA Kits - UK*. [Online]. Available: `https://www.thermofisher.com/uk/en/home/life-science/antibodies/immunoassays/elisa-kits.html` (visited on 10/05/2019).

[244] A. Jan and H. A. Lashuel, *Cytotoxicity In Vitro using biophysical approaches*, E. Sigurdsson, M. Calero, and M. Gasset, Eds. Humana press, 2012, vol. 849,

ch. 16, pp. 227–243, ISBN: 9781617795510. DOI: 10.1007/978-1-61779-551-0.

[245]   L. Gürtler, "Difficulties and strategies of HIV diagnosis", *Lancet*, vol. 348, no. 9021, pp. 176–179, 1996, ISSN: 01406736. DOI: 10.1016/S0140-6736(96)01036-7.

[246]   S. Usuda, H. Okamoto, H. Iwanari, K. Baba, F. Tsuda, Y. Miyakawa, and M. Mayumi, "Serological detection of hepatitis B virus genotypes by ELISA with monoclonal antibodies to type-specific epitopes in the preS2-region product", *Journal of Virological Methods*, vol. 80, no. 1, pp. 97–112, 1999, ISSN: 01660934. DOI: 10.1016/S0166-0934(99)00039-7.

[247]   A. Roda, E. Michelini, M. Zangheri, M. Di, D. Calabria, and P. Simoni, "Trends in Analytical Chemistry Smartphone-based biosensors : A critical review and perspectives", *Trends in Analytical Chemistry*, vol. 79, pp. 317–325, 2016, ISSN: 0165-9936. DOI: 10.1016/j.trac.2015.10.019.

[248]   L. Jin, Y. Wakako, K. Takizawa, and E. Kondoh, " *In situ* imaging ellipsometer using a LiNbO3 electrooptic crystal", *Thin Solid Films*, vol. 571, pp. 532–537, 2014, ISSN: 00406090. DOI: 10.1016/j.tsf.2014.05.017.

Appendix A

Additional Information and Images

A.1   Derivation of Radiometric Psi and Delta

Taken directly from Cohn via Azzam:

$$E_{AO}^{te} = T_A^{te} R(-C) C_C^{fs} R(C - P) E_{PO}^{te} \tag{A.1}$$

Where superscripts denote the matrix co-ordinate system and subscripts denote the component, R represents transform matrices between reference systems, defined as:

Normalized E field output from the polarizer reference to the transmission (t) extinction(e) axes:

$$E_{PO}^{te} = K_P \begin{bmatrix} 1 \\ 0 \end{bmatrix} \tag{A.2}$$

Compensator; Quarter waveplate matrix reference to the fast (f) and slow (s) axes:

$$T_C^{fs} = K_C \begin{bmatrix} 1 & 0 \\ 0 & \rho_c \end{bmatrix} \tag{A.3}$$

The Sample matrix reference to the x, y axes:

$$T_S^{xy} = \begin{bmatrix} V_{ex} & 0 \\ 0 & V_{ey} \end{bmatrix} \tag{A.4}$$

The analyzer matrix reference to the transmission (t) extinction(e) axes:

$$T_A^{te} = K_A \begin{bmatrix} 1 & 0 \\ 0 & 0 \end{bmatrix} \tag{A.5}$$

The transformation matrix for an axes rotation by angle α The Sample matrix reference to the x, y axes:

$$R(\alpha) = \begin{bmatrix} \cos(\alpha) & \sin(\alpha) \\ -\sin(\alpha) & \cos(\alpha) \end{bmatrix} \tag{A.6}$$

Using equations 2 to 6 equation 1 can be reduced to:

$$E_{AO}^{te} = K_P K_A K_C V_{ey} \left\{ \begin{array}{l} \cos(A)\tan(\Psi)\exp(i\Delta)[\cos(C)\cos(P-C) - \rho_c\sin(C)\sin(P-C)] \\ + \sin(A)[\sin(C)\cos(P-C) + \rho_c\cos(C)\sin(P-C)] \end{array} \right\} \tag{A.7}$$

Where:

$$\frac{V_{ex}}{V_{ey}} = \tan(\Psi)\exp(i\Delta) \tag{A.8}$$

Assuming that for the compensator:

$$\rho_c = \exp(\frac{-i\pi}{2}) = -i \tag{A.9}$$

and setting:

$$G = K_P K_A K_C |V_{ey}| \tag{A.10}$$

the intensity of light exiting the analyzer $I(A)$:

$$I(A) = E_{AO}^{te}(E_{AO}^{te}) = \frac{G^2}{2} \left\{ \begin{array}{l} [1 + \cos(2C) \cdot \cos 2(P - C)] \cdot \cos^2(A) \cdot \tan^2(\Psi) \\[2mm] + [1 - \cos(2C) \cdot \cos 2(P - C)] \sin^2(A) \\[2mm] + [\sin(2C) \cdot \cos 2(P - C) \cos(\Delta) - \sin 2(P - C) \cdot \sin(\Delta)] \\[2mm] \cdot \sin(2A) \cdot \tan(\Psi) \end{array} \right\}$$

(A.11)

as Cohn describes, equation A.11 contains six variables, component angles 'P' and 'C' which can be treated as constants, Analyser 'A' which is adjusted to a minimum of three selected positions and the varying intensity $I(A)$ at the detector is recorded, this then leaves three unknowns: 'G' the system gain, Ψ and Δ. To confirm the integrity of their approach Cohn, Wagner and Kruger used four analyzer positions of 0, 45, 90 and -45 degrees. These angles were inserted into equation A.11 and solved to give:

$$\tan(\Psi) = \left\{ \sqrt{\frac{1 - \cos(2C) \cdot \cos 2(P - C)}{1 + \cos(2C) \cdot \cos 2(P - C)}} \cdot \sqrt{\frac{I(0°)}{I(90°)}} \right\}$$

(A.12)

$$\cos(\Delta) = \left\{ \frac{I(45°) - I(-45°)}{2\sqrt{I(0°)I(90^0)}} \cdot \frac{\tan 2(P - C)}{\sin(2C)} \right\}$$

(A.13)

Using the 1990 work by Cohn which evaluates a Fourier method to determine the radiometric values of Ψ and Δ removing the earlier limit of four analyzer angles and intensity measurements. Equation A.11 can be reformed:

$$I_P = I_{PCSA}(P) = [a \cos^2(P) \cdot \tan^2(\Psi) \begin{array}{l} + b \sin^2(P) + (c \cos(\Delta) \\[2mm] - d \sin(\Delta)) \cdot \sin(2P) \cdot \tan(\Psi)] \end{array}$$

(A.14)

where:

$$a = 1 + \cos(2C) \cdot \cos 2(A - C)$$

$$b = 1 - \cos(2C) \cdot \cos 2(A - C)$$

$$c = \sin(2C) \cdot \cos 2(A - C)$$ (A.15)

$$d = \sin 2(A - C)$$

To quote Cohn "The Fourier series approach is developed by observing that equation A.11 specifies that the measured intensity varies sinusoidally relative to the angle 'P'." Shown by rearranging the terms such that:

$$I_{PCSA}(P) = \frac{G^2}{2}[(a \tan^2(\Psi) + b) \begin{array}{l} + (a \tan^2(\Psi) - b) \cdot \cos(2P) \\ + 2 \tan(\Psi)(c \cos(\Delta) - d \sin(\Delta)) \sin(2P)] \end{array}$$ (A.16)

Cohn restates this in terms of two amplitude co-efficients for the sine and cosine terms:

$$I_{PCSA}(P) = u + v \cos(2P) + w \sin(2P)$$ (A.17)

With the co-efficients u, v and w determined by application of a sequential Fourier series approach to processing of the measured intensity values. Values which can be measured over a full range in equal incremental steps. Such that:

$$I_n = I\left(P_n = \frac{n \cdot \pi}{N}\right) \quad \text{for} \quad n = 1, 2, 3 \ldots N > 5$$

With the Fourier co-efficients described as:

$$u = \frac{1}{N} \sum_{n=0}^{N} I_n$$ (A.18)

$$v = \frac{2}{N} \sum_{n=0}^{N} I_n \cos\left(\frac{4\pi n}{N}\right)$$ (A.19)

$$w = \frac{2}{N} \sum_{n=0}^{N} I_n \sin\left(\frac{4\pi n}{N}\right) \tag{A.20}$$

Which can be used to solve for Ψ and Δ :

$$\tan(\Psi) = \left(\sqrt{\frac{b}{a}}\sqrt{\frac{u+v}{u-v}}\right) \tag{A.21}$$

$$\cos(\Delta) = \left(\frac{w}{\sqrt{u^2 - v^2}}\right) - \arctan\frac{d}{c} \tag{A.22}$$

Dr. Gunn in defining a radiometric algorithm for the AIE, took the approach of Cohn and applied it to the situation where a liquid crystal variable polarizer and retarder can sequentially step change the polarization parameter 'P' and the phase retardance acting as a variable compensator 'C' allowing for the Analyzer angle 'A' to remain fixed.

$$I_{PCSA} = I_O \cdot \begin{cases} \cos^2(A) \cdot \tan^2(\Psi) \cdot [1 + \cos^2(2C) \cdot \cos(2(P-C))] \\ + \sin^2(A) \cdot [1 - \cos(2C) \cdot \cos(2(P-C)) + \cos(\Delta') \cdot \sin(2C) \cdot \sin(2(P-C))] \\ + \sin(2A) \cdot \tan(\Psi) \cdot [\cos(\Delta) \cdot (\sin(2C) \cdot \cos(2(P-C)) \\ + \cos(\Delta') \cdot \cos(2C) \cdot \sin(2(P-C))) - \sin(2(P-C)) \cdot \sin(\Delta) \cdot \sin(\Delta')] \end{cases} \tag{A.23}$$

If N measurements are made for each polarization angle and phase retardance n (not to be confused with refractive index $\tilde{N} and n$) then from the measured intensities.

Setting the phase retardation to zero and the number of polarization angle steps to N equally divided between 0 and 180 degrees:

$$\Delta' = 0 \qquad P_n = \frac{n \cdot \pi}{N} \qquad \text{for} \quad n = 1, 2, 3 \ldots N$$

$$I(P) = U + (V \cdot \cos(2P)) + (W \cdot \sin(2P)) \tag{A.24}$$

$$U = I_o(\cos^2(A)\tan^2 \Psi) + \sin^2(A) = \frac{1}{2\pi}\sum_{n=0}^{N} I(P_n) \tag{A.25}$$

$$V = I_o(\sin^2(A) - \cos^2(A) \cdot \tan^2 \Psi) = \frac{1}{\pi}\sum_{n=0}^{N} I(P_n) \cdot \cos(P_n) \tag{A.26}$$

$$W = I_o\sin(2A) \cdot \tan \Psi \cdot \cos(\Delta) = \frac{1}{\pi}\sum_{n=0}^{N} I(P_n) \cdot \sin(P_n) \tag{A.27}$$

$$\tan(\Psi) = \tan(A)\sqrt{\left(\frac{U-V}{U+V}\right)} \tag{A.28}$$

$$\cos(\Delta) = \frac{W}{U} \cdot \frac{\cos^2(A) \cdot \tan^2(\Psi) + \sin^2(A)}{\sin(2A) \cdot \tan(\Psi)} \tag{A.29}$$

Setting the polarization angle to 90 degrees and varying the phase retardance steps to N equally divided between 0 and 360 degrees:

$$\Delta_n' = \frac{n \cdot 2\pi}{N} \qquad P_n = \frac{\pi}{2} \qquad \text{for} \quad n = 1,2,3\ldots N$$

$$I(\Delta') = X + (Y \cdot \cos(\Delta')) + (Z \cdot \sin(\Delta') \tag{A.30}$$

$$X = I_o(\cos^2(A)\tan^2 \Psi) + \sin^2(A) = \frac{1}{2\pi}\sum_{n=0}^{N} I(\Delta_n') \tag{A.31}$$

$$Y = I_o(\sin^2(A) - \cos^2(A) \cdot \tan^2 \Psi) = \frac{1}{\pi}\sum_{n=0}^{N} I(P_n) \cdot \cos(\Delta_n') \tag{A.32}$$

$$Z = I_o\sin(2A) \cdot \tan \Psi \cdot \cos(\Delta) = \frac{1}{\pi}\sum_{n=0}^{N} I(P_n) \cdot \sin(\Delta_n') \tag{A.33}$$

$$\tan(\Psi) = \tan(A)\sqrt{\left(\frac{X-Y}{X+Y}\right)} \tag{A.34}$$

$$\sin(\Delta) = \frac{-Z}{X} \cdot \frac{\cos^2(A) \cdot \tan^2(\Psi) + \sin^2(A)}{\sin(2A) \cdot \tan(\Psi)} \tag{A.35}$$

$$W = [\sin(2A) \cdot \tan(\Psi) \cdot \cos(\Delta)] \cdot I_p \tag{A.36}$$

$$I_P = \frac{U}{(\cos^2(A) \cdot \tan^2(\Psi)) + \sin^2(A)} \tag{A.37}$$

Hence:

$$(W \cdot \cos^2(A) \cdot \tan^2(\Psi)) + (W \cdot \sin^2(A)) = U \cdot \sin(2A) \cdot \tan(\Psi) \cdot \cos(\Delta) \tag{A.38}$$

So:

$$\cos(\Delta) = \frac{(W \cdot \cos^2(A) \cdot \tan^2(\Psi)) + (W \cdot \sin^2(A))}{U \cdot \sin(2A) \cdot \tan(\Psi)} \tag{A.39}$$

$$I_? = \frac{X}{(\cos^2(A) \cdot \tan^2(\Psi)) + \sin^2(A)} = \frac{Y}{(\sin^2(A) - \cos^2(A) \cdot \tan^2(\Psi))} \tag{A.40}$$

Hence:

$$\frac{\cos^2(A) \cdot \tan^2(\Psi)}{X} + \frac{\sin^2(A)}{X} = \frac{\sin^2(A)}{Y} - \frac{\cos^2(A) \cdot \tan^2(\Psi)}{Y} \tag{A.41}$$

$$\cos^2(A) \cdot \tan^2(\Psi)\left(\frac{1}{Y} - \frac{1}{X}\right) = \sin^2(A)\left(\frac{1}{Y} - \frac{1}{X}\right) \tag{A.42}$$

$$\tan^2(\Psi) = \tan^2(A)\left(\frac{X-Y}{XY}\right) \cdot \left(\frac{XY}{X+Y}\right) = \tan^2(A)\left(\frac{X-Y}{X+Y}\right) \tag{A.43}$$

$$\tan(\Psi) = \tan(A)\sqrt{\left(\frac{X+Y}{X-Y}\right)} \tag{A.44}$$

To find Delta from X & Z

$$\frac{-\sin(2A) \cdot \tan(\Psi) \cdot \sin(\Delta)}{Z} = \frac{\cos^2(A) \cdot \tan(\Psi)) + \sin^2(A)}{X} \tag{A.45}$$

Re-arranging for Δ

$$\sin(\Delta) = \frac{-Z((\cos^2(A) \cdot \tan(\Psi)) + \sin^2(A))}{X(\sin(2A)\tan(\Psi))} \tag{A.46}$$

Cleaning Silicon Wafers RCA-1 Method

Standard Operating Procedure: 12-01-16

Overview:
This method of cleaning silicon wafers was first developed by Werner Kern and co-workers, James Amick and Arthur Stoller, in the early 1960's at the RCA laboratories as the first part of a two-step process to remove trace contaminants that may contaminate the production of semi-conductor devices.

The process works by oxidative desorption of organic residues with $H_2O_2 - NH_4OH - H_2O$ in a ratio of 1-1-5 respectively, at a temperature of 70-80ºC.

Time Scale:
The process takes approximately 30-40 minutes to complete.

Safety Equipment:
Gloves, lab coat, safety glasses.

Materials:
Hydrogen peroxide (H_2O_2 30%), ammonium hydroxide (NH_4 OH 27%), de-ionized water glass bath container, hot plate

Preparation:
Setup should take 5 minutes with a further 10 minutes to heat the solution followed by 15 minutes soak and 5 minutes to rinse and dry.

The recipe is 5 parts de ionized water (H_2O), 1 part 27% ammonium hydroxide (NH_4OH) and 1 part 30% hydrogen peroxide (H_2O_2).

Procedure:
Place 50ml of de-ionized water into a fused glass (Pyrex) beaker and add 10ml of 27% ammonium hydroxide (NH_4OH). Heat the mixture to $75º \pm 5º$ centigrade. Remove from the hot plate and add 10ml of 30% hydrogen peroxide (H_2O_2). The solution will bubble indicating that the wafers can be added for cleaning. Allow to soak for 15 minutes.

Once complete. remove the wafers and transfer to a second beaker filled and constantly overflowing with DI water to dilute and remove any remaining cleaning solution. Remove each wafer under flowing water and dry using a gentle stream of nitrogen.

Cleaning up:
RCA1 is a mixture of ammonia and bleach which, once cooled, can be disposed by diluting and flushing with cold water down a standard drain. Do not keep old solution for re-use.

Safety:
All standard lab safety practices must be followed. The RCA1 process should only be conducted in a fume hood, using nitrile gloves, lab coat and safety glasses. Never leave the process unattended, hydrogen peroxide is an explosive chemical and should not be stored near a source of heat or ignition. Small spills should be absorbed with blue roll immediately. Large spills should be contained with a lab spill kit and reported.

In case of contact with skin or eyes, flush the area immediately with water for 10-15 minutes and remove any contaminated clothing. Seek attention from a first aider to help minimise any chemical burns and ensure correct reporting.

Centrifuge Protocol for the Isolation of Extracellular Vesicles

Based on: Thery, Clayton, et al "Isolation and Characterization of Exosomes from Cell Culture Supernatants and Biological Fluids" C P Cell Bio (2006) 3.22.1-3.22.29

John Tomes ▸ Aberystwyth University ▸ Revision: 01 Date: 15-Sep-17

Summary Flow Chart:
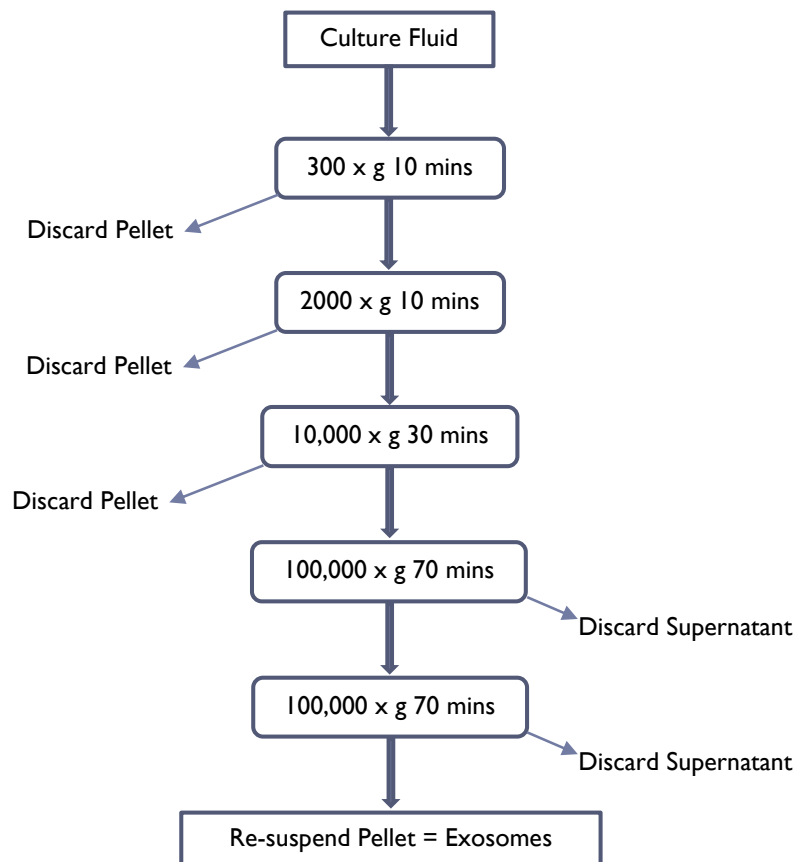
Centrifuge Protocol for the Isolation of Extracellular Vesicles

Based on: Thery, Clayton, et al "Isolation and Characterization of Exosomes from Cell Culture Supernatants and Biological Fluids" C P Cell Bio (2006) 3.22.1-3.22.29

The aim of this protocol is to isolate extracellular vesicles from culture fluids. It is specifically tailored to concentrate exosomes in the range 25-125nm diameter. Each step describes the 'g' forces and duration required. Example rpm for specific centrifuges are given, clearly this will change if you use different centrifuges or rotors http://www.sciencegateway.org/tools/rotor.htm may help if you need to make changes.

The protocol described in steps 1to 6 can be represented by model, a plot of which is shown in figure 1. The plot shows particle diameter and the percentage of that particle size which should be collected from the initial culture media into the final pellet. An Excel spreadsheet that calculates and plots this model can be used to evaluate any changes you may wish to make to some or all of the protocol steps. For example, variations in spin speed, tube volume or duration are easily adjusted. However, changes in media and particle densities, temperature, viscosity etc. can also be incorporated. It is available for download at: https://www.dropbox.com/s/ddexstf50uut553/Centrifuge%20Calculator.xlsx?dl=0

Step1: Remove cells and large debris.

1) Place 25ml of culture fluid containing EV's into clean falcon tubes.
2) Ensure tubes are balanced to 0.2 gram.
3) Centrifuge in a swing bucket rotor 300x g for 10 minutes at 4°C.
4) Carefully pipette off 23 to 24ml of supernatant leaving behind the pellet of cells and debris as undisturbed as possible.

For the Eppendorf SW-A-4-81 (eg. The unit in botany) 25ml @ 1350 rpm = Average effective g of 310x.
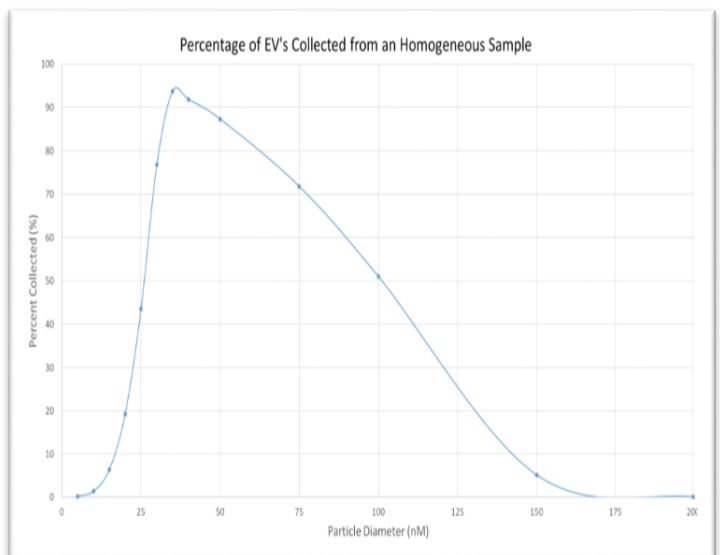
Figure 1.

Step 2: Remove dead cells.

1) Place 23ml of supernatant from step 1 into fresh Falcon tubes.
2) Ensure tubes are balanced to 0.2 gram.
3) Centrifuge in a swing bucket rotor at 2000x g for 10 minutes at 4°C.
4) Carefully pipette off 21to 22ml of supernatant leaving behind the pellet of cells and debris as undisturbed as possible.

For the Eppendorf SW-A-4-81 (eg. The unit in botany) 23ml @ 3400 rpm = an average effective g of 1986x.

Step 3: Remove cellular debris.

1) Place 21ml of supernatant from step 2 into clean polycarbonate ultra-centrifuge tubes.
2) Ensure tubes are balanced to 0.02 gram.
3) Mark one side of the tube with waterproof marker and align in the rotor to help indicate pellet position.
4) Centrifuge in the 50.2ti rotor at 10,000x g for 30 minutes at 4°C.
5) Carefully pipette off the supernatant and keep. Leave behind a small amount liquid to avoid disturbing the pellet.
6) Clean the tubes (see notes).

For the Beckman Ultra XL with 50.2Ti rotor 21ml @ 10,000 rpm = Average effective g of 10,600x

Step4: Pellet exosomes and loose protein.

1) Place 21ml of supernatant from step 3 into clean polycarbonate ultra-centrifuge tubes.
2) Ensure tubes are balanced to 0.02 gram.
3) Mark one side of the tube with waterproof marker and align in the rotor to help indicate pellet position.
4) Centrifuge in the 50.2ti rotor at 100,000x g for 70 minutes at 4°C.
5) Pour off the supernatant, (which can be then stored at -80 °C for other work) removing it as completely as possible.
6) Re-suspend the pellet in 1ml PBS using a pipette. Gently washing the pellet free from the wall of the tube.

For the Beckman Ultra XL with 50.2Ti rotor 21ml @ 30,800 rpm = Average effective g of 100,680x

Step 5: Wash to remove most protein.

1) Add a further 15ml of PBS to the tube and gently vortex for a few seconds to mix.
2) Balance the tubes to 0.02 grams.
3) Mark one side of the tube with waterproof marker and align in the rotor to help indicate pellet position.
4) Centrifuge in the 50.2ti rotor at 100,000x g for 70 minutes at 4°C.

7) Again pour off the supernatant, removing it as completely as possible.

For the Beckman Ultra XL with 50.2Ti rotor 16ml @ 30,300 rpm = Average effective g of 100,430x

Step 6: Final re-suspension of exosomes.

1) To re-suspend the pellet add a small volume of PBS (50 to 100µl) and aspirate onto the pellet using a pipette. Gentle vortexing may help.
2) Place in aliquots of convenient size and store at -80 °C. Avoid repeated freeze thaw cycles.

Ultra tubes: Cleaning and notes on use.

To clean polycarbonate ultra-centrifuge tubes:

- Wash by hand with a mild detergent diluted around 10-to-1 with distilled water.
- Quarter fill the tubes with 10% Hydrogen Peroxide (H_2O_2) and vortex for 2 mins. Rinse 4 times with double distilled water and allow to air dry naturally.

Notes:

- Polycarbonate tubes should not be exposed to a detergent with a pH higher than 8.
- Tubes and caps should not be washed in dishwashers, temperatures and detergents are too harsh.
- Solvents such as ethanol or acetone react unfavorably with polycarbonate and should not be used. Consult bulletin IN-175 for a table of tube material/solvent compatibilities, available:
  https://www.beckmancoulter.com/ucm/idc/groups/public/documents/webasset/glb_bci_149441.pdf
- If modifying the protocol do not fill ultra tubes with any less than 16ml of liquid, it leads to rapid failure of the tube and a risk of implosion.

▶Protocol for Gold Labeling of Extracellular Vesicles

John Tomes ▶ Aberystwyth University ▶ 16-Feb-18

Summary Flow Chart:

Prepare EVs

↓

Adsorb EVs on to TEM grids

↓

Gold Label + Glutaraldehyde fix

↓

Contrast Stain with Uranyl Oxalate

↓

Embed with Methyl Cellulose

↓

Observe at 80kV
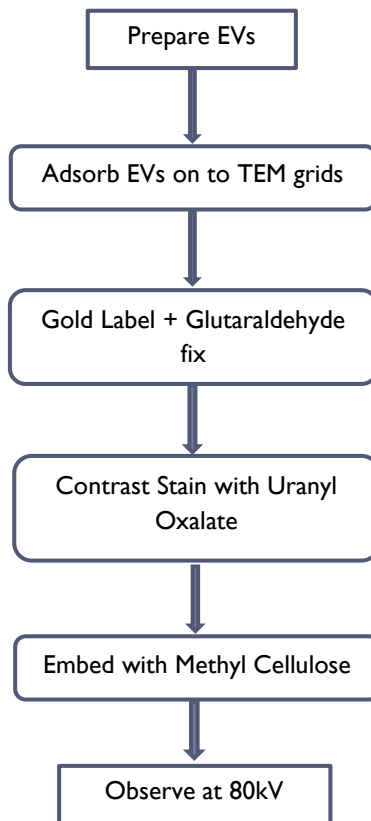
Protocol for Gold Labeling of Extracellular Vesicles

Taken from: Théry, Clayton, et al "Isolation and Characterization of Exosomes from Cell Culture Supernatants and Biological Fluids" C P Cell Bio (2006) 3.22.1-3.22.29

The aim of this protocol is to Immuno Gold Label extracellular vesicles (EVs) for observation by transmission electron microscopy (TEM).

The protocol that is described in steps 1 to ? is proposed by Théry and Clayton et al (2006) as a simple and reliable method for the visualization of EV preparations.

Recipes for the various reagents are given in the notes section.

Important points:

Drops of reagents are placed on areas of clean Parafilm and grids are transferred between drops by careful use of forceps or (recommended) a stainless steel loop fabricated as described in the notes section.

It is important to keep the Formvar coating on TEM grids wet at all times on the side of EV adsorption but dry on the opposite side.

Step1: Prepare the EVs.

1) Thaw purified EVs that are frozen.
2) Mix with an equal volume of 4% Paraformaldehyde (PFA).
3) EVs in 2% PFA can be stored at 4°C for 1 week.

Step 2: Adsorb EVs onto TEM grids.

1) Place 5 to 10 µl of prepared PFA EV solution onto clean parafilm.
2) Float a Formar-carbon coated TEM grid on the droplet, film side facing the EV solution.
3) Cover and let the EVs adsorb for 20 minutes in a dry environment.

Step 3: Wash in PBS.

1) Place 100 µl of PBS onto an area of clean Parafilm.
2) Transfer the grid, membrane side down, floating it on the PBS droplet to wash twice for 3 minutes.

Step4: Glycine quench.

1) Place 50µl of PBS/50mM glycine solution onto a clean area of Parafilm and transfer the grid to it (as before and with all subsequent operations, membrane side facing the solution).
2) Allow to stand for 3 minutes.
3) Repeat for a total of 4 washes.

Step 5: Block Non-specific binding sites.

1) Transfer the grid to a 100 µl drop of CTM-T and allow to stand for 10 minutes.

Step 6: Incubate with antibody.

1) Transfer the grid to a 5 µl drop of the first antibody, which has been suitably diluted in CTM-T.
2) Allow to stand for 30 minutes.

Step 7: Wash the sample.

1) Transfer the grid to a 100 µl drop of CTM-T and allow to stand for 10 minutes.
2) Repeat for a total of 6 washes.

Step 8: Incubate second antibody.

1) Transfer the grid to a 5 µl drop of secondary gold labeled antibody suitably diluted in CTM-T and allow to stand for 20 minutes.
2) Transfer the grid to a 100 µl drop of PBS and allow to stand for 2 minutes.
3) Repeat for a total of 8 washes.

Step 9: Stabilize antibody reaction.

1) Transfer the grid to a 50 µl drop of 1% Glutaraldehyde for 5 mins.
2) Transfer the grid to a 100 µl drop of DDH$_2$O and wash for 2 mins
3) Repeat for a total of 8 washes.

Step 10: Contrast and stain as per Protocol 4.

Observation under the TEM at 80kV should reveal cup shaped membrane vesicles. It is thought that this characteristic morphology is a result of the processing protocol and not a fundamental feature of EVs.

Example TEM micrographs are shown in figures 1 to 4.
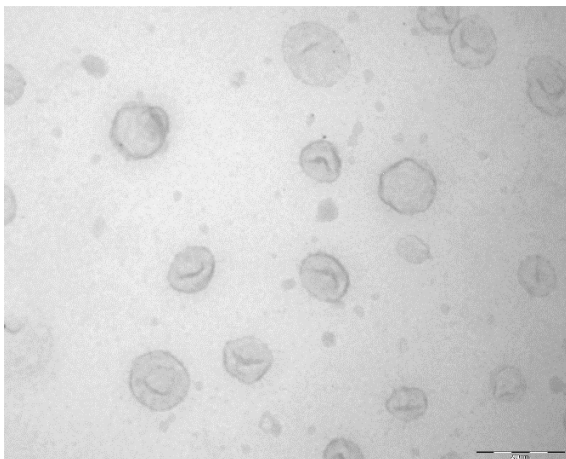
Figure 1: Rumen fluke (*C. daubneyi*) EVs that have been trypsin shaved of surface exposed proteins.
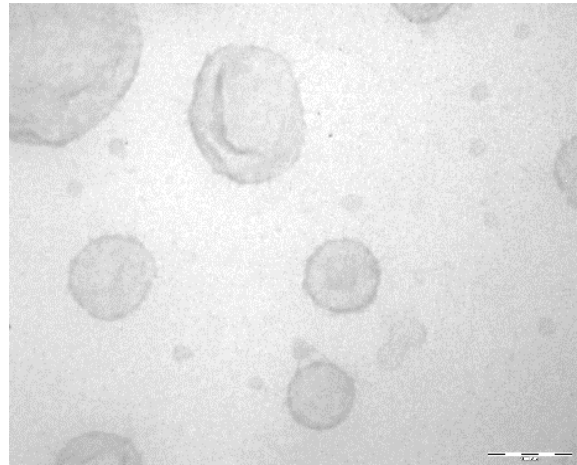
Figure 2: Rumen fluke (*C. daubneyi*) close up.
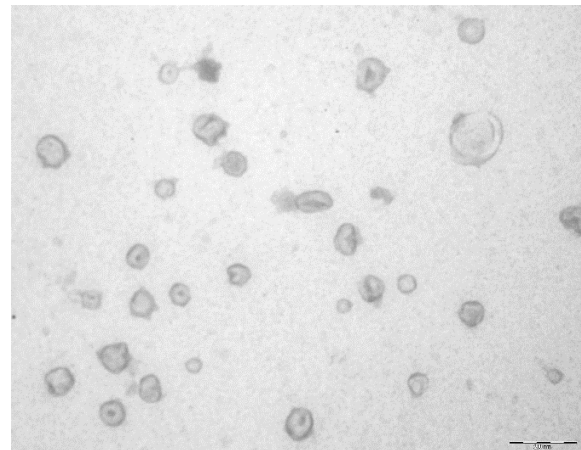
Figure 3: Liver fluke (*F.hepatica*) EVs.
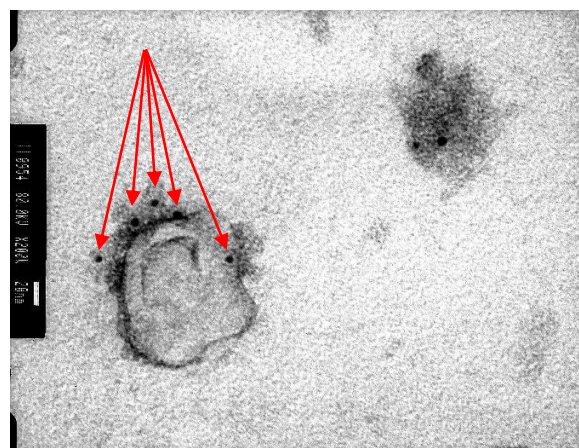
Figure 4. Close up of liver fluke (*F.hepatica*) EV Immunogold labeled (Arrows indicate 5nm gold particles).

Notes: Recipes for reagents used.

Sodium phosphate buffer 0.1 M

Add 3.1 g of $NaH_2PO_4 \cdot H_2O$ and 10.9 g of Na_2HPO_4 (anhydrous) to distilled water to make a volume of 1000 mL. Check the pH of the final solution which should be 7.4. This buffer can be stored for up to 1 month at 4°C.

Paraformaldehyde (PFA) 4% (w/v)

Dissolve 4 grams of PFA powder in 45ml of 0.1 M sodium phosphate buffer and heat to 65°C while stirring. If needed add drops of 1M NaOH (sodium hydroxide) until the solution clears. Bring to 50ml using 0.1M sodium phosphate buffer. Cool and filter, store at -20 °C in 5ml aliquots. Use immediately on thawing and do not refreeze.

Glutaraldehyde 1% (v/v)

Dilute the stock glutaraldehyde fixative that you have (typically 8%, 25% or 70%) to 1% dilution using Sodium Phosphate buffer 0.1M. Store at -20 °C for up to 6 months and then after thawing up to 1 week at 4 °C

Uranyl acetate (4%w/v) pH4

Dissolve 2 grams of uranyl acetate powder into 50 ml of distilled water. Just before use pass the amount needed through a 0.22µm syringe filter. Store remaining stock solution at 4 °C for up to 4 months protected from light.

Caution: This material is mildly radioactive and toxic. Follow the relevant institute guidelines on safe use and disposal.

Uranyl-Oxalate solution (pH7)

Prepare a 0.15 M solution of oxalic acid by dissolving 0.945 grams of oxalic acid powder in 50ml of distilled water.

Mix a 1:1 ratio of: 4% Uranyl acetate and oxalic acid solution. Adjust the pH to 7 by adding 25%(w/v) NA_4OH in drops. Store at 4°C for up to 1 month protected from light.

Methyl Cellulose-UA

Heat 196 ml of distilled water to 90°C and add 4 grams of methyl cellulose powder while stirring. Rapidly cool on ice to 10°C while constantly stirring. Continue slow stirring overnight at 4°C. Stop stirring and allow solution to stand for 3 days at 4°C. Bring to a final volume of 200ml with distilled water. Place the solution in Ultra tubes and centrifuge at 100,000xg for 95 minutes at 4°C. Collect the supernatant and store for up to 3 months at 4°C.

Mix 1 part 4% UA with 9 parts 2% methyl cellulose. Mixed just before use.

Picture1 Shows a stainless steel loop used for handling TEM grids. It is made by holding a loop of stainless steel wire in pliers and twisting a 4mm diameter steel rod round and round until the wire tightens against the rod forming a tight loop. The loop is the glued to a pipette tip using epoxy resin.

Picture 1

RESEARCH ARTICLE

The importance of extracellular vesicle purification for downstream analysis: A comparison of differential centrifugation and size exclusion chromatography for helminth pathogens

Chelsea N. Davis ⓘ *[☾], Helen Phillips[‡], John J. Tomes ⓘ [‡], Martin T. Swain[‡], Toby J. Wilkinson[‡¤], Peter M. Brophy[‡], Russell M. Morphew[☾]

Institute of Biological, Environmental and Rural Sciences, Aberystwyth University, Aberystwyth, United Kingdom

[☾] These authors contributed equally to this work.
¤ Current address: The Roslin Institute and R(D)SVS, University of Edinburgh, Edinburgh, United Kingdom
‡ These authors also contributed equally to this work.
* chd31@aber.ac.uk

Abstract

Background

Robust protocols for the isolation of extracellular vesicles (EVs) from the rest of their excretory-secretory products are necessary for downstream studies and application development. The most widely used purification method of EVs for helminth pathogens is currently differential centrifugation (DC). In contrast, size exclusion chromatography (SEC) has been included in the purification pipeline for EVs from other pathogens, highlighting there is not an agreed research community 'gold standard' for EV isolation. In this case study, *Fasciola hepatica* from natural populations were cultured in order to collect EVs from culture media and evaluate a SEC or DC approach to pathogen helminth EV purification.

Methodology/Principal findings

Transmission electron and atomic force microscopy demonstrated that EVs prepared by SEC were both smaller in size and less diverse than EV resolved by DC. Protein quantification and Western blotting further demonstrated that SEC purification realised a higher EV purity to free excretory-secretory protein (ESP) yield ratio compared to DC approaches as evident by the reduction of soluble free cathepsin L proteases in SEC EV preparations. Proteomic analysis further highlighted DC contamination from ESP as shown by an increased diversity of protein identifications and unique peptide hits in DC EVs as compared to SEC EVs. In addition, SEC purified EVs contained less tegumental based proteins than DC purified EVs.

Conclusions/Significance

The data suggests that DC and SEC purification methods do not isolate equivalent EV population profiles and caution should be taken in the choice of EV purification utilised, with certain protocols for DC preparations including more free ES proteins and tegumental artefacts. We propose that SEC methods should be used for EV purification prior to downstream studies.

Author summary

Recent pathogen research has identified extracellular vesicle (EV) release from many organisms. EVs are small membrane bound organelles, which have different origins, sizes and composition. It is important that the optimal EV purification method is realised in order to obtain high quality EVs to have confidence in understanding EV biology and function. In this study, the zoonotic parasite, *Fasciola hepatica*, was cultured as a case study to investigate the importance of EV purification from helminth culture media. Investigating two purification methods, it was found that size exclusion chromatography EV isolation led to a reduction of contaminating excretory-secretory and tegumental proteins. This research highlighted that purification methods do not isolate equivalent EV population profiles with similar EV purities and that size exclusion chromatography methods are likely better suited for downstream helminth EV studies and application development, compared to a differential centrifugation method.

Introduction

Extracellular vesicle (EV) purification is challenging to standardise due to the diversity of sample composition producing EVs (cell cultures and body fluids), the need for high recovery of functional EVs, the quality of EV preparation and the simplicity of isolation [1–5]. Therefore, there is no current gold standard for EV isolation [6].

The most widely accepted method to isolate EVs involves differential centrifugation (DC). This method encompasses sequential centrifugations, increasing in speed and time, to pellet particles decreasing in size [1,2,4–11]. DC is highly reliable, yet it is a labour-intensive procedure, requiring large sample volumes to obtain low EV yields [2,4,12]. Furthermore, EV yield and purity is dependent upon DC parameters such as the rotor type, centrifugal force, centrifugation period and temperature [4,11,13]. Consequently, protocol standardisation is difficult, leading to incomparable EV characterisation and functional investigations [4,5]. To overcome EV purification challenges, many downstream EV investigations require further isolation procedures to accommodate DC, to improve sample purity and validate research analysis.

Recently, size exclusion chromatography (SEC) has been used to successfully purify EVs. SEC has been observed to separate protein aggregates and lipoproteins from EV samples as well as preclude EV or protein aggregation [1,3,4,9,14–16]. However, elution fractions containing a high yield of protein, also contain small EVs (<75 nm), meaning SEC can be selective upon EV size collection. In addition, the purest vesicle elution fraction post SEC produces low yields, so the quantity of fraction collection is dependent upon the EV purity needed for experimental investigation [14]. However, research has observed that SEC EV isolation produces greater sample purity, compared to DC and precipitating agents (Polyethylene glycol and

PRotein Organic Solvent PRecipitation, PROSPR) as evidenced by EV markers (Alix and CD9) in greater concentration intensity in EV samples [2,15,17]. Potentially, SEC could be reproducible in all research settings, as it is easy to use, removes most contaminating proteins and maintains EV morphology.

Many studies in independent laboratories confirm both pathogenic flatworm and nematode helminths produce EVs, albeit during *in vitro* ex-host experimentation. Of note is the recent expansion of information on the EVs of the liver fluke *Fasciola hepatica*. Fascioliasis, infection with either *F. hepatica* or *F. gigantica*, is a major neglected zoonotic disease that infects humans and ruminant species worldwide [18,19]. At least 2.4 million people are currently infected in over seventy countries, with millions more at risk of this food borne disease [20]. Furthermore, the disease is a significant animal health and food security issue, costing the global livestock industry an excess of $3 billion *per* annum [21]. In the absence of protective vaccines, control is usually via anthelmintics, with triclabendazole (TCBZ) being the drug of choice, especially for acute disease caused by pathogenic juvenile *F. hepatica*. *F. hepatica* resistance towards TCBZ has spread widely, threatening future chemotherapeutic based control [22]. Therefore, the development of novel approaches and options for *F. hepatica* control must be considered a research and government priority.

The recent discovery of *F. hepatica* EVs identified in excretory-secretory products (ESP) has led to us re-evaluating the host-pathogen interface [23,24]. EVs of pathogen origin are enriched with pathogen molecules, thus they could potentially be utilised for improved control. In pathogens, EVs have been found to function to either promote or inhibit host immunity with recognised EV immunogenic properties highlighting EVs as vaccine preparations [25]. Furthermore, EVs have the ability to transport molecules to recipient cells, which could be utilised for drug delivery [26]. Therefore, EVs have a major role in pathogen infection and could be exploited to develop novel therapeutic approaches. Thus, it is important that the optimal EV purification method is utilised to obtain high purity EVs, which represent the whole biological EV population that would likely interact with the host environment.

Furthermore, given that all parasitic helminth EV studies completed to date have utilised DC without further EV enrichment, it is vital for the field to look at alternative EV isolation strategies [23,24,27–35]. This is particularly pertinent given the need for more functional studies into EV biology thus requiring EVs of high purity. Literature suggests that SEC is a suitable EV purification method to compare against DC purification methodology, which has been primarily used in helminthology, for the aim of investigating the most advantageous method for purifying helminth EVs from culture media for further downstream analysis, where EVs isolated are a biological representation of the helminth EV population. Therefore, in the current study, the EVs from adult *F. hepatica*, as a model pathogenic helminth, have been purified allowing the comparison of SEC EV purification, to the widely accepted method of DC EV preparation.

This study has discovered that SEC EV isolation leads to smaller sized and lower diversity EV populations, with importantly a higher EV purity to free ESP yield, a less diverse EV proteome and different EV gene enrichment profiles compared to DC purified EVs. Therefore, the data suggests that DC and SEC purification methods do not isolate equivalent EV population profiles and caution should be taken in the choice of EV purification utilised with functional assays incorporated into the isolation pipeline. This research has highlighted SEC methods with functional assays as the methodology of choice for helminth pathogen EV studies and application development in the absence of a gold standard purification method.

Methods

F. hepatica collection and culture

A local collaborating abattoir (Wales, U.K.), where animals were processed as part of the normal work of the abattoir, gave consent for the collection of live adult *F. hepatica* from naturally infected ovine livers of animals immediately post-slaughter, where *F. hepatica* were maintained as previously described [36]. Briefly, *F. hepatica* were thoroughly washed in phosphate buffered saline (PBS) at 37˚C to remove host material. *F. hepatica* were then transported to the laboratory in *Fasciola* saline (Dulbecco's modified Eagle's medium (DMEM) (w/o NaHPO$_3$ and PO$_4$) plus 2.2 mM Ca (C$_2$H$_3$O$_2$), 2.7 mM MgSO$_4$, 61.1 mM glucose, 1 μM serotonin, 5 μg/mL gentamycin, 15 mM N-2-hydroxyethylpiperazine-N′-2-ethanesulfonic acid (HEPES), pH7.4) at 37˚C for 1 hour. Following incubation, *F. hepatica* were maintained in fresh *Fasciola* saline (1 ml/ *F. hepatica*) at 37˚C for 5 hours. All *F. hepatica* remained alive after *in vitro* culture incubations. Both *F. hepatica* and the culture media was immediately frozen and stored at -80˚C, until further experimentation.

EV purification: differential centrifugation (DC)

EVs were purified from the culture media based on the method according to Thery *et al.* [37] with slight modifications. In brief, culture media was centrifuged at 300 *x g* for 10 minutes at 4˚C and then at 700 *x g* for 30 minutes at 4˚C, removing any large particulates. The supernatant was ultracentrifuged at 100,000 *x g* for 80 minutes at 4˚C (Optima L-100 XP ultracentrifuge (Beckman Coulter, High Wycombe, UK) using a Type 50.2 Ti rotor) and the EV depleted culture media was removed and stored at -80˚C. Of note, the 10,000 *x g* centrifugation step for 30 minutes carried out by Thery *et al.* [37] was not undertaken within the current methodology to ensure isolation of the whole biological EV population. Therefore, it should be acknowledged that debris may be still present in the EV enriched sample. The pellet was washed in PBS and vortexed until the pellet had been suspended in solution. The ultracentrifugation step was repeated and the supernatant was discarded. The pellet was then re-suspended in 200 μl PBS by vortexing and stored at -80˚C until further experimentation.

EV purification: Size exclusion chromatography (SEC)

Culture media was centrifuged at 300 *x g* for 10 minutes at 4˚C and then at 700 *x g* for 30 minutes at 4˚C, removing any large particulates. The sample was then concentrated using 10 KDa MWCO Amicon Ultra-15 Centrifugal Filter Units (Merck Millipore), following the manufacturer's guidelines. Briefly, the sample was centrifuged at 4000 *x g* for 20 minutes at 4˚C, until approximately 500 μl of sample was retained in the filter. Filtration flow through was stored at -80˚C. The sample was passed through qEVoriginal SEC columns (IZON science), utilising the manufacturer's optimised protocol. Briefly, the column was rinsed with 10 ml of filtered (0.2 μm, Life Sciences) PBS. The sample was then added to the SEC column and the first 2.5 ml of flow through was discarded. The next 2.5 ml of flow through, containing EVs, was collected and stored at -80˚C. The column was then washed with 10 ml PBS, which was combined with the filtration flow through to create EV depleted SEC ESP.

Transmission electron microscopy (TEM)

EV samples and culture media, containing *F. hepatica* ESP depleted of EVs, were fixed onto formvar/carbon coated copper grids (agar scientific) by adding 10 μl sample to the grid for 45 minutes on ice. Grids were then placed on the viscous of 4% v/v uranyl acetate for five minutes on ice. Grids were stored at room temperature for at least 24 hours before being imaged using

the transmission electron microscope (Jeol JEM1010 microscope at 60 kV). Images were developed and the size of 200 EVs per purification method were measured (nm) using imageJ (https://imagej.nih.gov/ij/) and statistically analysed by Mann-Whitney U test in R studio (https://www.rstudio.com/).

Atomic force microscopy (AFM)

EV samples were diluted 1:10 with deionised water and adsorbed onto freshly cleaved mica sheets (Agar Scientific AGG250-1) for two minutes and dried under a nitrogen stream. Samples were then scanned with a Park Systems E100 AFM, using silicon probes (NT-MTD: NSG-01 & NSG-03PT) in non-contact mode. Topographic height and phase images were scanned at 512 x 512 pixels at a rate of 0.2 Hz. Images were analysed using Gwyddion software (www.gwyddion.net/).

Sodium dodecyl sulfate polyacrylamide gel (SDS-PAGE) electrophoresis

F. hepatica somatic sample was prepared by homogenising *F. hepatica* in homogenisation buffer (20 mM potassium phosphate buffer (pH 7.4), 0.1% (v/v) triton X-100 and protease inhibitor tablets, EDTA-free) (0.5 ml/ *F. hepatica*) on ice, before centrifuging at 21,000 $x\,g$ at 4˚C for 30 minutes. The supernatant was termed the cytosolic fraction, and was stored at -20˚C until further experimentation.

Culture media, containing *F. hepatica* ESP depleted from EVs from both purification methods, was precipitated with an equal volume of ice-cold 20% (w/v) trichloroacetic acid (TCA) in acetone for one hour at -20˚C. The sample was centrifuged at 21,000 x g, 4˚C for 20 minutes. The pellet was washed twice in ice-cold acetone with centrifugation 21,000 x g, 4˚C for 20 minutes between washes. The pellet was left to air dry at -20˚C for 15 minutes, before being resuspended in PBS and stored at -20˚C until further experimentation.

EV samples were centrifuged at 100,000 x g at 4˚C for 30 minutes and the supernatant was discarded. Lysis buffer (PBS, 0.1% (v/v) triton X-100 and protease inhibitor tablets, EDTA-free) was added to the pellet and the sample was sonicated for 30 seconds and then rested on ice for 30 seconds and repeated three times. Following lysis, the sample was centrifuged at 100,000 x g at 4˚C for 30 minutes and the soluble fraction in the supernatant was TCA precipitated as above and stored at -20˚C until further use. The insoluble fraction was washed following the protocol of Hart *et al.* [38]. Briefly, the pellet was re-suspended in sodium carbonate buffer (0.1 M Na_2CO_3 (pH 11), 10 mM EDTA, 20 mM DTT and protease inhibitor tablets, EDTA-free), vortexed and left for one hour at 4˚C. The sample was then centrifuged at 100,000 x g at 4˚C for 30 minutes and the supernatant was discarded. The pellet was washed in sodium carbonate buffer, vortexed, left for 30 minutes at 4˚C and centrifuged as previously described. This wash step was repeated before the pellet was re-suspended in solubilisation buffer (20 mM potassium phosphate (pH 7.4), 4% SDS (w/v) and protease inhibitor tablets, EDTA-free). The sample was heated to 95˚C for five minutes and then stored at -20˚C until further experimentation.

Samples were quantified using either the bicinchoninic acid assay (Thermo scientific) or Bradford assay (Sigma), following the manufacturer's protocol. Comparisons between sample protein concentrations were statistically analysed using Kruskal-Wallis test with the Dunn's Post-hoc test using Sidak correction in R package (https://www.r-project.org/), where significance was considered p<0.05. Laemmli protein 4 x sample buffer (Bio-rad) was added to the sample (3:1 ratio) and heated to 95˚C for 10 minutes. The samples were then loaded into 7 cm 12.5% Tris/glycine polyacrylamide gels and run using the Protean III system (Bio-Rad). Gels were run at 70 V, until the dye front passed through the stacking gel, and then the voltage was

increased to 150 V until completion. Gels were fixed (40% ethanol (v/v), 10% acetic acid (v/v)) and stained with colloidal Coomassie Brilliant blue (Sigma). Gels were imaged using the GS-800 calibrated densitometer (Bio-rad).

Western blotting

Samples were prepared and run upon SDS-PAGE gels as previously mentioned. Gels were electrophoretically transferred onto Hybond-C extra nitrocellulose paper (GE Healthcare) using a Trans-Blot Cell at 40 V for two hours in transfer buffer (192 mM Glycine, 25 mM Tris-HCL (pH 8.3), 20% (v/v) methanol) according to the method of Towbin *et al*. [39]. Transfer efficiency was determined by staining the membrane with amido black (0.1% amido black (w/v), 10% acetic acid (v/v), 25% isopropanol (v/v)) for one minute. The membrane was then destained (10% acetic acid (v/v) and 25% isopropanol (v/v)), and washed three times in Tris buffered saline (100 mM Tris-HCL (pH 7.5), 0.9% sodium chloride (w/v)) with 1% Tween 20 (v/v) (TTBS). The membrane was then blocked overnight in TTBS and 5% skimmed milk powder (v/v) on a rocker at 4˚C.

Primary antibody, either anti-glutathione transferase sigma class (Anti-FhGST-S1) at 1:20,000 [40], Anti-*Fasciola* cathepsin L1 at 1:6,000 (Anti-FhCat-L1) which was commercially made (Lampire) from polyclonal antibodies to a purified recombinant cathepsin L1 from *F. hepatica* expressed in yeast and raised in rabbits or Anti-fatty acid binding protein V (Anti-FhFABP-V) at 1:2,000 which was commercially made (Lampire) from polyclonal antibodies to a purified recombinant fatty acid binding protein V from *F. hepatica* expressed in yeast and raised in rabbits, in TTBS and 1% skimmed milk (v/v) was added to blocked membranes. Anti-FhGST-S1 and Anti-FhCat-L1 primary antibodies are known to have high specificity however, Anti-FhFABP-V is known to be reactive to FABP I, FABP II, FABP III and FABP V. The membrane was rocked for one hour at room temperature. The membrane was then washed three times for five minutes in TBS. The secondary antibody (IgG, anti-rabbit IgG (whole molecule) conjugated to alkaline phosphatase (AKP, Sigma) dilution 1: 30,000) in TTBS was then added to the membrane and rocked for one hour at room temperature. Membrane washing was then repeated as previously described. Recognised proteins were visualised using 5-bromo-4-chloro-3-indoyl phosphate/nitro blue tetrazolium liquid substrate system. In brief, 33 μl 5-bromo-4-chloro-3-indoyl phosphate (50 mg/ml) and 330 μl nitro blue tetrazolium (10 mg/ml) was added to 10 ml substrate buffer (0.1 M Tris, 100 mM sodium chloride, 5 mM magnesium chloride, (pH 9.5)). The detection solution was added to the membrane on the rocker at room temperature until either visualisation of banding occurred or up to five minutes. The reaction was stopped by water washes. Membranes were scanned using the GS-800 calibrated densitometer (Bio-rad).

In-gel tryptic digestion, mass spectrometry and protein identification

All protein bands were excised from one dimensional SDS-PAGE electrophoresis and digested as described in Morphew *et al*. [41]. Briefly, protein bands were washed in 50% (v/v) acetonitrile and 50% (v/v) 50 mM ammonium bicarbonate at 37˚C until destained. Destained bands were dehydrated in 100% acetonitrile at 37˚C for 15 minutes, before being removed and dried at 50˚C. Protein bands were then incubated with 10 mM dithiothreitol in 50 mM ammonium bicarbonate for 30 minutes at 80˚C. The supernatant was discarded before bands were incubated with 55 mM iodoacetamide in 50 mM ammonium bicarbonate for 20 minutes at room temperature in the dark. The supernatant was discarded and the bands were washed twice for 15 minutes at room temperature with 50% (v/v) acetonitrile and 50% (v/v) 50 mM ammonium bicarbonate. Excess was removed before 100% acetonitrile was added to the bands at room

temperature for 15 minutes. The supernatant was removed and bands were dried at 50˚C. Bands were rehydrated and digested using 50 mM ammonium bicarbonate containing trypsin (modified trypsin sequencing grade, Roche, UK) at 10 ng/µl at 37˚C overnight. The supernatant was stored, before 100% acetonitrile was added to the bands at room temperature for 15 minutes, followed by adding 50 mM ammonium bicarbonate to the bands at room temperature for 15 minutes. This step was repeated and from each step, the supernatant was removed and pooled for each band. The 100% acetonitrile step was repeated, and supernatant pooled, before the samples were vacuum dried (Maxi dry plus, Heto) and re-suspended in 20 µl of 0.1% (v/v) formic acid for tandem mass spectrometry.

Liquid Chromatography tandem mass spectrometry (Agilent 6550 iFunnel Q-TOF) coupled to a HPLC-Chip (1200 series, Agilent Technologies, Cheshire, UK) was used for peptide separations. The HPLC-Chip/Q-TOF system was equipped with a capillary loading pump (1200 series, Agilent Technologies) and a nano pump (1200 series, Agilent Technologies). Sample injection was conducted with a micro auto sampler (1100 series, Agilent Technologies), where 1 µl of sample in 0.1% formic acid was loaded on to the enrichment column at a flow of 2.5 µL/min followed by separation at a flow of 300 nL/min. A Polaris Chip was used (G4240-62030, Agilent Technologies), comprising a C18 enrichment/trap column (360 nl) and a C18 separation column (150 mm x 75 Âµm), where ions were generated at a capillary voltage of 1950 V. The solvent system was: solvent A (ultra-pure water with 0.1% formic acid), and solvent B (90% acetonitrile with 0.1% formic acid). The liquid chromatography was performed with a piece-linear gradient using 3–8% of solvent B over 0.1 minutes, 8–35% solvent B over 14.9 minutes, 35–90% solvent B over five minutes and hold at 90% solvent B for two minutes. Tandem mass spectrometry was performed in AutoMS2 mode in the 300–1700 Da range, at a rate of 5 spectra per second, performing MS2 on the 5 most intense ions in the precursor scan. Masses were excluded for 0.1 minutes after MS/MS was performed. Reference mass locking was used for internal calibration using the mass of 391.2843 Da.

Peak lists were generated with Mass Hunter Qualitative Analysis software (V B.06, Agilent Technologies) and exported as Mascot Generic Files. Samples were processed following Morphew *et al.* [42]. Briefly, samples were submitted to MASCOT daemon (Matrix Science, v2.4.1) MS/MS ions search against *F. hepatica* gene sequences, accessed through WormBase ParaSite (http://parasite.wormbase.org/, accession PRJEB6687, version WBPS9). Search parameters included setting the enzyme to trypsin with one missed cleavage allowed, setting fixed modifications to carbamidomethylation with variable modifications set for oxidation of methionine, fixing monoisotopic masses with unrestricted protein masses with peptide and fragment mass tolerances at ±1.2 Da and ±0.6 Da respectively (project accession PXD008737). Protein identifications were reported at a false discovery rate of 1%. For the overall list of proteins identified (data in S1 File), only proteins with at least 2 unique peptides and present in both biological replicates (n = 2) were selected. Protein sequences were searched using BLAST2GO (https://www.blast2go.com/) obtaining BLAST descriptions and gene ontology terms (data in S2 File). Gene ontology enrichment analysis was completed using GOATOOLS python package (https://github.com/tanghaibao/goatools) (data in S4 File) where the GO terms were not propagated up the hierarchy and $p < 0.05$ identified significance.

Results

EV morphological characteristics

In order to assess EV morphology post DC and SEC purification, both atomic force microscopy (AFM) and transmission electron microscopy (TEM) imaging were utilised. AFM and TEM identified that EV structures were characteristically diverse in size and morphology
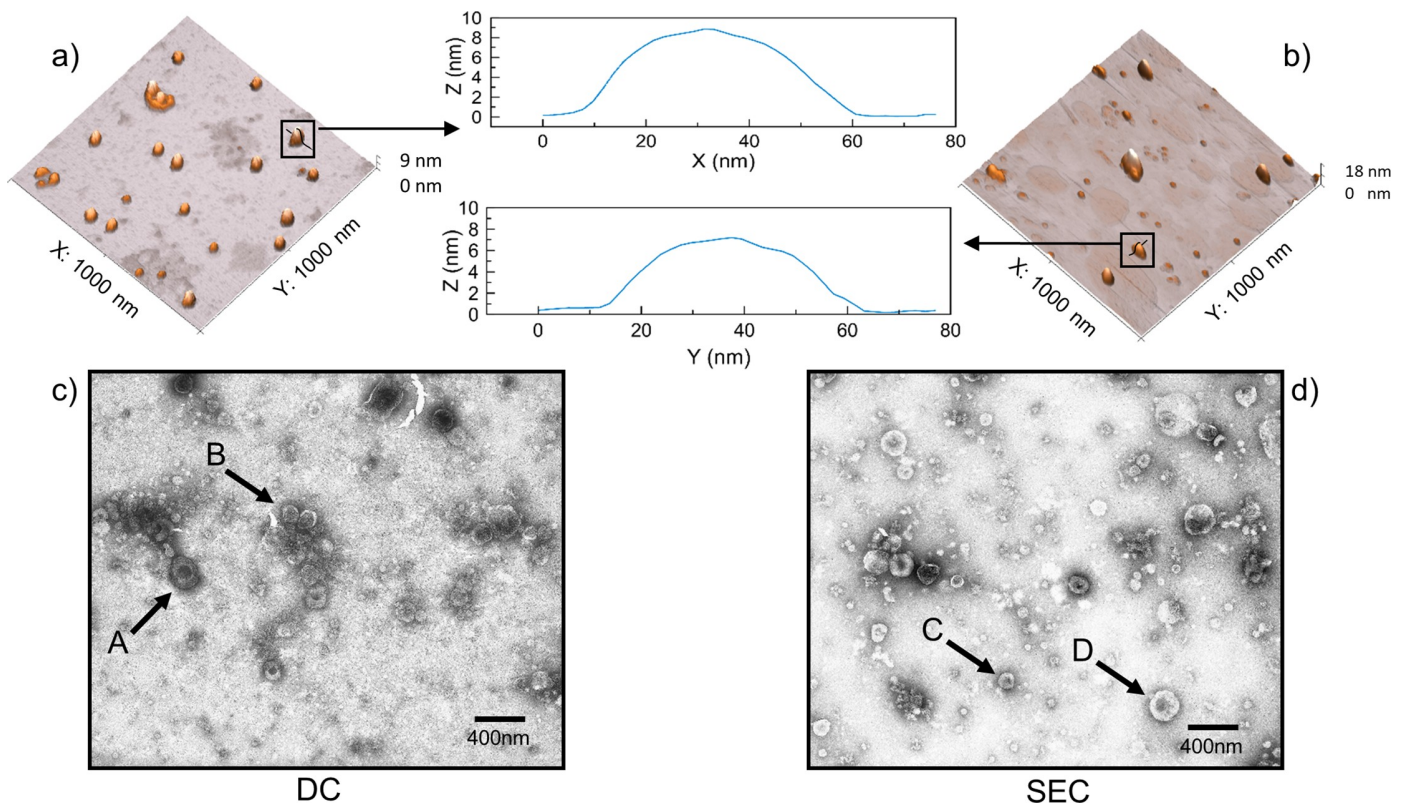
Fig 1. Topography profiles and micrographs of extracellular vesicles purified via differential centrifugation and size exclusion chromatography. Representative atomic force microscopy topography profiles (A and B) and transmission electron microscopy images (C and D) of extracellular vesicles purified from adult *F. hepatica* via differential centrifugation (A and C) and size exclusion chromatography (B and D). The central graphs represent individual extracellular vesicle topography from each purification method as determined by atomic force microscopy. Profiles identified that extracellular vesicle structures were similar using both differential centrifugation and size exclusion chromatography purification methods although size exclusion chromatography purified extracellular vesicles were significantly smaller (76 nm ± 44 SD) than differential centrifugation extracellular vesicles (95 nm ± 58 SD) (W = 14,726, p < 0.001) and differential centrifugation purified extracellular vesicles with a greater range of extracellular vesicle sizes than size exclusion chromatography (differential centrifugation range = 505 nm, size exclusion chromatography range = 285 nm). Arrows on TEM images highlight different sized EVs where A = 130.5 nm, B = 235.0 nm, C = 111.7 nm and D = 226.4 nm.

using both DC and SEC purification methods, representing a biological population of EVs ([Fig 1]). When comparing EV dimensions following TEM analysis, SEC EVs were significantly smaller (76 nm ± 44 SD) than DC EVs (95 nm ± 58 SD) (n = 200) (W = 14,726, p < 0.001) and DC purified EVs displayed a greater range of EV sizes than SEC (DC range = 505 nm, SEC range = 285 nm). All observed EVs were intact in TEM images for both purification methods. Aggregation of EVs and contaminants in the image background was observed using both purification methods in AFM and TEM images.

TEM micrographs produced for the culture media containing *F. hepatica* ESP depleted of EVs identified few EVs (data not shown). In addition, EVs were not found within the ultrafiltration flow through during the SEC purification method (data not shown). In all non-EV preparations debris and additional non-EV contaminants were identified.

EV comparative protein concentrations

EV preparations obtained from both DC and SEC purification methods were quantified for protein content for ESP (protein content for residual ESP after EV purification), whole lysed EV samples and soluble and insoluble EV fractions ([Fig 2]). All samples quantified were

Fig 2. Protein quantification of extracellular vesicle preparation fractions from differential centrifugation and size exclusion chromatography purification. Fractions produced from either differential centrifugation or size exclusion chromatography methods (excretory-secretory protein, whole lysed extracellular vesicle, soluble extracellular vesicle protein and insoluble extracellular vesicle protein) were assayed for protein levels and statistically analysed (Kruskal-Wallis test, with Dunn's Post-hoc test using Sidak correction) for differences. Asterisks identify significance where $p < 0.05$.

unrelated biological replicates. Analysis of the EV preparation via the DC purification method revealed comparable protein quantities between ESP (average = 30 μg, n = 3) and whole lysed EV samples (average = 40 μg, n = 3), even though the whole lysed EV samples had greater quantity variation (ESP range = 20 μg, whole lysed EV range = 140 μg). However, this protein profile was not replicated for SEC derived EV preparations. Protein quantity of SEC ESP was nearly threefold that of the lysed EV samples (ESP average = 240 μg, n = 3, whole lysed EV average = 80 μg, n = 3), even though whole lysed EV samples had a greater quantity variation (ESP range = 90 μg, whole lysed EV range = 180 μg). Furthermore, SEC purified samples produced a higher protein yield than DC in both ESP and whole lysed EV samples, with ESP showing a significant increase (D = -3.13, p = 0.02, n = 3). Similarly, SEC produced a greater protein yield of soluble and insoluble EV fraction protein (soluble protein average = 170 μg, n = 9, insoluble protein average = 210 μg, n = 9) than DC (soluble protein average = 30 μg, n = 9, insoluble protein average = 60 μg, n = 9). Both EV purification methods showed that there was a greater protein quantity of insoluble EV protein compared to soluble EV protein, with the SEC soluble fraction containing significantly less protein than insoluble protein fraction (D = -0.43, p = 0, n = 9).

EV comparative proteome analysis

Whole lysed EV and ESP samples displayed different protein profiles as observed by one dimensional sodium dodecyl sulfate-polyacrylamide gel (SDS-PAGE) electrophoresis, suggesting that both EV purification methods selectively isolate EVs away from *F. hepatica* secretions
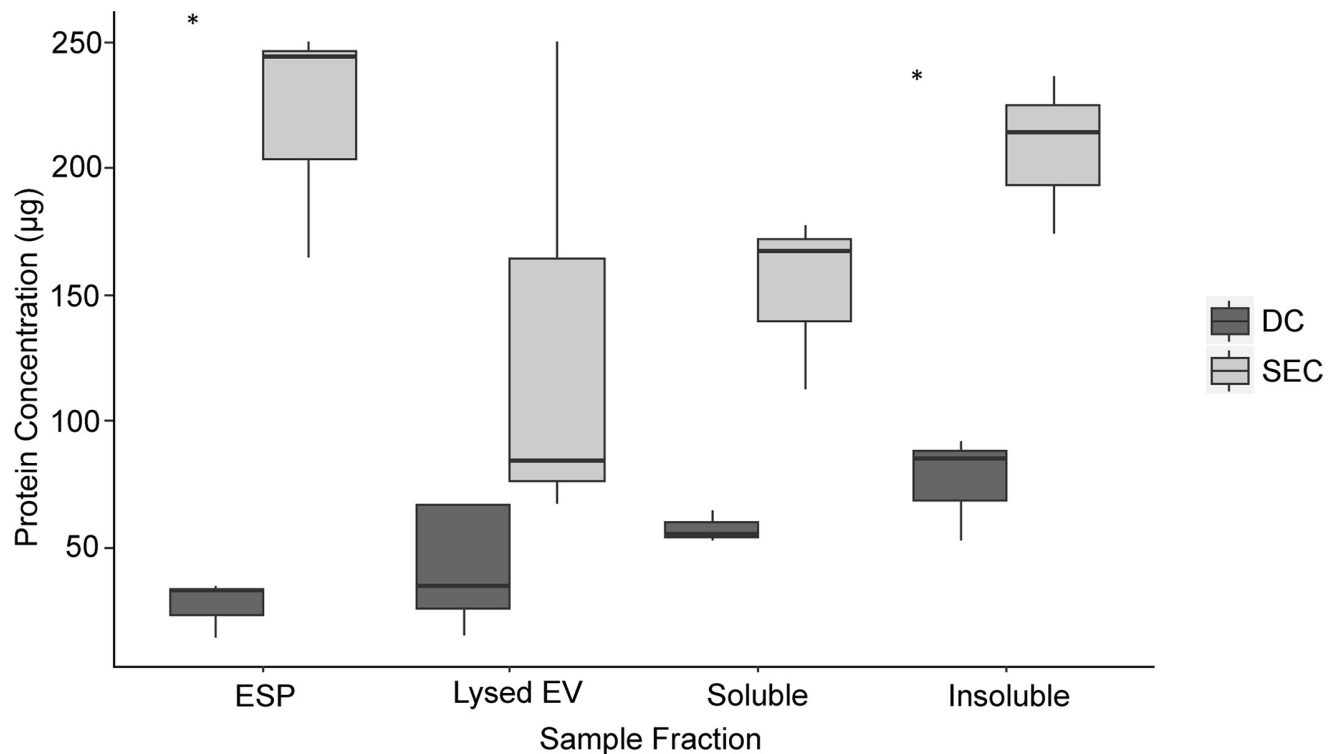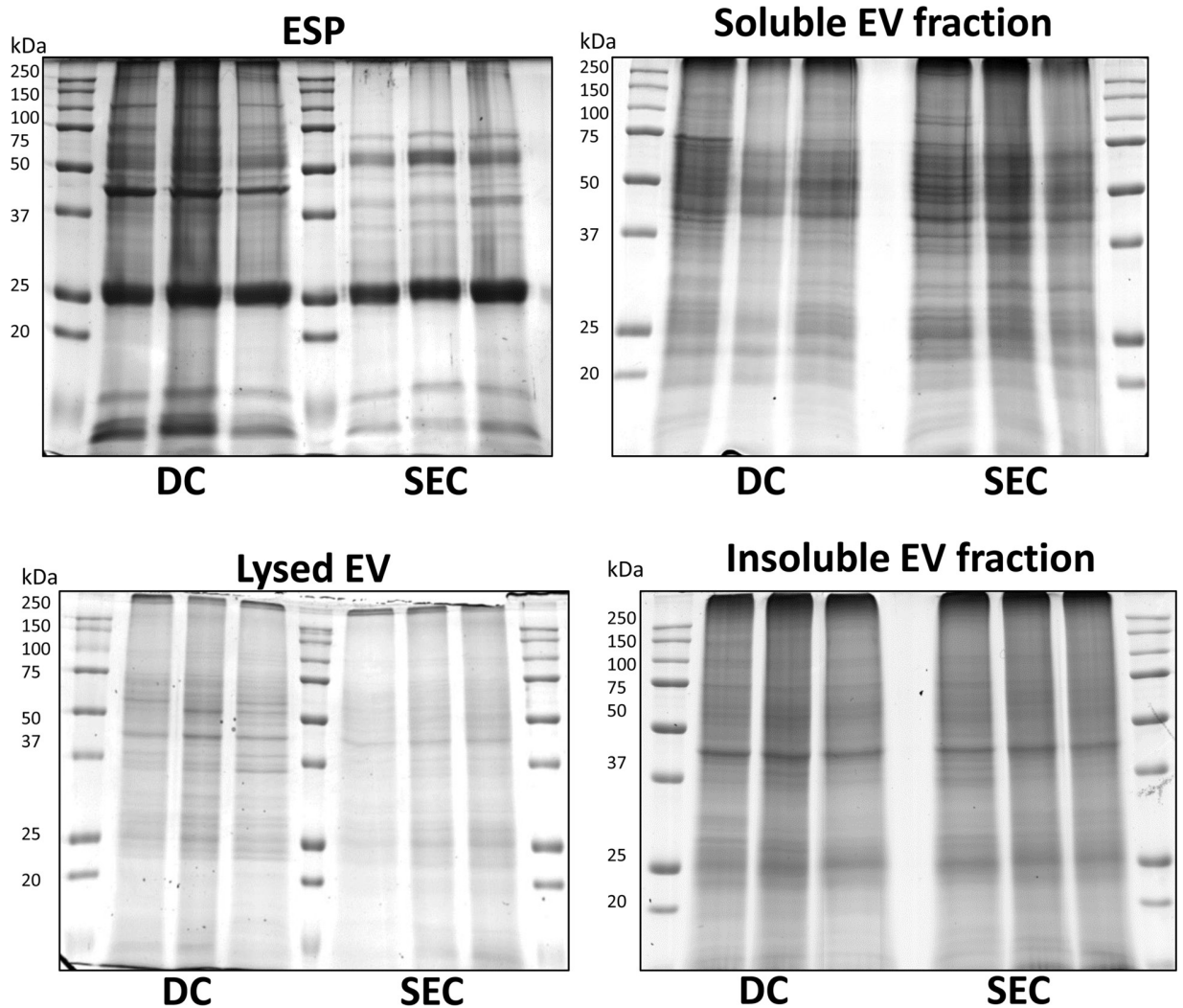
Fig 3. Protein profiles of extracellular vesicle fractions from differential centrifugation and size exclusion chromatography purification.
Biological triplicate protein profiles as observed by one dimensional SDS-PAGE electrophoresis of excretory-secretory protein (10 μg protein), whole lysed extracellular vesicle (10 μg protein), soluble extracellular vesicle protein (20 μg protein) and insoluble extracellular vesicle protein (20 μg protein). All proteins were run on 12.5% SDS-PAGE electrophoresis gels and Coomassie blue stained.

https://doi.org/10.1371/journal.pntd.0007191.g003

or ESP (Fig 3). In addition, biological replication of EV preparations indicated that protein quantification and preparation was reproducible as all sample replicates produced comparable protein banding patterns. Comparing lysed EV preparation protein profiles using DC and SEC purification methods, banding differences were identifiable, especially between 50–100 kDa and 25–37 kDa markers. Differences were less noticeable within the protein profiles of the soluble and insoluble EV fraction proteins and between the method by which the EVs were purified.

Following SDS-PAGE, mass spectrometry was employed to identify key differences between the profiles from a combined analysis of the soluble and insoluble EV protein fractions from SEC and DC isolated EVs. Following analysis, SEC purification revealed 68% protein matching between the soluble and insoluble SEC EV fractions with a 63% similarity of proteins for DC purified soluble and insoluble fractions. Following the combination of the

soluble and insoluble protein identifications the whole SEC and DC purified EV proteomes were further analysed to identify key protein differences between the purification methods. Interestingly, 77% of proteins were comparable between SEC biological replicates and 77% between DC biological replicates.

In DC purified EVs, 392 proteins were identified, while 321 proteins were observed using SEC purification across both replicates. Of these proteins, 276 were comparable between purification methods demonstrating differences and similarities between the two methodologies. When looking at unique proteins to each method, 116 proteins were found exclusively in DC purified EVs and 45 proteins were found exclusively in SEC purified EVs (data in S5 File). Gene ontology analysis identified that EV proteins mostly showed biologically function in organic substance and primary metabolic processes as well as single-organism cellular processes irrespective of EV purification method (S6 File). These categories encompass proteins such as cathepsin L and GAPDH. However, there were significant differences in gene ontology terms such as catabolic process and microtubule-based process which were only found in DC purified EVs, while many more 'regulatory-cell invasion' terms (i.e. cellular localisation and response to stress) were only found in SEC purified EVs. Catabolic process and microtubule-based process only found in DC purified EVs refers to proteins such as Mov34/MPN/PAD-1 family protein, ubiquitin—protein ligase and alpha-tubulin. While, 'regulatory-cell invasion' terms only found in SEC purified EVs includes ADP-ribosylation factor family protein, T-complex protein 1 zeta subunit and glutathione peroxidase. Considering molecular function, transmembrane transporter activity and substrate-specific transporter activity gene ontology terms were only identified in SEC purified EVs including proteins such as IC domain protein HAD ATPase P-type family and hypothetical proteins. For cellular components, catalytic complex and intrinsic component of the membrane were the only categories found uniquely in EVs purified from DC including multicatalytic endopeptidase, ATPase family protein and proteasome subunit alpha domain protein and cell periphery, cell projection, plasma membrane, plasma membrane part and plasma membrane region were the only unique components found in EVs purified from SEC including IC domain protein, HAD ATPase, P-type family, ADP-ribosylation factor family protein and hypothetical proteins.

When specifically looking at protein identifications, DC EVs consistently demonstrated a greater amount of unique peptides hit per protein than SEC. The top 50 proteins found in EVs purified using SEC were also present in the DC EV purified proteome. However, proteins relating to gene scaffolds BN1106_s90B000599 (ATPase family protein), BN1106_s1277 B000102 (HSP90 protein), BN1106_s63B000395 (hypothetical protein D915_01544) and BN1106_s285B000846 (unnamed protein product) were found in the top 50 proteins of DC purified EVs, but were not present in the SEC isolated EV proteome (highlighted within Table 1). Common EV markers from ExoCarta database (http://www.exocarta.org/) present in the top 50 EV proteins using both purification methods included heat shock proteins, glyceraldehyde-3-phosphate dehydrogenase, actin, 14-3-3 protein, annexin and tubulin. Unique EV markers, gelosin and phosphoglycerate kinase were found in the top 50 EV protein hits using DC purification, while a tetraspanin EV marker was found in the top 50 protein hits using SEC purified EVs.

EV proteins unique to SEC or DC purification were further investigated to assess the likelihood of non-EV contamination in each preparation likely from *F. hepatica* ESP or the tegument using data from recent proteomic studies (data in S5 File) [23,24,43–46]. Of the 45 proteins identified in SEC purified EVs only, 7 proteins were observed previously in ESP with 11 proteins identified previously in tegumental preparations. Looking at the 116 proteins identified in DC purified EVs only, 11 proteins were previously observed in ESP proteomic studies with an additional 27 proteins located in tegumental proteomic studies. Of note is the reduced

Table 1. Top 50 extracellular vesicle protein accessions purified by differential centrifugation and size exclusion chromatography. BLAST descriptions were chosen upon the lowest E-value hit and top accessions were identified by the highest unique peptide hits. Data analysed using BLAST2GO. Highlighted cells in grey shading signify proteins identified in the top 50 proteins of DC or SEC purified EVs, but were not present in the full EV proteome of the opposite purification methodology. Full protein identifications can be found in S3 File.

	Size Exclusion Chromatography					Differential Centrifugation			
Rank	Sequence ID	Description	Unique Peptide Hits	Total Peptide Hits	Rank	Sequence ID	Description	Unique Peptide Hits	Total Peptide Hits
1	BN1106_s3182B000117	myosin heavy chain	115	437	1	BN1106_s3182B000117	myosin heavy chain	135	605
2	BN1106_s309B000234	heat shock protein 70	109	1659	2	BN1106_s309B000234	heat shock protein 70	120	1906
3	BN1106_s1300B000145	SJCHGC06288 protein	100	1994	3	BN1106_s1300B000145	SJCHGC06288 protein	107	2046
4	BN1106_s175B000200	hexokinase	97	1440	4	BN1106_s1320B000236	heat shock protein 90	104	843
5	BN1106_s819B000364	annexin A7	96	1480	5	BN1106_s819B000364	annexin A7	99	1812
6	BN1106_s3585B000136	myoferlin	95	669	6	BN1106_s4069B000247	alpha-actinin	98	880
7	BN1106_s617B000566	leucine amino peptidase	94	1528	7	BN1106_s617B000566	leucine amino peptidase	97	1460
8	BN1106_s4069B000247	alpha-actinin	87	633	8	BN1106_s1403B000129	hypothetical protein	94	1627
9	BN1106_s2907B000133	hypothetical protein	86	1441	9	BN1106_s1871B000313	programmed cell death 6-interacting protein	93	902
10	BN1106_s1403B000129	hypothetical protein	82	964	10	BN1106_s2907B000133	hypothetical protein	92	1777
11	BN1106_s274B000296	Adenosine Triphosphate binding cassette subfamily	82	749	11	BN1106_s175B000200	hexokinase	92	1344
12	BN1106_s945B000218	Annexin	81	663	12	BN1106_s3585B000136	myoferlin	90	736
13	BN1106_s3227B000227	phosphopyruvate hydratase	78	567	13	BN1106_s90B000599	Adenosine Triphosphase family protein	89	200
14	BN1106_s2471B000098	PREDICTED: phosphatidylcholine translocator ABCB4	77	635	14	BN1106_s2471B000098	PREDICTED: phosphatidylcholine translocator ABCB4	86	572
15	BN1106_s1320B000236	heat shock protein 90	77	521	15	BN1106_s3904B000042	14-3-3 protein	83	1029
16	BN1106_s1871B000313	programmed cell death 6-interacting protein	76	851	16	BN1106_s606B000246	alpha-tubulin	83	787
17	BN1106_s233B000262	hypothetical protein	74	527	17	BN1106_s3227B000227	phosphopyruvate hydratase	82	598
18	BN1106_s246B000252	phosphoenolpyruvate carboxykinase	69	602	18	BN1106_s246B000252	phosphoenolpyruvate carboxykinase	81	909
19	BN1106_s204B000249	calpain	69	546	19	BN1106_s945B000218	Annexin	80	712
20	BN1106_s2349B000188	severin	69	462	20	BN1106_s7079B000034	hypothetical protein	80	615
21	BN1106_s3261B000048	otoferlin	65	360	21	BN1106_s2697B000090	leucine Rich repeat-containing domain protein	80	500
22	BN1106_s1081B000242	chain A, Sigma class glutathione S-transferase	64	472	22	BN1106_s274B000296	Adenosine Triphosphate binding cassette subfamily	78	669
23	BN1106_s500B000161	annexin	63	413	23	BN1106_s233B000262	hypothetical protein	76	484
24	BN1106_s3904B000042	14-3-3 protein	62	846	24	BN1106_s2907B000132	actin	75	805
25	BN1106_s2615B000090	dysferlin	61	449	25	BN1106_s1153B000359	tubulin beta-4	71	619
26	BN1106_s468B000343	xaa-pro dipeptidase	60	851	26	BN1106_s2349B000188	severin	70	1062
27	BN1106_s3747B000112	hypothetical protein	60	529	27	BN1106_s4469B000065	fructose-bisphosphate aldolase class I	68	622
28	BN1106_s4252B000085	uncharacterized protein	60	475	28	BN1106_s5174B000030	glyceraldehyde-3-phosphate dehydrogenase	68	408
29	BN1106_s658B000223	hypothetical protein	58	825	29	BN1106_s3261B000048	otoferlin	68	386
30	BN1106_s7079B000034	hypothetical protein	58	531	30	BN1106_s658B000223	hypothetical protein	67	929
31	BN1106_s686B000273	14-3-3 protein	54	480	31	BN1106_s500B000161	Annexin	67	544

(Continued)

Table 1. (Continued)

Size Exclusion Chromatography					Differential Centrifugation				
Rank	Sequence ID	Description	Unique Peptide Hits	Total Peptide Hits	Rank	Sequence ID	Description	Unique Peptide Hits	Total Peptide Hits
32	BN1106_s3266B000046	annexin	54	381	32	BN1106_s4860B000047	Tubulin beta chain	66	748
33	BN1106_s2091B000373	DnaK family protein	54	278	33	BN1106_s2615B000090	Dysferlin	66	534
34	BN1106_s1515B000336	filamin-C	52	139	34	BN1106_s1277B000102	Heat shock protein 90	65	148
35	BN1106_s5174B000030	glyceraldehyde-3-phosphate dehydrogenase	51	243	35	BN1106_s468B000343	Xaa-Pro dipeptidase	64	766
36	BN1106_s2907B000132	actin	50	441	36	BN1106_s204B000249	calpain	64	431
37	BN1106_s3172B000053	14-3-3 protein	49	513	37	BN1106_s4413B000122	hypothetical protein	64	421
38	BN1106_s4469B000065	fructose-bisphosphate aldolase class I	49	431	38	BN1106_s63B000395	hypothetical protein	63	184
39	BN1106_s617B000567	leucyl aminopeptidase	48	507	39	BN1106_s3172B000053	14-3-3 protein	62	545
40	BN1106_s2100B000128	hypothetical protein	48	301	40	BN1106_s4252B000085	uncharacterized protein	61	524
41	BN1106_s1191B000313	hypothetical protein	48	183	41	BN1106_s3747B000112	hypothetical protein	60	584
42	BN1106_s3001B000132.	hypothetical protein	47	255	42	BN1106_s1081B000242	chain A, Sigma class glutathione S-transferase	59	369
43	BN1106_s6821B000024	hypothetical protein	45	351	43	BN1106_s617B000567	leucyl aminopeptidase	58	457
44	BN1106_s55B000373	hypothetical protein	44	97	44	BN1106_s686B000273	14-3-3 protein	57	468
45	BN1106_s584B000346	glucose transporter-2 protein	43	260	45	BN1106_s2091B000373	DnaK family protein	57	283
46	BN1106_s4860B000047	tubulin beta chain	42	235	46	BN1106_s3033B000087	phosphoglycerate kinase	57	231
47	BN1106_s584B000350	glucose transporter-2 protein	41	320	47	BN1106_s285B000846	unnamed protein product	56	442
48	BN1106_s4560B000072	tetraspanin family protein	41	223	48	BN1106_s6821B000024	hypothetical protein	55	437
49	BN1106_s1614B000280	alkyl hydroperoxide reductase/ Thiol specific antioxidant family	41	204	49	BN1106_s2349B000191	gelsolin repeat protein	54	286
50	BN1106_s487B000135	hypothetical protein	41	180	50	BN1106_s487B000135	hypothetical protein	52	177

https://doi.org/10.1371/journal.pntd.0007191.t001

abundance of the potential tegumental proteins in the SEC preparation in comparison to DC EV preparations. Based on the number of unique or total peptides for each protein as an relative assessment of abundance, potential tegument identifications from DC prepared EVs were in greater quantities (Average of 14 unique peptides and 47 total peptides per protein) compared to EVs from SEC preparations (Average of 9 unique peptides and 15 total peptides per protein).

Of interest in the DC prepared EVs was the identification of 5 proteins that have previously been well documented in the proteome of *F. hepatica* eggs. Specifically, two ferritin-like proteins (BN1106_s709B000642 & BN1106_s709B000627), heat shock protein-35a (BN1106_s7572B000046), oxidoreductase (BN1106_s3715B000086) and an omega class glutathione S-transferase (BN1106_s1029B000154) which were all identified within DC EVs only.

Comparative gene enrichment

Gene enrichment was undertaken to determine significant over-representation of biological characteristics within the DC and SEC purified proteomes, compared to the *F. hepatica* genome set. Gene enrichment analysis revealed enriched gene ontology terms for both purification methods in biological process, molecular function and cellular component categories

against the *F. hepatica* genome (S7 File). Several gene ontology terms were enriched, which were not represented in EVs from both purification methods. For example, in biological processes, ATP synthesis coupled proton transport, carbohydrate metabolic process, cellular iron ion homeostasis, DNA replication, gluconeogenesis, iron ion transport, protein transport, proton transport, regulation of protein phosphorylation, DNA templated transcription and transmembrane transport were enriched in DC purified EVs only, where categories included proteins such as ATP synthase F1 beta subunit and peptidase T1 family. While nucleocytoplasmic transport, nucleosome assembly, oxidation-reduction process, phosphatidylinositol metabolic process, protein dephosphorylation, proteolysis, regulation of actin filament polymerization, small GTPase mediated signal transduction and translation including proteins such as Ras family protein and aldehyde dehydrogenase family protein were not enriched in DC purified EVs. Pairwise comparisons of DC purified EVs compared to SEC purified EVs demonstrated that, when considering biological processes, there were significantly less translation gene ontology terms (p = 0.02) and significantly more DNA-templated regulation of transcription gene ontology terms (p = 0.04), when considering cellular components there were significantly less ribosome gene ontology terms (p = 0.04) and when considering molecular function, structural constituents of the ribosome gene ontology terms (p = 0.02) were significantly less enriched.

Comparative Western blotting

The relative abundances of three proteins, which are well recognised to be located in *F. hepatica* ESP, EVs and somatic fractions, were compared utilising Western blotting. Somatic, ESP, soluble and insoluble EV fraction samples were assessed using both DC and SEC EV purification approaches (Fig 4). Equal concentrations of each protein sample was assayed for each EV purification Western blot. Anti-fatty acid binding protein V (Anti-FhFABP-V) antibody recognition was observed within somatic, ESP and soluble EV fractions using both purification methods but not within the insoluble EV fraction yet, DC EV purification demonstrated a marginally higher anti-FABP V recognition in EV soluble protein concentrations than SEC methods. Recognition with anti-glutathione transferase sigma class (Anti-FhGST-S1), identified in all fractions (somatic, ESP, insoluble and soluble EV), was notably observed to a greater extent within the insoluble EV fraction using SEC purification rather than DC purification.

Anti-*Fasciola* cathepsin L1 (Anti-FhCat-L1) antibody recognition was identified in all fractions (somatic, ESP and soluble EV) with the exception of insoluble EV preparations. Of note is the increased recognition of *Fasciola* cathepsin L1 observed in the soluble EV fraction of DC purified EVs when compared to SEC EVs. Furthermore, there was greater recognition by Anti-FhCat-L1 in the ESP following SEC purification rather than DC. To further investigate the abundance of cathepsin L proteases in DC and SEC EVs the proteomic data sets generated in the current work were examined to reveal which cathepsin L proteases were identified in the respective EV preparations (Table 2). Cathepsin L protease identifications revealed a greater number of CL1 clade (CL1A and CL1D) identified in EVs purified by SEC, rather than EVs purified by DC. In addition, DC purified EVs contained a greater number of the CL5 clade members.

Discussion

Given recent discoveries that EVs function in host-pathogen communication promoting or inhibiting host immunity, it is vital that reliable protocols for EV isolation, away from ESP, are conducted for downstream studies and application development. Therefore, the current work aimed to assess the current standard procedure for helminth pathogen EV analysis, DC, with a
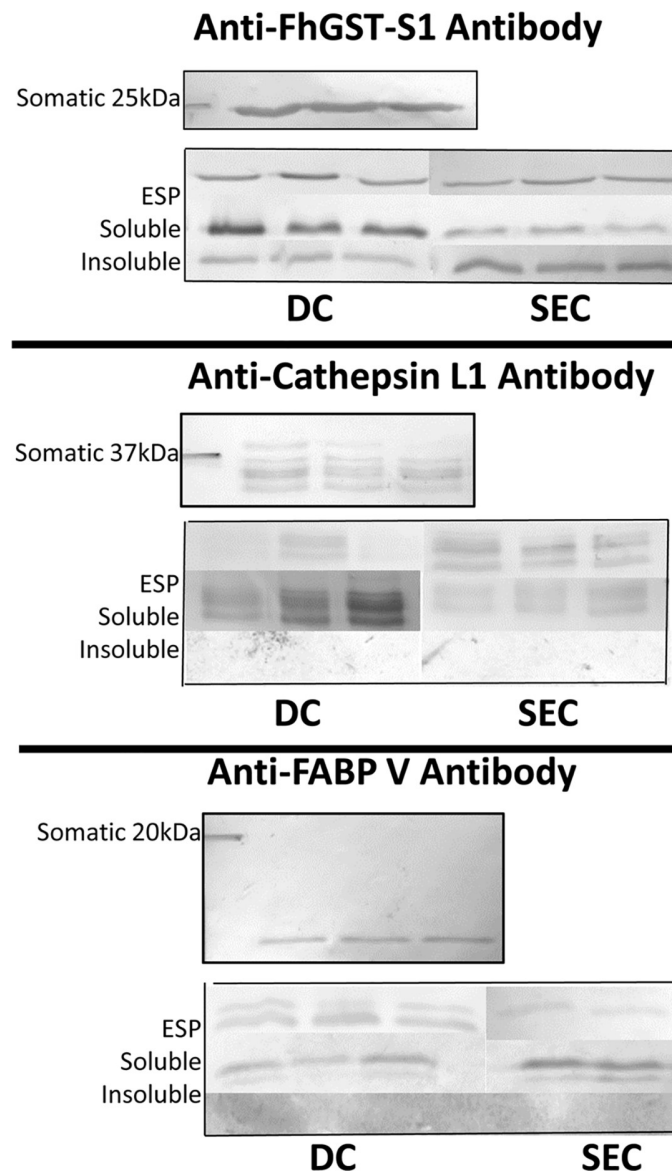
Fig 4. Extracellular vesicle protein preparation Western blot profiles purified using differential centrifugation and size exclusion chromatography. Extracellular vesicle preparation western blot profiles of somatic (10 μg protein), excretory-secretory protein (10 μg protein), soluble extracellular vesicle protein (20 μg protein) and insoluble extracellular vesicle protein (20 μg protein). Biological triplicates were analysed on 12.5% SDS-PAGE electrophoresis gels and transferred to nitrocellulose membranes for immune recognition. Samples of extracellular vesicle preparations purified using either the differential centrifugation method or size exclusion chromatography method were probed with anti-glutathione transferase sigma class (Anti-FhGST-S1), Anti-*Fasciola* cathepsin L1 (Anti-FhCat-L1) or anti-fatty acid binding protein V (Anti-FhFABP-V).

https://doi.org/10.1371/journal.pntd.0007191.g004

SEC approach well-established outside of the pathogen field when purifying EVs from culture media.

EV morphological characteristics assessed after both DC and SEC purification methods, identified that SEC purified EVs on average were smaller (76 nm ± 44 SD) and less diverse in size than DC purified EVs (95 nm ± 58 SD), indicating different EV populations were likely isolated by each method. DC purified EV size and diversity (27 nm and above) were similar to

Table 2. Cathepsin L proteases identified in extracellular vesicles purified by differential centrifugation and size exclusion chromatography. Protein accession numbers were chosen upon the lowest E-value hit and top accessions were identified by the highest unique peptide hits. Protein clades were identified from references [24,41,47,48].

Sequence ID	Protein Accession	Description [species]	Size Exclusion Chromatography		Differential Centrifugation	
			Unique Peptide Hits	Total Peptide Hits	Unique Peptide Hits	Total Peptide Hits
BN1106_s8490B000026	AAB41670.2	secreted cathepsin L1A [*Fasciola hepatica*]	29	109	23	91
BN1106_s4636B000039	AAF44676.1	cathepsin L5 [*Fasciola gigantica*]	-	-	9	13
BN1106_s10332B000011	ACJ12893.1	cathepsin L1D [*Fasciola hepatica*]	14	43	8	22
BN1106_s7289B000014	AAB41670.2	secreted cathepsin L1A [*Fasciola hepatica*]	12	19	-	-
BN1106_s8098B000020	ASK40163	ProCathepsin L2 [*Fasciola hepatica*]	10	21	9	22
BN1106_s7456B000012	ABV90502.1	cathepsin L1D, partial [*Fasciola gigantica*]	6	12	-	-
BN1106_s6354B000017	ATW63990.1	Pro cathepsin L5 [*Fasciola hepatica*]	5	10	6	14
BN1106_s10332B000010	ACJ12894.1	cathepsin L1D [*Fasciola hepatica*]	5	8	-	-

https://doi.org/10.1371/journal.pntd.0007191.t002

EV size predictions made by the centrifugation calculator [49]. Centrifugation calculators further predict that 38% of free protein will be purified in solution using DC purification methods. Furthermore, DC of EVs is more successful when sedimentation coefficients of the particles to be distinguished differ significantly [49]. For example, different centrifugation forces are required to obtain optimal EV to protein yield for different cell lines [50]. Thus, the difficulty of DC based standardisation across laboratory settings and sample types is becoming clearer.

During the current analysis, EVs were observed to aggregate together and contaminants co-purified were visible utilising both purification methods. However, Nordin *et al.* [2] demonstrated that DC purified EVs were fused, disrupted (62%) and aggregated when compared to SEC purified EVs yet, in the current investigation, EVs from either purification method were not damaged. It has been noted that forced filtration of samples can cause EV rupture and deformity, so sample preparation and SEC methods are advised to be performed using gravity only methods [1,6,11]. Aggregates are more likely to occur when high concentrations of EVs are present in a small volume with non-vesicular material; circumstances which are more likely within DC purification strategies rather than SEC purification of EVs [8]. However, EV aggregates may be overestimated by TEM and AFM methodology whereby surfaces capture EVs. Furthermore, vesicle morphology can be influenced by TEM and AFM methodology processes [6,51,52]. Both methods exhibited EV loss as demonstrated by the presence of EVs in the flow through (ESP), confirming that both purification methods are selective upon EV isolation.

When analysing the protein composition of purified EVs, it was apparent that SEC methods purified a greater protein yield within the EV samples (whole lysed, soluble protein fraction and insoluble protein fraction) when compared to DC preparations. These findings compare well with research identifying a greater number of particles to protein yield via SEC methods compared to DC methods and other commercial EV purification systems [2,14,15,53,54]. SEC has further been found to remove contaminating proteins from difficult sample types compared to DC such as albumin, cholesterol and apolipoprotein AI from blood plasma EVs and lipopolysaccharide binding protein from prokaryote EVs [14,55,56]. Conversely, Mol *et al.*, [57] observed no significant differences in EV protein or particle yield between both purification methods. There is an inverse relationship between EV purity and the protein yield, where the lower the ratio the more impure the sample [1,10]. Therefore, sample purity may have

consequent effects on experimental investigations [10]. Similar protein levels were observed between whole lysed EV and ESP samples purified by DC, yet the protein concentration of ESP was nearly threefold that of the whole lysed EV samples during SEC purification. This suggests again that SEC purification methods have an increased EV purity to protein yield ratio than DC based methods. This significant variation in ESP protein yield is most likely a direct result from sample wash steps involved with DC purification of EVs. Therefore, multiple wash steps are likely to increase EV loss and, as Webber and Clayton [10] acknowledged, are ineffective at removing protein contaminants, where there was only a 2-fold increase in particle to protein yield, compared to the crude pellet. Furthermore, there is the possibility that protein will sediment along with EVs during DC rather than be separated from EVs. Thus, in the current work SEC EV purification delivered a higher yield EV preparation in addition to higher yields of EV depleted ESP.

Whole lysed EV and ESP samples displayed different protein profiles as observed by one dimensional SDS-PAGE electrophoresis, suggesting that both EV purification methods isolate EVs from remaining *F. hepatica* secretions or ESP to varying degrees of purity. Following mass spectrometry analysis, we identified a greater total number of proteins associated with DC purified EVs than SEC purified EVs. However, SEC purified EV samples showed a greater diversity of EV functions in biological process, molecular function and cellular component gene ontology categories than DC purified EVs. The most common gene ontology terms identified in biological process, molecular function and cellular component were present in EVs from both purification methods. A comparable result was found investigating cell culture EVs, where fewer proteins (388 proteins) were identified in SEC purified EVs than in DC purified EVs (421 proteins), although fewer proteins (147 proteins) overlapped between SEC and DC EVs compared to the current study [53]. This result further suggests that DC purification alters EV protein composition to a greater extent than SEC purification, possibly isolating different EV subpopulations, as well as purifying greater amounts of contaminant. Thus, supporting SEC purification methods for an increased EV purity to protein yield ratio than DC based methods.

The most abundant proteins found in *F. hepatica* EVs, per rank, showed DC consistently had a greater amount of unique peptides hit per protein than SEC. Cwiklinski *et al.* [24] similarly analysed *F. hepatica* EV proteome where all 180 proteins identified were also found in the current investigation. However, the top unique peptide hits (where soluble and insoluble fraction data was combined) from Cwiklinski *et al.* [24] were not comparable to the current experimental results. Cwiklinski *et al.* [24] did not investigate a biological representation of the whole *F. hepatica* EV proteome, but instead EVs isolated from 120,000 *x* g ultracentrifugation spin only. In addition, a different mass spectrometry methodology and analysis was performed likely explaining DC EV differences. The top 50 proteins observed in EVs purified using SEC were also present in the DC EV purified proteome. However, three proteins were identified in the top 50 proteins of DC purified EVs, but were not present in the full SEC isolated EV proteome. Common EV markers were present in the top 50 EV proteins using both purification methods although tetraspanin was identified in the top 50 EV protein hits using SEC purification only and gelosin and phosphoglycerate kinase EV markers were observed in the top 50 protein hit using DC purification only. This may indicate that SEC and DC purification methods also purify different EV sub-populations, or that EV sub-populations are purified in differing quantities within each method.

Further investigation discovered that there was a 2.6 fold greater number of protein identifications in DC purified EVs only, compared to SEC purified proteins. Of these DC EV unique proteins many have been identified previously in ESP and tegument proteomic studies. With pathogens, the separation of EVs from additional pathogen components such as the

platyhelminth tegument is vital to fully assess the role of the pathogen EV. The recognised increase of tegumental proteins found within the DC purified EVs further supports that SEC purified EVs have a greater EV purity to protein yield than DC purified EVs. Furthermore, current international EV purification methods report that chromatographic methods, including SEC, produce less contamination by non-vesicular proteins and macromolecule structures than ultracentrifugation, thus is likely to account for the reduction of tegumental proteins in SEC EVs [58].

Akin to the work of Benedikter et al. [53] gene enrichment analysis demonstrated comparable enriched gene ontology terms for both purification methods in biological process, molecular function and cellular component categories against the F. hepatica genome. Interestingly, only GO terms for translation biological process ribosome cellular component and structural constituent of the ribosome were significantly less enriched in DC purified EVs compared to SEC purified EVs, while DNA-templated regulation of transcription was enriched significantly in DC purified EVs compared to SEC purified EVs. This further suggests that DC and SEC purification methods isolate differing EV populations with altered functions. Cwiklinski et al. [24] previously discovered that EV sub-populations secreted from F. hepatica, contained different relative peptidase activities. A range of other studies have also identified that nucleic acids [59–64] and proteins [60,64–67] are selectively packed into EV subtypes. It has further been found that purification methodologies have differential affinity for protein EV markers and by extension for different EV sub-population using human urine samples [68]. This research further supports the current work in that DC and SEC purification methods isolated EVs of different function and different levels of purity.

An increased EV purity to protein yield ratio demonstrated in SEC purification over DC based methods was further reinforced by Western blotting revealing higher recognition by Anti-FhFABP V, Anti-FhGST-S1 and Anti-FhCat-L1 in the EV soluble fraction using DC purification rather than SEC. Only protein fragments from FABP III were identified within the mass spectrometry peptide analysis from the FABP protein family. Importantly, comparable levels of recognition by Anti-FhFABP V and Anti-FhGST-S1 were seen in DC and SEC ESP depleted of EVs, yet a greater recognition from Anti-FhCat-L1 was observed in SEC EV depleted ESP demonstrating increased separation of ESP from EVs in SEC methods. Baranyai et al. [55], also using Western blotting, demonstrated that SEC produced a greater EV purity to protein yield ratio, as higher albumin concentrations were seen in DC methods than SEC methods in mouse blood plasma. Correspondingly, vesicle markers have been found at greater concentrations in EV samples using SEC methods than DC [2]. Interestingly, there were a greater variety of cathepsin L protease isoforms identified in EVs purified by SEC, rather than EVs purified by DC. Of these proteins, there was a greater number of cathepsin L1A and cathepsin L1D, but a lower abundance of cathepsin L5 in SEC purified EVs, compared to DC purified EVs. Cathepsin L proteases have functional roles within immune evasion, nutrition and migration. In particular, cathepsin L1 and L2 proteases degrade host haemoglobin, immunoglobulin and interstitial matrix proteins such as fibronectin, laminin, and native collagen [69,70]. Different cathepsin L protease clades, have distinct substrate abilities, indicating that they have different roles in parasite biology. In the case of cathepsin L5, these roles are yet to still be determined [47,71]. In previous proteomic studies investigating the surface and membrane fractions of F. hepatica EVs [24], members of the CL1 clade (1A,1B and 1D) have all been identified to be membrane associated, yet members of CL5 have not. Therefore, the SEC approach identified more membrane associated cathepsin L in comparison to DC, identifying increased soluble cathepsin L derived from the EV contents or from contamination from ESP.

Interestingly, Anti-FhGST-S1 recognition was strongly observed in the insoluble EV fraction and a higher protein abundance of FhGST-S1 was suggested using SEC purification.

Therefore, FhGST-S1 could potentially act as a novel marker for *F. hepatica* EVs given its identification in the insoluble EV fraction. The function of FhGST-S1 in *F. hepatica* includes prostaglandin synthesis which establishes host infection, egg development and embryogenesis, host immune modulation and potential triclabendazole drug response in phase III sequestration based detoxification [40]. Recent studies have found that parasite EVs can communicate with host cells therefore, the function FhGST-S1 in *F. hepatica* EVs could involve host infection establishment and host immune modulation [23,28,29,72–82]. However, further investigation upon this proposal is required to determine the role and location of FhGST-S1 in EVs. This finding indicates the importance of EV purification methodology upon accurately identifying the abundance of pathogen markers and vaccine candidates in EVs.

To claim that SEC should be used as a gold standard method for isolating EVs from parasite culture media, additional isolation methodologies (density gradient, sucrose cushion, precipitation methods and immunoaffinity isolation) will need to be compared with SEC methodology. It is acknowledged that within any purification method, many variables, such as the number of wash steps, will affect the purity and functionality of purified EVs. Given that all EV helminth studies to date have used DC purification for downstream analysis, the present study findings suggest a change in approach may be required with SEC providing a promising purification method for isolating EVs from *in vitro* helminth cultures for downstream functional analysis in terms of minimising non-EV contaminants.

There is a strong demand for an established uniform protocol for EV purification. However, instead of finding the ultimate 'gold standard' for EV purification, from this investigation it appears to be of more importance that EV purity is standardised, rather than the purification protocol. Possibly, rather than the helminth EV field aiming to isolate EVs using a 'gold standard' method, there should be a 'gold standard' of purity assessment of EV samples used for experimentation, dependent upon the sample type (e.g. plasma, urine, cell culture media and parasite culture media). EV specific markers are also likely to be important to identify EV sample purity. Specific EV markers would add value to the assessment of EV sample purity and thus could be species specific. This is especially pertinent given that current EV markers are based on mammalian work [83]. In the current study, differential abundance of protein families (CAT L clades and egg based proteins) were noted during proteomic analysis that could be utilised for *Fasciola* specific EV purity markers. This would improve the standardisation of protocols and the comparability of results from scientific research.

Thorough proteomic investigation on EV protein composition from EVs purified by DC and SEC methodology identified that SEC purified EVs contained proteins with more functional properties than DC purified EVs. However, in order to confirm increased EV functionality and the improved functional benefit of using SEC for EV purification compared to other methodologies, additional functional studies comparing the isolation methodologies by independent host-parasite interaction groups would be required. For example, SEC and DC purified EVs could be cultured with host cells *in vitro* and host cell transcriptome data could be compared between the two isolation conditions, following the methodology undertaken using DC purified *O. viverrini* EVs [76]. However, as the findings from the current study support that SEC purified EVs contained proteins with more functional properties than DC purified EVs, speculation upon the validity of other EV functional studies which have purified EVs from parasite culture media using DC methodology is necessary. Therefore, more comparative research is required to understand the influence of EV purification methodologies upon functional studies.

In summary, the current study has challenged whether the most accepted EV purification technique in helminth research is optimal for functional studies, in comparison to SEC methods. Our discoveries using *F. hepatica* as a pathogen case study, suggest that SEC purification has a higher EV purity to protein yield ratio than DC purified EVs evidenced by reduced

contamination from ESP and tegumental components, whilst still maintaining EV morphological characteristics. Furthermore, gene ontology terminology proposed that DC and SEC purification methods isolate differential EV sub-populations. Given the demonstrated variation in purification methodologies and the importance of understanding the function of EVs for potential downstream studies and application development, the authors suggest that for EV functional assays the purification methodology used should be of importance when designing experiments. This research has highlighted SEC EV isolation as a potential key methodology for functional EV research.

Supporting information

S1 File. MASCOT (Matrix Science, v2.4.1) extracellular vesicle protein accession information for each band sample analysed by liquid Chromatography tandem mass spectrometry per replicate.
(XLSX)

S2 File. BLAST2GO (https://www.blast2go.com/) extracellular vesicle reported protein accession information and Level 3 gene ontology descriptions of protein identifications found in differential centrifugation and size exclusion chromatography purified extracellular vesicles.
(XLSX)

S3 File. MASCOT (Matrix Science, v2.4.1) unique and total peptide hits for extracellular vesicle protein accessions purified by differential centrifugation and size exclusion chromatography.
(XLSX)

S4 File. GOATOOLS in python software gene enrichment analysis of extracellular vesicles purified using differential centrifugation and size exclusion chromatography.
(XLSX)

S5 File. The abundance of differential centrifugation or size exclusion chromatography purified extracellular vesicle only protein accessions and their association with other *F. hepatica* ESP or parasite tegument proteomic studies.
(XLSX)

S6 File. Level 3 Gene ontology descriptions of extracellular vesicle protein identifications purified using differential centrifugation and size exclusion chromatography, differential centrifugation extracellular vesicle samples only and size exclusion chromatography extracellular vesicle samples only in (a) biological process, (b) molecular function and (c) cellular component functional categories in graphical format.
(PDF)

S7 File. Gene enrichment comparison of extracellular vesicles purified using differential centrifugation and size exclusion chromatography methodology within (a) biological process, (b) cellular component and (c) molecular function categories against the F. hepatica genome in graphical format.
(PDF)

Acknowledgments

University, England) and Dr Neil Young (University of Melbourne, Australia) for providing FhA, FhB and FhC databases, and Prof. Andrew Devitt (Aston University, England) and Dr Ivana Milic (Aston University, England) for the use of qNano particulate analysis (IZON science). We are grateful to Randall Parker Foods (Wales) for providing consent to retrieve *F. hepatica* from infected sheep livers.

Author Contributions

References

1. Abramowicz A, Widlak P, Pietrowska M. Proteomic analysis of exosomal cargo: the challenge of high purity vesicle isolation. Mol Biosyst [Internet]. 2016; 12:1407–19. Available from: http://dx.doi.org/10.1039/C6MB00082G PMID: 27030573

2. Nordin JZ, Lee Y, Vader P, Mäger I, Johansson HJ, Heusermann W, et al. Ultrafiltration with size-exclusion liquid chromatography for high yield isolation of extracellular vesicles preserving intact biophysical and functional properties. Nanomedicine Nanotechnology, Biol Med. 2015; 11(4):879–83.

3. Welton JL, Webber JP, Botos L-A, Jones M, Clayton A. Ready-made chromatography columns for extracellular vesicle isolation from plasma. J Extracell vesicles [Internet]. 2015; 4:27269. Available from: http://www.pubmedcentral.nih.gov/articlerender.fcgi?artid=4376847&tool=pmcentrez&rendertype=abstract https://doi.org/10.3402/jev.v4.27269 PMID: 25819214

4. Pocsfalvi G, Stanly C, Fiume I, Vékey K. Chromatography and its hyphenation to mass spectrometry for extracellular vesicle analysis. J Chromatogr A. 2016; 1439:26–41. https://doi.org/10.1016/j.chroma.2016.01.017 PMID: 26830636

5. Franquesa M, Hoogduijn MJ, Ripoll E, Luk F, Salih M, Betjes MGH, et al. Update on controls for isolation and quantification methodology of extracellular vesicles derived from adipose tissue mesenchymal stem cells. Front Immunol. 2014; 5(OCT):525.

6. Szatanek R, Baran J, Siedlar M, Baj-Krzyworzeka M. Isolation of extracellular vesicles: Determining the correct approach (Review). Int J Mol Med [Internet]. 2015; 36(1):11–7. Available from: http://www.pubmedcentral.nih.gov/articlerender.fcgi?artid=4494580&tool=pmcentrez&rendertype=abstract https://doi.org/10.3892/ijmm.2015.2194 PMID: 25902369

7. Balaj L, Atai NA, Chen W, Mu D, Tannous BA, Breakefield XO, et al. Heparin affinity purification of extracellular vesicles. Sci Rep [Internet]. 2015; 5:10266. Available from: http://www.pubmedcentral.nih.gov/articlerender.fcgi?artid=4437317&tool=pmcentrez&rendertype=abstract https://doi.org/10.1038/srep10266 PMID: 25988257

8. Linares R, Tan S, Gounou C, Arraud N, Brisson AR. High-speed centrifugation induces aggregation of extracellular vesicles. J Extracell vesicles [Internet]. 2015; 4:29509. Available from: /pmc/articles/PMC4689953/?report = abstract https://doi.org/10.3402/jev.v4.29509 PMID: 26700615

9. de Menezes-Neto A, Sáez MJF, Lozano-Ramos I, Segui-Barber J, Martin-Jaular L, Estanyol Ullate JM, et al. Size-exclusion chromatography as a stand-alone methodology identifies novel markers in mass spectrometry analyses of plasma-derived vesicles from healthy individuals. J Extracell Vesicles [Internet]. 2015; 4(0):27378. Available from: http://www.journalofextracellularvesicles.net/index.php/jev/article/view/27378

10. Webber J, Clayton A. How pure are your vesicles? J Extracell vesicles [Internet]. 2013; 2(7):1–6. Available from: http://www.pubmedcentral.nih.gov/articlerender.fcgi?artid=3760653&tool=pmcentrez&rendertype=abstract

11. Witwer KW, Buzás EI, Bemis LT, Bora A, Lässer C, Lötvall J, et al. Standardization of sample collection, isolation and analysis methods in extracellular vesicle research. J Extracell vesicles [Internet]. 2013; 2:1–25. Available from: http://www.pubmedcentral.nih.gov/articlerender.fcgi?artid=3760646&tool=pmcentrez&rendertype=abstract

12. Kim J, Shin H, Kim J, Kim J, Park J. Isolation of high-purity extracellular vesicles by extracting proteins using aqueous two-phase system. PLoS One. 2015; 10(6):e0129760. https://doi.org/10.1371/journal.pone.0129760 PMID: 26090684

13. Cvjetkovic A, Lötvall J, Lässer C. The influence of rotor type and centrifugation time on the yield and purity of extracellular vesicles. J Extracell vesicles [Internet]. 2014; 3:3–4. Available from: http://www.ncbi.nlm.nih.gov/pmc/articles/PMC3760649/%5Cnhttp://www.pubmedcentral.nih.gov/articlerender.fcgi?artid=3760649&tool=pmcentrez&rendertype=abstract%5Cnhttp://www.pubmedcentral.nih.gov/articlerender.fcgi?artid=3967015&tool=pmcentrez&rendertype=abstrac

14. Böing AN, Pol E Van Der, Grootemaat AE, Coumans F a., Sturk A, Nieuwland R. Single-step isolation of extracellular vesicles from plasma by size-exclusion chromatography. Int Meet ISEV Rotterdam. 2014; 3:118.

15. Gámez-Valero A, Monguió-Tortajada M, Carreras-Planella L, Franquesa M, Beyer K, Borràs FE. Size-Exclusion Chromatography-based isolation minimally alters Extracellular Vesicles' characteristics compared to precipitating agents. Sci Rep [Internet]. 2016; 6(1):33641. Available from: http://www.nature.com/articles/srep33641

16. Lozano-Ramos I, Bancu I, Oliveira-Tercero A, Armengol MP, Menezes-Neto A, Del Portillo HA, et al. Size-exclusion chromatography-based enrichment of extracellular vesicles from urine samples. J Extracell Vesicles. 2015; 4(2015):1–11.

17. Bo AN, Pol E Van Der, Grootemaat AE. Single-step isolation of extracellular vesicles by size-exclusion chromatography. J Control Release. 2014; 1:1–11.

18. Charlier J, Vercruysse J, Morgan E, Dijk JVAN, Williams DJL. Recent advances in the diagnosis, impact on production and prediction of Fasciola hepatica in cattle. 2014; 141(3):326–35.

19. Omar MA, Metwally AM, Sultan K. Molecular and phylogenetic status of Fasciola sp., of cattle in Qena, Upper Egypt. Pak J Biol Sci [Internet]. 2013; 16(15):726–30. Available from: http://www.ncbi.nlm.nih.gov/pubmed/24506000 PMID: 24506000

20. WHO. Fascioliasis [Internet]. 2015. Available from: file:: http://www.who.int/foodborne_trematode_infections/fascioliasis/en/

21. Boray JC. Immunology, Pathobiology and Control of Fasciolosis. Boray JC, editor. Merck AgVet; 1997. 83–87 p.

22. Brennan GP, Fairweather I, Trudgett A, Hoey E, McCoy, McConville M, et al. Understanding triclabendazole resistance. Exp Mol Pathol. 2007; 82(2):104–9. https://doi.org/10.1016/j.yexmp.2007.01.009 PMID: 17398281

23. Marcilla A, Trelis M, Cortes A, Sotillo J, Cantalapiedra F, Minguez MT, et al. Extracellular vesicles from parasitic helminths contain specific excretory/secretory proteins and are internalized in intestinal host cells. PLoS One [Internet]. 2012; 7(9):e45974. Available from: http://www.ncbi.nlm.nih.gov/pubmed/23029346 PMID: 23029346

24. Cwiklinski K, de la Torre-Escudero E, Trelis M, Bernal D, Dufresne PJ, Brennan GP, et al. The Extracellular Vesicles of the Helminth Pathogen, Fasciola hepatica: Biogenesis Pathways and Cargo Molecules Involved in Parasite Pathogenesis. Mol Cell Proteomics [Internet]. 2015; 14(12):3258–73. Available from: http://www.mcponline.org/lookup/doi/10.1074/mcp.M115.053934 PMID: 26486420

25. Schorey JS, Cheng Y, Singh PP, Smith VL. Exosomes and other extracellular vesicles in host-pathogen interactions. EMBO Rep [Internet]. 2015; 16(1):24–43. Available from: http://embor.embopress.org/cgi/doi/10.15252/embr.201439363 PMID: 25488940

26. Schorey JS, Harding C V. Extracellular vesicles and infectious diseases: new complexity to an old story. J Clin Invest [Internet]. 2016; 126(4):1181–9. Available from: http://www.ncbi.nlm.nih.gov/pubmed/27035805%5Cnhttp://www.pubmedcentral.nih.gov/articlerender.fcgi?artid=PMC4811136%5Cnhttp://www.ncbi.nlm.nih.gov/pubmed/27035809%5Cnhttp://www.pubmedcentral.nih.gov/articlerender.fcgi?artid=PMC4811125 https://doi.org/10.1172/JCI81132 PMID: 27035809

27. Wang L, Li Z, Shen J, Liu Z, Liang J, Wu X, et al. Exosome-like vesicles derived by Schistosoma japonicum adult worms mediates M1 type immune- activity of macrophage. Parasitol Res. 2015; 114(5):1865–73. https://doi.org/10.1007/s00436-015-4373-7 PMID: 25855345

28. Buck AH, Coakley G, Simbari F, McSorley HJ, Quintana JF, Le Bihan T, et al. Exosomes secreted by nematode parasites transfer small RNAs to mammalian cells and modulate innate immunity. Nat Commun. 2014; 5:5448. https://doi.org/10.1038/ncomms6448

29. Coakley G, McCaskill JL, Borger JG, Simbari F, Robertson E, Millar M, et al. Extracellular Vesicles from a Helminth Parasite Suppress Macrophage Activation and Constitute an Effective Vaccine for Protective Immunity. Cell Rep. 2017; 19(8):1545–57. https://doi.org/10.1016/j.celrep.2017.05.001 PMID: 28538175

30. Fromm B, Ovchinnikov V, Høye E, Bernal D, Hackenberg M, Marcilla A. On the presence and immuno-regulatory functions of extracellular microRNAs in the trematode Fasciola hepatica. Parasite Immunol. 2017; 39(2):e12399.

31. Nowacki FC, Swain MT, Klychnikov OI, Niazi U, Ivens A, Quintana JF, et al. Protein and small non-coding RNA-enriched extracellular vesicles are released by the pathogenic blood fluke *Schistosoma mansoni*. J Extracell Vesicles [Internet]. 2015; 4(1):28665. Available from: https://www.tandfonline.com/doi/full/10.3402/jev.v4.28665

32. Hansen EP, Kringel H, Williams AR, Nejsum P. Secretion of RNA-Containing Extracellular Vesicles by the Porcine Whipworm, *Trichuris suis*. J Parasitol [Internet]. 2015; 101(3):336–40. Available from: http://www.bioone.org/doi/10.1645/14-714.1 PMID: 25723295

33. Zamanian M, Fraser LM, Agbedanu PN, Harischandra H, Moorhead AR, Day TA, et al. Release of Small RNA-containing Exosome-like Vesicles from the Human Filarial Parasite Brugia malayi. PLoS Negl Trop Dis. 2015; 9(9):e0004069. https://doi.org/10.1371/journal.pntd.0004069 PMID: 26401956

34. Sotillo J, Pearson M, Potriquet J, Becker L, Pickering D, Mulvenna J, et al. Extracellular vesicles secreted by Schistosoma mansoni contain protein vaccine candidates. Int J Parasitol. 2016; 46(1):1–5. https://doi.org/10.1016/j.ijpara.2015.09.002 PMID: 26460238

35. Tzelos T, Matthews JB, Buck AH, Simbari F, Frew D, Inglis NF, et al. A preliminary proteomic characterisation of extracellular vesicles released by the ovine parasitic nematode, Teladorsagia circumcincta. Vet Parasitol. 2016; 221:84–92. https://doi.org/10.1016/j.vetpar.2016.03.008 PMID: 27084478

36. Morphew RM, Wilkinson TJ, MacKintosh N, Jahndel V, Paterson S, McVeigh P, et al. Exploring and Expanding the Fatty-Acid-Binding Protein Superfamily in Fasciola Species. J Proteome Res. 2016; 15 (9):3308–21. https://doi.org/10.1021/acs.jproteome.6b00331 PMID: 27495901

37. Théry C, Amigorena S, Raposo G, Clayton A. Isolation and characterization of exosomes from cell culture supernatants and biological fluids. Curr Protoc Cell Biol. 2006;Chapter 3:Unit 3.22.

38. Hart EH, Brophy PM, Prescott M, Bartley DJ, Wolf BT, Hamilton J V. A new enabling proteomics methodology to investigate membrane associated proteins from parasitic nematodes: Case study using ivermectin resistant and ivermectin susceptible isolates of Caenorhabditis elegans and Haemonchus contortus. Vet Parasitol. 2015; 207(3–4):266–75. https://doi.org/10.1016/j.vetpar.2014.12.003 PMID: 25537855

39. Towbin H, Staehelin T, Gordon J. Electrophoretic transfer of proteins from polyacrylamide gels to nitrocellulose sheets: Procedures and some applications. Proc Natl Acad Sci U S A. 1979; 76(9):4350–4. PMID: 388439

40. LaCourse EJ, Perally S, Morphew RM, Moxon J V., Prescott M, Dowling DJ, et al. The Sigma class glutathione transferase from the liver fluke fasciola hepatica. PLoS Negl Trop Dis. 2012; 6(5):e1666. https://doi.org/10.1371/journal.pntd.0001666 PMID: 22666515

41. Morphew RM, Wright HA, LaCourse EJ, Porter J, Barrett J, Woods DJ, et al. Towards delineating functions within the Fasciola Secreted Cathepsin L protease family by integrating in vivo based sub-proteomics and phylogenetics. PLoS Negl Trop Dis. 2011; 5(1):e937. https://doi.org/10.1371/journal.pntd.0000937 PMID: 21245911

42. Morphew RM, MacKintosh N, Hart EH, Prescott M, LaCourse EJ, Brophy PM. In vitro biomarker discovery in the parasitic flatworm Fasciola hepatica for monitoring chemotherapeutic treatment. EuPA Open Proteomics. 2014; 3:85–99.

43. Haçariz O, Baykal AT, Akgün M, Kavak P, Sağiroğlu MŞ, Sayers GP. Generating a detailed protein profile of Fasciola hepatica during the chronic stage of infection in cattle. Proteomics. 2014; 14(12):1519–30. https://doi.org/10.1002/pmic.201400012 PMID: 24733753

44. Robinson MW, Menon R, Donnelly SM, Dalton JP, Ranganathan S. An Integrated Transcriptomics and Proteomics Analysis of the Secretome of the Helminth Pathogen Fasciola hepatica: proteins associated with invasion and infection of the mammalian host. Mol Cell Proteomics [Internet]. 2009; 8(8):1891–907. Available from: http://www.pubmedcentral.nih.gov/articlerender.fcgi?artid=2722771&tool=pmcentrez&rendertype=abstract%0Ahttps://www.ncbi.nlm.nih.gov/pubmed/19443417 PMID: 19443417

45. Wilson RA, Wright JM, de Castro-Borges W, Parker-Manuel SJ, Dowle AA, Ashton PD, et al. Exploring the Fasciola hepatica tegument proteome. Int J Parasitol. 2011; 41(13–14):1347–59. https://doi.org/10.1016/j.ijpara.2011.08.003 PMID: 22019596

46. Di Maggio LS, Tirloni L, Pinto AFM, Diedrich JK, Yates JR, Benavides U, et al. Across intra-mammalian stages of the liver fluke Fasciola hepatica: A proteomic study. Sci Rep [Internet]. 2016; 6(September):1–14. Available from: http://dx.doi.org/10.1038/srep32796

47. Norbury LJ, Hung A, Beckham S, Pike RN, Spithill TW, Craik CS, et al. Analysis of Fasciola cathepsin L5 by S2subsite substitutions and determination of the P1-P4specificity reveals an unusual preference. Biochimie. 2012; 94(5):1119–27. https://doi.org/10.1016/j.biochi.2012.01.011 PMID: 22285967

48. Martínez-Sernández V, Perteguer MJ, Hernández-González A, Mezo M, González-Warleta M, Orbegozo-Medina RA, et al. Comparison of recombinant cathepsins L1, L2, and L5 as ELISA targets for serodiagnosis of bovine and ovine fascioliasis. Parasitology Research. 2018;1–14.

49. Livshts MA, Khomyakova E, Evtushenko EG, Lazarev VN, Kulemin NA, Semina SE, et al. Isolation of exosomes by differential centrifugation: Theoretical analysis of a commonly used protocol. Sci Rep. 2015; 5:17319. https://doi.org/10.1038/srep17319 PMID: 26616523

50. Jeppesen DK, Hvam ML, Primdahl-Bengtson B, Boysen AT, Whitehead B, Dyrskjøt L, et al. Comparative analysis of discrete exosome fractions obtained by differential centrifugation. J Extracell Vesicles. 2014; 3(1).

51. Pearson LJ, Klaharn I, Thongsawang B, Manuprasert W, Saejew T, Somparn P, et al. Multiple extracellular vesicle types in peritoneal dialysis effluent are prominent and contain known biomarkers. PLoS One. 2017; 12(6):e0178601. https://doi.org/10.1371/journal.pone.0178601 PMID: 28594924

52. Wu Y, Deng W, Klinke II DJ. Exosomes: improved methods to characterize their morphology, RNA content, and surface protein biomarkers. Analyst [Internet]. 2015; 140(19):6631–42. Available from: http://xlink.rsc.org/?DOI=C5AN00688K https://doi.org/10.1039/c5an00688k PMID: 26332016

53. Benedikter BJ, Bouwman FG, Vajen T, Heinzmann ACA, Grauls G, Mariman EC, et al. Ultrafiltration combined with size exclusion chromatography efficiently isolates extracellular vesicles from cell culture media for compositional and functional studies. Sci Rep. 2017; 7(1):15297. https://doi.org/10.1038/s41598-017-15717-7 PMID: 29127410

54. Lobb RJ, Becker M, Wen Wen S, Wong CSF, Wiegmans AP, Leimgruber A, et al. Optimized exosome isolation protocol for cell culture supernatant and human plasma. J Extracell Vesicles [Internet]. 2015; 4(1):27031. Available from: https://www.tandfonline.com/doi/full/10.3402/jev.v4.27031

55. Baranyai T, Herczeg K, Onódi Z, Voszka I, Módos K, Marton N, et al. Isolation of exosomes from blood plasma: Qualitative and quantitative comparison of ultracentrifugation and size exclusion chromatography methods. PLoS One. 2015; 10(12):e0145686. https://doi.org/10.1371/journal.pone.0145686 PMID: 26690353

56. Dauros Singorenko P, Chang V, Whitcombe A, Simonov D, Hong J, Phillips A, et al. Isolation of membrane vesicles from prokaryotes: a technical and biological comparison reveals heterogeneity. J Extracell Vesicles [Internet]. 2017; 6(1):1324731. Available from: https://www.tandfonline.com/doi/full/10.1080/20013078.2017.1324731 PMID: 28717421

57. Mol E.A, Goumans M.J, Doevendans P.A, Sluijter J.P.G, Vader P. Higher functionality of extracellular vesicles isolated using size-exclusion chromatography compared to ultracentrifugation. Nanomedicine Nanotechnology, Biol Med. 2017; 13(6):2061–5.

58. Gardiner C, Vizio D Di, Sahoo S, Thery C, Witwer KW, Wauben M, et al. Techniques used for the isolation and characterization of extracellular vesicles: Results of a worldwide survey. J Extracell Vesicles. 2016; 5(1):32945.

59. Akers JC, Ramakrishnan V, Kim R, Phillips S, Kaimal V, Mao Y, et al. miRNA contents of cerebrospinal fluid extracellular vesicles in glioblastoma patients. J Neurooncol. 2015; 123(2):205–16. https://doi.org/10.1007/s11060-015-1784-3 PMID: 25903655

60. Willms E, Johansson HJ, Mäger I, Lee Y, Blomberg KEM, Sadik M, et al. Cells release subpopulations of exosomes with distinct molecular and biological properties. Sci Rep. 2016; 6::22519. https://doi.org/10.1038/srep22519 PMID: 26931825

61. Godlewski J, Ferrer-Luna R, Rooj AK, Mineo M, Ricklefs F, Takeda YS, et al. MicroRNA Signatures and Molecular Subtypes of Glioblastoma: The Role of Extracellular Transfer. Stem Cell Reports. 2017; 8(6):1497–505. https://doi.org/10.1016/j.stemcr.2017.04.024 PMID: 28528698

62. Lazaro-Ibanez E, Sanz-Garcia A, Visakorpi T, Escobedo-Lucea C, Siljander P, Ayuso-Sacido, Yliperttula M. Different gDNA content in the subpopulations of prostate cancer extracellular vesicles: Apoptotic bodies, microvesicles, and exosomes. Prostate. 2014; 74(14):1379–90. https://doi.org/10.1002/pros.22853 PMID: 25111183

63. Lázaro-Ibáñez E, Lunavat TR, Jang SC, Escobedo-Lucea C, Oliver-De La Cruz J, Siljander P, et al. Distinct prostate cancer-related mRNA cargo in extracellular vesicle subsets from prostate cell lines. BMC Cancer. 2017; 17(1):92. https://doi.org/10.1186/s12885-017-3087-x PMID: 28143451

64. Collino F, Pomatto M, Bruno S, Lindoso RS, Tapparo M, Sicheng W, et al. Exosome and Microvesicle-Enriched Fractions Isolated from Mesenchymal Stem Cells by Gradient Separation Showed Different Molecular Signatures and Functions on Renal Tubular Epithelial Cells. Stem Cell Rev Reports. 2017; 13(2):226–43.

65. Royo F, Schlangen K, Palomo L, Gonzalez E, Conde-Vancells J, Berisa A, et al. Transcriptome of Extracellular Vesicles Released by Hepatocytes. PLoS One. 2013; 8(7):e68693. https://doi.org/10.1371/journal.pone.0068693 PMID: 23874726

66. Bobrie A, Colombo M, Krumeich S, Raposo G, Théry C. Diverse subpopulations of vesicles secreted by different intracellular mechanisms are present in exosome preparations obtained by differential ultracentrifugation. J Extracell Vesicles. 2012; 1(1).

67. Kowal J, Arras G, Colombo M, Jouve M, Morath JP, Primdal-Bengtson B, et al. Proteomic comparison defines novel markers to characterize heterogeneous populations of extracellular vesicle subtypes. Proc Natl Acad Sci [Internet]. 2016; 113(8):E968–77. Available from: http://www.pnas.org/lookup/doi/10.1073/pnas.1521230113 PMID: 26858453

68. Royo F, Zuñiga-Garcia P, Sanchez-Mosquera P, Egia A, Perez A, Loizaga A, et al. Different EV enrichment methods suitable for clinical settings yield different subpopulations of urinary extracellular vesicles from human samples. J Extracell vesicles [Internet]. 2016; 5(7):29497. Available from: http://www.pubmedcentral.nih.gov/articlerender.fcgi?artid=4759834&tool=pmcentrez&rendertype=abstract

69. Berasain P, Carmona C, Frangione B, Dalton JP, Goñi F. Fasciola hepatica: Parasite-secreted proteinases degrade all human IgG subclasses: Determination of the specific cleavage sites and identification of the immunoglobulin fragments produced. Exp Parasitol. 2000; 94(2):99–110. https://doi.org/10.1006/expr.1999.4479 PMID: 10673346

70. Dalton JP, Neill SO, Stack C, Collins P, Walshe A, Sekiya M, et al. Fasciola hepatica cathepsin L-like proteases: biology, function, and potential in the development of first generation liver fluke vaccines. Int J Parasit. 2003; 33:1173–81.

71. Smooker PM, Whisstock JC, Irving JA, Siyaguna S, Spithill TW, Pike RN. A single amino acid substitution affects substrate specificity in cysteine proteinases from Fasciola hepatica. Protein Sci. 2000; 9 (12):2567–72. https://doi.org/10.1110/ps.9.12.2567 PMID: 11206078

72. Wang L, Yu Z, Wan S, Wu F, Chen W, Zhang B, et al. Exosomes derived from dendritic cells treated with Schistosoma japonicum soluble egg antigen attenuate DSS-Induced Colitis. Front Pharmacol. 2017; 8(SEP).

73. Twu O, de Miguel N, Lustig G, Stevens GC, Vashisht AA, Wohlschlegel JA, et al. Trichomonas vaginalis Exosomes Deliver Cargo to Host Cells and Mediate Host:Parasite Interactions. PLoS Pathog. 2013; 9 (7):e1003482. https://doi.org/10.1371/journal.ppat.1003482 PMID: 23853596

74. Dowling DJ, Hamilton CM, Donnelly S, La Course J, Brophy PM, Dalton J, et al. Major secretory antigens of the helminth Fasciola hepatica activate a suppressive dendritic cell phenotype that attenuates Th17 cells but fails to activate Th2 immune responses. Infect Immun [Internet]. 2010; 78(2):793–801. Available from: http://www.ncbi.nlm.nih.gov/pubmed/19917714 PMID: 19917714

75. Mantel PY, Hoang AN, Goldowitz I, Potashnikova D, Hamza B, Vorobjev I, et al. Malaria-infected erythrocyte-derived microvesicles mediate cellular communication within the parasite population and with the host immune system. Cell Host Microbe. 2013; 13(5):521–34. https://doi.org/10.1016/j.chom.2013.04.009 PMID: 23684304

76. Chaiyadet S, Sotillo J, Smout M, Cantacessi C, Jones MK, Johnson MS, et al. Carcinogenic liver fluke secretes extracellular vesicles that promote cholangiocytes to adopt a tumorigenic phenotype. J Infect Dis. 2015; 212(10):1636–45. https://doi.org/10.1093/infdis/jiv291 PMID: 25985904

77. Chowdhury IH, Koo SJ, Gupta S, Liang LY, Bahar B, Silla L, et al. Gene Expression Profiling and Functional Characterization of Macrophages in Response to Circulatory Microparticles Produced during Trypanosoma cruzi Infection and Chagas Disease. J Innate Immun. 2017; 9(2):203–16. https://doi.org/10.1159/000451055 PMID: 27902980

78. Kim MJK, Jung BK, Cho J, Song H, Pyo KH, Lee JM, et al. Exosomes secreted by Toxoplasma gondii-infected L6 cells: Their effects on host cell proliferation and cell cycle changes. Korean J Parasitol. 2016; 54(2):147–54. https://doi.org/10.3347/kjp.2016.54.2.147 PMID: 27180572

79. Mantel PY, Hjelmqvist D, Walch M, Kharoubi-Hess S, Nilsson S, Ravel D, et al. Infected erythrocyte-derived extracellular vesicles alter vascular function via regulatory Ago2-miRNA complexes in malaria. Nat Commun. 2016; 7:12727. https://doi.org/10.1038/ncomms12727 PMID: 27721445

80. Sisquella X, Ofir-Birin Y, Pimentel MA, Cheng L, Abou Karam P, Sampaio NG, et al. Malaria parasite DNA-harbouring vesicles activate cytosolic immune sensors. Nat Commun. 2017; 8(1):1985. https://doi.org/10.1038/s41467-017-02083-1 PMID: 29215015

81. Regev-Rudzki N, Wilson DW, Carvalho TG, Sisquella X, Coleman BM, Rug M, et al. Cell-cell communication between malaria-infected red blood cells via exosome-like vesicles. Cell. 2013; 153(5):1120–33. https://doi.org/10.1016/j.cell.2013.04.029 PMID: 23683579

82. Szempruch AJ, Sykes SE, Kieft R, Dennison L, Becker AC, Gartrell A, et al. Extracellular Vesicles from Trypanosoma brucei Mediate Virulence Factor Transfer and Cause Host Anemia. Cell. 2016; 164(1–2):246–57. https://doi.org/10.1016/j.cell.2015.11.051 PMID: 26771494

83. Soares RP, Xander P, Costa AO, Marcilla A, Menezes-Neto A, Del Portillo H, et al. Highlights of the São Paulo ISEV workshop on extracellular vesicles in cross-kingdom communication. J Extracell Vesicles. 2017; 6(1).

DC-SIGN mediated internalisation of glycosylated extracellular vesicles from *Schistosoma mansoni* increases activation of monocyte-derived dendritic cells

Marije E. Kuipers, Esther N.M. Nolte-'t Hoen, Alwin J. van der Ham, Arifa Ozir-Fazalalikhan, D. Linh Nguyen, Clarize M. de Korne, Roman I. Koning, John J. Tomes, Karl F. Hoffmann, Hermelijn H. Smits & Cornelis H. Hokke

Published online: 30 Apr 2020.

Submit your article to this journal ⌁

Article views: 762

View related articles ⌁

View Crossmark data ⌁

Taylor & Francis
Taylor & Francis Group

RESEARCH ARTICLE

OPEN ACCESS | Check for updates

DC-SIGN mediated internalisation of glycosylated extracellular vesicles from *Schistosoma mansoni* increases activation of monocyte-derived dendritic cells

Marije E. Kuipers [ID]a,b, Esther N.M. Nolte-'t Hoen [ID]b, Alwin J. van der Ham [ID]a, Arifa Ozir-Fazalalikhan [ID]a, D. Linh Nguyena, Clarize M. de Korne [ID]a, Roman I. Koning [ID]c, John J. Tomes [ID]d, Karl F. Hoffmann [ID]d, Hermelijn H. Smits [ID]a* and Cornelis H. Hokke [ID]a*

aDepartment of Parasitology, Leiden University Medical Center, Leiden, Netherlands; bDepartment of Biomolecular Health Sciences, Faculty of Veterinary Medicine, Utrecht University, Utrecht, Netherlands; cDepartment of Cell & Chemical Biology, Leiden University Medical Center, Leiden, Netherlands; dInstitute of Biological, Environmental and Rural Sciences (IBERS), Aberystwyth University, Aberystwyth, UK

ABSTRACT

Helminths like *Schistosoma mansoni* release excretory/secretory (E/S) products that modulate host immunity to enable infection. Extracellular vesicles (EVs) are among these E/S products, yet molecular mechanisms and functionality of *S. mansoni* EV interaction with host immune cells is unknown. Here we demonstrate that EVs released by *S. mansoni* schistosomula are internalised by human monocyte-derived dendritic cells (moDCs). Importantly, we show that this uptake was mainly mediated via DC-SIGN (CD209). Blocking DC-SIGN almost completely abrogated EV uptake, while blocking mannose receptor (MR, CD206) or dendritic cell immunoreceptor (DCIR, CLEC4A) had no effect on EV uptake. Mass spectrometric analysis of EV glycans revealed the presence of surface N-glycans with terminal Galβ1-4(Fucα1-3)GlcNAc (LewisX) motifs, and a wide array of fucosylated lipid-linked glycans, including LewisX, a known ligand for DC-SIGN. Stimulation of moDCs with schistosomula EVs led to increased expression of costimulatory molecules CD86 and CD80 and regulatory surface marker PD-L1. Furthermore, schistosomula EVs increased expression of IL-12 and IL-10 by moDCs, which was partly dependent on the interaction with DC-SIGN. These results provide the first evidence that glycosylation of *S. mansoni* EVs facilitates the interaction with host immune cells and reveals a role for DC-SIGN and EV-associated glycoconjugates in parasite-induced immune modulation.

Introduction

Schistosoma mansoni is one of the major helminth parasites of humans with over 200 million people infected [1,2]. In the initial phase of infection, schistosome larvae (cercariae) penetrate the skin of the host and transform into schistosomula. These schistosomula larvae will migrate to the circulatory system, develop into adult worms that mate and lay eggs [3]. *S. mansoni* can live up to 10 years in its host because it has developed successful mechanisms to evade immune responses. To establish this immune evasion, the parasite releases excretory/secretory (E/S) products that act on the host immune system [4]. Among these E/S products are extracellular vesicles (EVs) and evidence is accumulating that parasite-derived EVs contribute to parasite-host interaction [5]. The molecular composition of EVs from *S. mansoni* larvae and adult worms life stages has been partially characterized [6–8], but the interaction of their EVs with host cells remains unexplored.

For schistosomes to initiate and maintain infection, modulating host innate and adaptive immune responses is crucial [9]. Mouse models have shown that cercarial penetration triggers migration of innate antigen presenting cells (APCs), such as macrophages and dendritic cells (DCs), towards the skin draining lymph nodes [10]. These APCs have upregulated costimulatory molecules, like CD86 and major histocompatibility complex (MHC) class II, which are important for initiating adaptive immune responses. *In vitro* stimulation of mouse bone marrow-derived DCs (BMDCs) with E/S from schistosomula shows a similar pattern: increased costimulatory molecules and MHC class II expression and increased pro-inflammatory cytokine release (IL-6, IL-12, and TNF-α) [11]. Furthermore, cercarial secretions can upregulate the expression of IL-10 and programmed death ligand (PD-L)1 and 2 in human monocyte-derived (mo)DCs, suggesting that the parasite additionally utilizes regulatory pathways to dampen

adaptive immune responses [12]. Relatively little is known about the exact molecular or structural components derived from schistosomula that induce immunomodulatory effects. Thus far, it has been shown that recombinant tetraspanins, transmembrane proteins associated to adult worm EVs [13], induce IL-10 and Th1 cytokine responses by peripheral blood mononuclear cells [14]. Whether schistosomula EVs have similar effects on human DCs has not been investigated.

Studies exploring the molecular content of schistosomula E/S have shown that part of the cytokine responses by mouse macrophages and whole blood of infected individuals is induced by glycosylated antigens in the E/S [15,16]. Schistosome glycoconjugates can be recognized by host pathogen recognition receptors (PRRs) on APCs, in particular the C-type lectin receptors (CLRs) such as the mannose receptor (MR, CD206) [17], dectin-1/2 [18], dendritic cell immunoreceptor (DCIR, CLEC4A, CD367) [19] and dendritic cell-specific ICAM-3-grabbing nonintegrin (DC-SIGN, CD209) [20]. A well-known immunogenic glycan-motif, Galβ1-4(Fucα1-3)GlcNAc or LewisX (LeX), is present on glycoproteins in schistosomula and egg E/S and can be recognized by DC-SIGN [21] as well as MR [22], leading to different effects depending on the structural context of the LeX motif. Pathogen-associated molecular patterns (PAMPs) containing high-mannose (oligomannose) structures, which form ligands for MR and DC-SIGN [23] have also been found on glycoproteins in E/S from schistosomes [24]. This raises the question whether schistosomula EVs expose glycans instrumental in targeting to host immune cells and whether these EV-associated glycans play a role in modifying subsequent immune responses. While it is known that mammalian EVs contain glycoconjugates, publications on the structure and function of EV glycans are very limited so far [25–29].

In order to gain insights into the interaction of schistosome EVs with the immune system we studied the interaction of schistosomula EVs with human moDCs and found that the EVs are internalised mainly via DC-SIGN. We show that N-glycans on the surface and glycolipids of the EVs contain DC-SIGN ligands, including LeX. Furthermore, we demonstrate that these EV preparations increase the activation status of moDCs, affecting both immunostimulatory and immunoregulatory pathways which were partly dependent on the interaction with DC-SIGN. Our study provides evidence for a specific CLR-mediated uptake of EVs that substantiates the importance of EV-associated glycoconjugates in pathogen-host interaction.

Materials and methods

Schistosomula culture

Infected *Biomphalaria glabrata* snails were incubated in water at 30°C for 2 h to shed cercariae of the Puerto Rican-strain of *S. mansoni* by exposure to light. The collected cercariae in water were stored on ice for 1.5 h to immobilize them and were subsequently pelleted by centrifugation at 440 × g. After removal of the supernatant, 12 mL of pre-warmed (37°C) DMEM (Dulbecco's Modified Eagle Medium, high glucose with L-glutamine, Lonza, Basel, Switzerland) supplemented with 200 U/ml penicillin and 200 μg/ml streptomycin (Sigma-Aldrich, St. Louis, MO, USA), was added to transform the cercariae to schistosomula by providing mechanical force via pipetting and incubating for 20 min at 37°C [30]. Cercarial bodies were separated from their tails using an orbital shaker. The collected schistosomula were resuspended in DMEM at a concentration of 7,500 schistosomula/mL and cultured in 25 cm^2 polystyrene flasks (Greiner Bio-One, Alphen a/d Rijn, The Netherlands) at 37°C and 5% CO_2 for 72 h.

EV isolation and staining

Schistosomula E/S products were enriched for EVs by differential centrifugation as previously described, with minor modifications [6]. Briefly, the collected culture supernatant (9–34 mL per culture, 7,500 schistosomula/mL) was centrifuged in 15 mL tubes (Greiner Bio-One) twice at 500 × g (k-factor 115,790.8) for 2 min (4°C) (SX4750A rotor and an Allegra X-15 R centrifuge) (Beckman Coulter, Brea, CA, USA) with low brake to remove remaining parasites. To remove any residual debris, the supernatant was subsequently centrifuged at 700 × g (k-factor 82,764.4) for 20 min (4°C, low brake). Next, an EV-enriched pellet was obtained by centrifugation of the supernatant at 31,000 rpm (average around 120,000 × g, k-factor 216.3) for 80 min at 4°C (max. acceleration and brake), followed by three wash steps with cold phosphate buffered saline (PBS) (B. Braun, Melsungen, Germany) in thin-wall polypropylene tubes using an SW41 Ti rotor and an Optima XE-90 ultracentrifuge (Beckman Coulter). For binding/uptake experiments, EVs were stained with PKH26 (Sigma-Aldrich) after the first ultracentrifugation step by addition of 80 μL Diluent C to the resuspended EV-enriched pellet and incubation of 93 μL diluted PKH26 (1.5 μL in 100 μL Diluent C) for 3 min at RT before addition of 11 mL PBS. Unconditioned culture medium incubated without

parasites was processed (and stained) following the same procedures and was used as (dye) control. EV-enriched pellets (from 66,300–253,200 schistosomula) for *in vitro* experiments were resuspended in 510 μL PBS, for transmission electron microscopy (TEM) and glycan analysis in 100 μL PBS, and for cryo EM in 40 μL PBS. All were stored at −80°C until further use except for 1 cryo EM sample, which was processed directly after EV isolation. We have submitted all relevant data of our experiments to the EV-TRACK knowledgebase (EV-TRACK ID: EV190032) [31].

Transmission electron microscopy

EV preparations were generated in Leiden and visualized by TEM at Aberystwyth University, as described previously [6]. Briefly, 10 μl of EV-enriched sample was fixed with an equal volume of 4% glutaraldehyde, adsorbed onto Formvar/carbon-coated copper grids (Agar scientific, Stansted, UK) for 40 min, and subsequently contrast stained with 2% uranyl acetate (pH 4) for 10 min. Processed samples were then visualized on a Jeol 1010 transmission electron microscope operated at 80 kV. Images were recorded with a Kodak MegaPlus camera Model 1.4i, other than the addition of scale bars, no further image processing was done. Sizes were measured by hand using Fiji/ImageJ software [32].

Nanoparticle tracking analysis (NTA)

EV-enriched suspensions were diluted 1:100 in PBS (to obtain 25–100 particles per frame at camera level 16) before analysing the concentration and size distribution by nanoparticle tracking analysis (NTA) using a NanoSight NS500 (Malvern Panalytical, Malvern, UK) equipped with an sCMOS camera. For each EV-enriched pellet, three videos of 30 seconds were recorded on three different camera levels: 12, 14 and 16. The analysis was done with NTA3.3 software and a detection threshold of 5. The average particle concentration of nine videos per EV-enriched sample, after subtraction of the NTA background data from PBS alone, was used for further experiments. We additionally measured the protein concentration of the EV-enriched pellets with microBCA according to the manufacturers protocol (Pierce, Thermo Fisher Scientific, Waltham, MA, USA).

Cryo electron microscopy

Previously frozen or freshly isolated EV preparations (EV from 86,00–112,00 schistosomula in 40 μL PBS) were visualized by cryo EM. Copper EM grids

supporting a carbon film with regularly spaced 2 micron holes (R2/2, Quantifoil, Jena, Germany) were glow-discharged in air at 0.2 mbar for 2 min at 20 mA (EMITECH K950X with glow discharger unit). A 3 μL drop of sample was applied to the grid and transferred into the environmental chamber of a Leica EM grid plunger (Leica Microsystems, Wetzlar, Germany) operating at RT and between 92% and 94% humidity. Excess sample was blotted away for 1 second using filter paper (Whatman no.1) and without waiting plunged into a mixture of ethane/propane (63/37 v/v) cooled with liquid nitrogen to −193°C. After vitrification, grids were stored under liquid nitrogen and transferred into a cryo holder (type 626, Gatan, Germany). In total 238 cryo-EM projection images were recorded by 1 second exposures at spot 5 on a FEI Tecnai F12 at 120 kEV on a 4 k × 4 k CCD camera (Eagle, Thermo Fisher Scientific) at a magnification of 13,500 × (0.85 nm pixel size) and a defocus value ~ −8 microns. Size measurement was performed by hand using Fiji/ImageJ software [32]. After removing double images and images with no EVs, 233 images were used to measure a total of 1056 EVs, which were subsequently quantified in segments of 20 nm (i.e. 21–40 nm, 41–60 nm, 61–80 nm … 861–880 nm, 881–900 nm).

Human monocyte-derived dendritic cells (moDCs)

Venous blood of healthy volunteers who provided informed consent, approved by the Institutional Review Board of Leiden University Medical Centre, was used to isolate monocytes and differentiate to moDCs as previously described [33]. Immature DCs were harvested on day 5 or 6, counted, seeded at 5×10^4 cells/well in a 96 well flat-bottom plate, and rested overnight at 37°C and 5% CO_2. Subsequently, cells were stimulated with or without a pre-incubation of 30 min with 10 mM EGTA (Sigma-Aldrich), 20 μg/mL αDC-SIGN/CD209 (clone AZN-D1, custom order without sodium-azide) (Beckman Coulter), 20 μg/mL αMR/CD206 (clone 15–2) (BioLegend, San Diego, CA, USA), 20 μg/mL αDCIR/CLEC4A (clone 111F8.04, Dendritics, Novus Biologicals, Centennial, CO, USA), and 20 μg/mL mouse IgG1 isotype control (clone P3.6.2.8.1) (Invitrogen, Thermo Fisher Scientific) in the presence of αFcgammaR-binding inhibitor (eBioscience, Invitrogen) and in the presence or absence of the maturation factors IL-1β (25 ng/mL) (BioLegend) and TNF-α (50 ng/mL) (Sino Biological, Beijing, P.R. China) or LPS (100 ng/mL) (InvivoGen, San Diego, CA, USA). As a positive control for the αMR, PF-647-labelled recombinant omega-1 was used [22,34]. EV-enriched pellets were thawed only once

and several EV batches were pooled before incubation with the cells (6×10^9 EV/mL or mentioned otherwise). To investigate the effect of surface de-N-glycosylation, EVs were incubated with or without peptide N-glycosidase F (PNGase F) (4 U/100 μL, Roche Diagnostics, Almere, The Netherlands) at 37°C for 20 h before moDC incubation. Supernatants were collected from >85% CD1a$^+$ cell cultures after 24 h stimulation and IL-6 (Sanquin, Amsterdam, The Netherlands), IL-10 (BioLegend), and IL-12p70 (BD Biosciences, Franklin Lakes, NJ, USA) cytokine production was determined with ELISA according to the manufacturers protocols. Stimulated moDCs were washed, stained, and measured by flow cytometry on a FACSCanto II (BD Bioscience) and using the following antibodies: CD1a-BV421 (clone HI149) (BioLegend), HLA-DR-APC-eF780 (clone LN3) (eBioscience), PD-L2/CD273-FITC (clone MIH18) (Miltenyi Biotec, Bergisch Gladbach, Germany), CD86-FITC (clone 2331 (FUN-1)), CD40-APC (clone 5C3), CD80-V450 (clone L307.4), PD-L1/CD274-PE-Cy7 (clone MIH1) (all BD Bioscience) with the addition of Fc receptor binding inhibitor (eBioscience) and Aqua live/dead staining (Invitrogen). Flow cytometric measurements were analysed with FlowJo (version 10, BD Bioscience).

Confocal microscopy

5×10^4 moDCs/chamber were seeded onto poly-L-lysine (Sigma-Aldrich) coated coverslips of a 4 chamber glass bottom dish (ø35 mm; Greiner Bio-One) for 24 h. Cells were pre-incubated with EGTA or αDC-SIGN+αFcgammaR-binding inhibitor as described above, incubated with PKH-labelled schistosomula EV-enriched pellets for 5 h, subsequently washed, and treated with Hoechst (Sigma-Aldrich). Images were taken at 37°C and 5% CO_2 on a Leica TCS (true confocal scanning SP8 WLL (white light laser) microscope (Leica Microsystems). The sequential scanning mode was applied to image Hoechst (excitation: 405 nm, emission: 420–470 nm) and PKH26 (excitation: 561 nm, emission: 570–630 nm). For imaging the uptake of EVs, a 63× objective (Leica HC PL APO 63×/1.40na OIL CS2) was used. The z-stacks were recorded and maximum projections of the recorded z-stacks were generated using the Leica software (LAS X version 1.1.0.12420; Leica Microsystems).

N-glycan and glycolipid-glycan analysis

For the N-glycan analysis, EV-enriched pellets (in PBS) from >100,000 cultured schistosomula were lyophilized, resuspended in 100 μL milliQ water, sonicated and subsequently reduced and denatured for 10 min at 95°C with the addition of SDS and β-mercaptoethanol which were neutralized by adding NP-40 (Sigma-Aldrich). Full details on N-glycan isolation has been described previously [35]. N-glycans were released by PNGase F (4 U/100 μL) incubation for 24 h at 37°C and cleaned up by collection in the flow through of reversed phase (RP) C18-cartridges (JT Baker, Phillipsburg, NJ, USA) followed by isolation on carbon cartridges (Supelclean ENVI-carb SPE, Sigma-Aldrich). In addition, directly after isolation, intact EV preparations in PBS were treated with PNGase F for 24 h at 37°C to release directly accessible N-glycans (surface glycans). The total suspension was subsequently transferred to a thin-wall polypropylene tube and topped up with PBS. The EVs were pelleted by ultracentrifugation at 42,000 rpm (average around $120,000 \times g$, k-factor 85.4) for 65 min at 4°C (max. acceleration and brake) using a TLS-55 rotor and an Optima TLX (Beckman Coulter). Next, the supernatant containing the PNGase F released N-glycans was collected and these N-glycans were isolated with C18- and carbon-cartridges. The EV-enriched pellet without PNGase F accessible surface N-glycans was resuspended in PBS, lyophilized, sonicated, reduced, denatured, and treated with PNGase F to isolate remaining N-glycans as above.

For glycolipid-glycans analysis, EV-enriched pellets were lyophilized, resuspended in milliQ water, sonicated, and subjected to extraction with chloroform and methanol (MeOH). The upper phase was collected after sonication and centrifugation. Similar volume as collected was replaced with 50% MeOH and the previous steps were repeated twice. All collected upper phases of the extraction were applied to an RP C18-cartridge and flow-through and wash fractions were combined and applied to another C18-cartridge. Glycolipids were eluted from the cartridges with chloroform/MeOH/water and dried under a flow of nitrogen. The glycolipids were subsequently dissolved in 200 μL 50 mM sodium acetate with 0.1% sodium taurodeoxycholate hydrate (Sigma-Aldrich), sonicated, and heated to 60°C for 10 min. 2 mU of recombinant endoglycoceramidase II (*Rhodococcus* sp.) (rEGCase II) (Takara-bio, Kusatsu, Shiga, Japan) was added to release the lipid-bound glycans. After 24 h at 37°C, another 2 mU was added and the sample was incubated at 37°C for another 24 h. The purification of released lipid-glycans was performed as described for the N-glycans using RP C18- and carbon cartridges.

To support glycan structure assignments, part of the isolated N-glycans and glycolipid-glycans were additionally treated with hydrofluoric acid (HF), which removes labile substitutions including α1-3 linked

fucoses. All isolated glycans were labelled with 2-aminobenzoicacid and purified by Biogel P10 (Bio-Rad, Hercules, CA, USA). The labelled glycans were measured by MALDI-TOF-MS with 2,5-dihydroxybenzoic acid (Bruker Daltonics, Bremen, Germany) as matrix using UltrafleXtreme mass spectrometers (Bruker Daltonics) in the negative-ion reflectron mode. When necessary, samples were cleaned up with ZipTip C18 (Merck Millipore, Burlington, MA, USA) before MALDI-TOF-MS. The obtained mass spectra were smoothed and the base-line was subtracted using FlexAnalysis (version 3.4, Bruker Daltonics). Glycan compositions were identified from the peak lists using GlycoWorkbench (Version 3) [36]. Peaks with a signal to noise ratio below 2 were excluded and masses are registered as deprotonated $[M-H]^-$. 2-AA was taken into account as a fixed reducing-end modification. For the interpretation of the relative most abundant signals for spectral assignments we used (when available) previously published structural data from *S. mansoni* glycans [35]. In the spectra, the structure of the most likely or most abundant isomer of the composition is indicated.

RNA extraction and qPCR analysis

Human moDCs were pre-incubated with or without αDC-SIGN, αMR, or IgG1 isotype and stimulated with IL-1β and TNF-α and schistosomula EV-enriched preparations as described above. After 6 h stimulation at 37°C and 5% CO_2, cells were stored on ice for 10 min, harvested, washed with cold PBS, snap frozen, and stored at −80°C till RNA extraction. RNA was extracted with the RNeasy Kit (Qiagen, Hilden, Germany) according to the manufacturer's protocol. RNA was quantified using NanoDrop 1000 Spectrophotometer (Thermo Fisher Scientific) and cDNA synthesis was performed on 0.2 μg RNA according to standard procedures. Primer Express (Applied Biosystems, Waltham, MA, USA) was used to design primers that were synthesized by Biolegio (Nijmegen, The Netherlands). Sequences of the primers were: β-actin_Forward(F): 5′- GCTACGAGCTGCCTGACGG-3′; β-actin_Reverse(R): 5′- CAGCGAGGCCAGGATGGAG CC-3′; β-2-M_F: 5′- TGCCGTGTGAACCATGTGA-3′; β-2-M_R: 5′-CCAAATGCGGCATCTTCAA-3′; RPLPO _F: 5′-GGCGACCTGGAAGTCCAACT-3′; RPLPO_R: 5′-CCATCAGCACCACAGCCTTC-3′; IL-10_F: 5′-ACCT GCCTAACATGCTTCGAG-3′; IL-10_R: 5′- CCA GCTGATCCTTCATTTGAAAG-3′; TNF-α_F: 5′-TCT TCTCGAACCCCGAGTGA-3′; TNF-α_R: 5′-CCTCT GATGGCACCACCAG-3′; IL-12p35_F: 5′-CTCCTGGAC CACCTCAGTTTG-3′; IL-12p35_R: 5′-TTGTCTGGCCT TCTGGAGCA-3′. Quantitative real-time PCR (qPCR) was performed using CFX96 instruments (Bio-Rad Laboratories) and CFX Maestro (Bio-Rad) software. Technical duplicates with <1 C_q value difference were averaged and gene expression was calculated with the $\Delta\Delta C_q$ method using the average C_q of the reference genes β-actin, β-2-M, and RPLPO to normalize [37].

Statistical analyses

All data were analysed using a paired student *t*-test or repeated measures One-way ANOVA (P values <0.05 were considered significant) with Tukey's or Dunnett's Multiple Comparison Test in GraphPad Prism 5.0 (GraphPad Software, Inc., La Jolla, CA, USA).

Results

Cryo electron microscopy reveals ultrastructural characteristics of schistosomula EVs

Schistosomula were cultured for 72 h and EV-enriched preparations were obtained from schistosomula E/S by sequential (ultra)centrifugation steps. TEM confirmed isolation of vesicles in the size-range between 35 and 190 nm (Figure 1(a–b)). NTA analysis showed a size-range of 30–650 nm with a minor peak around 40 nm and three major peaks around 110, 160, and 350 nm (Figure 1(c)). Culture medium without parasites that was processed similarly (medium control) and PBS alone only showed minor peaks between 60 and 150 nm as NTA background (Figure 1(c)). The average particle concentration measured with NTA was $2.33E^{10}$/100,000 schistosomula and the average protein concentration of EV-enriched preparations was 6 μg/ 100,000 schistosomula.

Although the TEM images corresponded with previous observations [6], there was a discrepancy in the sizes measured with the TEM and NTA. Therefore, we additionally analysed the EV preparations with cryo EM to visualise the near native state of the EVs and measure their size (Figure 1(d)). Interestingly, the cryo EM revealed thin filament-like structures covering the EV surface in 45.5% of all measured EV and in >70% of EVs when excluding EVs smaller than 100 nm. The filamentous structures ranged from 10 to 340 nm in length (average length of 128.5 nm) additional to the size of the EV diameter to the EV membrane (Figure 1(e)). These surface structures were most likely lost during the sample preparation for negative stained TEM (Figure 1(a)) and thus not observed, while NTA size measurement did include these structures as shown by similar size ranges between NTA and cryo EM.
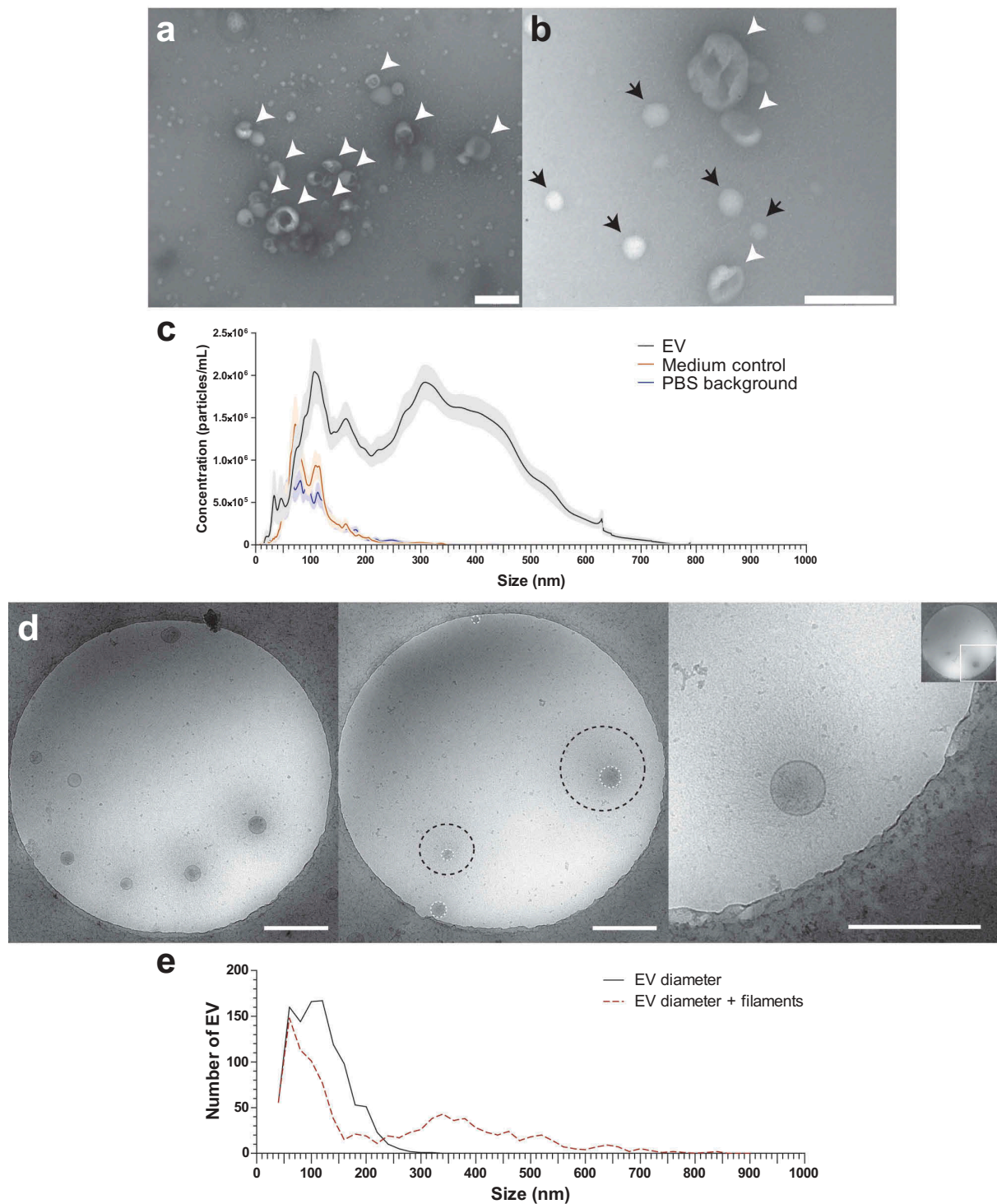
Figure 1. TEM, NTA and cryo EM measurement of schistosomula EVs.

EV-enriched preparations analysed by transmission electron microscopy at 60,000 × (a) and 120,000 × magnification (b). Scale bars are 200 nm. EVs are pointed out with arrow heads, the small (<60 nm) structures (black arrows) in (b) are artefacts and were also observed in PBS only. In addition, EVs were analysed by nanoparticle tracking analysis (NTA) (c). The graph shows the average of 17 schistosomula EV-enriched preparations (black line), 10 medium controls (dark orange line), and 15 PBS (background) in which the preparations were resuspended (blue line), averages are shown with SEM (lighter areas). Cryo EM of EVs at 13,500 × magnification (d). Scale bars are 500 nm. The EV membrane and stretch of the filamentous structures are indicated in the middle pane with white dashed circles and black dashed circles, respectively. Right pane shows a close up of one EV with filaments. Quantification of the EV sizes excluding (EV diameter) or including (EV diameter + filaments) the thin filaments from a total of 1056 EVs (e). EM pictures are representative for four biological replicates.

Internalisation of schistosomula EV by human moDCs is calcium dependent

To investigate the interaction of schistosomula EVs with human moDCs, EVs were first labelled with the fluorescent dye PKH26. MoDCs ($0.25E^6$ moDC/mL) were incubated with a maximum of $6E^9$ EV/mL, which is equivalent to approximately 10 moDCs

receiving the number of EVs released by one schistosomulum during three days of culture. After 2 h of incubation, there was a dose-dependent increase in EV binding/uptake by the CD1a+ moDCs indicated by an increased geometric mean fluorescence intensity (geoMFI) relative to cells in medium only (Figure 2). Furthermore, the fluorescence of cells incubated with dye control was unchanged, indicating that the increase
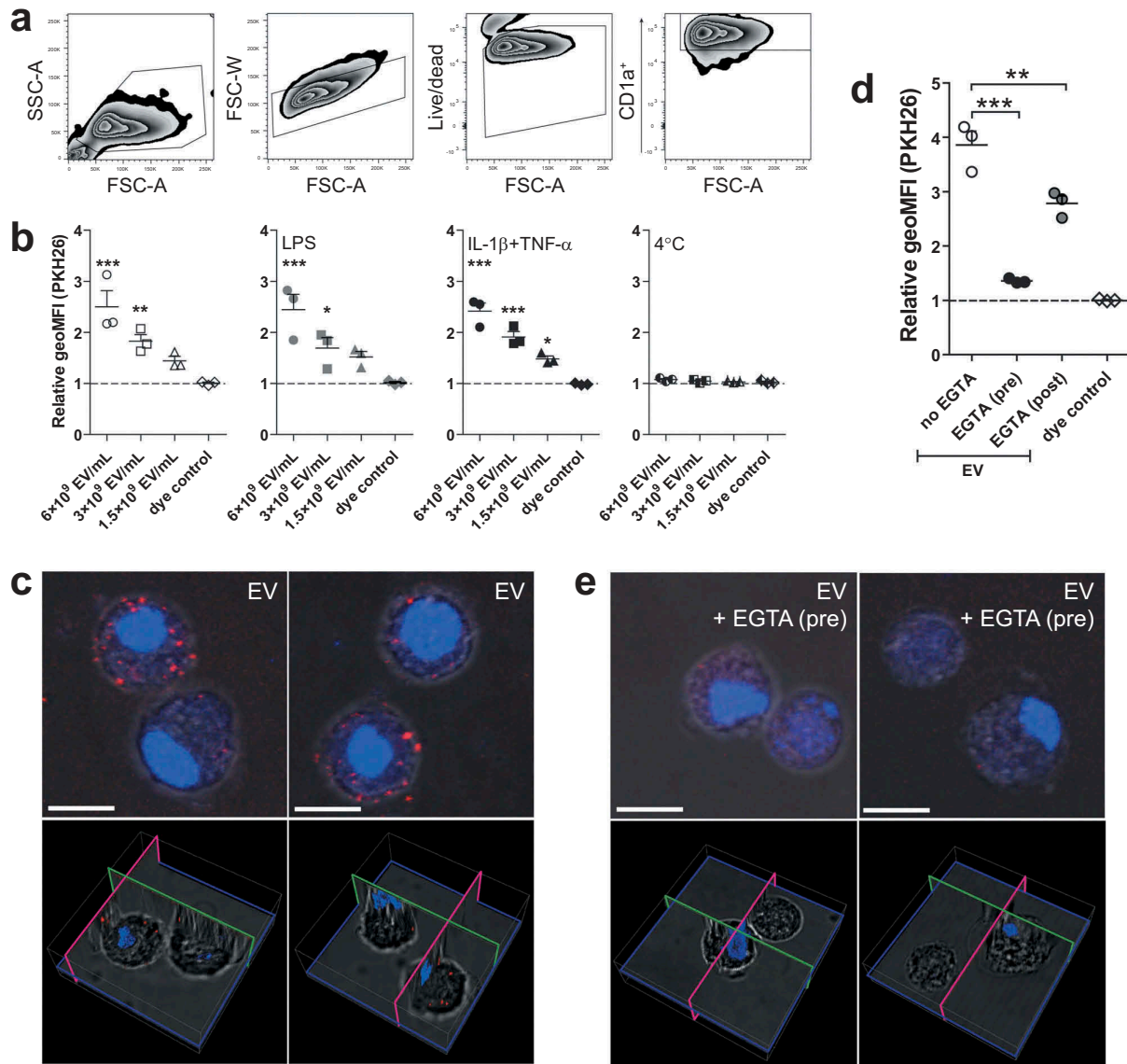

Figure 2. Dose dependent uptake of schistosomula EVs by human moDC is temperature and calcium dependent.

Measured PKH26 fluorescence (PKH26 labelled EVs) of CD1a+ cells was obtained via gating as pictured in (a). The geoMFI (geometric mean fluorescent intensity) of PKH26 is shown relative to unstimulated cells (b). MoDC from three donors. EV uptake visualized by confocal microscopy (c). Images show maximum projections (top panels) and 3D visualizations (bottom panels) of recorded z-stacks of two different fields. PKH26-labelled EVs are stained in red and the nuclei in blue (Hoechst). Selected pictures are representative for three donors. Human moDC incubated with EVs with either EGTA added pre- or post-incubation (d). Confocal images of moDC pre-treated with EGTA followed by EV incubation (e). Scale bars are 10 μm. Mean±SEM *$p < 0.05$, **$p < 0.01$, ***$p < 0.001$, using repeated measures ANOVA with Dunnett's Multiple Comparison Test compared to cells in medium only (b) or repeated measures ANOVA with Tukey's Multiple Comparison Test (d). SSC-A, side-scatter; FSC-A, forward-scatter

in MFI was due to binding/uptake of labelled EVs and not due to dye aggregates [38]. EV binding/uptake by moDCs did not change due to stimulation of the cells with LPS or in the presence of IL-1β+TNF-α. Incubation at 4°C instead of 37°C did not lead to binding/uptake of EVs by the moDCs (Figure 2), suggesting that the interaction with and uptake of the schistosomula EVs by target cells are active processes. We visually confirmed that EVs were internalised by moDCs with confocal microscopy (Figure 2(c)).

MoDCs are known to express C-type lectin receptors that bind glycan motifs present on schistosome E/S components in a calcium dependent manner [39]. To investigate whether moDCs also recognise schistosomula EVs via CLR-glycan motif interactions, moDCs were incubated with fluorescently labelled EVs in the presence of the calcium chelator EGTA and subsequently analysed by flow cytometry and confocal microscopy (Figure 2(d–e)). Pre-incubation of EGTA almost completely abrogated the fluorescence signal and EV internalisation of moDCs compared to EV-exposed moDCs without EGTA pre-incubation, indicating calcium dependent interaction with moDCs such as CLRs. Next, when EGTA was added after incubation with EVs in order to remove EVs bound to CLRs, this resulted in only a minor reduction of fluorescence signal (Figure 2(d)), confirming that most of the EVs were internalised by moDCs rather than bound to the surface.

Schistosomula EVs contain CLR ligands on their surface

We next analysed the glycosylation of schistosomula EVs to assess whether ligands for CLRs were present. First, the overall N-glycan content of the EV-enriched preparations was determined by mass spectrometry (Figure 3(a)). MALDI-TOF mass spectra of PNGase F released N-glycans were assigned based on the detailed glycan structure descriptions available for overall N-glycan preparations of *S. mansoni* schistosomula [35]. Interestingly, the spectrum of N-glycans from the EV preparation was highly similar to previously published spectra of total extracts of three-day cultured schistosomula [24,35]. The major signals are from oligomannosidic structures of complex glycans with a core(α6)-fucose and one or two antennae consisting of Galβ1–4GlcNAc (LacNAc, LN) and/or LeX. Structures with a core-xylose modification or GalNAcβ1–4GlcNAc (LacDiNAc or LDN) antennae with five to nine fucose residues were observed at relatively low levels (Figure 3(b)). These results show that schistosomula EVs contain similar N-glycans as

previously found in total schistosomula extracts, including LeX and oligomannose motifs, which are both ligands for DC-SIGN and MR [21,23].

To identify specific N-glycans that might be available for interaction with CLRs on the surface of EVs, we treated intact EVs with PNGase F to release all ("surface") N-glycans that were accessible to the enzyme. MALDI-TOF-MS analysis was performed on both the released "surface" N-glycans as well as on the remaining N-glycans of the PNGase F-treated ("shaved") EVs (Figure 3(c–d)), which likely represent glycans on the inside of the EVs. Interestingly, the most abundantly detected N-glycans on the EV surface contained one or two LeX antennae (Figure 3(c)) while the major glycans of the "shaved" EVs were the oligomannosidic structures (Figure 3(d)). These results show that the glycoproteins on the surface of schistosomula EVs carry a specific subset of N-glycans with LeX motifs, which are potential ligands for DC-SIGN or MR in the context of pathogen-host interactions [19,40,41].

EVs are internalised via DC-SIGN but not MR or DCIR

To investigate whether DC-SIGN or MR on moDCs were involved in uptake of schistosomula EVs via glycan motifs on these EVs, moDCs were pre-incubated with antibodies blocking DC-SIGN or MR and subsequently incubated with labelled schistosomula EVs for 2 h (Figure 4(a–b)). In addition we investigated EV binding after blocking DCIR, a receptor expressed on moDCs that does not bind LeX containing glycans but has been shown to bind *S. mansoni* cercarial extract [19]. Blocking DC-SIGN led to almost complete inhibition of EV uptake while blocking the MR, DCIR, or pre-incubation with the isotype control did not reduce EV internalisation. Inhibition of EV internalisation after DC-SIGN block was confirmed by confocal microscopy (Figure 4(c)). This reveals that schistosomula EVs were internalised by moDCs via DC-SIGN.

EV-associated glycolipid-glycans include DC-SIGN ligands

Given that the EV surface contained DC-SIGN ligands, including the LeX motif, we investigated whether EV deprived from surface N-glycans by PNGase F treatment would still be internalised by moDCs. Interestingly, the PNGase F-treated EVs showed a minor but not significant reduction in internalisation, and the EV uptake could still be inhibited by blocking DC-SIGN (Figure 5(a)). Since it has been shown that cercariae produce glycolipid-glycans that contain LeX
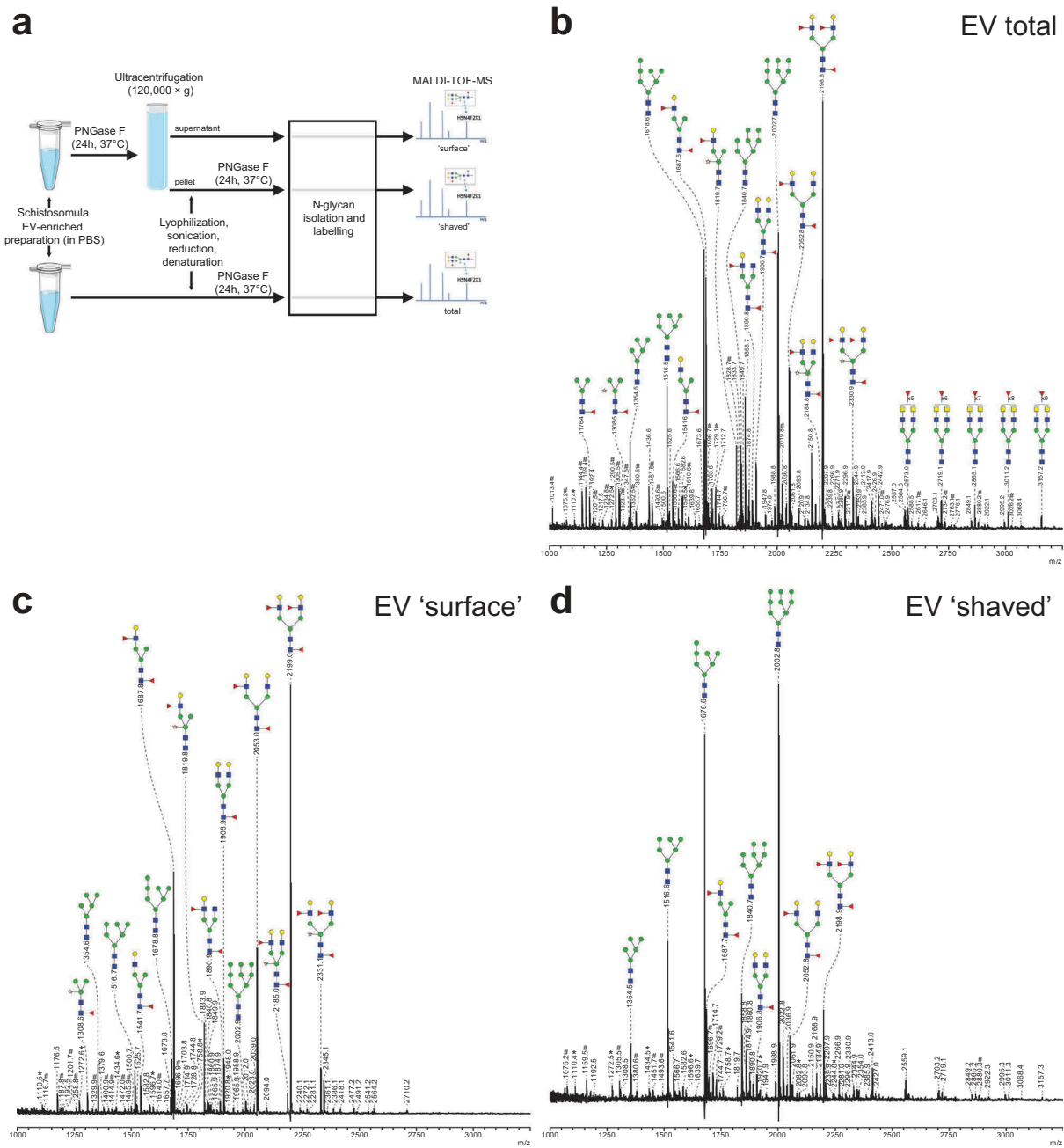
Figure 3. Schistosomula EV-surface N-glycans include DC-SIGN ligands.

Basic scheme of the protocol for obtaining the N-glycan spectra (images adjusted from Servier Medical Art) (a), details can be found in the materials and methods. PNGase F released N-glycans measured by MALDI-TOF-MS from total (b), intact (PGNase F accessible N-glycans, "surface") (c), and PNGase F treated (PGNase F non-accessible N-glycans on either surface or inside of the EV, "shaved") (d) EV-enriched preparations. Signals are labelled with monoisotopic masses. Putative structural assignments were deduced from these masses based on hydrofluoric acid (HF) treatment (data not shown) and published data of schistosomula glycans [34]. Spectra shown are representative for three biological replicates. Red triangle, fucose; yellow circle, galactose; green circle, mannose; blue square, N-acetylglucosamine; yellow square, N-acetylgalactosamine; white star, xylose; *, signals corresponding to a hexose oligomer of unknown origin; #, non-glycan signals

and other potential DC-SIGN ligands [35,42], we additionally determined the total lipid-derived glycan profile of the schistosomula EVs (Figure 5(b)). Here we detected a heterogeneous set of highly α3-fucosylated glycolipid structures, mostly similar to the glycolipid-glycans found in total schistosomula extract [35]. Interestingly, these lipid-glycans had terminal motifs that contained LeX, Fucα1-3Galβ1-4(Fucα1-3)GlcNAc (pseudo-LewisY
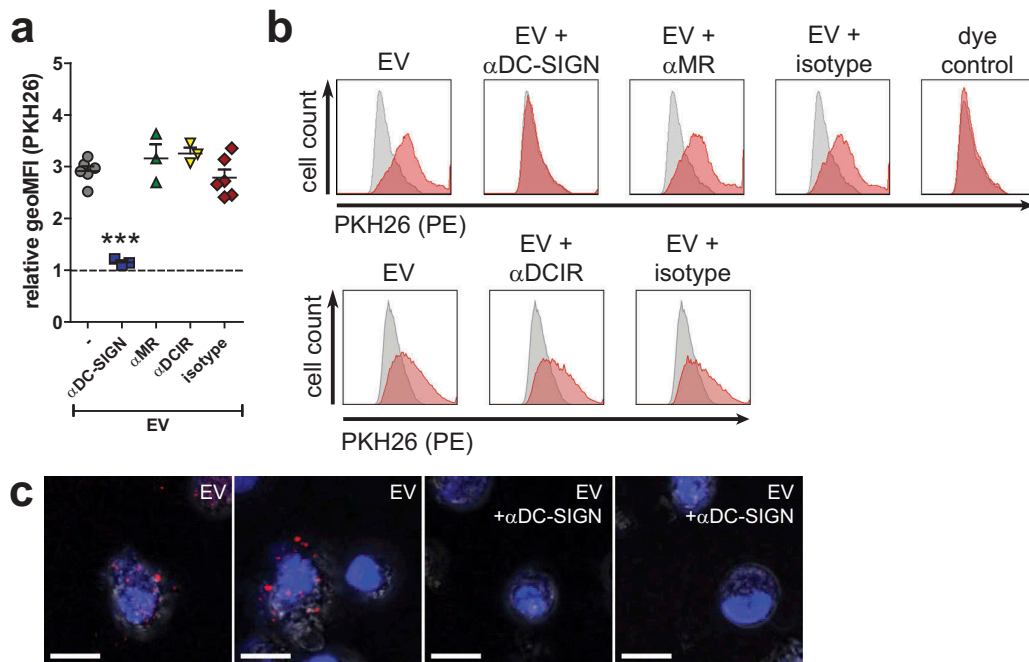
Figure 4. Schistosomula EVs are internalised via interactions with CLR DC-SIGN.

PKH26 fluorescence of CD1a+ cells with indicated pre-incubations (x-axis). The geoMFI (geometric mean fluorescent intensity) is shown relative to cells in medium only (a). MoDC from three to six donors. Representative histograms of two donors from same data plotted in a (b). Confocal microscopy visualisation of EV uptake and inhibition of EV uptake when DC-SIGN was blocked (c). Images show maximum projections of recorded z-stacks. PKH26-labelled EVs are stained in red and the nuclei in blue (Hoechst). Scale bar is 10 μm. Selected images are representative for three donors. Mean±SEM ***$p < 0.001$, using repeated measures ANOVA with Tukey's Multiple Comparison Test. MR, mannose receptor

(LeY)) and GalNAcβ1–4(Fucα1–3)GlcNAc (LDN-F) (Figure 5(b) insert), which are all previously described ligands of DC-SIGN [42,43]. These data suggest that additional to surface N-glycans, EV-associated lipid-glycans play a role in interaction with DC-SIGN.

Schistosomula EVs induced increased cytokine release and costimulatory molecule expression on moDCs

Next, we investigated whether incubation of moDCs with schistosomula EVs affect their activation status and cytokine production. We first incubated human moDCs for 24 h with EV-enriched preparations but observed no or very low release of cytokines. Therefore, in addition to EVs, moDCs were co-cultured with IL-1β and TNF-α, cytokines that are released by immune cells upon schistosome infection [3], allowing us to further investigate whether EVs could change the activation status of moDCs. Under these conditions, schistosomula EVs significantly increased IL-6, IL-10 and IL-12 secretion by moDCs (Figure 6(a)).

Furthermore, a significant upregulation of the costimulatory molecules CD80, CD86 and regulatory surface molecule PD-L1 was observed, while there was no significant effect on CD40, HLA-DR and PD-L2 expression (Figure 6(b)). These data suggest that the EV-enriched preparations were mostly synergizing or augmenting other inflammatory signals.

Role for DC-SIGN in EV-augmented immune responses

Since schistosomula-derived EVs were mainly internalised via DC-SIGN, we hypothesized that inhibiting this receptor would alter the observed augmented immune responses of moDCs by the EVs. Blocking DC-SIGN during a 24 h EV stimulation, however, did not show a significant effect on IL-6, IL-10 and IL-12 release (Figure 7(a)) nor on the expression of the co-stimulatory surface markers CD80, CD86, HLA-DR, PD-L1 and PD-L2 after 48 h stimulation (Figure 7(b)). To understand why the blocking of DC-SIGN did not consistently influence the enhanced immune responses of moDCs by the EVs whereas it almost completely blocked EV internalisation after 2 h, we studied EV uptake in the presence of DC-SIGN blocking antibodies after 48 h of
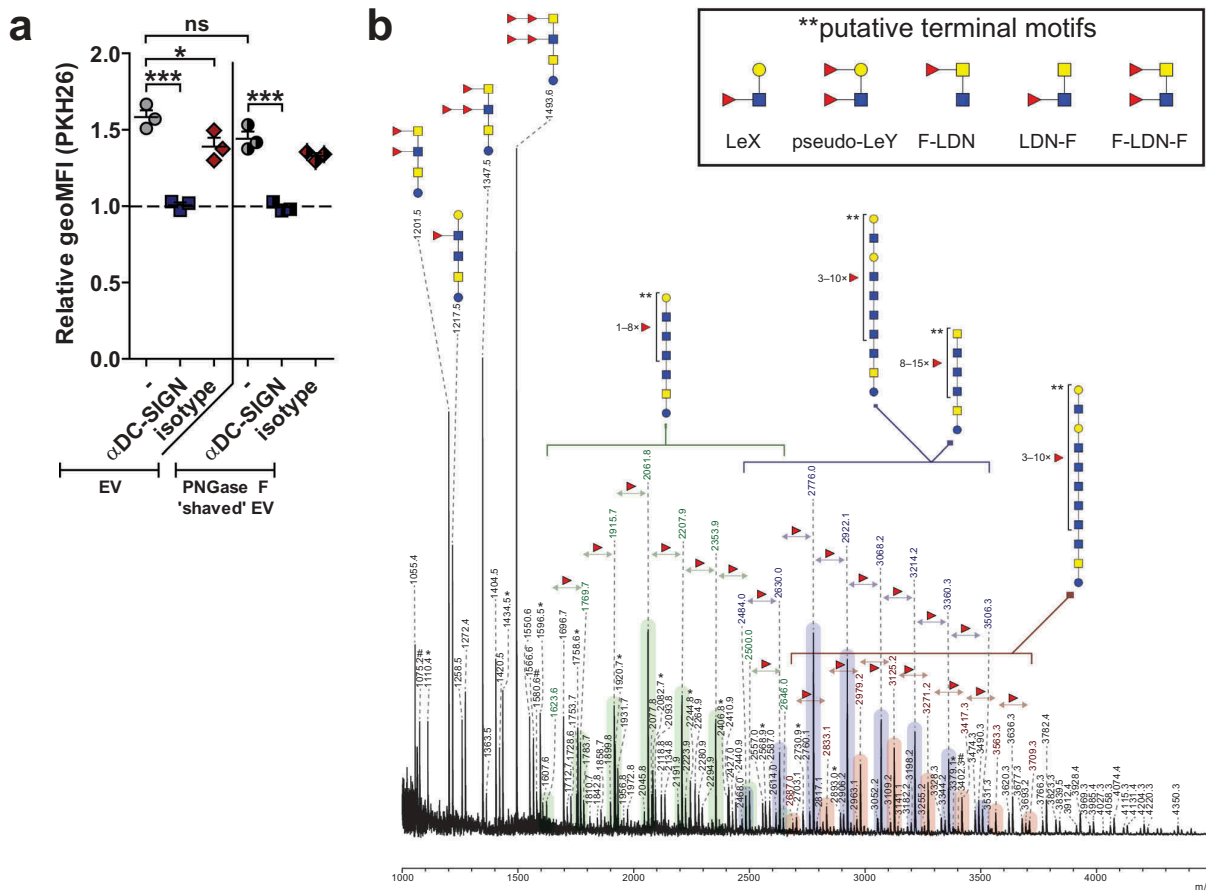
Figure 5. Internalisation of schistosomula EVs without surface N-glycans via DC-SIGN and EV-associated glycolipid-glycans.

The geoMFI (geometric mean fluorescent intensity) of PKH26 relative to unstimulated moDC after 2 h incubation with labelled EVs that were treated without or with PNGase F (a). Pre-incubations are indicated on the x-axis. MoDC from 3 donors. Mean±SEM *$p < 0.05$, ***$p < 0.001$, using repeated measures ANOVA with Tukey's Multiple Comparison Test. EV-derived glycolipid-glycans measured by MALDI-TOF-MS (b). Signals are labelled with monoisotopic masses. Putative structural assignments were deduced from these masses based on published data of schistosomula glycans [34] and on hydrofluoric acid (HF) data (not shown). Coloured bars indicate the corresponding core structure with varying numbers of fucose substitutions. Putative terminal motifs formed by these fucoses are indicated in the insert. The spectrum shown is representative for three biological replicates. Red triangle, fucose; yellow circle, galactose; blue square, N-acetylglucosamine; yellow square, N-acetylgalactosamine; LeX, LewisX; LeY, LewisY; F-LDN/LDN-F/F-LDN-F, fucosylated LacDiNAc *, signals corresponding to a hexose oligomer of unknown origin; #, non-glycan signals

incubation. Blocking of DC-SIGN significantly reduced EV internalisation after 48 h (Figure 7(c)). However, the vast majority of the moDCs were still positive for the fluorescent dye, although the fluorescent intensity was lower when DC-SIGN was blocked (Figure 7(d)). Possibly other mechanisms than those mediated by DC-SIGN play a role in EV internalisation by moDCs after prolonged exposure. To investigate whether blocking of DC-SIGN does interfere with moDC function during shorter incubations with schistosomula-derived EVs, moDCs were stimulated with EVs in the absence or presence of blocking antibodies for 6 h, after which cytokine mRNA expression was determined. Indeed, at this time point, the effect of blocking DC-SIGN was more prominent with a significant reduction in TNF-α mRNA and a trend for lower IL-10 mRNA expression (Figure 7(e)). IL-12p35 mRNA levels were also reduced in most donors, though not significant. These results show that, within the first hours of exposure but not at a longer timescale, the moDC immune profile is influenced by schistosomula EVs through internalisation via DC-SIGN.

Discussion

Schistosome parasites are master regulators of host immune responses and they release various molecules
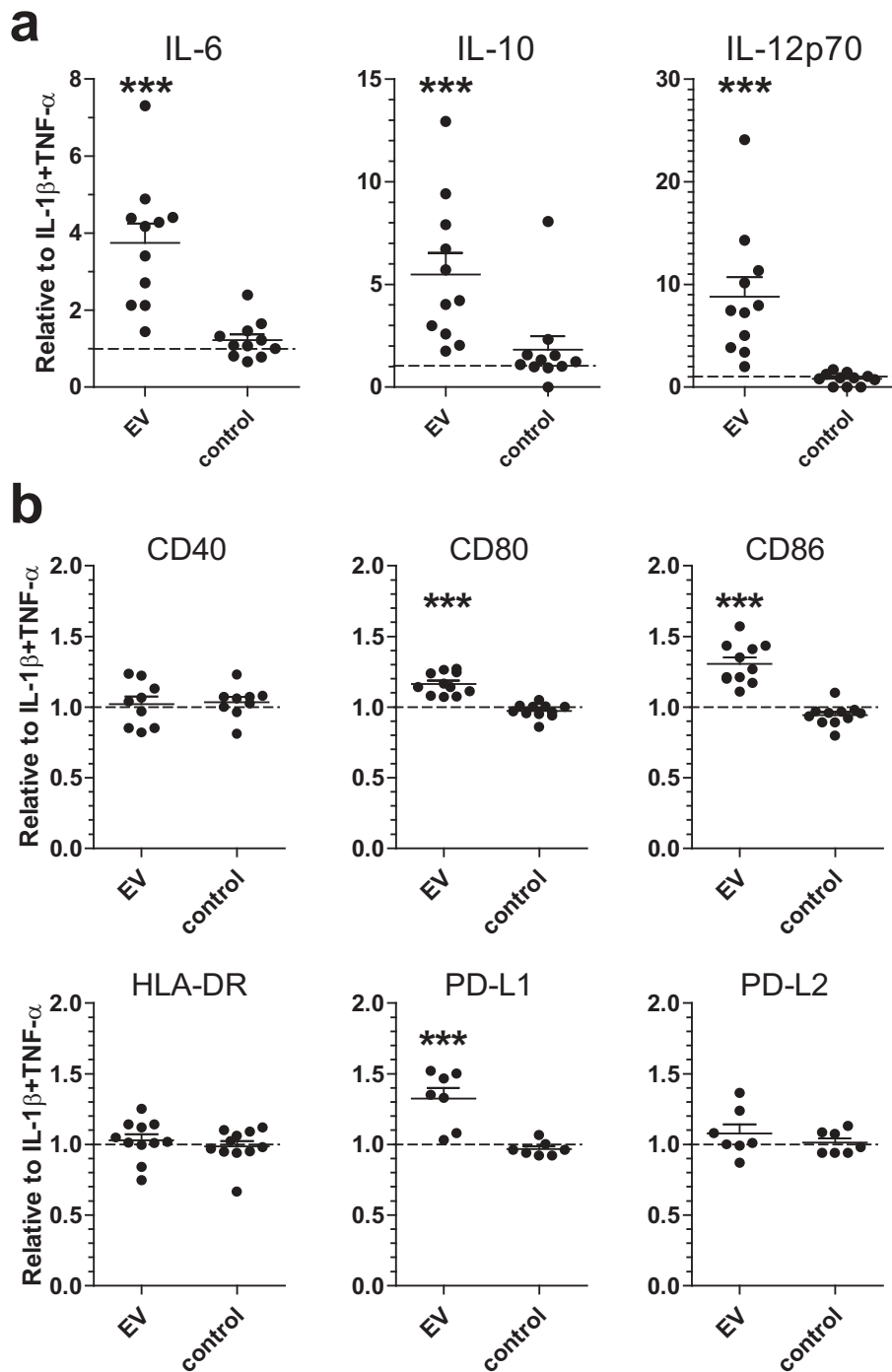
a

IL-6

IL-10

IL-12p70

b

CD40

CD80

CD86

HLA-DR

PD-L1

PD-L2

Figure 6. Schistosomula EVs augment moDC immune responses.

Released cytokines (a) and surface marker expression (b) of moDC incubated with EVs. The control is medium without parasites that has been cultured and processed exactly like the schistosomula EVs. Data points are shown as fold change relative to moDC with IL-1β and TNF-α for that specific donor. MoDC from 7 to 11 donors. Mean±SEM ***$p < 0.001$, using repeated measures ANOVA with Dunnett's Multiple Comparison Test

and products to achieve this. Here we demonstrate that *S. mansoni* schistosomula release EVs that contain LeX antigens on their surface. Interaction of the glycosylated EVs with DC-SIGN on moDCs lead to internalisation and enhanced expression of both immunostimulatory and regulatory effector molecules. Thus, schistosome
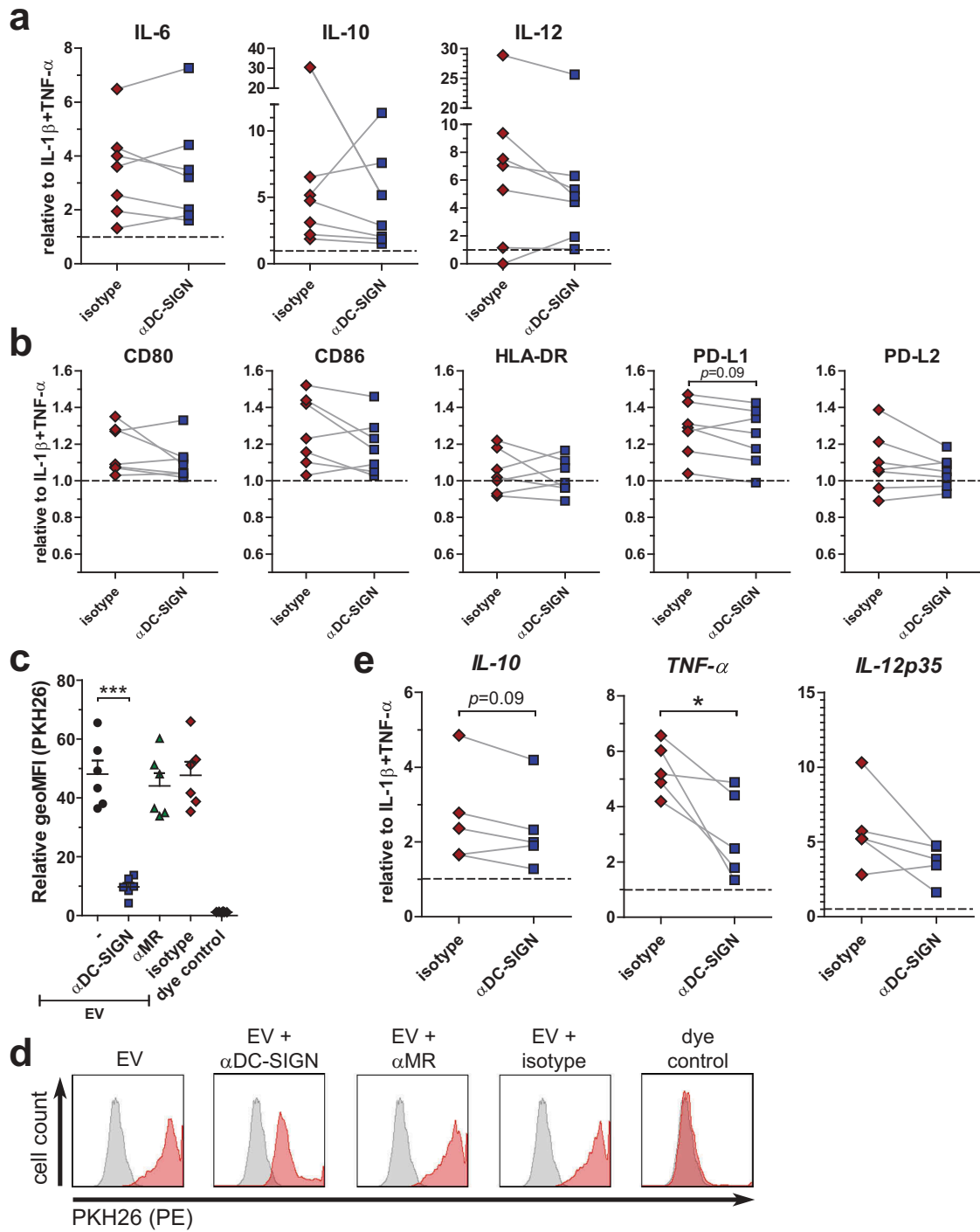
Figure 7. Role for DC-SIGN in augmented immune responses by schistosomula EVs.

Released cytokines (a) and surface marker expression (b) of moDC with indicated pre-incubations (x-axes) before EV incubation. Linked points represent data from one donor. Data is shown as fold change relative to moDC with IL-1β and TNF-α from that specific donor ($n = 7$). Summary of geometric mean fluorescent intensity (geoMFI) of moDC incubated with PKH26-labelled EVs for 48 h, relative to medium control (c) ($n = 6$). Histograms of moDC from one representative donor from data plotted in c (d). Relative expression of mRNA from moDC after 6 h EV incubation and indicated pre-incubations (x-axes) (e) ($n = 5$). *$p < 0.05$, ***$p < 0.001$, using repeated measures ANOVA with Tukey's Multiple Comparison Test (c) or paired student t-test (a, b, e)

EVs appear to contribute to immune modulation by the parasite.

Schistosomula are multicellular organisms, having various organs and cells as potential sources of their released EVs. It has been shown that micron-sized vesicles are released from their acetabular glands [11,44] and it is suggested that EVs can also derive from the tegument [6]. Since multicellular organisms release heterogeneous populations of EVs, it is likely that the moDCs can internalise these EVs via various receptors and/or routes [13]. The schistosomula-derived EV populations described here were heterogeneous in size, which we analysed with NTA (Figure 1(c)) and cryo EM (Figure 1(e)). The size of EVs may influence uptake routes, as has been shown for *Helicobacter pylori* outer membrane vesicles (OMVs): small OMVs were taken up via caveolin-mediated endocytosis and bigger OMVs via micropinocytosis and endocytosis [45]. The major population of EVs >300 nm we observed have not been described before for *S. mansoni* schistosomula [6]. Although we used a similar schistosomula EV isolation protocol as Nowacki et al [6], the isolated EVs in that paper were only visualised by TEM of negatively stained EVs and not by NTA. With this same technique, our isolated schistosomula EVs also showed similar sizes <200 nm (Figure 1(a–b)) but only with the NTA and cryo EM the EV population >300 nm was detectable. EVs >300 nm have not been found among adult worms EVs [7,8,46]. Schistosomes are organisms with a complex life cycle and the schistosomula and adult worm life stages differ in size, shape, molecular, and cellular make up, and interaction with the host and its immune system [2,47]. Therefore, it is likely that different life stages of the parasite produce different EV populations regarding molecular content [6,48] as well as size. Furthermore, the adult worm EVs published have been isolated by different protocols which may further explain differences between the observed sizes of EVs derived from various schistosome different life stages.

Interestingly, our cryo EM data showed that around half of the schistosomula-derived EVs were covered with thin filament-like structures (Figure 1(d)). These structures have not been described for eukaryotic EVs so far. It remains to be explored what the molecular composition of these EV-associated structures is and whether these structures are specific for *S. mansoni* and/or specifically related to the schistosomula life stage. These thin filaments resemble the electron-dense surface layer of extracellular proteins and LPS or glycocalyx on some bacteria [49,50] and their released OMVs [51]. We hypothesize that the structures on schistosomula EVs are composed of large, complex glycoconjugates and/or include proteins with attached glycan polymers, similar to the mammalian glycocalyx consisting of proteoglycans with attached glycosaminoglycans [25]. Altogether, the EM analyses emphasize that cryo EM provides improved visualisation of the near native state of isolated EVs compared to TEM of negatively stained EVs.

EVs released by *S. mansoni* schistosomula were internalised by human moDCs (Figure 2). Previous studies have demonstrated that *S. japonicum* EVs derived from adult worms and eggs are also internalised by host cells [46,52–54]. This indicates, together with our data, that at least three lifecycle stages of *Schistosoma* in humans release EVs that interact with the host. By chelating extracellular calcium with EGTA, schistosomula EV could not bind to or be taken up by the moDC (Figure 2(d–e)). This suggests that the interaction of the EVs with the moDC was via the ligation of glycoconjugates to CLRs, which is calcium dependent, and not via protein-protein interaction. By inhibiting specific CLRs we show that internalisation of schistosomula EVs by moDCs is primarily facilitated by DC-SIGN (Figure 4). This CLR is known to bind schistosome egg [21], cercarial [43], and worm antigens [55], via glycan motifs including mannotriose, LeX, LDN-F, and pseudo-LeY [19,42,43]. In contrast, CLR DCIR mainly binds LeB (LewisB) and sulpho-LeA (LewisA) motifs [19], and indeed, blocking this receptor did not reduce EV uptake by the moDC. Previously, it was shown that the egg-derived glycoprotein omega-1, which carries LeX containing N-glycans highly similar to those found here on the EVs (Figure 3), is mainly internalised by moDCs via the MR [22]. However, when blocking the MR, EV internalisation was not inhibited. This difference of internalisation routes between omega-1 and EVs could be explained by the characteristics of the two CLRs: DC-SIGN has one carbohydrate recognition domain (CRD), is present as tetramers, and it clusters in (lipid raft) nanodomains that are distributed on the cell membrane. Clustering increases the avidity of low affinity glycan-lectin interactions and allows this receptor to interact at multiple sites with pathogens that differ greatly in size [56]. On the other hand, the MR consists of multiple CRDs, which results in binding of multivalent or repetitive ligands to a single MR monomer [57]. Considering these aspects, larger particles such as EVs would favour DC-SIGN mediated uptake while smaller glycosylated proteins are more likely to be internalised via other receptors, such as the MR. A very recent publication substantiates this theory by showing that tumour-derived apoptotic EVs with high-mannose glycans on their surface were mainly internalised via interaction with DC-SIGN and not the MR [58]. Furthermore, it

suggests that, together with our findings, DC-SIGN mediated EV uptake may be a widely occurring mechanism, across a broad spectrum of species and may not be exclusive to schistosomula-derived EVs. Of note is that helminths, including *S. mansoni*, lack sialic acid in their glycan repertoire, which is a fundamental difference with mammalian glycans. It was recently found that EVs released by human glioblastoma cells had complex sialic acid-capped N-glycans on their surface that mainly bound to Siglec-9 on moDCs [59]. When sialic acids on the EV surface were enzymatically removed and LeY was inserted, EV uptake by moDC and binding of the EVs to DC-SIGN were increased. Furthermore, EVs from murine hepatic cell lines expose sialyl-LeX on the EV surface and removing the sialic acids with neuraminidase significantly increased EV uptake by M1 cell lines [28]. However, no DC-SIGN blocking experiments were performed in these studies. Thus, the question remains whether EV internalisation via DC-SIGN is specific for schistosomula EVs, or whether it is a more general mechanism via which EVs from both pathogens and mammalian cells are internalised. However, we cannot exclude the possibility that internalisation of schistosomula EVs may be facilitated via different CLRs in a different host. For example, the murine macrophage galactose-type lectin (MGL-1) can bind to LeX [60] while the human MGL cannot [61]. Human MGL binds to LDN motifs, which were absent in our schistosomula EV glycan analyses.

So far, most research on glycosylation of pathogen-derived EVs focussed on lipopolysaccharides of bacterial OMVs [62–65]. Only very recently, the presence of glycoconjugates on the surface of EVs released by the helminth *Fasciola hepatica* was studied using lectin microarrays [66]. Here we performed a more detailed structural analysis of glycans associated with EVs released by a helminth parasite. Using mass spectrometry we showed the presence of mainly complex type N-glycans with LeX motifs as well as oligomannose and high mannose glycans (Figure 3(b)) and the presence of lipid-linked glycans with LeX, pseudo-LeY, and other α3-fucosylated glycan motifs (Figure 5(b)). The EV N-glycan profile was qualitatively very similar to that of whole schistosomula [35]. The overall glycosylation pattern associated with this particular schistosome life stage was reflected in the EVs, however, with differences in relative abundances of the glycans. Biological replicates of the parasite culture and EV isolation generated at two different laboratories (Leiden and Aberystwyth) showed similar N-glycan profiles, confirming the reproducibility of the EV isolation protocol and glycan patterns [6]. Mostly complex glycans with LeX motifs were cleaved

from intact EVs by incubation with PNGase-F (Figure 3 (c)), implicating that these structures were on the EV surface. Glycoconjugates on the EV surface can influence their cellular internalisation, as was shown for bacterial OMV [65], murine hepatic cell line EVs [28], tumour-derived EVs [58,59] and *F. hepatica* adult worm EVs [66]. Interestingly, PNGase F treated EVs were still internalised by moDC via DC-SIGN (Figure 5(a)). This indicates that other glycans with DC-SIGN ligands such as the fucosylated lipid-linked glycans play a role in this process, either specifically or in addition to the N-glycans. Mass spectrometry analysis showed the presence of EV-associated glycolipid-glycans (Figure 5(b)) containing several structures that were reported previously for schistosomula [35], but with more extended higher molecular weight structures. Our data indicate that many of the EV lipid-derived glycans contain motifs such as LeX, pseudo-LeY and other α3-linked fucose containing motifs that can bind to DC-SIGN [42,43], which may explain why PNGase-F treated EVs could still be internalised via DC-SIGN. Furthermore, *S. mansoni* produce various O-glycans [35], which are possibly also present on EVs and contribute to EV-CLR interaction. We therefore suggest that both N-glycans and glycolipid-glycans, and possibly O-glycans, contribute to the interaction of the EVs with DC-SIGN. This interaction is most likely via LeX motifs, which are abundant in these glycan types, with the possible contribution of other α3-fucosylated lipid-glycans.

Interestingly, the complex type N-glycans on the EV surface and many of the glycolipids of the schistosmula EVs contain antigenic glycan motifs that were previously shown to be the target of antibodies of various isotypes during schistosome infection. These motifs include N-glycan core-xylose, LeX, and the various fucosylated glycolipid motifs [67–69]. It is therefore tempting to speculate that EVs can either elicit these antibodies and/or that EVs are targeted by antibodies generated against other, similarly glycosylated, antigens produced by schistosomes during an infection. Antibodies that recognize and bind molecules on the EV surface can facilitate internalisation by APCs, for example via Fc receptors. Antibody-bound EVs can be targeted to different intracellular compartments compared to EVs without antibodies. This has been observed for EVs from the helminth *Heligmosomoides polygyrus* [70]. *H. polygyrus* EVs pre-incubated with antisera were targeted to lysosomes. However, lysosome targeting has also been observed for antigens internalised by DC-SIGN [71]. Another possibility is that EV uptake is enhanced after incubation with antisera, which was observed for *F. hepatica* EVs and RAW264.7 macrophages [66]. Differences in route of

uptake can possibly alter the fate of the EVs and thus possibly influence EV-induced immunomodulation.

Cross-species communication via EVs that contributes to modulation of host immune responses has been described previously for helminths, including *H. polygyrus* [70] and *Nippostrongylus brasiliensis* [72]. In this study, we observed that *S. mansoni* schistosomula EVs are capable of augmenting activation-induced cytokine secretion and surface molecule expression by human moDCs, including both immunostimulatory and regulatory factors (Figure 6). It has been suggested that a delicate balance between benefit for the host and benefit for the parasite contributes to overall survival of the parasite within the host with limited pathology [3]. The induction of pro-inflammatory cytokines is a natural response of the host to the skin-invading pathogen, however, this response is transient. Priming of a protective adaptive immune response is hampered, probably via the induction of regulatory responses by the parasite, such as increased IL-10 release and PD-L1 expression [12], allowing the parasite to develop into mature worms and start egg laying. Different molecules present in the heterogenous EV population may have contributed to the observed augmented immune responses. It is known that DC-SIGN signalling via fucose ligands, which are motifs found on the N-glycan and lipid-glycan structures of the EVs, mainly increases IL-10 and decreases pro-inflammatory responses [73]. In contrast, we observed that blocking DC-SIGN actually decreased pro-inflammatory TNF-α and IL-12 mRNA and did not fully reduce the responses to baseline (Figure 7(e)). Thus, it is likely to assume that schistosomula EVs contain a mix of various (glycosylated) proteins and RNAs (amongst other biological molecules, such as lipids [74]) that all may contribute to a combined effect on host immunity [6]. Indeed, the NTA data as well as the cryo EM show at least a variation in EV size and with or without the thin filaments, and it is tempting to speculate that these different EVs may show variation in their surface glycan profile and may have specific activities on host immunity. Interestingly, since total E/S from schistosomula increases IL-12, IL-6 and IL-10 release as well as CD86 expression by mouse BMDCs [11], it is tempting to suggest that part of the effects of the E/S are mediated by the EVs in that secretion.

In contrast to the strong blocking effect of anti-DC-SIGN antibodies on EV internalisation (Figure 4 and Figure 7(c)), however, blocking DC-SIGN did not significantly alter EV-augmented immune responses during prolonged stimulation (Figure 7(a–b)). The variation we detected among donors in reduction or increase of IL-10 release in the presence of blocking DC-SIGN (Figure 7(a)) was also observed in another study that examined glycan-mediated effects by larval E/S [75]. These donor-specific variances could be associated with intrinsic DC-SIGN levels, which vary highly between and within donors [76]. Furthermore, residual uptake of EVs via other processes such as (macro-) pinocytosis or protein–protein interaction could still have affected the immune activation of moDCs upon prolonged culture (Figure 7(d)). Shorter incubation, however, showed that part of the augmented immune profile of moDCs by schistosomula EVs was indeed dependent on interaction with DC-SIGN (Figure 7(e)) and provides evidence that interaction of glycans on the EV surface with DC-SIGN does play a role in immune modulation of host responses.

In conclusion, our study demonstrates that *S. mansoni* schistosomula release glycosylated EVs that carry LeX, pseudo-LeY, and other fucosylated motifs, and we reveal a distinct role for DC-SIGN in glycan-mediated internalisation of EVs by host immune cells. This interaction contributes to increased pro- and anti-inflammatory responses, substantiating that EVs play a role in host immune regulation by helminths to establish and control infection. Future studies on how EV-associated molecules contribute to immune modulation will further our understanding of parasite–host interactions and may provide insights for vaccine development.

Authors' contributions

M.E.K. contributed to conceiving the study, performed the schistosomula cultures, EV isolations, NTA, cryo EM measurements, moDC isolations/stimulations, ELISAs, flow cytometry, RNA extraction, qPCR, data analysis and drafting of the manuscript. A.J.H. assisted with moDC isolations/differentiation and constructing flow cytometry panels. A.O.F. performed shedding of snails to obtain cercariae and assisted with moDC isolations. D.L.N. performed the N-glycan characterization and assisted with the analysis of the spectra. C.M. K. performed the confocal microscopy and generated the confocal images. R.I.K. performed the cryo EM imaging and assisted with the subsequent analysis. J.J.T. performed the TEM imaging and contributed to the TEM analysis. K.F. H. contributed to the design of experiments, interpretation of the results and correcting the manuscript. E.N.-'tH. contributed to conceiving the study, the design of the experiments, overseeing the EV isolation, interpretation of the results and drafting of the manuscript. H.H.S. and C.H.H. both participated in conceiving the study, the design of the experiments, interpretation of the results and drafting of the manuscript. All authors read and approved the final manuscript.

Disclosure of interest

The authors report no conflict of interest.

ORCID

Marije E. Kuipers http://orcid.org/0000-0001-7012-3004
Esther N.M. Nolte-'t Hoen http://orcid.org/0000-0002-3172-9959
Alwin J. van der Ham http://orcid.org/0000-0002-4532-9120
Arifa Ozir-Fazalalikhan http://orcid.org/0000-0002-0613-8372
Clarize M. de Korne http://orcid.org/0000-0002-8193-0482
Roman I. Koning http://orcid.org/0000-0001-6736-7147
John J. Tomes http://orcid.org/0000-0003-1737-8600
Karl F. Hoffmann http://orcid.org/0000-0002-3932-5502
Hermelijn H. Smits http://orcid.org/0000-0001-9279-2890
Cornelis H. Hokke http://orcid.org/0000-0003-3545-7804

References

[1] Colley DG, Bustinduy AL, Secor WE, et al. Human schistosomiasis. Lancet. 2014;383(9936):2253–2264. .

[2] Maizels RM, Smits HH, McSorley HJ, et al. Modulation of host immunity by helminths: the expanding repertoire of parasite effector molecules. Immunity. 2018;49 (5):801–818.

[3] Mountford AP, Trottein F. Schistosomes in the skin: a balance between immune priming and regulation. Trends Parasitol. 2004;20(5):221–226.

[4] Maizels RM, McSorley HJ. Regulation of the host immune system by helminth parasites. J Allergy Clin Immunol. 2016;138(3):666–675.

[5] Wu Z, Wang L, Li J, et al. Extracellular Vesicle-mediated communication within host-parasite interactions. Front Immunol. 2018;9:3066.

[6] Nowacki FC, Swain MT, Klychnikov OI, et al. Protein and small non-coding RNA-enriched extracellular vesicles are released by the pathogenic blood fluke Schistosoma mansoni. J Extracell Vesicles. 2015;4:28665.

[7] Sotillo J, Pearson M, Potriquet J, et al. Extracellular vesicles secreted by Schistosoma mansoni contain protein vaccine candidates. Int J Parasitol. 2016;46(1):1–5.

[8] Samoil V, Dagenais M, Ganapathy V, et al. Vesicle-based secretion in schistosomes: analysis of protein and microRNA (miRNA) content of exosome-like vesicles derived from Schistosoma mansoni. Sci Rep. 2018;8 (1):3286.

[9] Maizels RM, Yazdanbakhsh M. Immune regulation by helminth parasites: cellular and molecular mechanisms. Nat Rev Immunol. 2003;3(9):733–744.

[10] Hogg KG, Kumkate S, Anderson S, et al. Interleukin-12 p40 secretion by cutaneous CD11c+ and F4/80+ cells is a major feature of the innate immune response in mice that develop Th1-mediated protective immunity to Schistosoma mansoni. Infect Immun. 2003;71(6):3563–3571.

[11] Paveley RA, Aynsley SA, Cook PC, et al. Fluorescent imaging of antigen released by a skin-invading helminth reveals differential uptake and activation profiles by antigen presenting cells. PLoS Negl Trop Dis. 2009;3 (10):e528.

[12] Winkel BMF, Dalenberg MR, de Korne CM, et al. Early induction of human regulatory dermal antigen presenting cells by skin-penetrating schistosoma mansoni cercariae. Front Immunol. 2018;9:2510.

[13] van Niel G, D'Angelo G, Raposo G, et al. Shedding light on the cell biology of extracellular vesicles. Nat Rev Mol Cell Biol. 2018;19(4):213–228.

[14] Egesa M, Lubyayi L, Tukahebwa EM, et al. Schistosoma mansoni schistosomula antigens induce Th1/Pro-inflammatory cytokine responses. Parasite Immunol. 2018;40(12):e12592.

[15] Jenkins SJ, Hewitson JP, Ferret-Bernard S, et al. Schistosome larvae stimulate macrophage cytokine production through TLR4-dependent and -independent pathways. Int Immunol. 2005;17(11):1409–1418.

[16] Paveley RA, Aynsley SA, Turner JD, et al. The Mannose Receptor (CD206) is an important pattern recognition receptor (PRR) in the detection of the infective stage of the helminth Schistosoma mansoni and modulates IFNgamma production. Int J Parasitol. 2011;41(13–14):1335–1345.

[17] van Die I, Cummings RD. The mannose receptor in regulation of helminth-mediated host immunity. Front Immunol. 2017;8:1677.

[18] Kaisar MMM, Ritter M, Del Fresno C, et al. Dectin-1/2-induced autocrine PGE2 signaling licenses dendritic cells to prime Th2 responses. PLoS Biol. 2018;16(4): e2005504.

[19] Bloem K, Vuist IM, van den Berk M, et al. DCIR interacts with ligands from both endogenous and pathogenic origin. Immunol Lett. 2014;158(1–2):33–41.

[20] van Liempt E, van Vliet SJ, Engering A, et al. Schistosoma mansoni soluble egg antigens are internalized by human dendritic cells through multiple C-type lectins and suppress TLR-induced dendritic cell activation. Mol Immunol. 2007;44(10):2605–2615.

[21] van Die I, van Vliet SJ, Nyame AK, et al. The dendritic cell-specific C-type lectin DC-SIGN is a receptor for Schistosoma mansoni egg antigens and recognizes the glycan antigen Lewis x. Glycobiology. 2003;13(6):471–478.

[22] Everts B, Hussaarts L, Driessen NN, et al. Schistosome-derived omega-1 drives Th2 polarization by suppressing protein synthesis following internalization by the mannose receptor. J Exp Med. 2012;209(10):1753–67, S1.

[23] Geijtenbeek TB, Gringhuis SI. C-type lectin receptors in the control of T helper cell differentiation. Nat Rev Immunol. 2016;16(7):433–448.

[24] Jang-Lee J, Curwen RS, Ashton PD, et al. Glycomics analysis of schistosoma mansoni egg and cercarial secretions. Mol Cell Proteomics. 2007;6(9):1485–1499.

[25] Gerlach JQ, Griffin MD. Getting to know the extracellular vesicle glycome. Mol Biosyst. 2016;12 (4):1071–1081.

[26] Williams C, Royo F, Aizpurua-Olaizola O, et al. Glycosylation of extracellular vesicles: current knowledge, tools and clinical perspectives. J Extracell Vesicles. 2018;7(1):1442985.

[27] Freitas D, Balmaña M, Poças J, et al. Different isolation approaches lead to diverse glycosylated extracellular vesicle populations. J Extracell Vesicles. 2019;8:1.

[28] Williams C, Pazos R, Royo F, et al. Assessing the role of surface glycans of extracellular vesicles on cellular uptake. Sci Rep. 2019;9:1.

[29] Shimoda A, Sawada S-I, Sasaki Y, et al. Exosome surface glycans reflect osteogenic differentiation of mesenchymal stem cells: profiling by an evanescent field fluorescence-assisted lectin array system. Sci Rep. 2019;9:1.

[30] Colley DG, Wikel SK. Schistosoma mansoni: simplified method for the production of schistosomules. Exp Parasitol. 1974;35(1):44–51.

[31] Consortium E-T, Van Deun J, Mestdagh P, et al. EV-TRACK: transparent reporting and centralizing knowledge in extracellular vesicle research. Nat Methods. 2017;14(3):228–232.

[32] Schindelin J, Arganda-Carreras I, Frise E, et al. Fiji: an open-source platform for biological-image analysis. Nat Methods. 2012;9(7):676–682.

[33] Hussaarts L, Smits HH, Schramm G, et al. Rapamycin and omega-1: mTOR-dependent and -independent Th2 skewing by human dendritic cells. Immunol Cell Biol. 2013;91(7):486–489.

[34] Wilbers RHP, Westerhof LB, van Noort K, et al. Production and glyco-engineering of immunomodulatory helminth glycoproteins in plants. Sci Rep. 2017;7:1.

[35] Smit CH, van Diepen A, Nguyen DL, et al. Glycomic analysis of life stages of the human parasite schistosoma mansoni reveals developmental expression profiles of functional and antigenic glycan motifs. Mol Cell Proteomics. 2015;14(7):1750–1769.

[36] Ceroni A, Maass K, Geyer H, et al. Glycoworkbench: a tool for the computer-assisted annotation of mass spectra of glycans †. J Proteome Res. 2008;7(4):1650–1659.

[37] Bustin SA, Benes V, Garson JA, et al. The MIQE guidelines: minimum information for publication of quantitative real-time PCR experiments. Clin Chem. 2009;55 (4):611–622.

[38] Simonsen JB. Pitfalls associated with lipophilic fluorophore staining of extracellular vesicles for uptake studies. J Extracell Vesicles. 2019;8(1):1582237.

[39] Hokke CH, van Diepen A. Helminth glycomics - glycan repertoires and host-parasite interactions. Mol Biochem Parasitol. 2017;215:47–57.

[40] van Kooyk Y, Geijtenbeek TBH. DC-SIGN: escape mechanism for pathogens. Nat Rev Immunol. 2003;3 (9):697–709.

[41] Everts B, Perona-Wright G, Smits HH, et al. Omega-1, a glycoprotein secreted by Schistosoma mansoni eggs, drives Th2 responses. J Exp Med. 2009;206(8):1673–1680.

[42] Meevissen MHJ, Driessen NN, Smits HH, et al. Specific glycan elements determine differential binding of individual egg glycoproteins of the human parasite Schistosoma mansoni by host C-type lectin receptors. Int J Parasitol. 2012;42(3):269–277.

[43] Meyer S, van Liempt E, Imberty A, et al. DC-SIGN mediates binding of dendritic cells to authentic Pseudo-Lewis Y glycolipids of Schistosoma mansoni Cercariae, the first parasite-specific ligand of DC-SIGN. J Biol Chem. 2005;280(45):37349–37359.

[44] Dorsey CH, Cousin CE, Lewis FA, et al. Ultrastructure of the Schistosoma mansoni cercaria. Micron. 2002;33 (3):279–323.

[45] Turner L, Bitto NJ, Steer DL, et al. Helicobacter pylori outer membrane vesicle size determines their mechanisms of host cell entry and protein content. Front Immunol. 2018;9:1466.

[46] Liu J, Zhu L, Wang J, et al. Schistosoma japonicum extracellular vesicle miRNA cargo regulates host macrophage functions facilitating parasitism. PLoS Pathog. 2019;15(6):e1007817.

[47] Dunne DW, Opinion CA. - A worm's eye view of the immune system: consequences for evolution of human autoimmune disease. Nat Rev Immunol. 2005;5 (5):420–426.

[48] Kifle DW, Pearson MS, Becker L, et al. Proteomic analysis of two populations of Schistosoma mansoni-derived extracellular vesicles: 15k pellet and 120k pellet vesicles. Mol Biochem Parasitol. 2020;236:111264.

[49] Hunter RC, Beveridge TJ. High-resolution visualization of Pseudomonas aeruginosa PAO1 biofilms by freeze-substitution transmission electron microscopy. J Bacteriol. 2005;187(22):7619–7630.

[50] Liu Y, Hidaka E, Kaneko Y, et al. Ultrastructure of Helicobacter pylori in human gastric mucosa and H. pylori-infected human gastric mucosa using transmission electron microscopy and the high-pressure freezing-freeze substitution technique. J Gastroenterol. 2006;41(6):569–574.

[51] Gui MJ, Dashper SG, Slakeski N, et al. Spheres of influence: porphyromonas gingivalis outer membrane vesicles. Mol Oral Microbiol. 2016;31(5):365–378.

[52] Wang L, Li Z, Shen J, et al. Exosome-like vesicles derived by Schistosoma japonicum adult worms mediates M1 type immune- activity of macrophage. Parasitol Res. 2015;114(5):1865–1873.

[53] Zhu L, Liu J, Dao J, et al. Molecular characterization of S. japonicum exosome-like vesicles reveals their regulatory roles in parasite-host interactions. Sci Rep. 2016;6:25885.

[54] Zhu S, Wang S, Lin Y, et al. Release of extracellular vesicles containing small RNAs from the eggs of Schistosoma japonicum. Parasit Vectors. 2016;9(1):574.

[55] van Stijn CM, Meyer S, van den Broek M, et al. Schistosoma mansoni worm glycolipids induce an inflammatory phenotype in human dendritic cells by cooperation of TLR4 and DC-SIGN. Mol Immunol. 2010;47(7–8):1544–1552.

[56] Garcia-Vallejo JJ, van Kooyk Y. The physiological role of DC-SIGN: a tale of mice and men. Trends Immunol. 2013;34(10):482–486.

[57] Gazi U, Martinez-Pomares L. Influence of the mannose receptor in host immune responses. Immunobiology. 2009;214(7):554–561.

[58] Horrevorts SK, Stolk DA, Ven RV, et al. Glycan-modified melanoma-derived apoptotic extracellular vesicles as antigen source for anti-tumor vaccination. Cancers (Basel). 2019;11:9.

[59] Dusoswa SA, Horrevorts SK, Ambrosini M, et al. Glycan modification of glioblastoma-derived extracellular vesicles enhances receptor-mediated targeting of dendritic cells. J Extracell Vesicles. 2019;8(1):1648995.

[60] Eriksson M, Serna S, Maglinao M, et al. Biological evaluation of multivalent lewis X-MGL-1 interactions. Chembiochem. 2014;15(6):844–851.

[61] Marcelo F, Supekar N, Corzana F, et al. Identification of a secondary binding site in human macrophage galactose-type lectin by microarray studies: implications for the molecular recognition of its ligands. J Biol Chem. 2019;294(4):1300–1311.

[62] Kaparakis M, Turnbull L, Carneiro L, et al. Bacterial membrane vesicles deliver peptidoglycan to NOD1 in epithelial cells. Cell Microbiol. 2010;12(3):372–385.

[63] Stevenson TC, Cywes-Bentley C, Moeller TD, et al. Immunization with outer membrane vesicles displaying conserved surface polysaccharide antigen elicits broadly antimicrobial antibodies. Proc Natl Acad Sci U S A. 2018;115(14):E3106–E15.

[64] Kuipers ME, Hokke CH, Smits HH, et al. Pathogen-derived extracellular vesicle-associated molecules that affect the host immune system: an overview. Front Microbiol. 2018;9:2182.

[65] O'Donoghue EJ, Sirisaengtaksin N, Browning DF, et al. Lipopolysaccharide structure impacts the entry kinetics of bacterial outer membrane vesicles into host cells. PLoS Pathog. 2017;13(11):e1006760.

[66] de la Torre-escudero E, Gerlach JQ, Bennett APS, et al. Surface molecules of extracellular vesicles secreted by the helminth pathogen Fasciola hepatica direct their internalisation by host cells. PLoS Negl Trop Dis. 2019;13(1):e0007087.

[67] Nkurunungi G, van Diepen A, Nassuuna J, et al. Microarray assessment of N-glycan-specific IgE and IgG profiles associated with Schistosoma mansoni infection in rural and urban Uganda. Sci Rep. 2019;9(1):3522.

[68] van Diepen A, Smit CH, van Egmond L, et al. Differential anti-glycan antibody responses in Schistosoma mansoni-infected children and adults studied by shotgun glycan microarray. PLoS Negl Trop Dis. 2012;6(11):e1922.

[69] Yang YY, Li XH, Brzezicka K, et al. Specific anti-glycan antibodies are sustained during and after parasite clearance in Schistosoma japonicum-infected rhesus macaques. PLoS Negl Trop Dis. 2017;11(2):e0005339.

[70] Coakley G, McCaskill JL, Borger JG, et al. Extracellular vesicles from a helminth parasite suppress macrophage activation and constitute an effective vaccine for protective immunity. Cell Rep. 2017;19(8):1545–1557.

[71] Engering A, Geijtenbeek TB, van Vliet SJ, et al. The dendritic cell-specific adhesion receptor DC-SIGN internalizes antigen for presentation to T cells. J Immunol. 2002;168(5):2118–2126.

[72] Eichenberger RM, Ryan S, Jones L, et al. Hookworm secreted extracellular vesicles interact with host cells and prevent inducible colitis in mice. Front Immunol. 2018;9:850.

[73] Gringhuis SI, Kaptein TM, Wevers BA, et al. Fucose-specific DC-SIGN signalling directs T helper cell type-2 responses via IKKepsilon- and CYLD-dependent Bcl3 activation. Nat Commun. 2014;5:3898.

[74] Giera M, Kaisar MMM, Derks RJE, et al. The Schistosoma mansoni lipidome: leads for immunomodulation. Anal Chim Acta. 2018;1037:107–118.

[75] Turner JD, Meurs L, Dool P, et al. Schistosome infection is associated with enhanced whole-blood IL-10 secretion in response to cercarial excretory/secretory products. Parasite Immunol. 2013;35(5–6):147–156.

[76] Baribaud F, Pohlmann S, Leslie G, et al. Quantitative expression and virus transmission analysis of DC-SIGN on monocyte-derived dendritic cells. J Virol. 2002;76(18):9135–9142.